The University Of Sheffield.

Kinetically Locked Metallomacrocycles as Self-Assembled Hosts for Biomolecules

By

Haslina Ahmad

A Thesis Submitted for the Degree of Doctor of Philosophy

August 2009

Department of Chemistry
University of Sheffield
Brook Hill
Sheffield
S3 7HF

Abstract

The first part of this thesis is concerned with the synthesis of a series of mononuclear ruthenium(II) and rhenium(I) complexes incorporating 2,2';4,4";4",4"'-quaterpyridyl ligand. The electronic and spectroscopic behaviour of the complexes is discussed. These complexes possess extremely interesting photophysical and electrochemical properties in themselves which can be exploited for the construction of higher order arrays. In order to compare the DNA binding ability of the metallomacrocycles constructed from the mononuclear building blocks, the binding of these complexes with CT-DNA has been studied using a variety of techniques including viscometry, continuous variation analysis (Job plots), UV-Visible absorption and luminescence emission spectroscopy, ITC and luminescence lifetime. In all cases the complexes bind *via* intercalation, with an affinity around 10^5 M^{-1} to 10^6 M^{-1}.

In consequent chapters, a series of self-assembled metallomacrocycles that incorporate ruthenium(II) and rhenium(I) metal centres are reported. The electronic and spectroscopic behaviour of the complexes is again discussed and compared to the respective building blocks. These complexes also possess extremely interesting photophysical properties and concomitant studies with biomolecules such as adenine, ATP, GTP, cGMP and uridine revealed that these macrocycles are able to act as hosts for such molecules in water. Indeed, the macrocycles have demonstrated the capability of binding to oligonucleotides, such as CT-DNA with binding affinities comparable to other mononuclear DNA binding substrates. Strikingly, the binding affinity and binding mode can be modulated upon changing the ancillary ligands of the macrocycles.

Publication Arising from this Work

D. Ghosh, H. Ahmad and J. A. Thomas, *Chem. Commun.*, **2009**, 2947-2949. "Kinetically locked luminescent metallomacrocycles as duplex DNA binding substrates"

Acknowledgements

In the first place I would like to record my gratitude to my wonderful supervisor, Jim Thomas for his supervision, advice, and guidance from the very early stage of this research as well as giving me extraordinary experiences through out the work. Above all and the most needed, he provided me unflinching encouragement and support in various ways. I am indebted to him more than he knows.

Thanks to Thomas group, past and present: Tim and Fingers who helped me a lot when I first started in Thomas group, Tom, Martin, Hanan, Adel, Dipesh, Ahmed, Mike, Reddy and Phil for creating such a great friendship at the office. A big list of mentions for various other people from the last few years, in no particular order: Abdu, Katie, Mehdi, Aisyah, Suriani, Ruth, Ian, Zoe, Yussofe, Sofia Derossi, Nick Tart, Blanka and Chris.

I would also like to thank the technical and academic staff in the Chemistry Department for all their help over the years; in particular, Mohammed for helping me out in using the lifetime machine and Harry Adams for the X-ray crystallography.

My parents deserve special mention for their inseparable support and prayers. Not to be forgotten, Lin and Rizal, for being supportive and caring siblings.

Words fail me to express my appreciation to my great husband, Firdaus whose dedication, love and persistent confidence in me, has taken the load off my shoulder. Thank you for being a good listener and accompanying me in my "Chemistry World". I owe him as he has unselfishly sacrificed his ambitions for these few years.

Declaration

Except where specific references have been made to other sources, the work in this thesis is the original work of the author. It has not been submitted, in whole or in part, for any other degree. Certain results have already been published in peer review journal.

Haslina Ahmad

August 2009

Abbreviations

A	Adenine
ATP	Adenosine-5'-triphosphate
AMP	Adenosine monophosphate
ADP	Adenosine diphosphate
bp	Base pairs
bpy	2,2'-bipyridine
C	Cytosine
cAMP	Cyclic adenosine-3',5'-monophosphate
cGMP	Cyclic guanosine-3',5'-monophosphate
CH_3CN	Acetonitrile
CT-DNA	Calf thymus DNA
CTP	Cytidine triphosphate
CV	Cyclic voltammetry
DMF	Dimethylformamide
DMSO	Dimethylsulfoxide
DNA	Deoxyribose nucleic acid
dppn	Benzodipyridophenazine
dppz	Dipyrido [3,2-a:2',3'-o] phenazine
dpq	1,10-phenanthroline-5,6-dione
E_p	Peak potential
ES-MS	Electrospray mass spectrometry
FAB-MS	Fast atom bombardment mass spectrometry
G	Guanine
GTP	Guanosine-5'-triphosphate
HOMO	Highest occupied molecular orbital
ITC	Isothermal titration calorimetry
LD	Linear dichroism
LUMO	Lowest unoccupied molecular orbital
MLCT	Metal-to-ligand charge transfer

MS	Mass spectrometry
MWCO	Molecular weight cut off
NMR	Nuclear magnetic resonance
phen	1,10-phenanthroline
qtpy	2,2';4,4";4",4"'- quaterpyridyl
T	Thymine
TTP	Thymidine triphosphate
UV	Ultra violet
Vis	Visible

Table of Contents

1 Introduction

This chapter offers a general overview of the issues relevant to this report. This includes a background to supramolecular chemistry, discussion of self-assembly process in the design of the supramolecular architectures and a review of the use of metal complexes as hosts and sensors.

1.1 Supramolecular Chemistry

Supramolecular chemistry has been explored vigorously since the introduction of this interdisplinary field over last 30 years ago. Just as conventional chemistry is concerned with bringing atoms together to create new molecules, supramolecular chemistry is concerned with bringing molecules together in new functional molecular architectures, usually using non-covalent weak intermolecular contacts, such as hydrogen bonds, aromatic л-stacking, dipolar interactions and van der Waals forces. The pioneering work of Pedersen, Lehn and Cram on the development of various host complexes that selectively bind specific guests was cited as an important contribution in the start of modern supramolecular chemistry.[1] Supramolecular chemistry has been defined by one of its key players, Jean-Marie Lehn, as the 'chemistry of molecular assemblies and of the intermolecular bond'.[2]

Supramolecular phenomena are readily found in nature. Supramolecular chemistry is partly inspired by biological ensembles in nature such as collagen and enzymes or protein assemblies in general. First and foremost among the motivations for exploring supramolecular chemistry is the desire to synthesise new robust, functional, and technologically important materials by mimicking nature. Scientists analysing natural systems have noted two major principles adapted for supramolecular chemistry: molecular recognition and self-assembly. The promise of useful molecular devices remains a motivation for the continuing

widespread interest in the field. Supramolecular species have been used in a wide variety of applications, such as catalysis, medicine, data storage and processing, to name but a few. Much of this work has focused on molecular design for achieving complementarily between single molecule hosts and guests.

1.2 Self-Assembly

Self-assembly, which is the spontaneous formation of well-defined molecular architectures from predetermined building blocks, has been widely utilised in the synthesis of supramolecular species.

During recent years, synthetic chemists have realised the potential application of self-assembly processes in the formation of higher order arrays. The advantages offered by this approach over traditional stepwise synthetic methods make this approach desirable: tedious and repetitive processes used in conventional organic methods results in decreases in overall yields. However with self-assembly process, the controlled use of intermolecular forces provides an efficient method for creating large, organised supramolecular systems, unhindered by the problems associated with multisteps classical organic route, thus giving high yields. Moreover, this approach, resulting in the generation of supramolecular assemblies under thermodynamic control, usually requires fewer steps than analogous covalent syntheses. The equilibrium present between reactants and products enables the kinetically labile intermolecular interactions to rearrange within the assembly, with error-checking and self-correction in the structures.

The ultimate inspiration for investigations into supramolecular self-assembly emanates from self-assembly of many living systems available in nature. One such example is the tobacco mosaic virus, which consists of a helical virus particle with a central strand of RNA sheathed by 2130 identical protein subunits. Each of these subunits contains 158 amino acids. This virus shows remarkable biological self-assembly process as it is able to self-reassemble accurately, and regain full functionality, after being decomposed into its component parts.[2]

Previous research into the self-assembly of supramolecular clusters has utilised weak interations such as hydrogen bonding, π-π stacking interactions, electrostatic forces, van der Waals forces and hydrophobic/hydrophilic interactions. Early example of such work include Rebek's self assembling "tennis ball" capsules[3] (**Figure 1.1**).

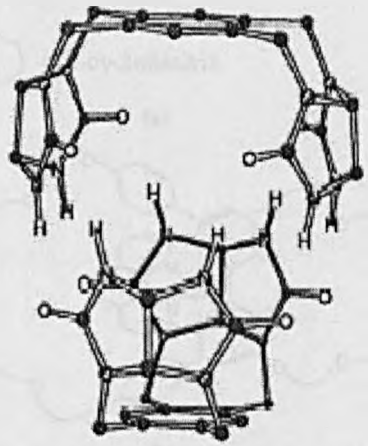

Figure 1.1: Rebek's "tennis ball".

This work has shown that multiple hydrogen-bonding interactions are ideal for the strict self-assembly of closed spherical molecules and capsules. This is due to the relatively weak, but directional nature of the interaction. Rebek's "tennis ball" capsules consists of two curved diphenylglycouril units linked by a durene based (1,2,4,5-tetramethyl benzene-based) spacer. This tennis ball shaped dimer was spontaneously self-assembled in both solution and in the solid state.

It was in 1980s when research into metal-ligand coordination interactions began as a way of directing the self-assembly processes. With a vast number of transition metals and multidentate ligands available, this approach provides versatility in the design of structures. Also this approach offers the potential of introducing functionality such as redox activity, photochemistry, electrochemistry *etc.* into the end product.

Some of the earliest examples of metal-directed self-assembly included the synthesis of a β-cyclodextrin rotaxane with Co(III) coordinated stoppers by Ogino *et al.* in 1981[4] and the Cu(I) directed assembly of a catenane by Sauvage *et al.* in 1983[5] (**Figure 1.2**).

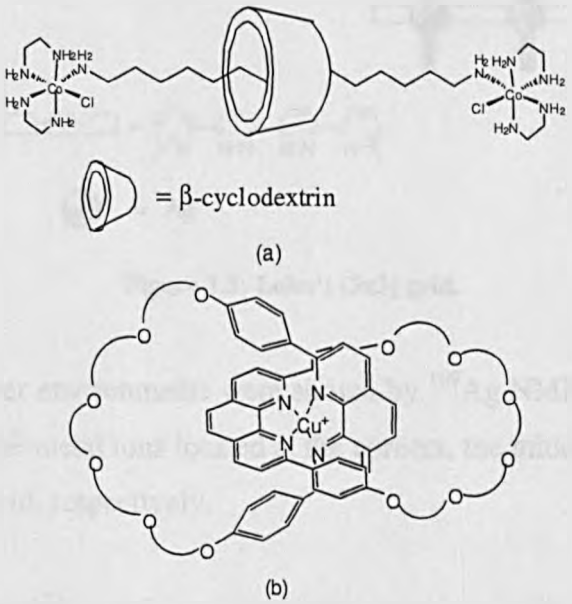

Figure 1.2: (a) Ogino's rotaxane. (b) Sauvage's Cu(I) containing catenane.

This work continued into more complex and elegant structures constructed by individual groups working in this area. A number of rack, ladder and grid structures have been produced *via* self-assembly. In 1994, Lehn *et al.*[6] synthesised a [3x3] grid system. The mixture of 6,6'-bis[2-(6-methylpyridyl)]-3,3'-bipyridizine ligands and 1.5 equivalents of $AgCF_3SO_3$ self-assembles to give the grid-like structure (**Figure 1.3**).

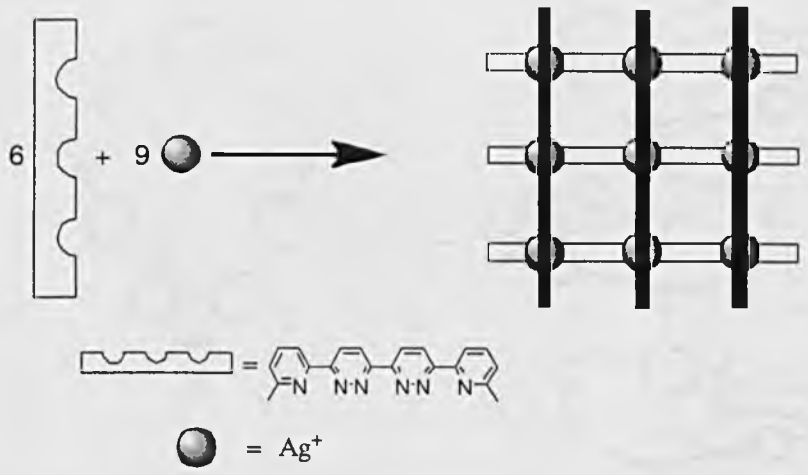

Figure 1.3: Lehn's [3x3] grid.

Three distinct silver environments were shown by ^{109}Ag NMR studies in a 4:4:1 ratio assigned to the metal ions located at the corners, the middle of each face and the centre of the grid, respectively.

Lehn and co-workers[7] have also looked at the systems consisting of two different ligands, one rod-like rigid linear ligands built on 2,2'-bipyridine and the other macrocyclic 1,10-phenanthroline components. In the presence of copper(I) ions, the rigid linear ligands and macrocyclic components self-assembled to produce rigid-rack multimetallic complexes of rotaxane (**Figure 1.4**).

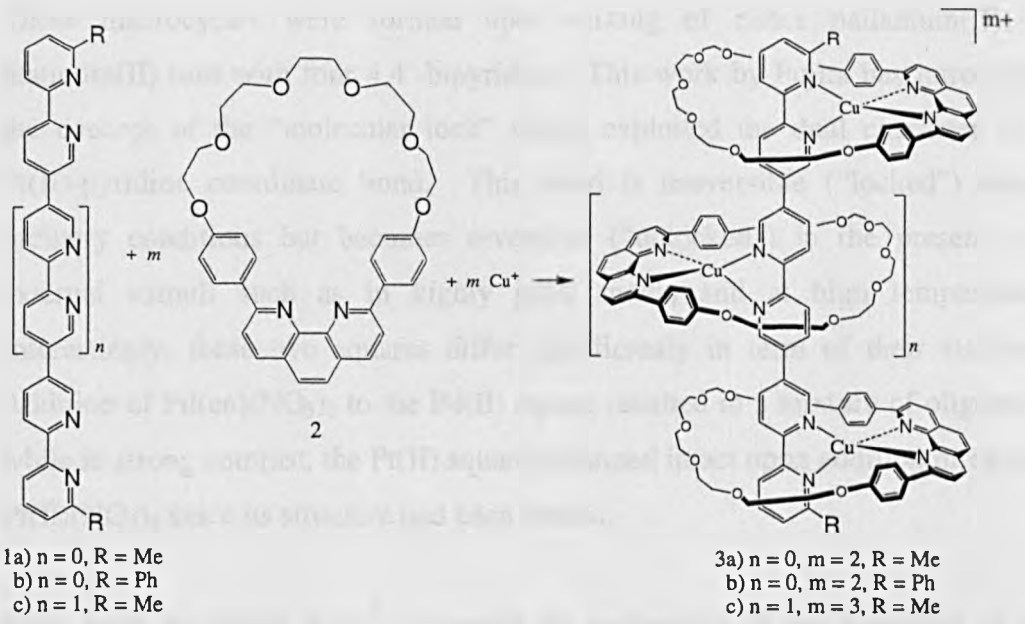

Figure 1.4: Self-assembled of a rigid-rack multimetallic complexes of rotaxane.

The utilisation of the self-assembly process in the construction of this rigid-rack like complexes illustrates the potential of this concept in the designing of more complex, higher ordered arrays.

In 1990, Fujita *et al.*[8] reported the synthesis of a tetranuclear palladium(II) and platinum(II) square *via* self-assembly process (**Figure 1.5**).

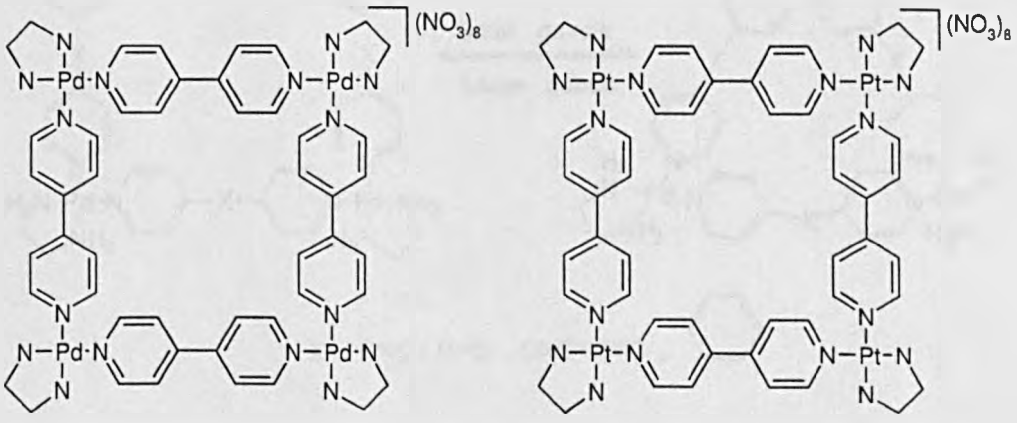

Figure 1.5: Fujita molecular squares.

These macrocycles were formed upon mixing of either palladium(II) or platinum(II) ions with four 4,4'-bipyridine. This work by Fujita has introduced the concept of the "molecular lock" which exploited the dual character of a Pt(II)-pyridine coordinate bond. This bond is irreversible ("locked") under ordinary conditions but becomes reversible ("unlocked") in the presence of external stimuli such as in highly polar media and at high temperature. Interestingly, these two squares differ significantly in term of their stability. Addition of $Pd(en)(NO_3)_2$ to the Pd(II) square resulted in a mixture of oligomers while in strong contrast, the Pt(II) square remained intact upon addition of excess $Pt(II)(NO_3)_2$ since its structure had been locked.

Later work by Fujita *et al.*[9] suggested the probability of the formation of an equilibrium structures tetranuclear squares and trinuclear triangles (**Figure 1.6**). This was later explained by Hong *et al.*[10] who found that the equilibration is controlled by molecular recognition and is indeed concentration dependent. The triangles are favoured in the presence of small guests and at lower concentration. In contrast, the squares are formed in the presence of large guests such as 1,3-adamantanedicarboxylic acid and at higher concentration.

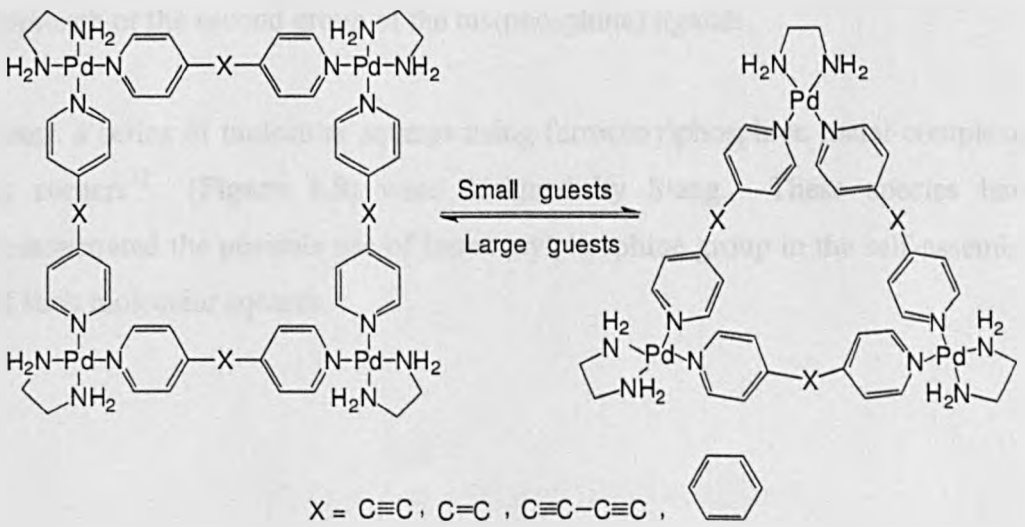

Figure 1.6: An equilibration between self-assembled molecular squares and triangles.

In 1994, Stang *et al.*[11] synthesised similar structures (**Figure 1.7**) but with phosphine protected corners. These phosphine containing species were highly soluble in organic solvents, but not in aqueous solvents.

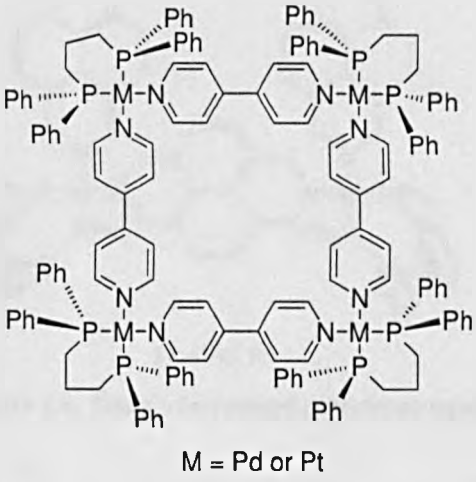

Figure 1.7: Stang's molecular squares.

Attempts to replace the 4,4'-bipyridine with pyrazine ligand resulted in the formation of just the monomer although at longer reaction times and at higher temperatures. This is due to the steric interaction of the phenyl groups of the bis(phosphine) ligands, which in the case of smaller pyrazine unit hindered the approach of the second group of the bis(phosphine) ligands.

Later, a series of molecular squares using ferrocenylphosphine metal complexes as corners[12] (**Figure 1.8**) were designed by Stang. These species have demonstrated the possible use of ferrocenylphosphine group in the self-assembly of such molecular squares.

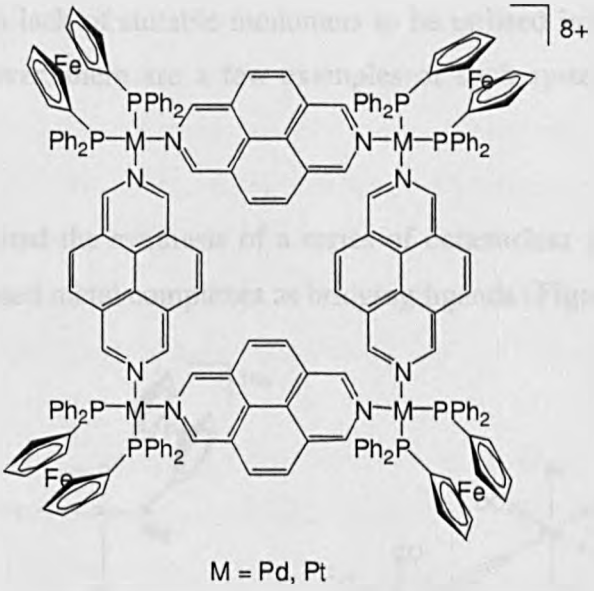

Figure 1.8: Stang's ferrocenyl containing squares.

In 1995, Hupp *et al.*[13] synthesised a series of rhenium containing squares (**Figure 1.9**). This was done by simply mixing $Re(CO)_5Cl$ with either 4,4'-bipyridine, 1,2-bis-*trans*-(4'-pyridyl)ethylene or pyrazine to give around 95 % yields of the square macrocycles. The X-ray crystallography data obtained for pyrazine containing square reveals a slight distortion in the square geometry, with the N-Re-N angles of 85.6° rather 90°.

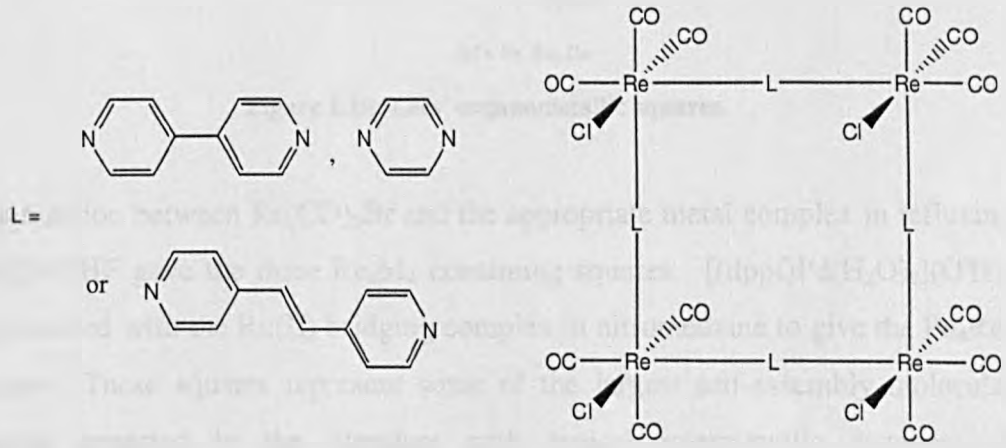

Figure 1.9: Hupp's rhenium containing squares.

Given that Ru^{II} centres are kinetically inert, there is obviously not much literature on self-assembly involving the ruthenium(II)-based complexes, although such metal complexes have rich electrochemical and photophysical properties.[14] This

is probably due to lack of suitable monomers to be utilised in the self-assembly processes. However, there are a few examples of such system that are worth mentioning here.

Lees *et al.*[15] reported the synthesis of a series of octanuclear molecular squares with terpyridyl based metal complexes as bridging ligands (**Figure 1.10**).

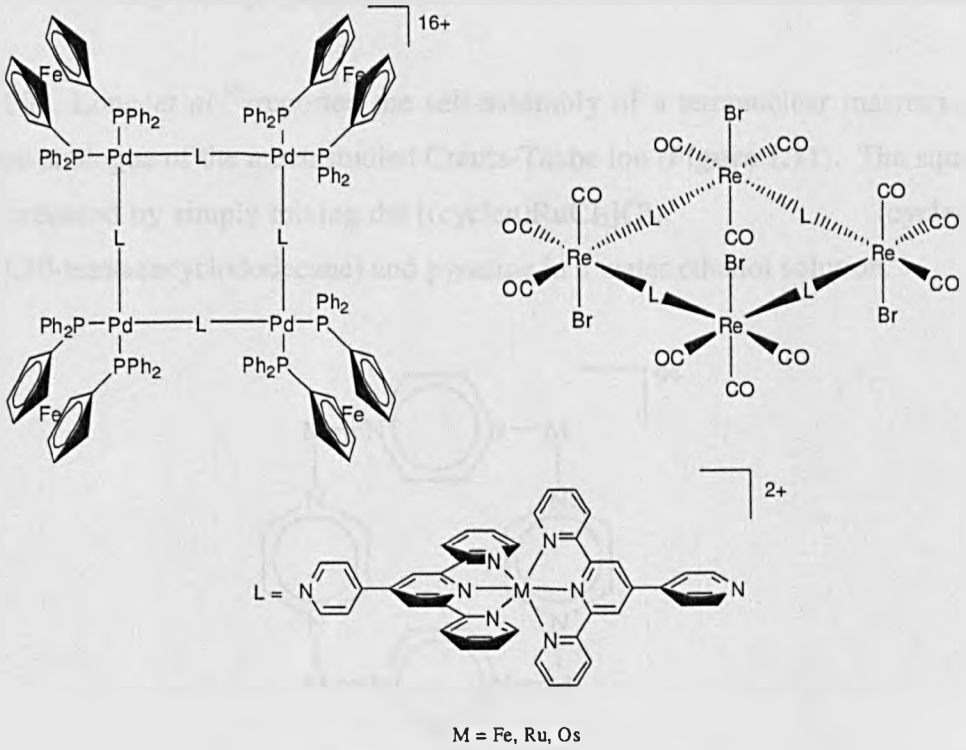

Figure 1.10: Lees' organometallic squares.

The reaction between $Re(CO)_5Br$ and the appropriate metal complex in refluxing MeCN-THF gave the three Re_4M_4 containing squares. $[(dppf)Pd(H_2O)_2](OTf)_2$ was reacted with the Ru(II) bridging complex in nitromethane to give the Pd_4Ru_4 square. These squares represent some of the largest self-assembly molecular squares reported in the literature with typical intermetallic distances of approximately 21Å. However, the arrangement of the terpyridyl units around the center metals results in much smaller internal cavities for these squares.

The photophysical studies show no detectable solution luminescence at room temperature for the Pd(II), Fe(II) and Ru(II) containing squares even though both

the pyridylterpyridine ligand and the Re corner units are luminescent on their own. This is down to the existence of metal-centered (MC) states lying in close to the MLCT states, thus provide an efficient, non-radiative decay pathway. However, the Os(II) containing square shows room temperature luminescence which is assigned to an Os(II) MLCT transition. This is due to stronger ligand field and lower oxidation potential of Os(II) compared to Ru(II) and Fe(II) which resulted in a large energy gap between the MLCT and Os(II) metal centred states.

In 2002, Long *et al.*[16] reported the self-assembly of a tetranuclear macrocyclic square analogue of the much studied Creutz-Taube ion (**Figure 1.11**). The square was prepared by simply mixing the $[(cyclen)RuCl_2]Cl_6$ (cyclen = 1,4,7,10-tetraazacyclododecane) and pyrazine in a water:ethanol solution.

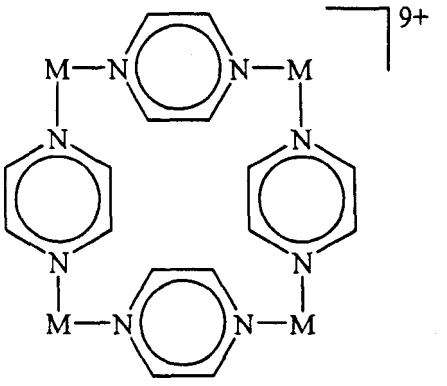

Figure 1.11: A tetranuclear macrocyclic square analogue of Creutz-Taube ion.

Crystallographic studies reveal a regular square structure with the Ru-N(pyrazine) of 2.020 and 2.049 Å, resulting in two distinct Ru atoms with basically similar coordination geometry. This indicates that this square is actually valence delocalised with four equivalent $Ru^{2.25+}$ centres. Likewise, comproportionation constants derived from the electrochemical data support the assignment of this square as a class III mixed-valence complex.[16] Surprisingly, its electronic absorption spectrum shows no strong absorption bands in the near

infra-red spectrum suggesting there is no intermetallic interaction occurring within the mixed valence states of this complex.

On the other hand, Thomas *et al.*[17] have reported a kinetically locked metallomacrocycles incorporating adenine based ligands through self-assembly using a [Ru([9]ane-S_3)] as templating moiety (**Figure 1.12**). The formation of the macrocyclic trimers has been evidenced from NMR and FAB-MS spectrometry studies. In addition, it was found that for suitably hindered adenine derivatives such as adenosine, the synthetic procedure appears to be general.

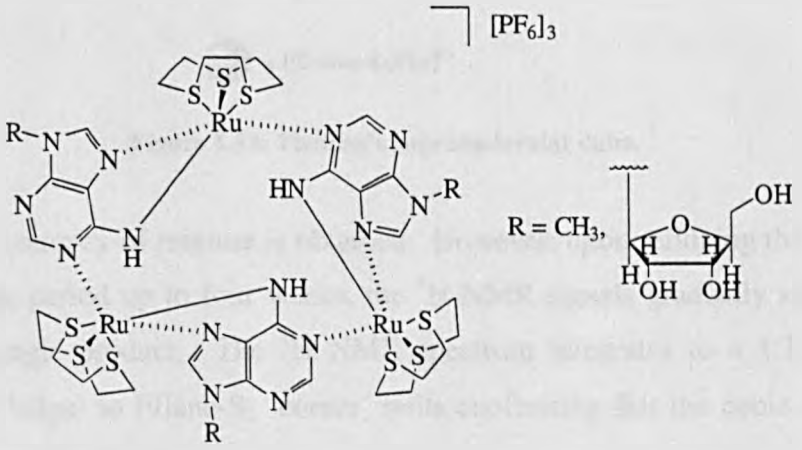

Figure 1.12: Metallomacrocycles incorporating adenine based ligands.

The coordination-driven methodology is not restricted to the formation of self-assembled molecular squares and molecular arrays. Extensive research has gone into the construction of self-assembling three dimensional supramolecular entities. In 1998, Thomas *et al.*[18] reported a self-assembly of a supramolecular cube made of 20 components. A reaction of [Ru([9]ane-S_3)Cl_2(DMSO)] and bipyridine in 8:12 ratio in nitromethane yielded the desired cube (**Figure 1.13**).

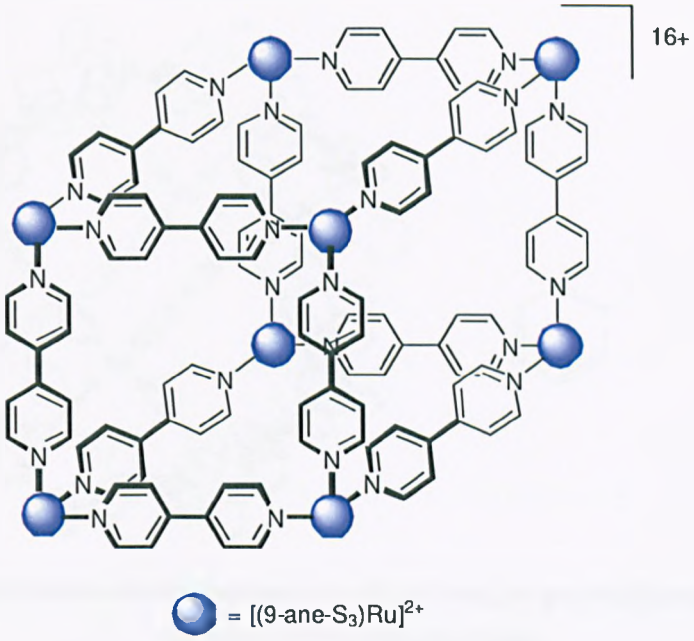

Figure 1.13: Thomas's supramolecular cube.

Initially, a complex of mixture is obtained. However, upon refluxing the mixture for a longer period up to four weeks, the ^{1}H NMR signals gradually simplifies, giving a single product. The ^{1}H NMR spectrum integrates to a 1:1 ratio of bipyridine 'edge' to [9]ane-S_3 'corner' units confirming that the cubic structure has self-assembled.

More recent work in Fujita group involving naked palladium centres and V-shaped ligands to afford finite spherical coordination network that is based on cuboctahedral geometry.[19] The cuboctahedron network consists of 36 components; 12 equivalent metal centres and 24 equivalent pyridyl ligands (**Figure 1.14**).

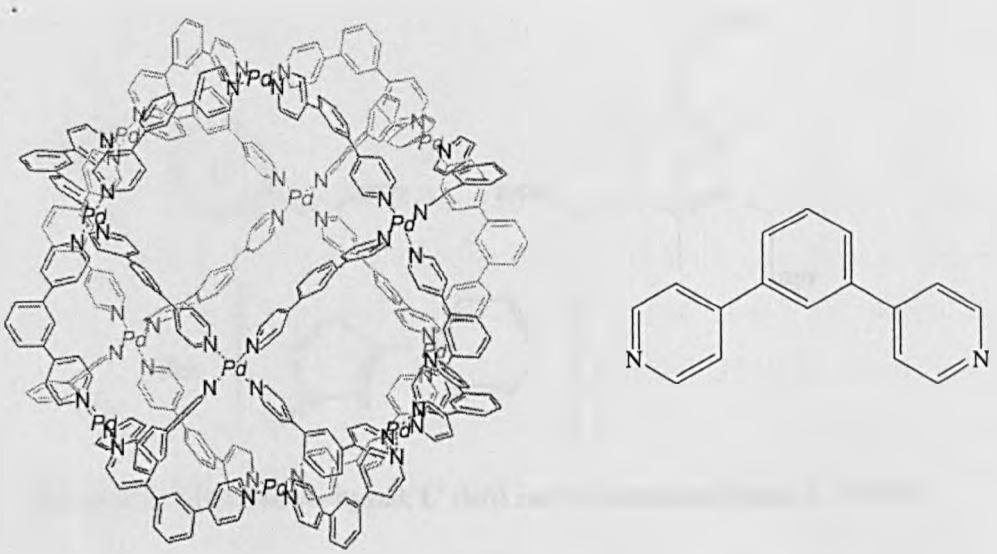

Figure 1.14: Fujita's cuboctahedron network (left) and the pyridyl ligand used for the formation of the structure (right).

The formation of a single product was confirmed by ^{1}H NMR spectroscopy which shows only five signals correspond to protons of the ligands. Moreover, there is hardly fragmentation observed in the mass spectrometry, except the dissociation of counter anions, which demonstrated the robustness of this species in solution.

Ward and co-workers have also synthesised impressive examples of polyhedral cage complexes that are either homoleptic or heteroleptic with respect to ligand composition.[20] The respective ligands that involved in this work are shown in **Figure 1.15**.

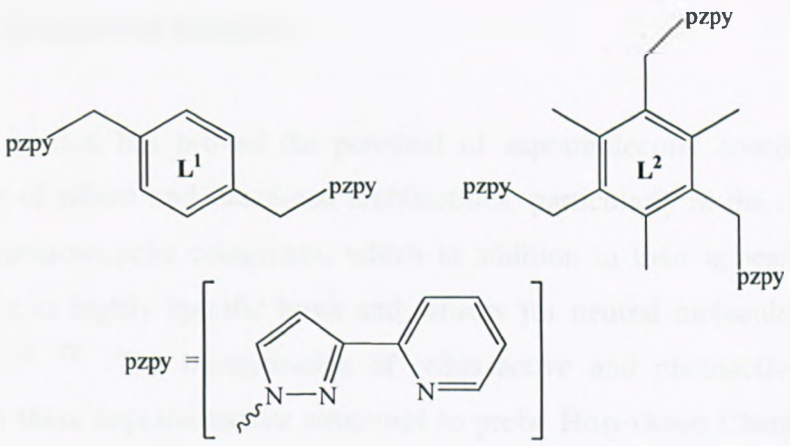

Figure 1.15: Bis-bidentate ligand, L^1 (left) and tris-bidentate ligand, L^2 (right).

The homoleptic cages are formed by reacting a bis-bidentate ligand with either zinc tetrafluoroborate or cadmium perchlorate, resulting in a capped truncated tetrahedral geometry. When the same bis-bidentate ligand is mixed with a tris-bidentate ligand and copper tetrafluoroborate in a 3:1:3 ratio, a cuboctahedral geometry is formed, which consists of both ligands (**Figure 1.16**). This work has shown that the use of a mixture of edge-bridging and face-capping ligands, could allow a formation of range of polyhedral cage structures.

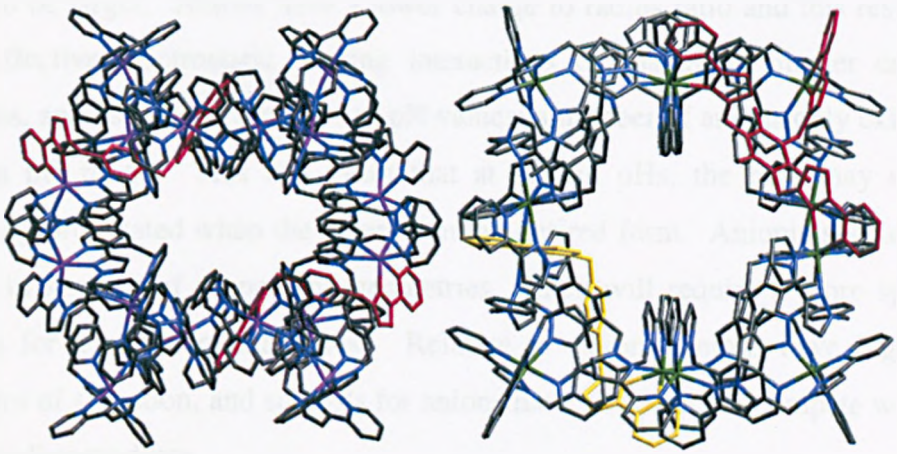

Figure 1.16: Structure of a capped truncated tetrahedral geometry (left) and structure of a cuboctahedral geometry (right).

1.3 Hosts and Sensors

Past research has proved the potential of supramolecular coordination in the design of robust and functional architectures, particularly in the construction of metallamacrocyclic complexes, which in addition to their appealing structures, can act as highly specific hosts and sensors for neutral molecules, cations and anions.[21, 22] The incorporation of redox-active and photoactive components within these supramolecular structures to probe Host-Guest Chemistry emerged as an alternative method to previous studies[23, 24] which relies upon NMR in order to define such interactions.

Recently, there is intense interest in the syntheses of host systems designed to recognise and sense anions as a consequence of the fundamental roles they play in a range of biological, chemical, medical and environmental processes. For example, Alzheimer's disease is linked to cystic fibrosis which is caused by misregulation of chloride transport through cell membranes by chloride ion channels. However, the design of anion receptors is particularly challenging for a number of reasons.[25] In general, anions are larger than cations and so receptors have to be larger. Anions have a lower charge to radius ratio and this results in less effective electrostatic binding interactions compared to smaller cations. Besides, anions may be sensitive to pH values; a number of anions only exist in a certain pH range. This can mean that at certain pHs, the host may not be correctly protonated when the anion is in the desired form. Anionic species also occur in a range of shapes and geometries, which will require a more specific design for a complementary host. Relative to cations, anions have high free energies of solvation, and so hosts for anions have to be able to compete with the surrounding medium.

The first structure synthesised resembling hosts targeted by this study was made by Fujita *et al.*[8] in 1990, who developed a generalised strategy for the kinetic locking of architectures self-assembled from square-planar templates. This work by Fujita has centered on kinetically labile, square planar geometries, consisting

of either four palladium(II) or four platinum(II) corners, linked by 4,4'-bipyridine groups and protected by ethylenediamine groups, as mentioned in self-assembly subtopic (**Figure 1.5**). The palladium corner square was shown to bind the trimethoxybenzene with a binding constant of 750 M^{-1} in aqueous solvent.

Much of this work has centered on kinetically labile, square-planar geometries. In 1995, Hupp *et al.*[13] first introduced self-assembly of host structures utilising octahedral *fac*-tricarbonyl Re(I) halide as corners, as mentioned previously (**Figure 1.9**). The incorporation of *fac*-tricarbonyl Re(I) metal centers into the macrocyclic structure offer rich photophysical properties and potential applications in sensors. At room temperature, the 4,4'-bipyridine and pyrazine squares were shown to be luminescent. However, there is no detectable luminescence obtained from the 1,2-bis-*trans*-(4'-pyridyl)ethylene square. The enhanced decay due to torsional motion about the C=C ethylene bond could be the reason of this non-detectable photoemission.

Other luminescent heterometallic square have also been synthesised by Hupp *et al.*[26] which containing two Re(I) centres and two Pd(II) centers (**Figure 1.17**).

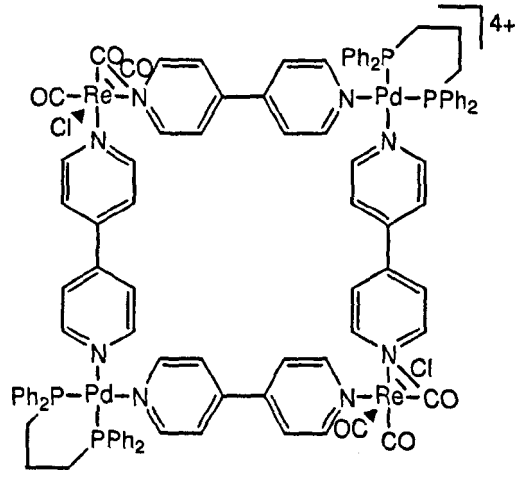

Figure 1.17: Hupp's heterometallic square.

The addition of tetraethylammonium perchlorate was found to increase the emission of this square. The ClO_4^- anion was presumed to bind into the host cavity with a binding constant of 900 M^{-1}.

The macrocycles which this project will concentrate most heavily on, are related to the one reported by Thomas *et al.*[27, 28, 29] (**Figure 1.18**).

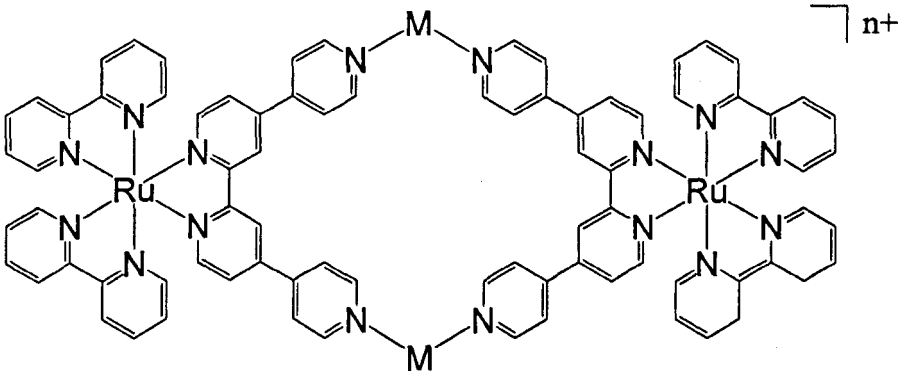

1, M = $[Pd(en)]^{2+}$, n = 8
2, M = $[Re(CO)_3]^+$, n = 4
3, M = $[Pt(en)]^{2+}$, n = 8

Figure 1.18: Thomas's bowl-shaped metallomacrocycles.

Thomas *et al.* have synthesised metallomacrocycles incorporating kinetically locked Ru(II) building blocks in the construction of the architectures. The utilisation of quaterpyridyl (qtpy) as the bridging ligand offers a more complex central cavity compared to simpler metallomacrocycles based on 4,4'-bipyridyl ligand.[22, 30, 31] X-ray crystallography studies[27] of **2** shows that three of the PF_6^- counter ions, are randomly displaced around the macrocycle. One ion however is distinctly seen to be in the central "pocket" of the macrocycle. This macrocycle is not planar like the other squares based on 4,4'-bipyridyl ligand.[8, 30] It is bent into a bowl shape due to the 60° angle of the qtpy bridging ligand and the preference of the six bonds about the rhenium centres to be at 90° to one another (in an octahedral manner).

Host-guest studies carried out using these macrocycles in water reveal they are receptors for polycyclic aromatic molecules. Upon addition of cyclic molecules such as 1,4-dimethoxybenzene and 1-naphthol, large changes in the absorption spectra of the macrocycles are observed. In addition, the presence of several isobestic points in the absorption titration spectra of 1-naphthol into aqueous solution of macrocycle **2** indicates a clean formation of 1:1 host-guest complex. However this macrocycle displays minimal emission changes upon binding the anions in aqueous solution. In contrast, in organic solutions, the complex functions as a luminescent sensor for anions with binding affinity and luminescent modulation being dependent on the structural nature and charge of the guest anion.

Whilst anions binding and sensing has become a major field within supramolecular chemistry, the recognition and sensing of nucleic acid constituents in water is another important challenge in supramolecular chemistry because of their many biological functions.[32, 33] Nucleobases, nucleosides and nucleotides such as adenosine-5'-triphosphate (ATP), guanosine-5'-triphosphate (GTP) and uridine are involved in important biological processes.[34, 35, 36, 37, 38] For example, ATP is known to be a multifunctional nucleotide that is most important as a molecular currency of intracellular energy transfer.[39] However, in water, which is relevant to biological applications, it is very difficult to recognise anions, as water is an important binding competitor, which buffers the interaction between the host-guest through forces like H-bonding. Therefore, multifunctional receptors with electronic and steric characteristics able to provide different binding contributions such as electrostatic charge-charge attractions, H-bond formation, and hydrophobic or π-π interactions are particularly of interests.[33, 40] As an output for such sensors, luminescence has emerged as an important detection method due to its simplicity, high detection limit, low cost and versatility.[41]

A number of synthetic receptors have been reported for the recognition and sensing of ATP.[42] However, it is much more difficult to selectively bind ATP

over the other triphosphate nucleotides due to the similarity of charge centred on the compounds. Recently, Bazzicalupi and coworkers[43] have reported a polyammonium receptor (**Figure 1.19**) which is able to discriminate ATP from other triphosphate nucleotides such as GTP, thymidine triphosphate (TTP) and cytidine triphosphate (CTP) in aqueous solutions.

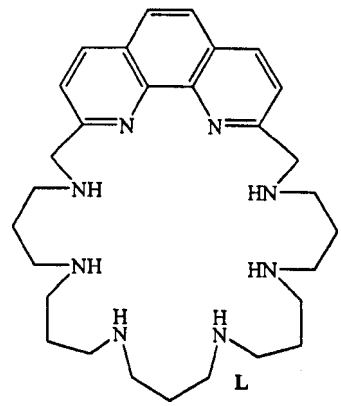

Figure 1.19: Polyammonium receptor L.

This polyammonium receptor, containing a phenanthroline ligand, is able to protonate in aqueous solutions affording polyammonium cations of the type $[H_xL]^{x+}$ (x = 1-6) which forms stable 1:1 complexes with anionic forms of triphosphate nucleotides ATP, GTP, CTP or TTP as well as adenosine diphosphate (ADP) and adenosine monophosphate (AMP). Fluorescence titration of the polyammonium receptor with ATP resulting in a completely quenched emission, while the other nucleotides only gave a partial quenching in the emission intensity and this effect only occurs in the presence of excess guest molecules. In addition, ^{31}P NMR spectra recorded on solutions containing the receptor and the nucleotides in a 1:1 molar ratio results in a significant downfield shift of the P_γ and P_β phosphorus atoms of the nucleotides with respect to the spectra in the absence of the receptor. This suggests that there are strong salt bridges between the anionic triphosphate unit and the cationic ammonium group of the receptor. Likewise, ^1H NMR spectra show remarkable upfield shifts of the ^1H signals of the nucleobases and the phenanthroline group of the receptor,

indicating a formation of π-stacking interactions between the nucleobases and the phenanthroline unit of the receptor.

Most of previous examples of hosts have been based on polyammonium receptors which employ electrostatic and π-stacking interactions as primary forces in the recognition of anions. However, work by Hamachi *et al.*[44] illustrates another example of a sensor which recognises anions in aqueous solutions based on metal-ligand interaction. The sensor consists of zinc-dipicolylamine-appended anthracene (Dpa)-Zn(II), which effectively binds and senses ATP in aqueous solutions (**Figure 1.20**).

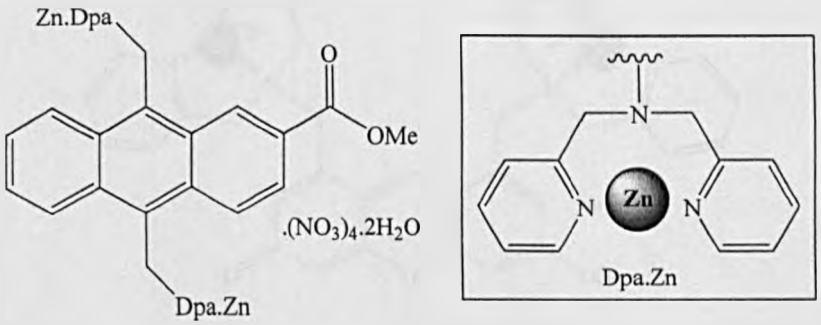

Figure 1.20: Zinc-dipicolylamine-appended anthracene (Dpa)-Zn(II) sensor.

Fluorescence titrations carried out for this receptor with ATP results in a 3-fold enhancement in the emission intensity with a binding constant of 2.2×10^6 M^{-1}. The binding affinty is about 10-fold greater than that of ADP and 30-fold greater than AMP, while similar titration with cyclic AMP results in a negligible change in the fluorescence intensity. This is clearly attributed to the difference in anionic charge of the nucleotides, with ATP being the most negatively charged, binding more strongly to the cationic Zn complex compared with ADP and AMP. Titrations were also carried out with other nucleoside triphosphates (GTP and CTP). These researchers found that the relative fluorescence emission response of the anthracene derivative receptor is rather weaker for CTP compare to ATP. In contrast, addition of GTP gradually attenuates the fluorescence intensity, which is most probably due to redox quenching involving the oxidation of the

guanine group. These results suggest that the receptor is able to show selectivity among the triphosphate nucleotides.

More recent work in the same group[45] involved the synthesis of a novel fluorescent chemosensor which selectively recognise nucleosides polyphosphates such as ATP with an off/on signal. Similar to previous receptor, this receptor also consists of 2,2'-dipicolylamine (Dpa)-Zn(II) as the binding motifs and a xanthene moiety as a fluorescent signalling unit (**Figure 1.21**).

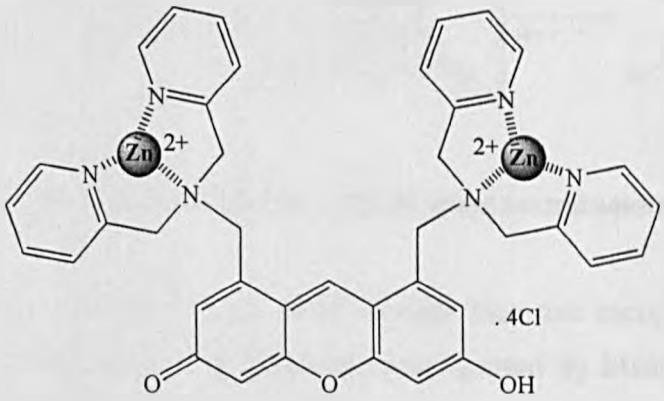

Figure 1.21: 1-2Zn(II) sensor.

The chemosensor 1-2Zn(II) showed a strong binding affinity in the range from 4.9×10^5 to 1.7×10^6 M^{-1} towards various polyphosphate derivatives such as XTP (X = A, G, C) and XDP (X = A, U), with more than 30-fold increase in the fluorescence intensity upon addition of 10 μM of ATP. Moreover, this receptor facilitates the naked eye detection of ATP with a detection limit of less than micromolar. However, titration with monophosphate species such as HPO_4^{2-}, AMP, cyclic guanosine monophosphate (cGMP), and phospho-diesters such as uridine diphosphate (UDP)-galactose or by other anions (SO_4^{2-}, NO_3^-, HCO_3^-, CH_3COO^-), gave no detectable change in the fluorescence intensity.

Depending on pH, the chemosensor 1-2Zn(II) is able to exist in an equilibrium between two forms in aqueous solution. However, it is found predominantly as

the deconjugated form II under neutral aqueous conditions (**Scheme 1.1**). This equilibrium explained the off/on fluorescence of 1-2Zn(II) receptor upon binding with nucleoside polyphosphates. The 'turn-on' fluorescence of this receptor is due to the binding-induced recovery of the conjugated form of the xanthene ring from its nonfluorescent deconjugated state which was formed by an unprecedented nucleophilic attack of zinc-bound water.

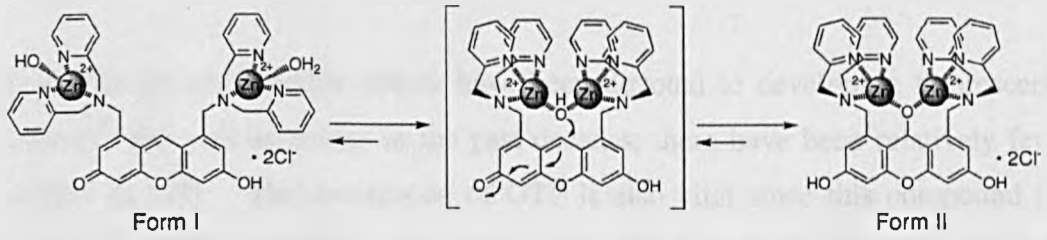

Scheme 1.1: Structure equilibrium of 1-2Zn(II) under neutral aqueous solutions.

Another example of colorimetric anion sensors that can recognise and sense biological anions in aqueous environment was reported by Máñez *et al.*[46] This 1,3,5-triarylpent-2-en-1,5-dione derivatives chromogenic sensor (**Figure 1.22**) shows a highly selective colour response for ATP in a mix organic-aqueous environment [dioxane/water (70/30 v/v)].

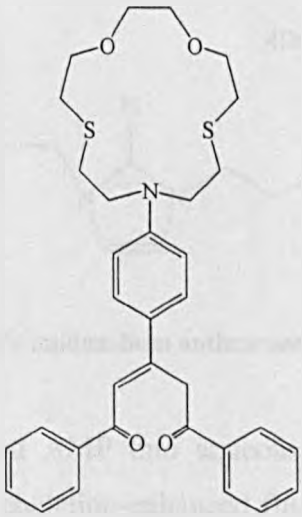

Figure 1.22: A selective chromogenic sensor for ATP.

At pH 6, the sensor produces a yellow solution either alone or in the presence of bromide, chloride, phosphate, GMP, or ADP while addition of sulfate results in a pale red solution. Strikingly in the presence of ATP, the yellow solution turns out to bright magenta colour. In addition, ATP is able to change the absorption spectrum of the sensor in the pH range of 4-8. This clearly indicates that the sensor is capable of acting as a selective chemosensor for ATP over other inorganic and biological anions.

Even though considerable efforts have been devoted to developing fluorescent sensors[47] for various anions in the past decades, there have been relatively few reports on GTP. The recognition of GTP is also vital since this compound is involved in RNA synthesis, citric acid cycle and acts as an energy source for protein synthesis.[48]

In 2004, Yoon *et al.* reported[49] a new water-soluble sensor which based on imidazolium anthracene derivative as shown in **Figure 1.23**.

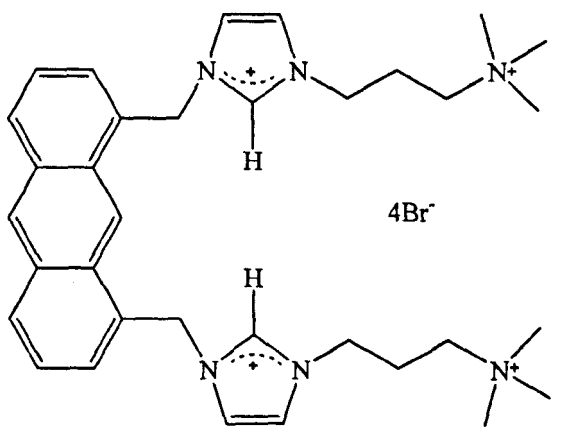

Figure 1.23: Yoon's imidazolium anthracene derivative sensor.

Titrations of ATP, ADP and AMP into aqueous solutions (pH 7.4, 10 mM HEPES) of host result in a chelation-enhanced fluorescence (CHEF) effect. In contrast, similar titration carried out for GTP with the receptor results in a chelation-enhanced fluorescence quenching (CHEQ) effect with a slight red-shift

in the emission wavelength. Interestingly, this receptor also shows potential of being a fluorescent chemosensor for GTP in 100 % aqueous solution as well as being able to differentiate between the structurally similar compounds GTP and ATP. The binding constant obtained from the fluorescence titration for GTP (K_a = 87000 M^{-1}) is about 6 times of that ATP (K_a = 15000 M^{-1}). In both cases, Job plot analyses indicate the formation of 1:1 complexes. There were also significant upfield shifts of the aromatic protons of anthracene moiety, GTP and ATP, respectively upon addition of 1 equivalent of GTP or ATP to the host solution in deuterated water.

Theoretically optimised structures of the imidazolium receptor indicate that there are π-H interactions between H atoms in NH_2 of GTP and from the H atom at C-2 position of ATP. The difference in π-H interactions strength between these molecules with imidazolium receptor is likely to be the reason for the selectivity towards GTP over ATP.

On the other hand, Ramaiah *et al.*[50] have reported a turn-on fluorescent sensor for GTP, through beneficial properties of a non-fluorescent cyclophane receptor and the fluorescence indicator, 8-hydroxy-1,3,6-pyrene trisulfonate (HPTS) as shown in **Figure 1.24**.

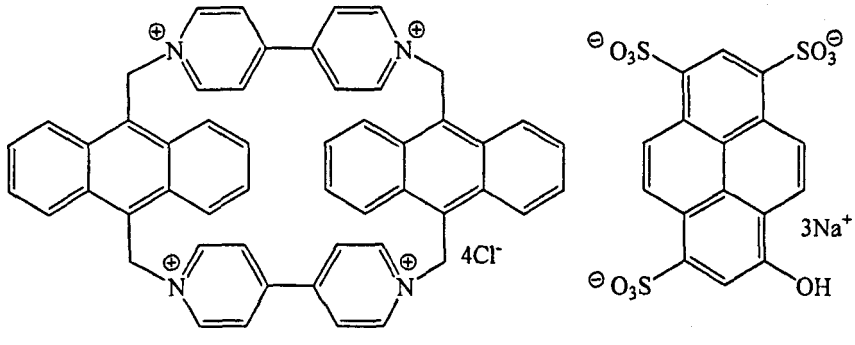

Figure 1.24: Cyclophane receptor (left) and HPTS unit (right).

A picosecond time-resolved fluorescence analysis, as well as cyclic voltammetry and NMR techniques confirmed the formation of a stable complex between the

HPTS and the cyclophane receptor. Later, the fluorescence indicator displacement (FID) experiments by various nucleotides and nucleosides were carried out and indicate that the HPTS is successfully displaced by nucleotides and nucleosides. Strikingly, GTP induced the maximum displacement of HPTS resulting in emission enhancement of approximately 150 fold which led to the visual detection of GTP through a "turn on" fluorescence. The displacement of HPTS from the cyclophane receptor was evident by the time-resolved fluorescence and NMR studies. It is believed that because GTP has a higher π-electron cloud density and lower ionisation potential than other nucleotides, it has a better interaction with the receptor through an "in concert" effect of electronic, π-stacking and electrostatic forces inside the cavity.

Nucleosides such as uridine and its analogues have been of benefit clinically and can be used as therapeutic agent in cardiovascular disease and hypertension,[51] respiratory dysfunction,[52] sleep dysfunction[53] and ischaemia, and hypoxia.[54] Hence, it is important to recognise these biomolecule due to their metabolic and pharmacological functions.

In 2006, Zhang *et al.*[55] reported a new saccharides sensor based on the tetrathiafulvalene (TTF)-anthracene dyad with two boronic acid groups (**Figure 1.25**). This sensor shows selectivity towards *D*-glucose in THF:H_2O (1:1, v/v) solution, and is also able to recognise uridine under the same conditions resulting in dramatic enhancement in the fluorescence spectra of the sensor.

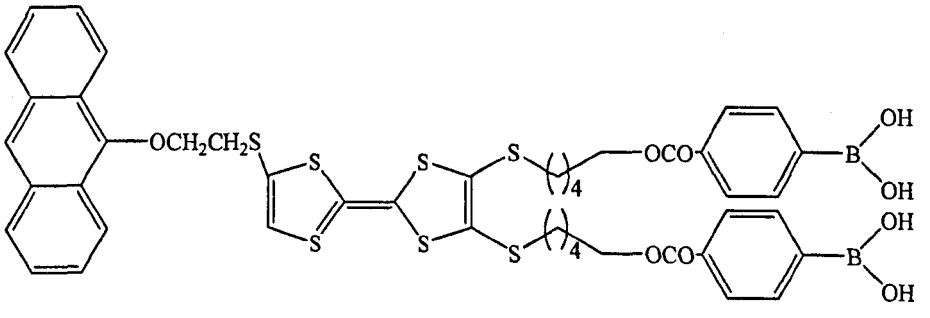

Figure 1.25: A saccharides sensor based on the tetrathiafulvalene (TTF) - anthracene dyad.

This sensor shows weak fluorescence on its own which is mainly due to photoinduced electron transfer (PET) between the excited anthracene and TTF units. Nucleosides such as uridine are able to bind the boronic acid moieties of the sensor through cis 2,3-diol group of the ribose sugar and as a result, photoreaction between the excited anthracene and TTF units is prohibited and thus results in large fluorescence enhancement.

Another group[56] reported a dizinc complex with a polyamine macrocycle which is able to selectively bind and sense uridine (**Figure 1.26**). The two zinc metals were designed to function as separated docking sites for substrates.

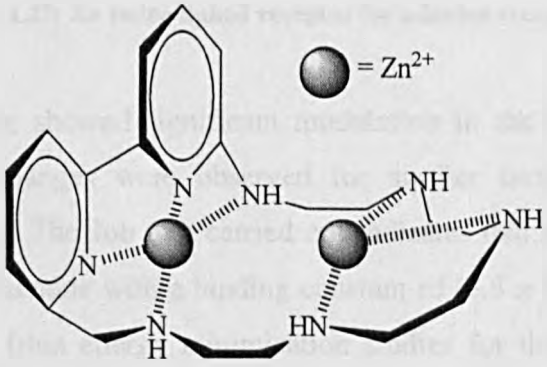

Figure 1.26: A dizinc complex with a polyamine macrocycle, $[Zn_2L]^{4+}$.

Potentiometric measurements and ^{1}H NMR studies confirmed that the dizinc complex bound the uridine, with significant upfield shift in the signals of both aromatic protons of uridine and the dipyridine units of the sensor. Titrations of uridine to the dizinc host solution indicate a formation of 2:1 adduct. Moreover, this compound shows selectivity for uridine over adenosine, cytidine and guanidine, which gave no effect on either the potentiometry or ^{1}H NMR measurements.

Whilst many synthetic receptors have been reported to-date for the recognition and sensing of biomolecules, the selectivity for adenine over all other nucleobases is still insufficient and remains as challenging problem. Recently,

Jang *et al.*[57] reported an imine-linked fluorescent receptor bearing both hydrogen donor and the hydrogen bond acceptor motifs that selectively binds adenine in CH_3CN/H_2O (95:5, v/v) solution over other nucleobases (**Figure 1.27**).

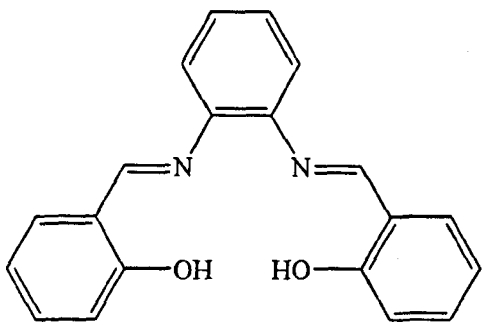

Figure 1.27: An imine linked receptor for adenine recognition.

Titration of adenine showed significant modulation in the fluorescence output while negligible changes were observed for similar titration with guanine, thymine and uracil. The Job plot carried out indicates that the receptor forms a 1:1 complex with adenine with a binding constant of $(3.8 \pm 0.3) \times 10^4\ M^{-1}$. The structure obtained from energy minimisation studies for the host-guest system indicates that the adenine was bound in the cavity of the host through two complementary hydrogen bonds between adenine and the receptor and this is also evident from the significant upfield shifts in the ^1H NMR spectrum.

On the other hand, work by Turkewitsch *et al.*[58] have concentrated on the recognition and sensing of cyclic nucleotides such as cyclic adenosine monophosphate (cAMP) and cyclic guanosine monophosphate (cGMP) due to their important role in biological information transfer processes.[59] This group reported a dye receptor which belongs to a family of 4-(*p*-dimethylaminostyryl) pyridinium salts as shown in **Figure 1.28**.

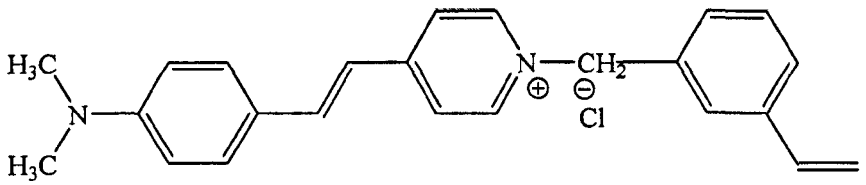

Figure 1.28: A dye receptor which shows preferences for cAMP and cGMP.

From the studies, they found that the dye receptor showed similar preferences for both cAMP and cGMP in aqueous solutions. Addition of both biomolecules to a receptor solution, respectively result in a hyperchromicity and also a bathochromic effects in the absorption spectra of the dye molecule. Likewise, dramatic enhancement in the fluorescence quantum yield, with a concomitant slight red shift of the emission wavelength was observed upon increasing concentrations of the guests. In contrast, titration of *D*-ribose-5-phosphate did not induce any changes. This suggests that other forces may also involved in the interactions of the dye receptor with cAMP and cGMP, such as stacking interaction between base of the nucleotides and the aromatic rings of the receptor instead of just charge-charge effects. Estimates of binding constants determined for the dye receptor with cAMP and cGMP are 212 ± 46 M^{-1} and 285 ± 18 M^{-1}, respectively. Although the receptor could not discriminate between the structurally similar cAMP and cGMP, this receptor has shown a capability of sensing both anions in water.

1.4 Aims

Anions are well known to play numerous fundamental roles in a range of chemical, biological and environmental processes. As a consequence of this, there is intense current interest being shown in the design and synthesis of receptors that are proficient at detecting anions in solution. Much of this work has centered on kinetically labile, square-planar metal geometries, such as Pd(II).[8, 11, 12] The advantage of using such moieties is that the self-assembly process is under thermodynamic control. Therefore, unlike conventional covalent

chemistry which typically yields kinetic product, entropy-enthalpy compensation effects predominate, thus yielding discrete, often highly complex architectures. The disadvantage of using such an approach is that the final product is, by definition, an equilibrium product and, as such, is not kinetically robust. Therefore, changes to equilibrium conditions may result in disassembly of the previously thermodynamic product. This can be problematical as, in many cases, the construction of molecular devices for hosts, sensors and molecular electronics will require kinetically robust architectures. Fujita and colleagues have shown that Pt(II) centers, which in normal ambient conditions are kinetically inert, become relatively labile at elevated temperatures and in highly polar media.[8] Using this effect, they have isolated macrocyclic, catenated and nanosized cage architectures. Unlike their Pd(II)-based analogues, these structures are remarkably stable. For example, addition of excess [Pt(en)(NO_3)$_2$] (en=ethylene diimine) to the square macrocycle constructed in this manner does not lead to any sign of subsequent product redistribution. However, this approach has yet to be systematically applied to metals that form octahedral complexes. The inclusion of such metal centers in kinetically locked architectures is appealing as, apart from supplying a structurally more complex connecting motif, octahedral centers can also possess attractive photophysical and electrochemical properties that can be exploited in the design of molecular devices. In this study, we decided to utilise the ruthenium(II) and rhenium(I) chemistry in the design of our host systems. The inclusion of such metal centres within supramolecular assemblies will lead to the production of robust and functional architectures, which can possibly act as highly specific hosts and sensors for biomolecules. Also, there are significant efforts in the synthesis of new molecules which can bind DNA and influence their activities, with the goals of controlling DNA processing, creating new chemotherapeutic or diagnostic agents and to enhance the fundamental understanding of DNA molecular recognition. A more complete understanding on how to target DNA will lead to a greater expanded ability for the chemists to design high selective DNA probes.

Given all these, and our interest in the design of hosts and sensors for anions as well as novel DNA probes, we decided to synthesise the architectures and explore their binding properties with selected biomolecules and Calf thymus DNA (CT-DNA) in aqueous environments.

2 Polypyridyl Complexes of Ruthenium(II) and Rhenium(I)

2.1 Background

Over the last 20-30 years, d^6 metal polypyridyl complexes have been extensively studied owing to their interesting photophysical properties and their chemical stability. These features makes them potentially useful in light harvesting,[60, 61, 62] non-linear optics[63, 64] and recently probes for biological systems.[65] This chapter is concerned with the chemistry of ruthenium(II) and rhenium(I) polypyridyl systems.

2.1.1 Ruthenium(II) Polypyridyl Chemistry

Ruthenium(II) polypyridyl chemistry has made rapid progress since the mid 1970s, stimulated by the wide range of applications that such compounds have seen and, potentially, will see in the future. Since the synthesis of the dinuclear complex $[\{(NH_3)_5Ru(\mu\text{-pz})Ru(NH_3)_5]^{5+}$ (pz is pyrazine) by Creutz and Taube[66] and the first report on the emission of $[Ru(bpy)_3]^{2+}$ by Paris and Brandt,[67] this group of metal complexes have been intensively investigated. This is primarily due to the wide range of photophysical and electronic properties shown by these complexes. Also, the extensive synthetic chemistry of these metal complexes makes them attractive building blocks for more complex systems. The resulting materials have very desirable redox and photophysical properties:[68] (a) high stability of the ground and excited states; (b) intense visible absorptions due to metal-to-ligand charge transfer (MLCT) bands; (c) relatively long-lived excited states that are typically on the microsecond time range and emission that is usually from radiative deactivation of the lowest lying triplet MLCT level; (d) reversible metal oxidation and ligand reductions, accessed at low potential; (e) the ability to tune the properties by careful choice of appropriate ligand.

2.1.2 Rhenium(I) Polypyridyl Chemistry

Studies by Wrighton and Morse in 1974 were the starting point for the intensive research into the photophysics and photochemistry of polypyridyl carbonyl complexes of Re(I).[69] Studies show that this group of complexes are able to luminesce from triplet MLCT state with lifetimes ranging between 100 ns and 100 μs.[70, 71, 72, 73]

2.2 Aims

The metal complex "building block" used in the self-assembly of anions hosts, $[Ru(bpy)_2(qtpy)][PF_6]_2$ has been reported before.[29, 74, 75] With the aim of modulating the photophysical properties of future host architectures, we investigated the synthesis of six novel building blocks of ruthenium(II) and rhenium(I) for the construction of similar macrocycles. This chapter is concerned with the synthesis and characterisation of these complexes. Four of the complexes reported in this chapter had been previously reported.[75, 76] However, to further study their photochemical properties, these monomers were resynthesised in this project.

2.3 Ligands Synthesis

2.3.1 2,2':4,4'':4',4'''-Quaterpyridyl [2.1]

Most of the synthesis in this work will be involving 2,2':4,4'':4',4'''-quaterpyridyl ligand (qtpy) **[2.1]** (**Figure 2.1**). This ligand was first reported in 1938 by Burstall as a byproduct of the reaction between 4,4'-bipyridine and iodine.[77] Since then this ligand has been used in numerous studies[74, 78, 79] due to the attractive features it offers. The quaterpyridyl ligand functions as an excellent building block for the construction of supermolecules containing clusters of photoactive and redox active sites. The qtpy ligand is well

suited to this approach as it not only contains a bidentate diimine site that can coordinate to a metal centre, but also contains two monodentate imine sites which can both coordinate to another metal centre.

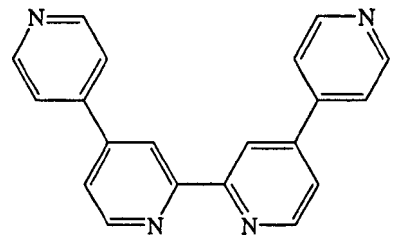

Figure 2.1: 2,2':4,4'':4':4'''-quaterpyridyl [2.1].

The ligand was prepared *via* the palladium catalysed, high temperature dimerisation of 4,4'-bpy, adapted from the procedure of Morgan and Baker[80] (**Scheme 2.1**), but with a slight modification to the procedure to improve the reaction yields. The reaction was carried out in two days at a higher temperature instead of three days with a slightly lower temperature. The yield obtained was 9.25 %, which is slightly higher than those reported in the literature.[80]

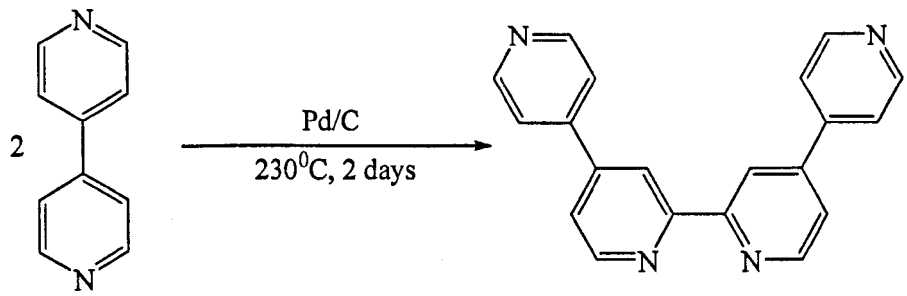

Scheme 2.1: Synthesis of 2,2':4,4'':4',4'''-quaterpyridyl.

4,4'-bipyridine and 10% palladium on carbon were heated in a sealed bomb at 230°C for 2 days. Chloroform was added and the mixture was refluxed for a further 30 minutes. Following filtration to remove the Pd/C, acetone was added to the resulting solids and the mixture was stirred. The resulting slurry was filtered, yielding a crop of crude quaterpyridyl. The volume of the filtrate was

reduced *in vacuo* by approximately 50 ml to yield more solid, which was again collected. The batches of crude quaterpyridyl were then combined and recrystallised from hot ethanol giving a cream solid. The product was fully characterised and was found to be consistent with previous reports.

2.3.2 Dipyrido [3,2-a:2',3'-c] Phenazine [2.2]

The other ligand that has been used in this thesis is the dipyrido [3,2-a:2',3'-c] phenazine (dppz) **[2.2]** which was synthesised following published procedures.[81] The ligand was prepared by condensation of 1,10-phenanthroline-5,6-dione (dpq) with *o*-phenylene-diamine in ethanol.[82] The dpq ligand is obtained by oxidation of the 1,10-phenanthroline (phen) in Br_2, nitric and sulphuric acid (**Scheme 2.2**).

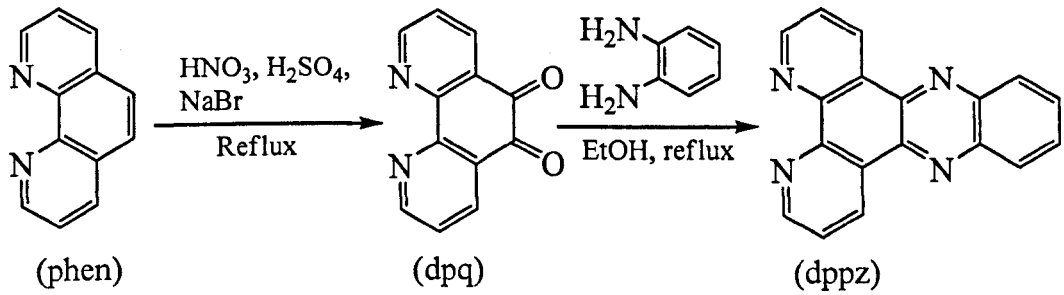

Scheme 2.2: Synthesis of dpq and dppz [2.2] ligands.

Research on metal complexes incorporating dppz has increased since the 1990s. Early complexes containing the dppz ligand include $[Ru(phen)_2(dppz)]^{2+}$ and $[Ru(bpy)_2(dppz)]^{2+}$, which both display attractive photophysical properties.[83, 84] The ability of the dppz to increase the surface area that is available for overlap with DNA is very desirable as this increase the chances of creating a full intercalating metal complex. This feature of dppz has led to research on "molecular DNA light switches"[85] as the excited state of these complexes are very dependent upon their microenvironment; in acetonitrile or hydrophobic solvents there is an emission from their metal-to-ligand charge transfer (MLCT), whereas in aqueous or protic solvents, the MLCT is completely quenched. This

light-switch effect has been attributed to the protection of phenazine nitrogen atoms from hydrogen bonding with water as opposed to being free in aqueous solution.

2.4 Synthesis of Ruthenium(II) Polypyridyl Complexes

A series of ruthenium(II) polypyridyl complexes has been synthesised.

2.4.1 Synthesis of $Ru(dppz)_2Cl_2$ [2.3], $Ru(phen)_2Cl_2$ [2.4] and $Ru(bpy)_2Cl_2$ [2.5]

The preparation of these starting materials were carried out according to the method of Meyer *et al.*,[86] that is by reacting two equivalents of corresponding bidentate ligand (dipyrido [3,2-a:2',3'-c] phenazine, 1,10-phenanthroline or 2,2'-bipyridyl) with $RuCl_3.3H_2O$ in the presence of LiCl in freshly distilled, dry DMF (**Scheme 2.3**). LiCl is added to ensure there are Cl^- ions present to prevent tri-substitution.

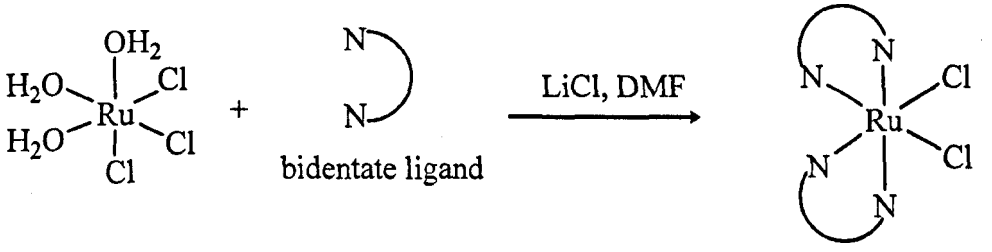

Scheme 2.3: Synthesis of $[RuL_2Cl_2]$ when L is bidentate ligand.

2.4.2 Synthesis of $[Ru(dppz)_2(qtpy)]^{2+}$[2.6], $[Ru(phen)_2(qtpy)]^{2+}$[2.7] and $[Ru(bpy)_2(qtpy)]^{2+}$[2.8]

Complex **[2.6]** was prepared by an adaptation of the method reported by Ward *et al.*[75] The starting material $Ru(dppz)_2Cl_2$ **[2.3]** and one equivalent of qtpy were refluxed in freshly distilled, dry ethylene glycol for one hour. Upon

cooling, the crude product was precipitated out by the addition of NH_4PF_6, and the deep red solid obtained was purified on a grade 1, neutral alumina column, eluting with a 1:1:9 KNO_3:water:acetonitrile mixture. The product was obtained in 75 % yield and characterised by ^1H NMR and FAB-MS spectroscopy. **[2.7]** and **[2.8]** were synthesised using the same method.

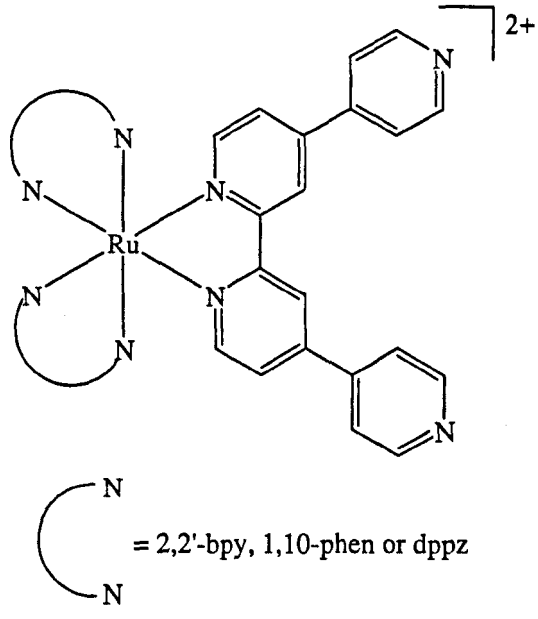

Figure 2.2: Complexes [2.6], [2.7] and [2.8].

2.4.3 Synthesis of $[Ru(dppz)_2(qtpyMe_2)]^{4+}$ [2.9], $[Ru(phen)_2(qtpyMe_2)]^{4+}$ [2.10] and $[Ru(bpy)_2(qtpyMe_2)]^{4+}$ [2.11]

The *N*-methylated derivative of **[2.6]** was then synthesised by adapting the method published by Ward *et al.*[75]

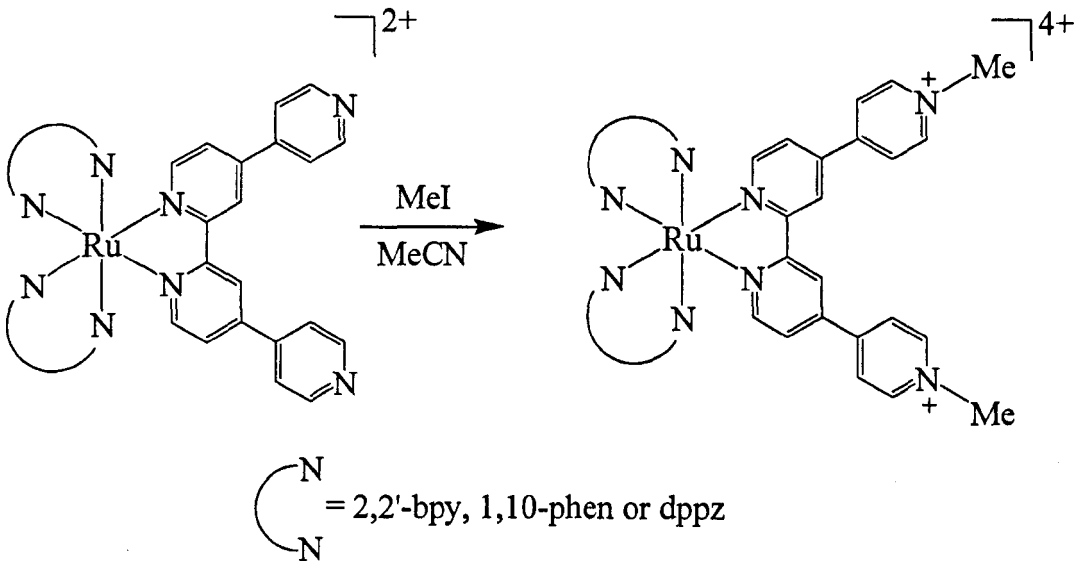

Scheme 2.4: Synthesis of [2.9], [2.10] and [2.11].

A mixture of the $[Ru(dppz)_2(qtpy)]^{2+}$ **[2.6]** and a fifteen-fold molar excess of methyl iodide in acetonitrile was stirred at 50°C for two days (**Scheme 2.4**). The solvent was removed on a rotary evaporator. The deep red residue was redissolved in aqueous methanol (1:1) and KPF_6, added to precipitate the product, which was collected by filtration and dried *in vacuo*. The complex obtained was characterised by ^1H NMR and FAB-MS spectroscopy. During the first attempt, a mixture of the $[Ru(dppz)_2(qtpy)]^{2+}$ and a ten-fold molar excess of methyl iodide in acetonitrile was stirred at 50°C overnight. However the NMR spectrum and the mass spectra obtained were not consistent with the desired product. NMR peak for protons next to the methylated nitrogen was split into two peaks at two different positions. This suggests that only one of the monodentate sites has been methylated. Later, we tried to extend the reaction time to two days instead of overnight, but still the results were not as expected. An attempt to use fifteen-fold excess of methyl iodide and two days of reaction time give the desired complex with consistent results. **[2.10]** and **[2.11]** were synthesised using a similar method.

2.5 Synthesis of Rhenium(I) Polypyridyl Complexes

Previous work[28] by Thomas group has involved the synthesis of $Re(qtpy)(CO)_3Cl$, $Re(qtpy)(CO)_3Br$ and $[Re(qtpy)(CO)_3(NCMe)][OTf]$. In this thesis, two of the complexes were resynthesised so that more detailed photophysical studies could be reported. Two new derivatives of these compounds are also reported.

2.5.1 Synthesis of $Re(qtpy)(CO)_3Cl$ [2.12] and $[Re(qtpy)(CO)_3(NCMe)]^{1+}$[2.13]

Complexes **[2.12]** and **[2.13]** (**Figure 2.3**) have been synthesised using previously reported methods.[28] These complexes were fully characterised and all data were consistent with the desired products.

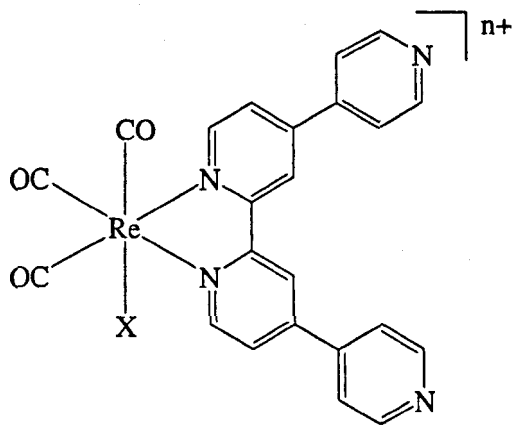

X = Cl (n = 0) or NCMe (n = 1)

Figure 2.3: Complexes [2.12] and [2.13].

2.5.2 Synthesis of $[Re(qtpyMe_2)(CO)_3Cl]^{2+}$ [2.14] and $[Re(qtpyMe_2)(CO)_3(NCMe)]^{3+}$ [2.15]

In addition, *N*-methylated derivative of **[2.12]** have been synthesised according an adaptation of method published by Ward *et al.*[75] The *N*-methylation of **[2.12]** and

[2.15] introduces an electron-accepting *N*-methylpyridinium group attached to the rhenium centre.

A mixture of **[2.12]** and a fifteen-fold molar excess of methyl iodide in acetonitrile was stirred at 50°C for two days (**Scheme 2.5**). The solvent was removed on a rotary evaporator. The red-orange residue was redissolved in aqueous methanol (1:1) and KPF_6, added to precipitate the product, which was collected by filtration and dried. This complex was fully characterised and the data obtained were consistent with the desired product. Complex **[2.15]** was synthesised using a similar method.

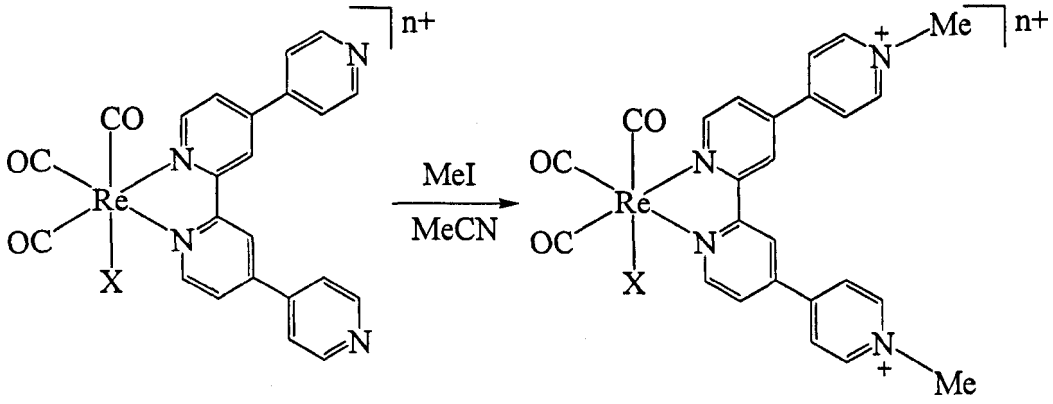

X = Cl (n = 0) or NCMe (n = 1) X = Cl (n = 2) or NCMe (n = 3)

Scheme 2.5: Synthesis [2.14] and [2.15].

2.6 ^{1}H NMR Spectroscopic Studies

2.6.1 $[Ru(dppz)_2(qtpy)]^{2+}$ [2.6]

The ^{1}H NMR spectra of $[Ru(dppz)_2(qtpy)]^{2+}$ **[2.6]** in d^3-acetonitrile are quite complicated. The downfield, aromatic region (**Figure 2.4**) is well defined and integrates to a total of 34 protons, which is consistent with the desired product [2.6]. The NMR spectrum obtained for $[Ru(bpy)_2(qtpy)]^{2+}$ reported previously[74, 75] was used as guidance in peak assignment for this complex. The

spectrum shows a similar pattern for the qtpy protons with inequivalence of the dppz units.

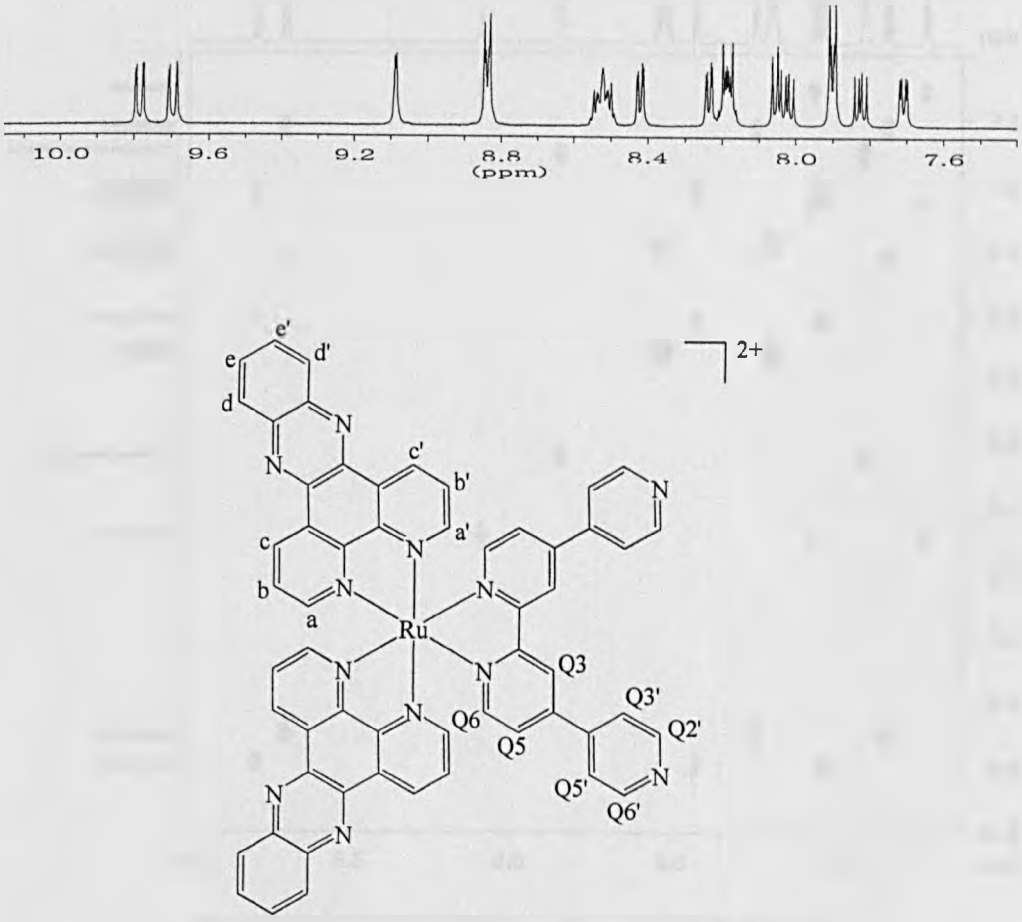

Figure 2.4: Downfield region of ^{1}H NMR spectrum of [2.6] in CD_3CN and proton labeling scheme.

UNIVERSITY OF SHEFFIELD LIBRARY

The exact assignment was made with the aid of a ^{1}H-COSY NMR spectrum (**Figure 2.5**).

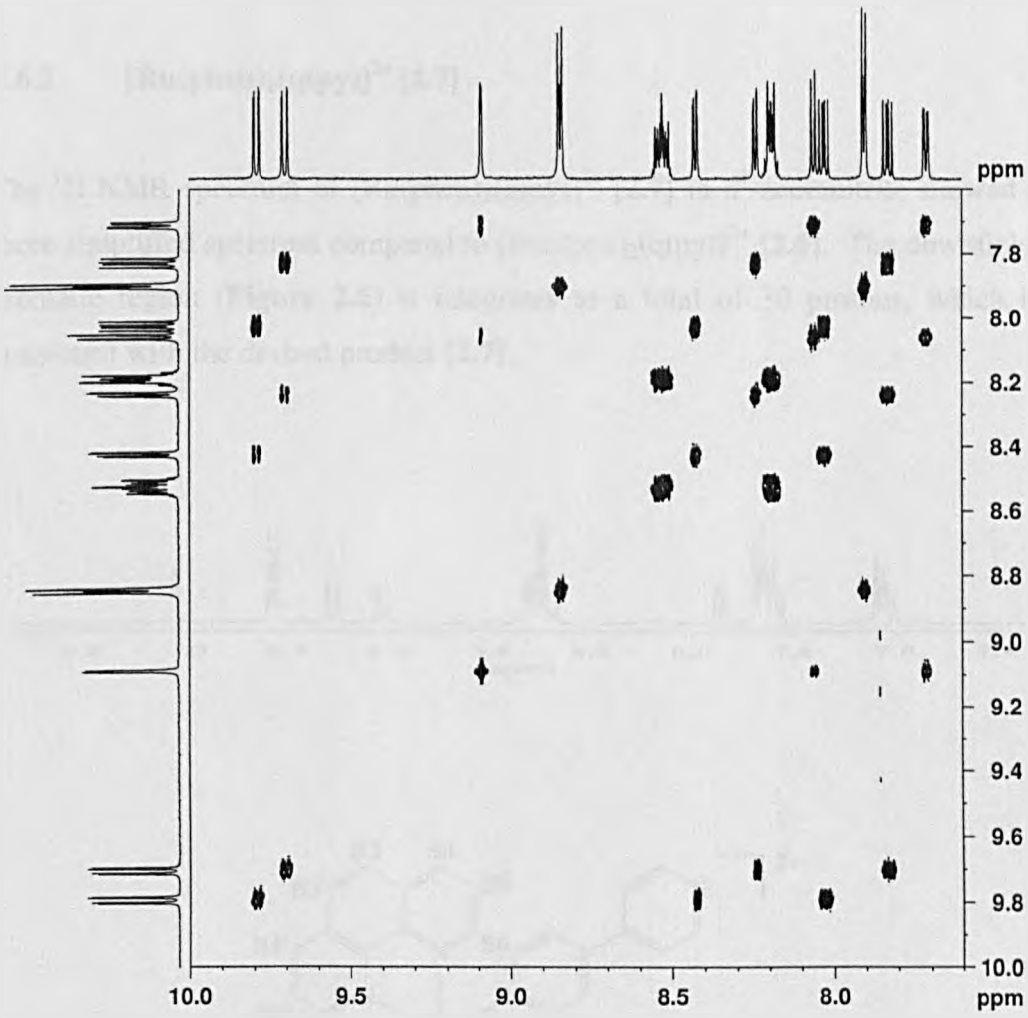

Figure 2.5: ^{1}H-COSY NMR spectrum of [2.6] in CD_3CN.

There are five signals which correspond to the protons of the qtpy. The signals at 7.71 ppm (Q5), 8.07 ppm (Q6) and 9.10 ppm (Q3) correspond to the protons on the inner qtpy rings, while those at 7.91 ppm (Q2',Q6') and 8.85 ppm (Q3',Q5') correspond to protons on the pendant pyridyl ring of qtpy. This assignment of protons agrees with those published by Ward *et al.*[75] We favoured this assignment as it agrees with the expected shifting for *N*-methylated derivative of this complex - *vide infra*. The signals at 7.83 ppm (e'), 8.03 ppm (e), 8.19 ppm (b,b'), 8.23 ppm (d'), 8.44 ppm (d), 8.54 ppm (c,c'), 9.68 ppm (a') and

9.79 ppm (a) correspond to dppz protons. The signals which correspond to dppz unit are quite complicated due to the inequivalence of the two dppz units.

2.6.2 $[Ru(phen)_2(qtpy)]^{2+}$ [2.7]

The ^1H NMR spectrum of $[Ru(phen)_2(qtpy)]^{2+}$ **[2.7]** in d^3-acetonitrile showed a more simplified spectrum compared to $[Ru(dppz)_2(qtpy)]^{2+}$ **[2.6]**. The downfield, aromatic region (**Figure 2.6**) is integrates to a total of 30 protons, which is consistent with the desired product **[2.7]**.

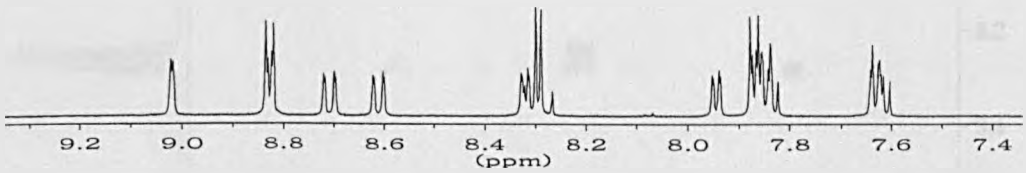

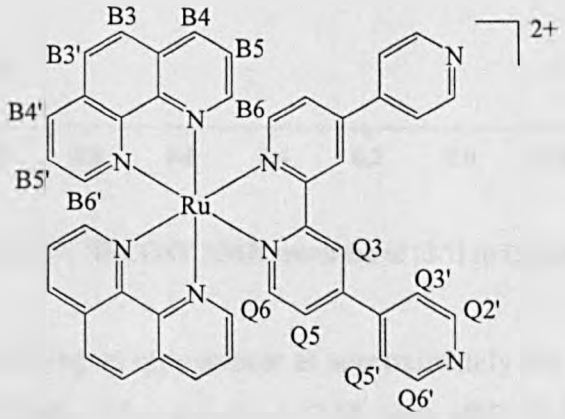

Figure 2.6: Downfield region of ^1H NMR spectrum of [2.7] in CD_3CN and proton labeling scheme.

The peak assignment was made with the aid of a ^{1}H-COSY NMR spectrum (**Figure 2.7**).

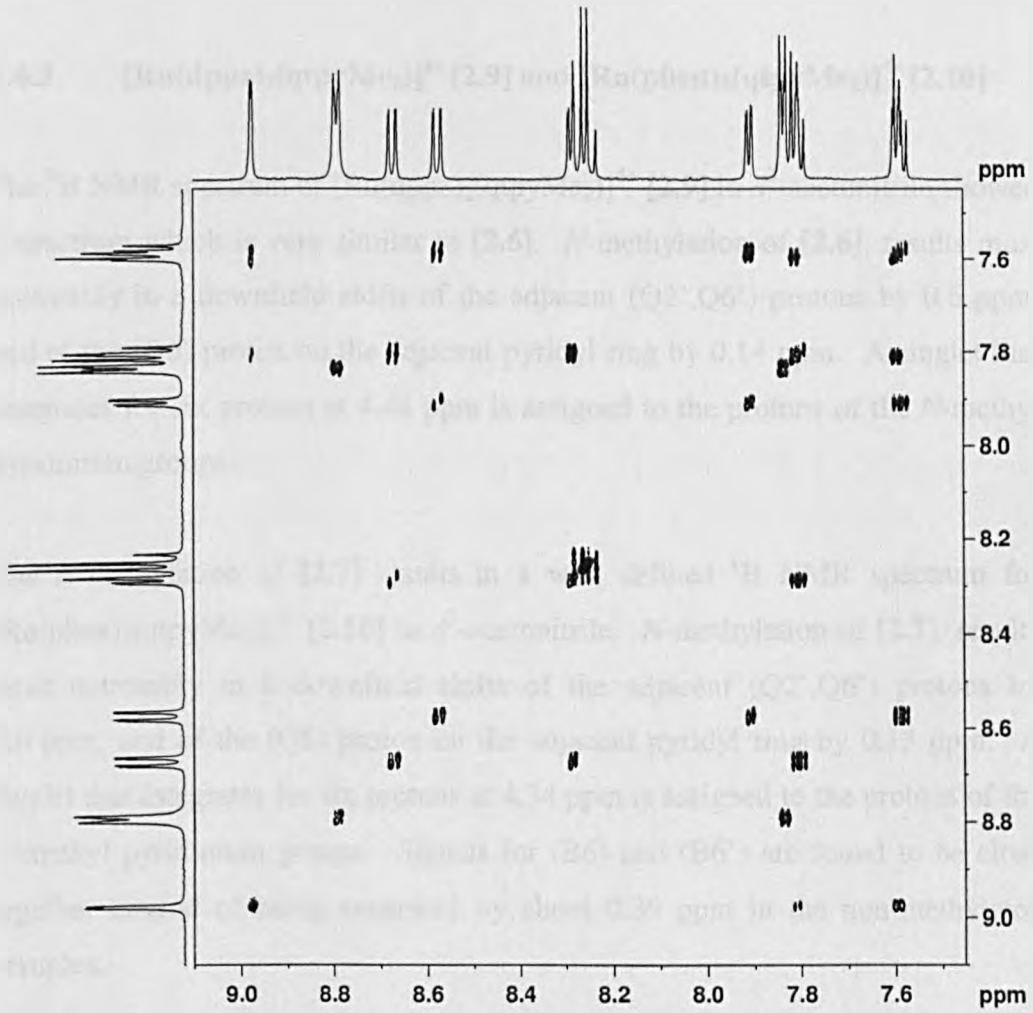

Figure 2.7: ^{1}H-COSY NMR spectrum of [2.7] in CD_3CN.

The signals corresponding to qtpy appear at approximately the same positions as those reported for **[2.6]**. The signals at 7.62 ppm (Q5), 7.82 ppm (Q6) and 9.02 ppm (Q3) correspond to the protons on the inner qtpy rings, while those at 7.87 ppm (Q2',Q6') and 8.83 ppm (Q3',Q5') correspond to protons on the pendant pyridyl ring of qtpy. However, the signals corresponding to the protons of phen are more complicated than the bpy signals in $[Ru(bpy)_2(qtpy)]^{2+}$. The signal for (B3,B3') is split into two peaks with separation about 0.10 ppm; the signals for (B6) and (B6') are separated by 0.38 ppm. This is expected due to the

rigidity of 1,10-phenanthroline ligand compared to 2,2'-bipyridyl. The signal for (B5,B5') is located at 7.58 ppm.

2.6.3 $[Ru(dppz)_2(qtpyMe_2)]^{4+}$ [2.9] and $[Ru(phen)_2(qtpyMe_2)]^{4+}$ [2.10]

The ^1H NMR spectrum of $[Ru(dppz)_2(qtpyMe_2)]^{4+}$ **[2.9]** in d^3-acetonitrile showed a spectrum which is very similar to **[2.6]**. *N*-methylation of **[2.6]**, results most noticeably in a downfield shifts of the adjacent (Q2',Q6') protons by 0.6 ppm, and of the (Q6) proton on the adjacent pyridyl ring by 0.14 ppm. A singlet that integrates for six protons at 4.44 ppm is assigned to the protons of the *N*-methyl pyridinium groups.

The *N*-methylation of **[2.7]** results in a well defined ^1H NMR spectrum for $[Ru(phen)_2(qtpyMe_2)]^{4+}$ **[2.10]** in d^3-acetonitrile. *N*-methylation of **[2.7]**, results most noticeably in a downfield shifts of the adjacent (Q2',Q6') protons by 0.6 ppm, and of the (Q6) proton on the adjacent pyridyl ring by 0.13 ppm. A singlet that integrates for six protons at 4.34 ppm is assigned to the protons of the *N*-methyl pyridinium groups. Signals for (B6) and (B6') are found to be close together instead of being separated by about 0.39 ppm in the non-methylated complex.

2.6.4 $[Ru(bpy)_2(qtpy)]^{2+}$ [2.8], $[Ru(bpy)_2(qtpyMe_2)]^{4+}$ [2.11], $Re(qtpy)(CO)_3Cl$ [2.12] and $[Re(qtpy)(CO)_3(NCMe)]^{1+}$ [2.13]

The ^1H NMR spectra for **[2.8]**, **[2.11]**, **[2.12]** and **[2.13]** have been found to be consistent with previous report.[28, 75]

2.6.5 $[Re(qtpyMe_2)(CO)_3Cl]^{2+}$ [2.14] and $[Re(qtpyMe_2)(CO)_3(NCMe)]^{3+}$ [2.15]

The ^1H NMR spectrum of $[Re(qtpyMe_2)(CO)_3Cl]^{2+}$ **[2.14]** in d^6-DMSO showed a spectrum which is very similar to **[2.12]**. Again, *N*-methylation of **[2.12]**, results most noticeably in a downfield shifts of the adjacent (Q2',Q6') protons by 0.7 ppm, and of the (Q6) proton on the adjacent pyridyl ring by 0.24 ppm. A singlet that integrates for six protons at 4.46 ppm proves that complex **[2.12]** has been methylated.

Complex **[2.15]** was recorded in d^3-acetonitrile and the spectrum obtained is well defined and integrates to a total of 23 protons, which is consistent with the desired product **[2.15]**. Signals for protons (Q2',Q6') was shifted downfield by 0.6 ppm while (Q6) proton on the adjacent pyridyl ring is shifted by 0.22 ppm. The upfield region of the spectrum showed two singlets signals, which integrates for the six protons of the *N*-methyl pyridinium groups and the three protons of the bound acetonitrile at 4.42 ppm and 2.11 ppm, respectively.

2.7 UV-Visible Spectroscopy

UV-Visible absorption spectra for all the ruthenium(II) and rhenium(I) complexes were recorded in acetonitrile at room temperature.

2.7.1 Ruthenium(II) Polypyridyl Complexes

For complexes **[2.6]** to **[2.11]**, the spectra are unremarkable and thus can be assigned by comparison with other complexes such as $[Ru(bpy)_3]^{2+}$ (**Figure 2.8**). Data are summarised in **Table 2.1**. Metal-to-ligand charge transfer transitions (MLCT) are observed for all the complexes at around 400 - 500 nm; this is typical for Ru(II)→L MLCT bands. The strong band between 200 - 290 nm is from a ligand-centred (LC) $\pi \rightarrow \pi^*$ transition.

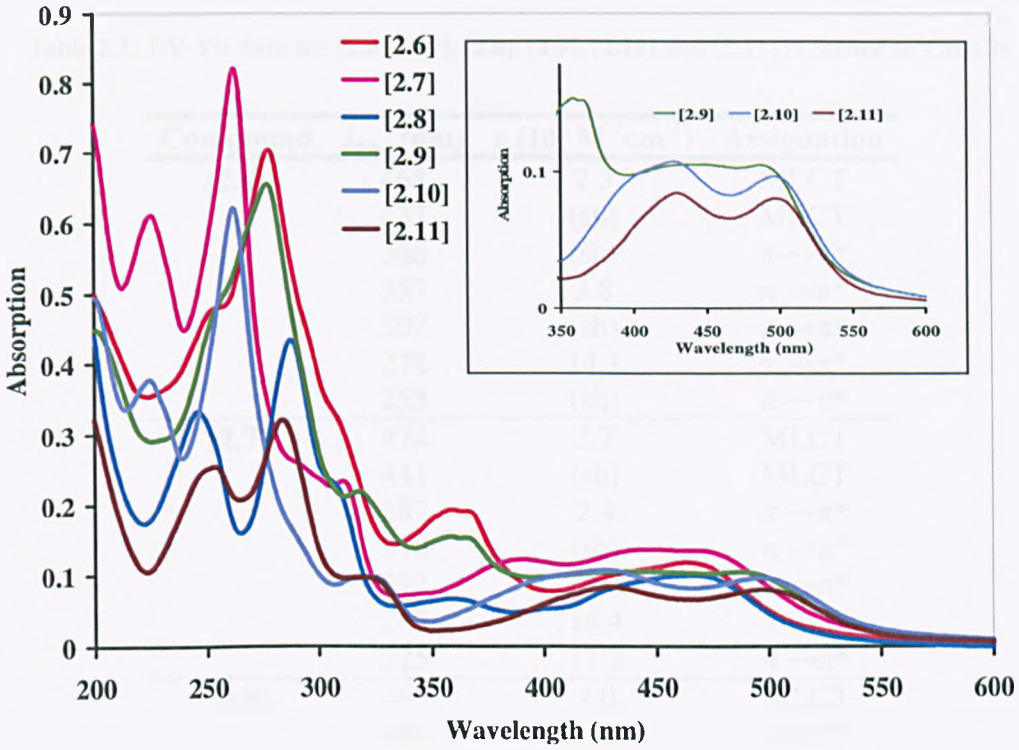

Figure 2.8: UV-Visible spectra of [2.6], [2.7], [2.8], [2.9], [2.10] and [2.11] recorded in acetonitrile. The inset shows the better resolved bands for [2.9], [2.10] and [2.11] upon quaternisation.

Upon methylation, the low energy bands are red shifted for the methylated complexes, **[2.9]**, **[2.10]** and **[2.11]**, respectively. For **[2.10]** and **[2.11]**, the MLCT bands between 400 and 500 nm appear as well separated, distinct peaks rather than one peak with shoulder. Both are still in the region due to d_π (Ru) $\rightarrow\pi^*$ transitions. However, the two bands are barely resolved in the spectrum of **[2.9]**, as they are equal in intensity and merge into a broad band. Quaternisation on the remote qtpy lowers the energy of the transition to that ligand, producing an increased resolution of the bands in the spectra of the methylated complexes. As with $[Ru(bpy)_2(4,4'\text{-}bpyMe)_2]^{4+}$, there are no distinct absorption bands arising from a charge transition between Ru(II) and the pyridinium acceptors.

Table 2.1: UV-Vis data for [2.6], [2.7], [2.8], [2.9], [2.10] and [2.11] recorded in CH_3CN.

Compound	λ_{max} (nm)	ε (10^4 $M^{-1}cm^{-1}$)	Assignation
[2.6]	468	2.3	MLCT
	437	(sh)	MLCT
	366	(sh)	$\pi \rightarrow \pi^*$
	357	3.8	$\pi \rightarrow \pi^*$
	307	(sh)	$\pi \rightarrow \pi^*$
	278	14.1	$\pi \rightarrow \pi^*$
	253	(sh)	$\pi \rightarrow \pi^*$
[2.7]	474	2.7	MLCT
	441	(sh)	MLCT
	387	2.4	$\pi \rightarrow \pi^*$
	310	(sh)	$\pi \rightarrow \pi^*$
	292	(sh)	$\pi \rightarrow \pi^*$
	263	16.4	$\pi \rightarrow \pi^*$
	225	12.2	$\pi \rightarrow \pi^*$
[2.8]	463	2.0	MLCT
	426	(sh)	MLCT
	359	1.3	$\pi \rightarrow \pi^*$
	306	(sh)	$\pi \rightarrow \pi^*$
	288	8.7	$\pi \rightarrow \pi^*$
	246	6.6	$\pi \rightarrow \pi^*$
[2.9]	490	2.0	MLCT
	434	(sh)	MLCT
	365	3.1	$\pi \rightarrow \pi^*$
	356	(sh)	$\pi \rightarrow \pi^*$
	317	(sh)	$\pi \rightarrow \pi^*$
	278	13.1	$\pi \rightarrow \pi^*$
	255	(sh)	$\pi \rightarrow \pi^*$
[2.10]	496	1.9	MLCT
	429	2.2	MLCT
	395	(sh)	$\pi \rightarrow \pi^*$
	326	1.9	$\pi \rightarrow \pi^*$
	314	(sh)	$\pi \rightarrow \pi^*$
	262	12.4	$\pi \rightarrow \pi^*$
	223	7.5	$\pi \rightarrow \pi^*$
[2.11]	498	1.6	MLCT
	427	1.7	MLCT
	322	(sh)	$\pi \rightarrow \pi^*$
	284	6.4	$\pi \rightarrow \pi^*$
	251	5.0	$\pi \rightarrow \pi^*$

2.7.2 Rhenium(I) Polypyridyl Complexes

Complexes **[2.12]** to **[2.15]** show intense absorption bands around 200 to 350 nm that are assigned to ligand centred $\pi \rightarrow \pi^*$ transitions characteristic of aromatic nitrogen donor ligands (**Figure 2.9**). Data are summarised in **Table 2.2**. The absorption band that occurs between 375 and 460 nm, with a tail extends to about 550 nm can be assigned to MLCT transition. As with the Ru(II) analogues, the low energy bands are red shifted upon methylation.

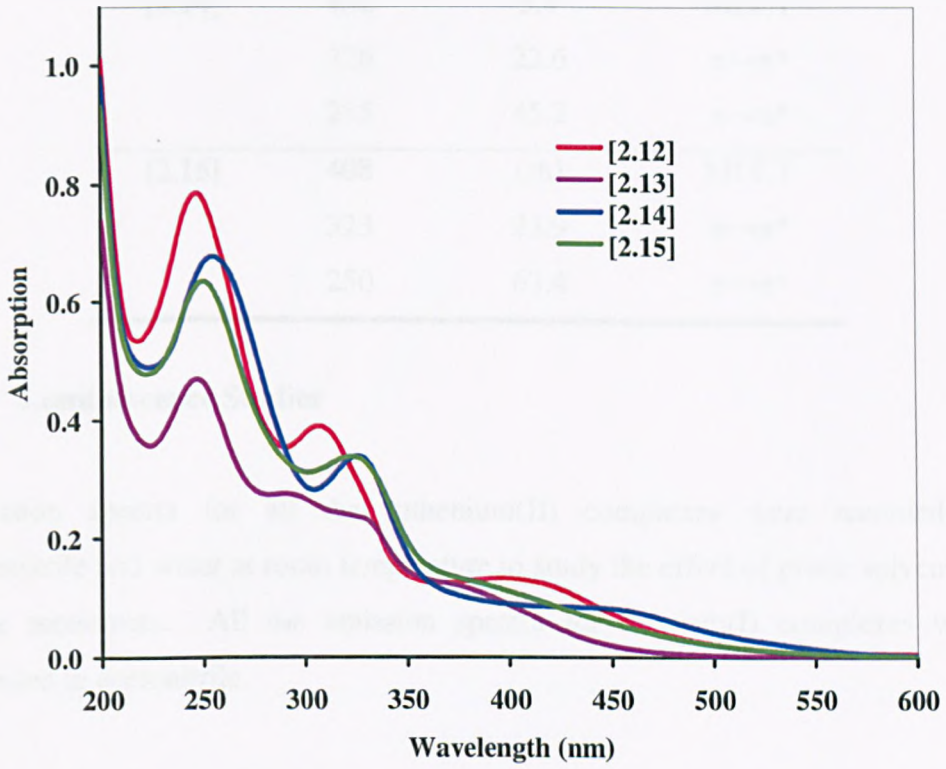

Figure 2.9: UV-Visible spectra of [2.12], [2.13], [2.14] and [2.15] recorded in acetonitrile.

Table 2.2: UV-Vis data for [2.12], [2.13], [2.14] and [2.15] recorded in CH_3CN.

Compound	λ_{max} (nm)	ε (10^3 $M^{-1}cm^{-1}$)	Assignation
[2.12]	403	8.7	MLCT
	307	19.4	$\pi \rightarrow \pi^*$
	247	39.2	$\pi \rightarrow \pi^*$
[2.13]	378	(sh)	MLCT
	325	(sh)	$\pi \rightarrow \pi^*$
	291	(sh)	$\pi \rightarrow \pi^*$
	247	46.7	$\pi \rightarrow \pi^*$
[2.14]	452	5.4	MLCT
	326	22.6	$\pi \rightarrow \pi^*$
	255	45.2	$\pi \rightarrow \pi^*$
[2.15]	408	(sh)	MLCT
	323	23.9	$\pi \rightarrow \pi^*$
	250	63.4	$\pi \rightarrow \pi^*$

2.8 Luminescence Studies

Emission spectra for all the ruthenium(II) complexes were recorded in acetonitrile and water at room temperature to study the effect of protic solvent on these monomers. All the emission spectra for rhenium(I) complexes were recorded in acetonitrile.

2.8.1 Ruthenium(II) Polypyridyl Complexes

All ruthenium complexes **[2.6]** to **[2.11]** show unstructured emissions in acetonitrile at room temperature (**Figure 2.10**) (data are normalised for clarity). The data are summarised in **Table 2.3**. Excitation at 470 nm for all the complexes results in emission between 600 to 700 nm. The emission quantum yield for **[2.6]**, **[2.7]** and **[2.8]** in acetonitrile are 0.127, 0.075 and 0.090, respectively. These quantum yields obtained are higher than those observed for $[Ru(bpy)_3]^{2+}$ under the same conditions ($\Phi_{em} = 0.062$).[87]

When methyl groups are attached to the qtpy ligands, complexes **[2.9]**, **[2.10]** and **[2.11]** emit weakly in acetonitrile (Φ_{em} = 0.033, Φ_{em} = 0.013 and Φ_{em} = 0.013, respectively). In addition, the emissions observed for the pyridinium complexes **[2.9]**, **[2.10]** and **[2.11]** are red-shifted to about 700 nm in acetonitrile. It seems likely that the low-energy emission is connected with the presence of the pyridinium group.[88]

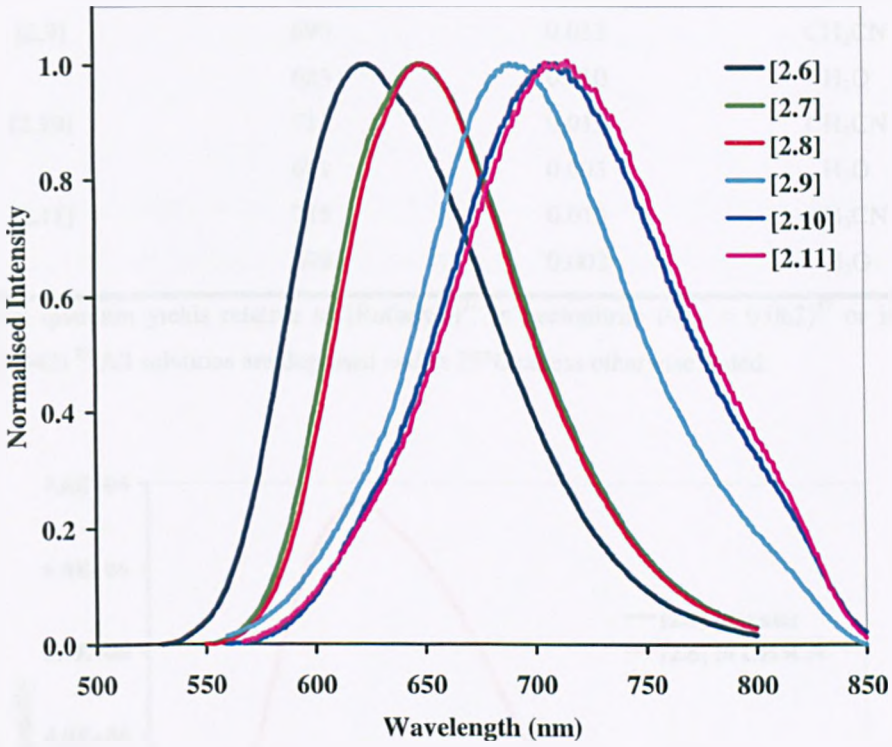

Figure 2.10: Luminescence spectra of [2.6], [2.7], [2.8], [2.9], [2.10] and [2.11] recorded in acetonitrile.

We were also interested to see the solvents effect on the luminescence of these ruthenium complexes. As expected, the emissions recorded for all the ruthenium(II) complexes are weaker in water relative to $[Ru(bpy)_3]^{2+}$ in water (Φ_{em} = 0.042).[89] This is obviously seen in the decrease in the emission intensity of ruthenium containing the dppz ligand **[2.6]** by fifty fold and a shifting of 43 nm to higher wavelength (**Figure 2.11**). As mentioned before, the excited state of dppz complexes is very dependent upon its microenvironment and thus it has been studied intensively as a molecular light switch.[85]

Table 2.3: Luminescence data for complexes [2.6], [2.7], [2.8], [2.9], [2.10] and [2.11].

Compound	λ_{max} (nm)	Φ_{em} [a]	Solvent
[2.6]	624	0.127	CH_3CN
	667	0.003	H_2O
[2.7]	648	0.075	CH_3CN
	651	0.048	H_2O
[2.8]	650	0.090	CH_3CN
	657	0.041	H_2O
[2.9]	690	0.033	CH_3CN
	683	0.010	H_2O
[2.10]	711	0.013	CH_3CN
	691	0.003	H_2O
[2.11]	715	0.013	CH_3CN
	699	0.002	H_2O

[a]Emission quantum yields relative to $[Ru(bpy)_3]^{2+}$ in acetonitrile (Φ_{em} = 0.062)[87] or in water (Φ_{em} = 0.042).[89] All solutions are degassed and at 25°C unless otherwise stated.

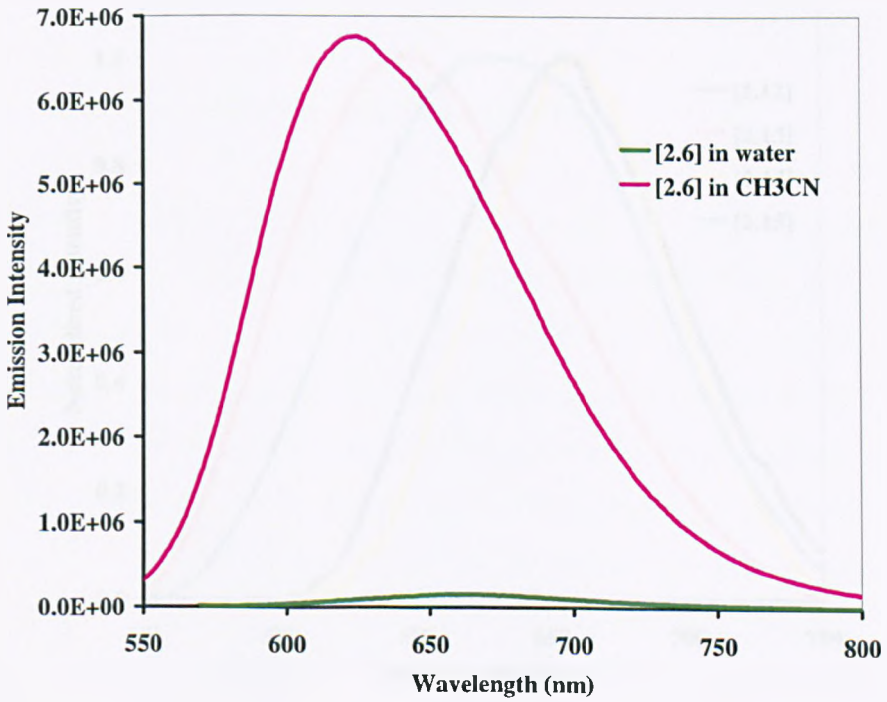

Figure 2.11: Luminescence spectra of [2.6] recorded in CH_3CN and water, respectively.

2.8.2 Rhenium(I) Polypyridyl Complexes

Spectra of the rhenium complexes are shown in **Figure 2.12** (data are normalised for clarity) and the data are summarised in **Table 2.4**.

All the complexes were excited at the wavelength characteristic of the transition MLCT. In this case, the excitation wavelength is at 385 nm. The emission at 656 nm of **[2.12]** is relatively weak (Φ_{em} = 0.007), however complex **[2.13]** emits more strongly (Φ_{em} = 0.050) and the emission is significantly blue shifted to 600 nm. This is due to the replacement of a π-donating halides to a π-accepting acetonitrile ligands results in stabilisation of the metal-centred HOMO. When methyl groups are attached to the qtpy ligands, complexes **[2.14]** and **[2.15]** emit weakly in acetonitrile (Φ_{em} = 0.002 and Φ_{em} = 0.007, respectively). *N*-methylation of the rhenium(I) complexes also results in a significant red shift in the emission of **[2.15]** to 621 nm.

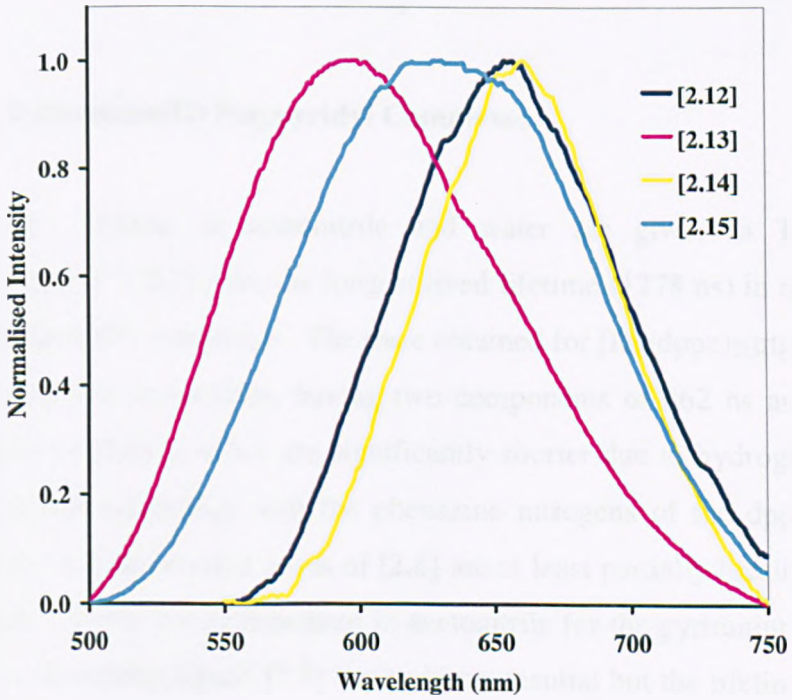

Figure 2.12: Luminescence spectra of [2.12], [2.13], [2.14], [2.15] recorded in acetonitrile.

Table 2.4: Luminescence data for complexes [2.12], [2.13], [2.14] and [2.15] in acetonitrile.

Compound	λ_{max} (nm)	Φ_{em}[a]
[2.12]	656	0.007
[2.13]	600	0.050
[2.14]	661	0.002
[2.15]	621	0.007

[a]Emission quantum yields relative to $[Ru(bpy)_3]^{2+}$ in acetonitrile (Φ_{em} = 0.062).[87] All solutions are degassed and at 25°C unless otherwise stated.

2.9 Luminescence Lifetimes

The radiative, k_r and nonradiative, k_{nr} rate constants were computed from the uncorrected emission spectra using equations (1) and (2) with the assumption that the intersystem crossing is unity.[74]

$$k_r = \frac{\phi_{em}}{\tau} \quad (1)$$

$$k_{nr} = \frac{1}{\tau} - k_r \quad (2)$$

2.9.1 Ruthenium(II) Polypyridyl Complexes

Luminescence lifetime in acetonitrile and water are given in **Table 2.5**. $[Ru(phen)_2(qtpy)]^{2+}$ **[2.7]** gave the longest lived lifetime (1278 ns) in acetonitrile for the ruthenium(II) complexes. The trace obtained for $[Ru(dppz)_2(qtpy)]^{2+}$ **[2.6]** is biexponential in acetonitrile, having two components of 862 ns and 314 ns. The lifetimes of **[2.6]** in water are significantly shorter due to hydrogen bonded water molecules interacting with the phenazine nitrogens of the dppz ligands. This suggests that the excited states of **[2.6]** are at least partially localised on the dppz ligands. Again, traces measured in acetonitrile for the pyridinium complex of this dppz containing ligand **[2.9]** is also biexponential but the lifetime in water is not significantly shorter as for **[2.6]**. This is very interesting as for this 4+ charge complex, it suggests that the lowest excited states is localised on the methylated quaterpyridyl. Baker *et al.*[74] observed that the LUMOs of the free

quaterpyridyl ligands are lowered upon quaternisation and thus this explain the lowest excited states being on the methylated quaterpyridyl.

Previous studies by Baker *et al.*[74] explored the luminescence lifetime of $[Ru(bpy)_2(qtpy)]^{2+}$ **[2.8]** and $[Ru(bpy)_2(qtpyMe_2)]^{4+}$ **[2.11]**, for completeness we repeated their experiments. We observed monoexponential decay for both **[2.8]** and **[2.11]** in water.

Typically, the radiative rate constants for Ru(II) polypyridyl complexes are in the range of 10^4 - 10^5 s^{-1}. We observed that the radiative rate constants for **[2.7]** and **[2.8]** are close to each other while the non-radiative rate constants for **[2.10]** and **[2.11]** are again similar in acetonitrile. On the other hand, the non-radiative rate constants for most of the complexes are considerably larger in water which agrees with the decrease in the emission intensity observed for the complexes.

Table 2.5: Luminescence lifetime data for ruthenium(II) complexes.

Compound	τ, ns	10^4 s^{-1}, k_r	10^4 s^{-1}, k_{nr}	Conditions[a]
[2.6]	862[b]; 314[c]	14.7[b], 40.4[c]	101[b]; 278[c]	CH_3CN
	42[b]; 8[c]	7.1[b], 37.5[c]	2373[b];12463[c]	H_2O
[2.7]	1278	5.9	72	CH_3CN
	795	6.0	119	H_2O
[2.8]	1050	8.6	87	CH_3CN
	509	8.1	188	H_2O
[2.9]	268[b]; 89[c]	12.3[b]; 37.1[c]	361[b]; 1086[c]	CH_3CN
	184[b]; 48[c]	5.4[b]; 20.8[c]	538[b]; 2063[c]	H_2O
[2.10]	79	16.5	1249	CH_3CN
	63	4.8	1583	H_2O
[2.11]	61	21.3	1618	CH_3CN
	51	3.9	1956	H_2O

[a]All solutions are degassed and at 25 °C unless otherwise stated. [b]First component. [c]Second component.

2.9.2 Rhenium(I) Polypyridyl Complexes

Data for the luminescence lifetimes in acetonitrile are summarised in **Table 2.6**. All the rhenium(I) complexes show monoexponential decays. Upon changing the chloride ligand to acetonitrile, an increase in emission energy, quantum yield and luminescence lifetime is observed. Previous studies by Guarr *et al.*[90] showed a similar observation for these types of complexes. The blue shift emission observed upon exchanging the chloride ligand with acetonitrile is most easily explained by changes in the Re(I)/Re(II) oxidation potential. On changing the chloride ligand for the acetonitrile ligand, the Re(I) oxidation state is stabilised due to back bonding interactions yielding higher emission energies.[91]

On the other hand, luminescence lifetime for **[2.15]** in acetonitrile (τ = 79 ns) is about five times smaller than that of **[2.13]** (τ = 377 ns), consistent with an increase in the rate of non-radiative decay. The pyridinium groups attached the qtpy ligand introduce a charge separation state which quenched the emission of **[2.15]**. It has been shown that $[Ru(bpy)_3]^{2+}$ can be oxidatively quenched by pyridinium ions which are weak oxidants.[88]

Table 2.6: Luminescence lifetime data for rhenium(I) complexes.

Compound	τ, ns	10^4 s^{-1}, k_r	10^4 s^{-1}, k_{nr}	Conditions[a]
[2.12]	21	33	4729	CH_3CN
[2.13]	317	15.8	300	CH_3CN
[2.14]	18	11.1	5544	CH_3CN
[2.15]	79	8.9	1257	CH_3CN

[a]All solutions are degassed and at 25 °C unless otherwise stated.

2.10 Electrochemistry Studies

Cyclic voltammograms of **[2.6]**, **[2.7]**, **[2.8]**, **[2.9]**, **[2.10]**, **[2.11]**, **[2.12]**, **[2.13]**, **[2.14]** and **[2.15]** were carried out at a scan rate 100 mVs^{-1} in acetonitrile

containing 0.1 M TBAP, as supporting electrolyte, under nitrogen atmosphere. Potentials were measured *vs.* Ag/AgCl.

2.10.1 Ruthenium(II) Polypyridyl Complexes

All complexes show typical behaviour for these types of complexes with a chemically reversible one electron oxidation of the Ru(II)/Ru(III) occuring around +1.2 V to +1.4 V, in agreement with similar complexes that have been described in literature.[74, 75] The electrochemical data are summarised in **Table 2.7**. For example, **Figure 2.13** shows the oxidation of complex **[2.6]**.

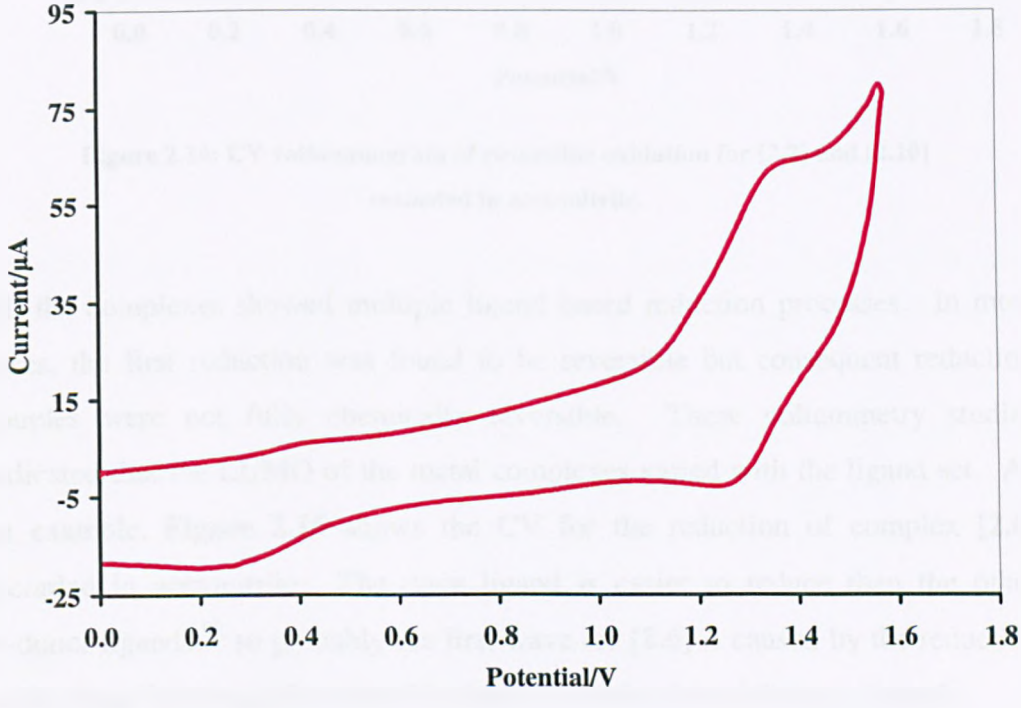

Figure 2.13: Electrochemical cyclic voltammogram for the oxidation of complex [2.6] recorded in acetonitrile.

The presence of pyridinium groups in **[2.9]**, **[2.10]** and **[2.11]** results in a slightly positive shift in the Ru(II)/Ru(III) oxidation waves under the same conditions. This is due to a slight electrostatic destabilisation of the Ru(III) oxidation state compared to the non-methylated complexes. As an example, **Figure 2.14** shows the CV, recorded in acetonitrile, for **[2.7]** and its methylated analogue **[2.10]**.

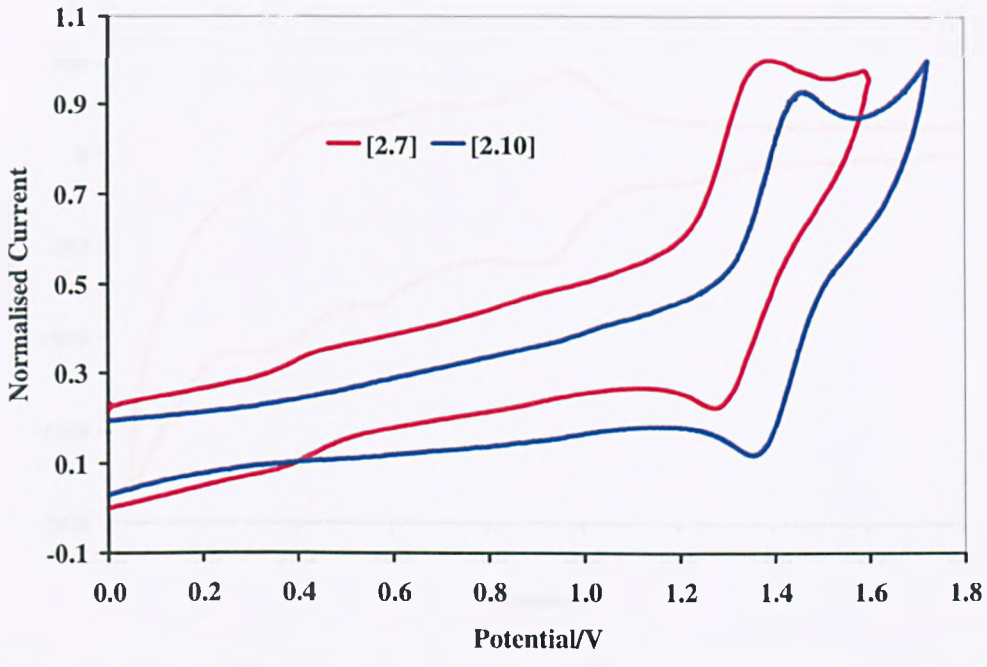

Figure 2.14: CV voltammogram of reversible oxidation for [2.7] and [2.10] recorded in acetonitrile.

All the complexes showed multiple ligand based reduction processes. In most cases, the first reduction was found to be reversible but consequent reduction couples were not fully chemically reversible. These voltammetry studies indicated that the LUMO of the metal complexes varied with the ligand set. As an example, **Figure 2.15** shows the CV for the reduction of complex **[2.6]** recorded in acetonitrile. The dppz ligand is easier to reduce than the other *N*-donor ligands,[92] so probably the first wave for **[2.6]** is caused by the reduction of the dppz ligand and the second is due to the reduction of the qtpy ligands.

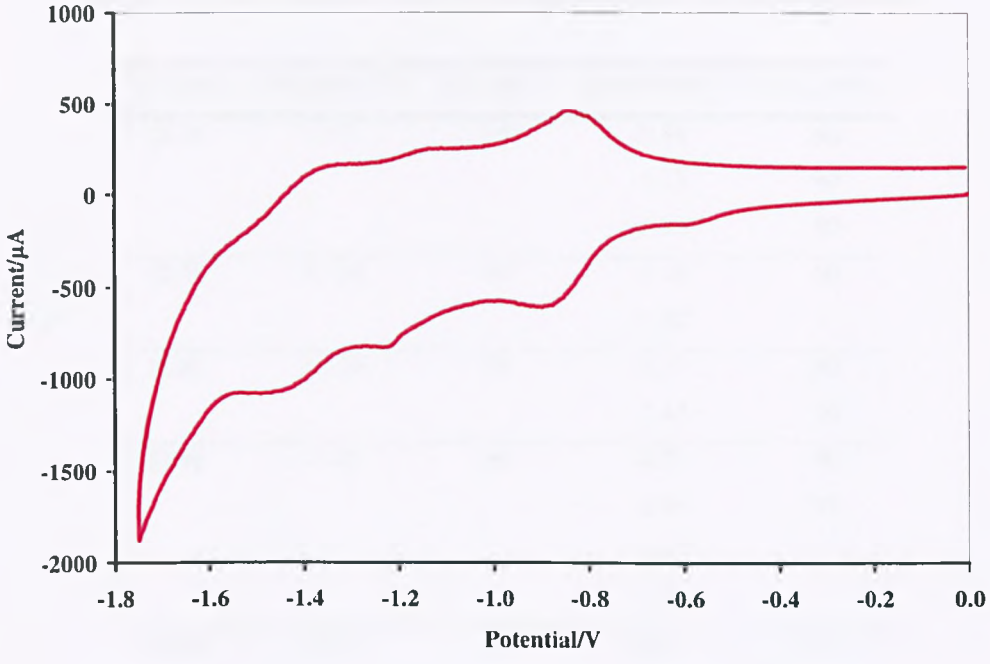

Figure 2.15: Electrochemical cyclic voltammogram for the reduction of complex [2.6] recorded in acetonitrile.

Complexes **[2.9]**, **[2.10]** and **[2.11]** show an additional reduction at around -0.70 V which is due to two closely spaced one-electron reductions of the two weakly interacting pyridinium groups. It has been shown that complete resolution into two distinct waves is not possible if the peak to peak potential difference is less than ~ 118 mV.[74, 75] Baker *et al.*[74] suggesting that upon quaternisation of the free quaterpyridyl ligands, the LUMOs of the free ligands are lowered. This supports the former assumption that the first two electrons appear to be added to the *N*-methyl pyridinium groups.

Table 2.7: Electrochemical data for the Ru(II) quaterpyridine complexes.

Complex	Oxidation (V)	ΔE_p (mV)	Reduction (V)	ΔE_p (mV)
[2.6]	+1.37	100	-0.89	60
			-1.23	90
			-1.44	80
[2.7]	+1.38	90	-1.10	50
			-1.39[a]	-
[2.8]	+1.38	90	-1.11	80
			-1.43	90
[2.9]	+1.45	90	-0.71	90
			-0.96	90
			-1.30[a]	-
			-1.59[a]	-
[2.10]	+1.43	90	-0.73	60
			-1.24[a]	-
			-1.47[a]	-
[2.11]	+1.46	90	-0.78	60
			-1.22	90
			-1.47	90

[a]Peak not fully chemically reversible, therefore only E_p is quoted.

2.10.2 Rhenium(I) Polypyridyl Complexes

All of the rhenium complexes display irreversible oxidations associated with Re(II)/Re(I) couple. As an example, **Figure 2.16** shows the irreversible oxidation for **[2.14]** recorded in acetonitrile. Data are summarised in **Table 2.8**.

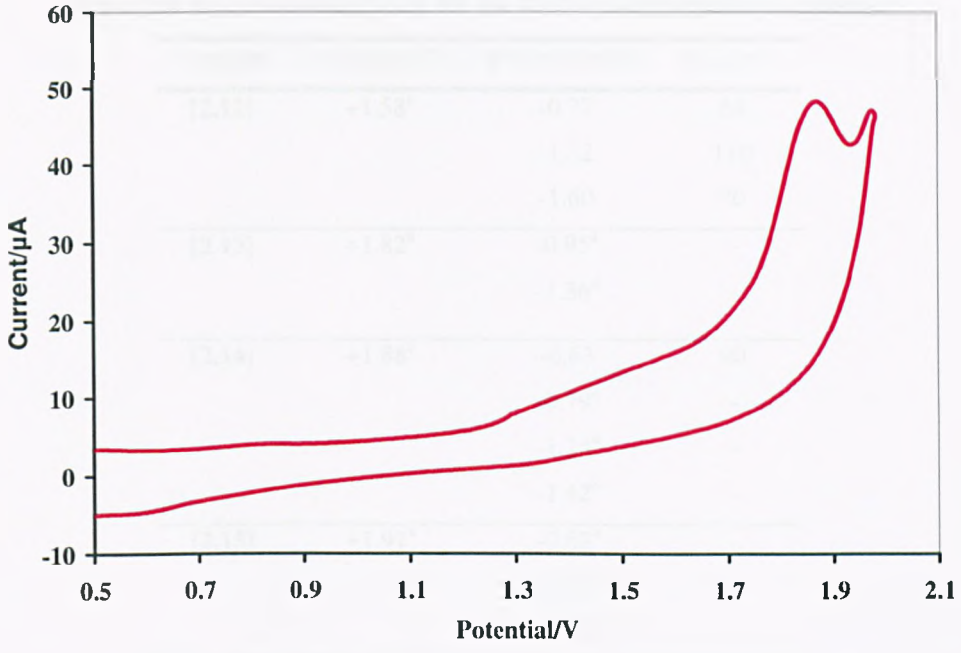

Figure 2.16: CV voltammogram of irreversible oxidation for [2.14] recorded in acetonitrile.

The oxidation of acetonitrile complex **[2.13]** was previously examined.[76] However, no oxidation was observed within the solvent window. In this study, we report the oxidation of **[2.13]** occurs at 1.82 V, a slightly more positive potential compared to that of **[2.12]**. On changing the chloride ligand for a acetonitrile ligand, the complexes are more difficult to oxidise. Acetonitrile is a good π-acceptor ligand, which has the ability to pull electrons away from the metal centre. Thus this stabilises the Re(I) oxidation state.

Table 2.8: Electrochemical data for the Re(I) quaterpyridine complexes.

Complex	Oxidation (V)	Reduction (V)	ΔE_p (mV)
[2.12]	+1.58[a]	-0.77	60
		-1.32	110
		-1.60	70
[2.13]	+1.82[a]	-0.95[a]	-
		-1.36[a]	-
[2.14]	+1.88[a]	-0.63	90
		-0.79[a]	-
		-1.24[a]	-
		-1.42[a]	-
[2.15]	+1.91[a]	-0.62[a]	-
		-0.83[a]	-
		-1.31[a]	

[a]Peak not fully chemically reversible, therefore only E_p is given.

The presence of pyridinium groups in **[2.14]** and **[2.15]** result in a slightly positive shift in potential for the Re(II)/Re(I) oxidation waves under the same conditions. Complexes **[2.14]** and **[2.15]** show additional reductions at around -0.60 V which are expected due to two one-electron transfers to the pyridinium groups.

All complexes display characteristic ligand-centred reductions. For complex **[2.12]**, all of these waves are reversible; however for **[2.13]** and **[2.15]**, all ligand reductions are irreversible.

2.11 Spectroelectrochemistry Studies

Ruthenium(II) polypyridyl complexes were studied using UV/Vis/NIR spectroelectrochemistry in acetonitrile using an OTTLE cell[93] at 253 K. Due to the irreversibility of their first reduction process, compounds **[2.7]** and **[2.9]** are not discussed here. The behaviour of **[2.6]**, **[2.8]**, **[2.10]** and **[2.11]** is discussed in this section.

Reduction of **[2.6]** to -0.95 V (i.e. after the first reduction processed observed by CV) gave rise to changes in the spectrum as shown in **Figure 2.17**.

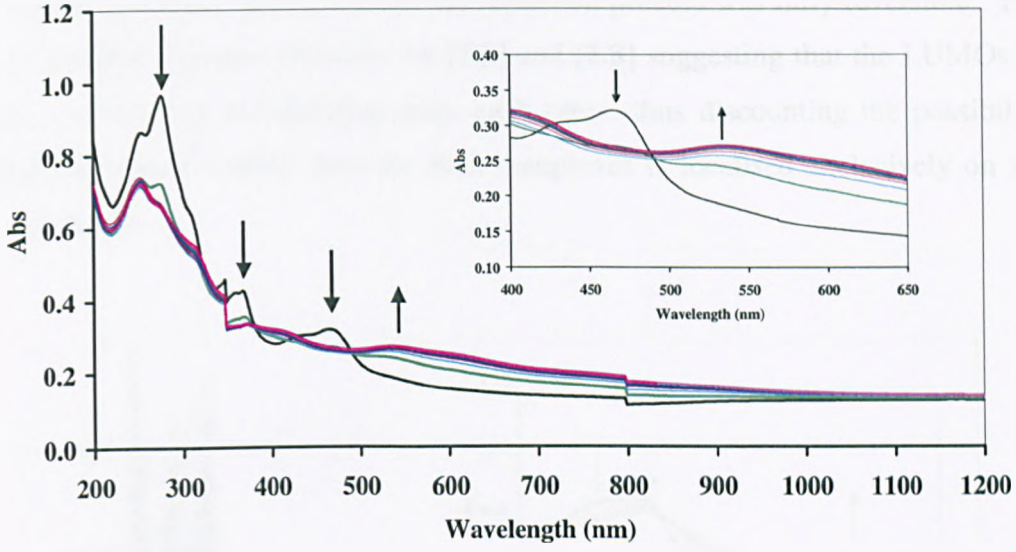

Figure 2.17: Change in absorption spectrum of [2.6] upon one electron reduction. The inset shows a better resolved band for MLCT.

Reduction of $[\mathbf{2.6}]^{2+}$ to $[\mathbf{2.6}]^{+}$ results in depletion of the MLCT band at 468 nm while a lower energy absorption band with a feature centred at 533 nm grows in. The band at 533 nm is probably due to a new π-π^* transition involving the reduced ligand. A band at 357 nm is depleted. A similar band in $[Ru(bpy)_2(dppz)]^{2+}$ is assigned as a MLCT associated with dppz ligand.[94] Reduction of this band suggests that the first reduction process involves Ru→dppz MLCT. A band at 278 nm is also reduced with a shoulder growing in at 253 nm. Evidently, the band that reduces is due to a π-π^* transition of the non-reduced ligand. Increasing the potential of the system back to 0 V regenerated the original spectrum; therefore the ligand-centred reduction process could be examined.

Reduction of **[2.8]** to -1.30 V results the change in the absorption spectrum shown in **Figure 2.18**. The MLCT process observed at 463 nm decreased in

intensity and is slightly red-shifted, while the lowest energy shoulder grows in upon reduction. In contrast to **[2.6]**, a band at 359 nm is increased. Bands at 288 nm and 246 nm were found to reduce in intensity. The latter are due to a π-π^* transition of the non-reduced ligand. Return to 0 V again regenerated the original spectrum, indicating that the reduction process was fully reversible. The spectroelectro results obtained for **[2.6]** and **[2.8]** suggesting that the LUMOs of these complexes are different from each other, thus discounting the possibility that the lowest excited state for both complexes is localised exclusively on the qtpy ligand.

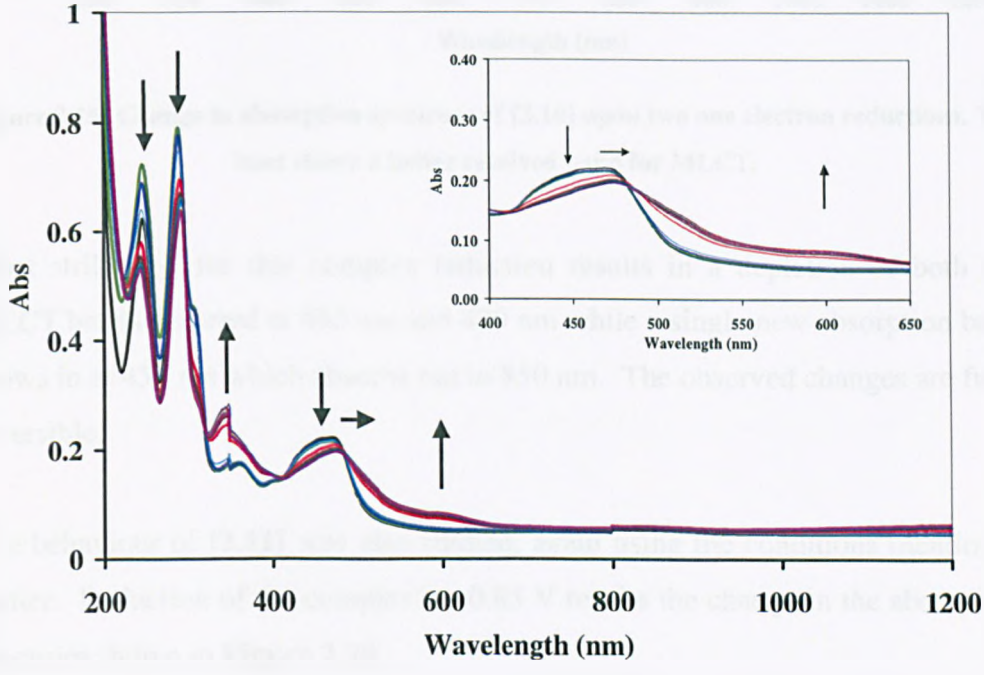

Figure 2.18: Change in absorption spectrum of [2.8] upon one electron reduction. The inset shows a better resolved band for MLCT.

Presumably, upon methylated, the lowest lying excited states will be localised on the qtpy in these mixed ligands complexes. Reduction of $[\mathbf{2.10}]^{4+}$ to $[\mathbf{2.10}]^{2+}$ gives changes in the absorption spectrum as shown in **Figure 2.19**.

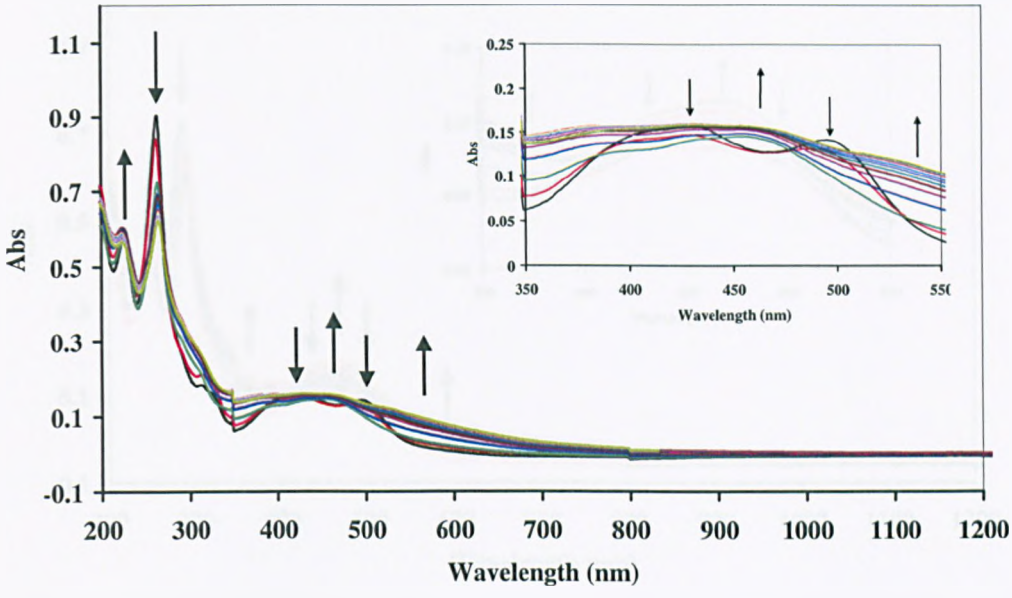

Figure 2.19: Change in absorption spectrum of [2.10] upon two one electron reductions. The inset shows a better resolved band for MLCT.

Most strikingly, for this complex reduction results in a depletion of both the MLCT bands centered at 496 nm and 429 nm while a single new absorption band grows in at 458 nm which absorbs out to 850 nm. The observed changes are fully reversible.

The behaviour of **[2.11]** was also studied, again using the conditions mentioned earlier. Reduction of the complex to -0.85 V results the change in the absorption spectrum shown in **Figure 2.20**.

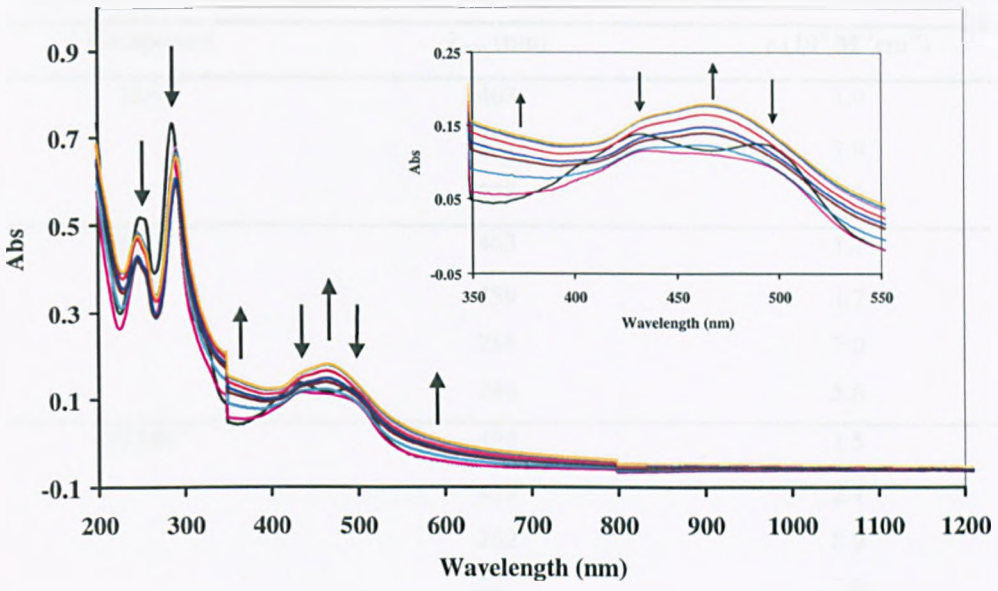

Figure 2.20: Change in absorption spectrum of [2.11] upon two one electron reductions. The inset shows a better resolved band for MLCT.

Again, reduction results in a depletion of both the MLCT bands centred at 498 nm and 427 nm with a new absorption band centred at 460 nm growing in, again this band absorbs out to 850 nm. Return to 0 V again regenerated the original spectrum, indicating that the reduction process was fully reversible.

Both **[2.10]** and **[2.11]** show very similar behaviours upon reduction, which indeed supports the earlier hypothesis that upon methylation, the lowest excited state involves the coordinated Me_2Qtpy ligand instead of the alternative Ru(II)-ancillary ligands. These results are also consistent with report by Baker which indicates that the LUMOs of the free quaterpyridyl ligands are lowered upon quaternisation and thus the lowest excited states are now clearly centred on the methylated quaterpyridyl.

Table 2.9: UV/Vis/NIR data for [2.6], [2.8], [2.10] and [2.11] upon reduction process.

Compound	λ_{max} (nm)	ε (10^4 $M^{-1}cm^{-1}$)
$[2.6]^+$	468	1.9
	357	2.9
	278	9.3
$[2.8]^+$	463	1.7
	359	1.7
	288	7.0
	246	5.6
$[2.10]^{2+}$	496	1.5
	429	2.1
	262	8.9
	223	7.8
$[2.11]^{2+}$	498	1.7
	427	1.7
	284	5.3
	251	4.3

2.12 X-Ray Crystallography Studies

Single crystals of **[2.6]**, **[2.7]** and **[2.8]** suitable for an X-ray structure analysis were obtained from slow vapour diffusion of benzene into a nitromethane solution. The structures described in this section were solved by Harry Adams in the department's X-ray structure determination service and a summary of the crystallographic data is contained in the Appendix.

The crystal structure of **[2.6]** is shown in **Figure 2.21**. The final refinement of the data for this crystal was 30 % and while it is not of sufficient quality for publication, it allows us to confirm the structure of **[2.6]**.

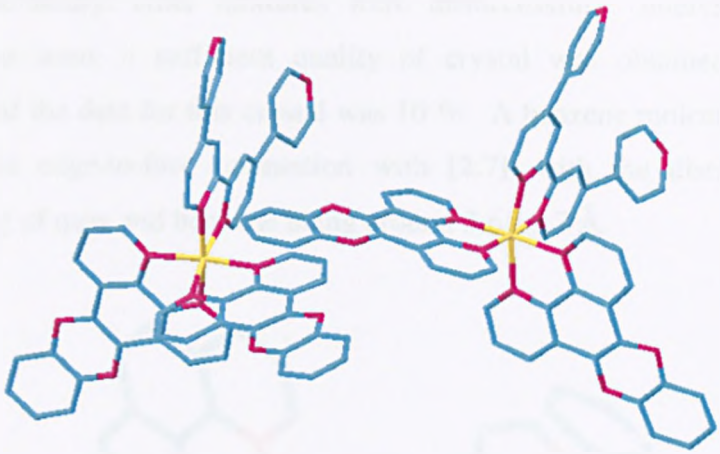

Figure 2.21: Structural representation of the cation found in the crystal structure of [2.6]. Hydrogen atoms, PF_6^- anions and solvent molecules are removed for clarity.

Packing of **[2.6]** reveals π-π stacking between the aromatic rings of the dppz, the distance between two dppz ligands of different metal cations are around 3.4 - 3.8 Å (**Figure 2.22**).

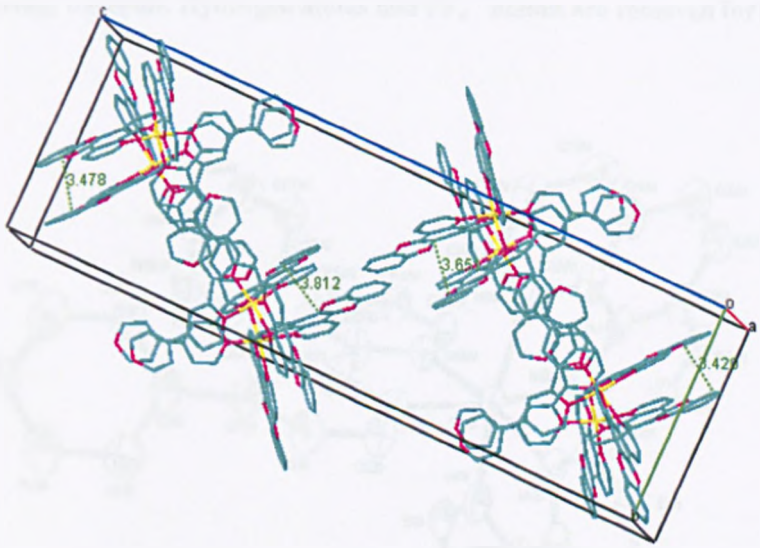

Figure 2.22: Packing structure of [2.6]. PF_6^- anions, hydrogen atoms and solvent molecules omitted for clarity.

The crystal structure of **[2.7]** is shown in **Figure 2.23**, and **Table 2.10** shows selected bond lengths and angles of the complex. Two PF_6^- anions are removed for clarity while a solvent molecule is shown. Attempts to grow crystal in

nitromethane-diethyl ether mixtures were unsuccessful. Interestingly, when benzene was used, a sufficient quality of crystal was obtained. The final refinement of the data for this crystal was 10 %. A benzene molecule was found to be in the edge-to-face orientation with **[2.7]**, with the distance between pyridine ring of qtpy and benzene being around 3.6 - 3.7 Å.

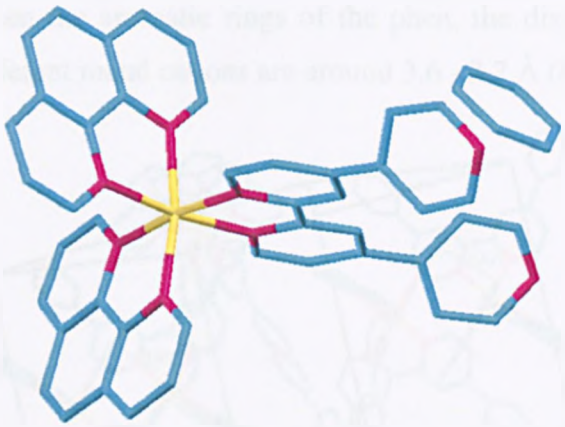

Figure 2.23: Structural representation of the cation found in the crystal structure of [2.7] with solvent molecule. Hydrogen atoms and PF_6^- anions are removed for clarity.

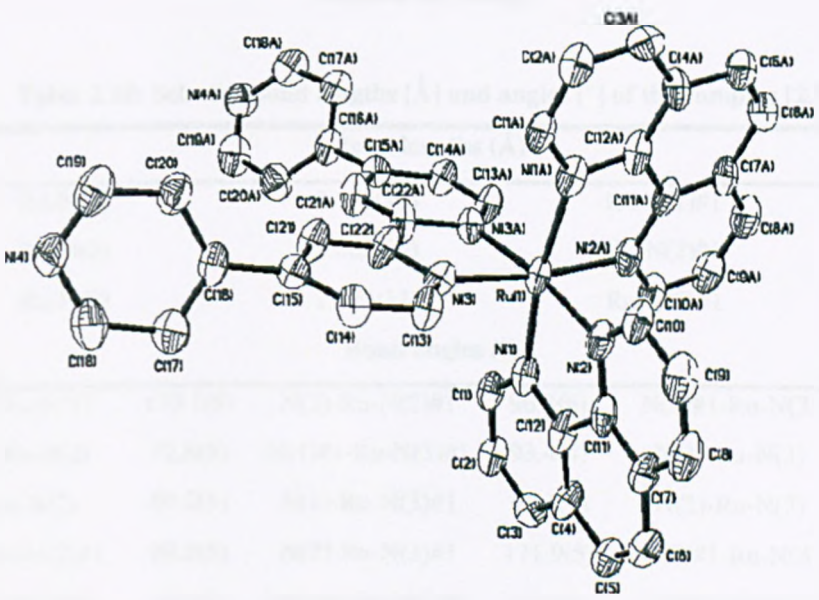

Figure 2.24: ORTEP plot of the cation in [2.7]. Hydrogen atoms, PF_6^- anions and solvent molecules are removed for clarity.

The ruthenium centre has a distorted octahedral coordination. The trans angles at the Ru(II) centre are close to octahedral 170.1°, 171.9° and 171.9°. The Ru-N bond length involving the phen ligand are 2.052(13) and 2.062(12) Å, while the bond lengths for the Ru-qtpy are larger, 2.073(11) Å. The bite angle of the phen is 80.2(5)°, and the bite angles for the qtpy is 78.8(6)°. Packing of **[2.7]** reveals π-π stacking between the aromatic rings of the phen, the distance between two phen ligands of different metal cations are around 3.6 - 3.7 Å (**Figure 2.25**).

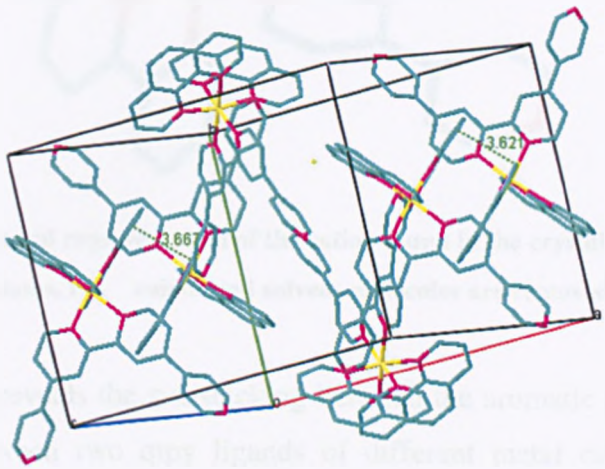

Figure 2.25: Packing structure of [2.7]. PF_6^- anions, hydrogen atoms and solvent molecules omitted for clarity.

Table 2.10: Selected bond lengths [Å] and angles [°] of the complex [2.7].

Bond lengths (Å)					
Ru-N(1)	2.052(13)		Ru-N(1)#1	2.052(13)	
Ru-N(2)	2.062(12)		Ru-N(2)#1	2.062(12)	
Ru-N(3)	2.073(11)		Ru-N(3)#1	2.073(11)	
Bond angles (°)					
N(1)#1-Ru-N(1)	170.1(6)	N(2)-Ru-N(2)#1	90.8(6)	N(1)#1-Ru-N(3)	94.3(4)
N(1)#1-Ru-N(2)	92.8(5)	N(1)#1-Ru-N(3)#1	93.4(4)	N(1)-Ru-N(3)	93.4(4)
N(1)-Ru-N(2)	80.2(5)	N(1)-Ru-N(3)#1	94.3(4)	N(2)-Ru-N(3)	95.4(4)
N(1)#1-Ru-N(2)#1	80.2(5)	N(2)-Ru-N(3)#1	171.9(5)	N(2)#1-Ru-N(3)	171.9(5)
N(1)-Ru-N(2)#1	92.8(5)	N(2)#1-Ru-N(3)#1	95.4(4)	N(3)#1-Ru-N(3)	78.8(6)

Symmetry transformations used to generate equivalent atoms:

#1 -x+1,y,-z+1/2

The crystal structure of **[2.8]** is shown in **Figure 2.26**. Although the final refinement of the data for this crystal was 17 % and it is not of sufficient quality for publication, it allows us to confirm the structure of **[2.8]**.

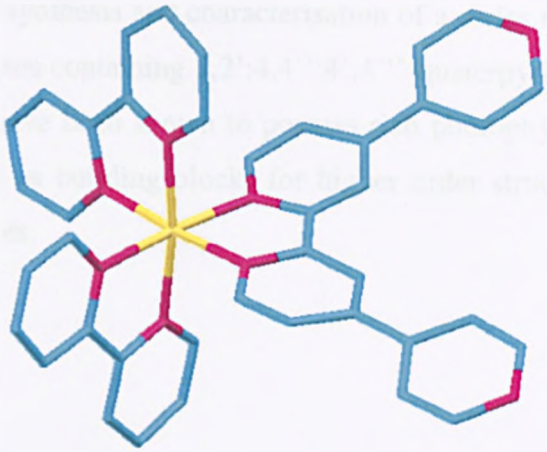

Figure 2.26: Structural representation of the cation found in the crystal structure of [2.8]. Hydrogen atoms, PF_6^- anions and solvent molecules are removed for clarity.

Packing of **[2.8]** reveals the π-π stacking between the aromatic rings of the qtpy, the distance between two qtpy ligands of different metal cations are around 3.6 - 3.8 Å (**Figure 2.27**).

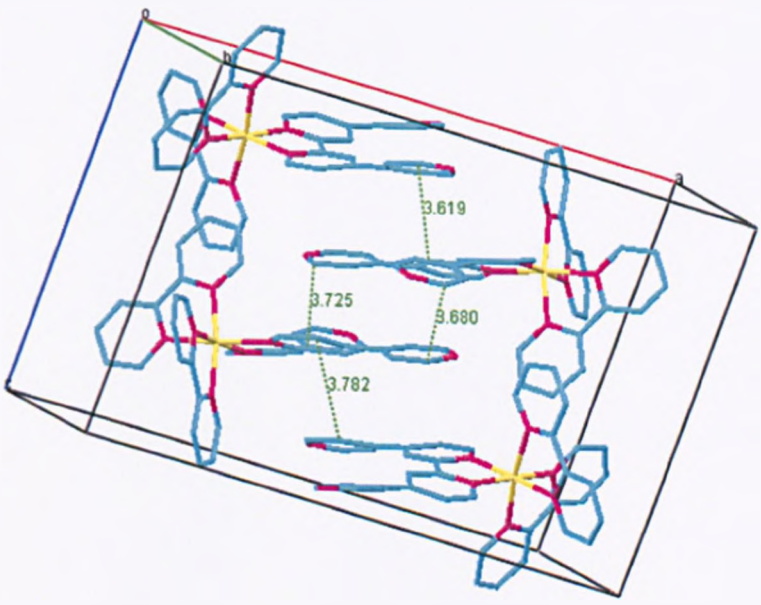

Figure 2.27: Packing structure of [2.8]. PF_6^- anions, hydrogen atoms and solvent molecules omitted for clarity.

2.13 Conclusion

In this chapter, the synthesis and characterisation of a series of ruthenium(II) and rhenium(I) complexes containing 2,2':4,4'':4',4'''-quaterpyridyl ligand has been discussed. They have been shown to possess rich photophysical characteristics and show potential as building blocks for higher order structures which can be used as anion sensors.

3 DNA Binding Studies on Ruthenium(II) and Rhenium(I) Polypyridyl Complexes

This chapter describes the interaction of the ruthenium(II) and rhenium(I) polypyridyl complexes, described in the previous chapter, with CT-DNA. In particular, we were interested to study how the DNA binding interactions of these mixed-ligand complexes were affected by changes in peripheral charge resulting from the addition of methyl groups attached to the qtpy ligand.

To place the studies in this chapter in context, a brief introduction into the structure of DNA and the properties of DNA binding substrates is included.

3.1 DNA

Since the discovery of the structure of deoxyribonucleic acid (DNA) over half a century ago, research on DNA has become a subject of intense interest. DNA is commonly known as a carrier of genetic information in all cellular life as well as in many viruses.[95] DNA is the template for living systems on earth and its study is central to the knowledge of life.

3.1.1 DNA Structure

DNA is a polymer of nucleotides constructed from three components; deoxyribose sugar residues, a phosphoryl group and four bases: purine adenine (A), purine guanine (G), pyrimidine cytosine (C) and pyrimidine thymine (T) (**Figure 3.1**).

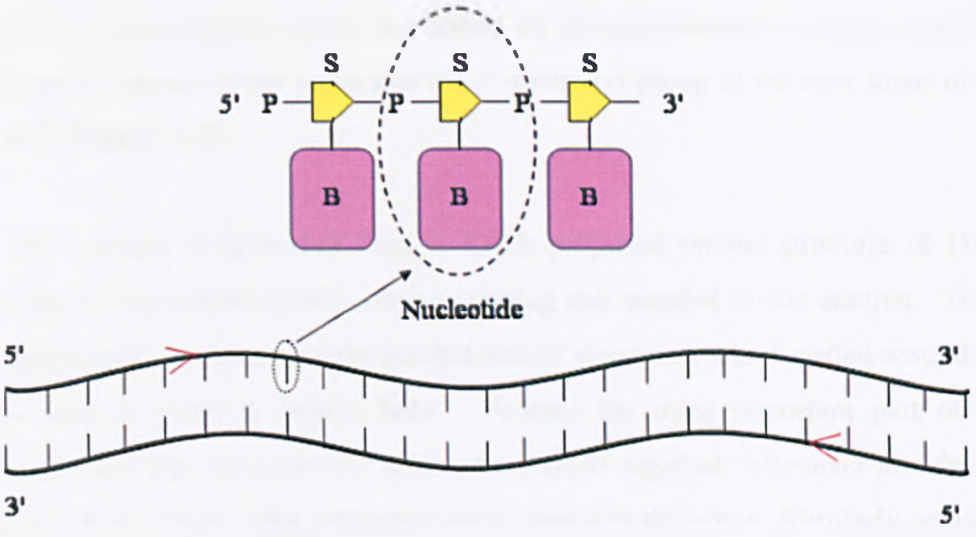

Figure 3.1: The two strands of DNA separated, showing a nucleotide, where S = deoxyribose sugar residue, P = phosphoryl group and B = nucleobase).[96]

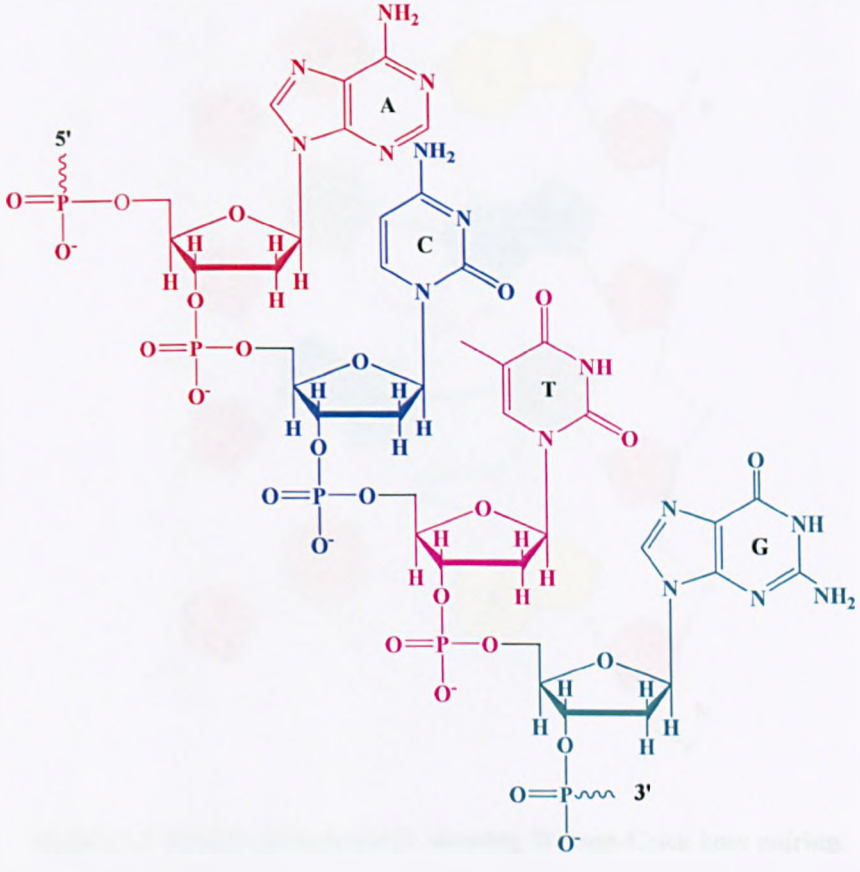

Figure 3.2: Structure of part of DNA chain: nucleosides joined by phosphodiester bond to grow nucleotides.

In DNA, the monomeric units are linked by phosphodiester bonds between the 5'-hydroxyl group of one sugar and the 3'-hydroxyl group of the next sugar in the chain[97] (**Figure 3.2**).

In 1953, James Watson and Francis Crick proposed on the structure of DNA consists of two polynucleotide chains running anti-parallel to one another. These complementary chains are right-handed helical structures which coiled around the same axis to create a double helix. Perhaps the most important part of the proposal was that the bases are hydrogen-bonded together; whenever an adenine appears in one chain, then a thymine must appear in the other. Similarly, guanine always pairs with cytosine (**Figure 3.3**).

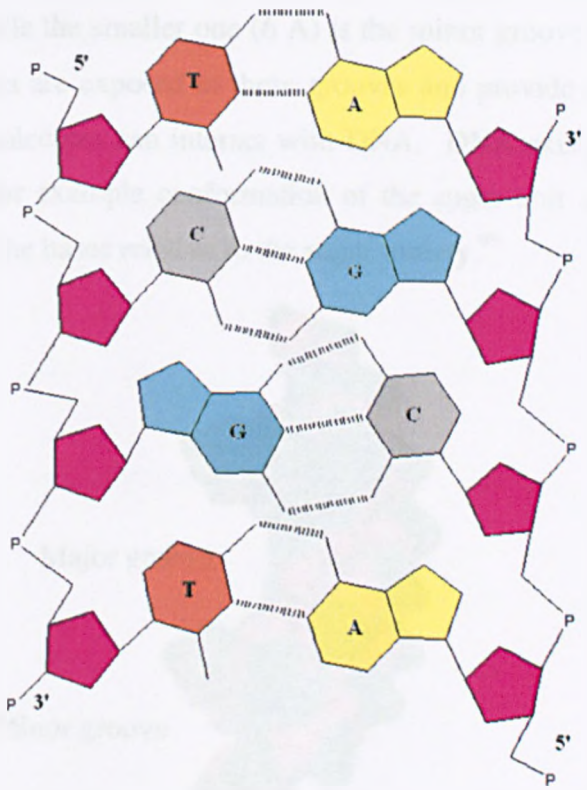

Figure 3.3: Double-stranded DNA showing Watson-Crick base pairing.

From **Figure 3.3**, we can see that the Watson-Crick guanine-cytosine pair has three hydrogen bonds, rather than two seen for adenine-thymine. This suggests that the DNA double helices with guanine-cytosine should be more stable than

those with adenine-thymine. The adjacent purine and pyrimidine units, which are located on the inside of the helix, are stabilised through π-π stacking interactions. On the other hand, the deoxyribose and phosphate moieties are on the outside of the helix and in contact with solvent. Interaction of the negative charges on the phosphates with the dipoles of water molecules is one of the factors that stabilises the DNA structure.[98]

3.1.1.1 The DNA Grooves

The other notable feature of the DNA structure resulting from the helical strands is that it has two grooves running diagonally through it. The grooves are unequal in size. For example, in B-DNA, a much wider groove (12 Å) is termed the major groove while the smaller one (6 Å) is the minor groove (**Figure 3.4**). The edges of the bases are exposed in these grooves and provide sites where protein or other small molecules can interact with DNA. DNA exists in many possible conformations; for example conformation of the sugar unit and the *syn* or *anti* conformation of the bases relative to the sugar moiety.[99]

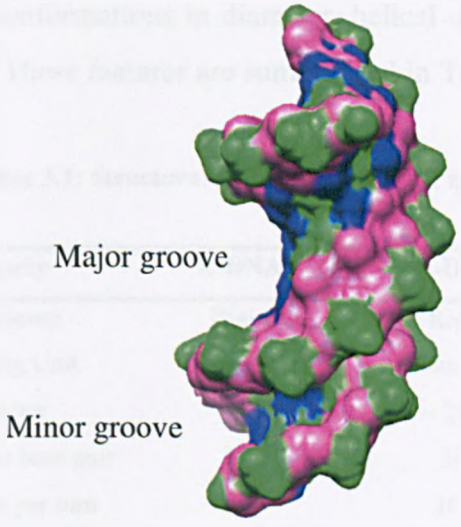

Figure 3.4: Structure of DNA: major and minor grooves (PDB ID: 1FQ2).[100]

The X-ray diffraction studies on heterogeneous DNA fibres provided by Rosalind Franklin[101] were essential in providing more understanding on DNA structure.

The three main possible conformations are A-DNA, B-DNA and Z-DNA (**Figure 3.5**).

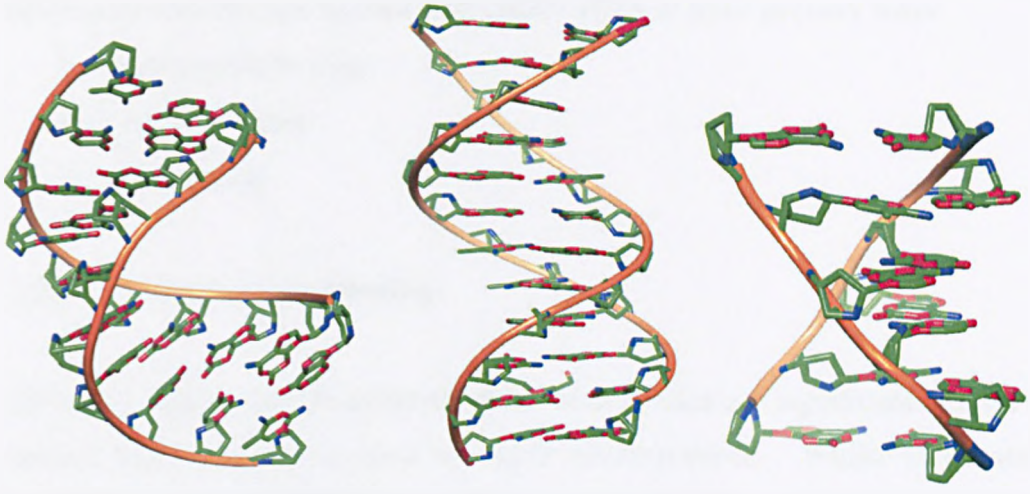

Figure 3.5: Major nucleic acid duplex conformations from left to right: A-DNA (PDB ID: 440D),[102] B-DNA (PDB ID: 1FQ2)[100] and Z-DNA (PDB ID: 2F8W).[100]

Whilst the first two conformations are right handed helices, the latter is left-handed helix. However, the most common conformation found under physiological condition is B-DNA.[103] There are some noticeable differences between these conformations in diameter, helical orientation and size and shape of the grooves. These features are summarised in **Table 3.1**.

Table 3.1: Structural features of ideal A-, B- and Z-DNA.[95, 103]

Property	A-DNA	B-DNA	Z-DNA
Helix Sense	Right	Right	Left
Repeating Unit	1 base pair	1 base pair	2 base pair
Diameter	~ 23 Å	~ 20 Å	~ 18 Å
Rotation per base pair	33°	36°	30°
Base pairs per turn	11	10.5	11.6
Helix rise per base	2.6 Å	3.4 Å	3.7 Å
Sugar pucker	C3' Endo	C2' Endo	C2' Endo at C C3' Endo at G
Major groove	Narrow and deep	Wide and deep	Narrow and deep
Minor groove	Wide and shallow	Narrow and deep	Narrow and deep

3.2 Non-covalent Binding to DNA

Molecules and ions can interact with duplex DNA in three primary ways:

- Electrostatic binding
- Groove binding
- Intercalation

3.2.1 Electrostatic Binding

DNA is a highly charged polymer which must condense a significant number of cations from solution to exist in stable conformations. Whilst electrostatic interactions involve binding of cations to the negatively charged phosphates located in the DNA backbone through interactions which are generally non-specific and reversible, this interactions results in an increase in the stability of the DNA conformation. Polyamines bind to DNA through such interactions as they are usually fully protonated at physiological conditions; thus the negatively charged phosphate backbone of the DNA serves as the complementary site for interactions. Spermidine and spermine are typical drugs for this type of interaction (**Figure 3.6**).[104, 105]

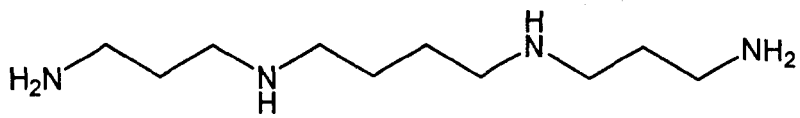

Spermine

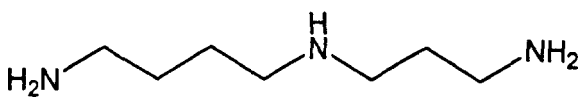

Spermidine

Figure 3.6: Structure of spermine and spermidine.

3.2.2 Groove Binding

The grooves resulting from the helical strands of duplex DNA serve as an alternative binding mode for ligands with DNA. Groove binding involves direct interactions of the bound molecules with the edges of the base pair in either major or minor grooves of the duplex DNA. Unlike other binding modes, groove binding can span many base-pairs and hence very high level of DNA sequence specific recognition can occur. **Figure 3.7** shows the hydrogen bond recognition sites of A-T and G-C base pairs that are accessible in the major and minor grooves.[106]

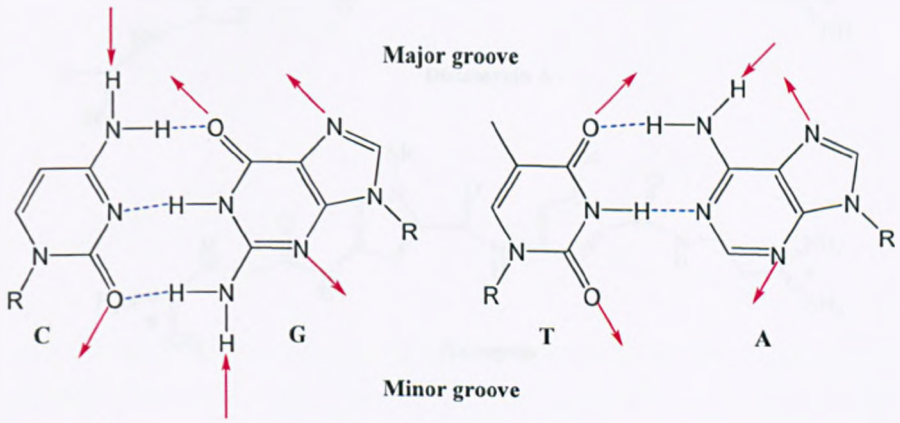

Figure 3.7: Hydrogen-bond recognition sites accessible from the grooves of DNA.

Many protein and oligonucleotide molecules exhibit binding specificity primarily through major groove interactions while small groove-binding molecules in general prefer the minor grooves. Typically, groove-binding molecules have several simple aromatic rings connected by bonds with torsional freedom so that they can twist and fit into the helical curve of the DNA groove. These molecules may fit better at A-T rather than G-C rich-sequences and they form van der Waals contact with the walls of the groove. Lower binding specifity to G-C rich sequence results from the fact that the presence of N2 amine group found in guanine, sterically inhibits penetration of molecules into this groove in G-C rich regions.[107, 108] Pullman and co-workers have also shown that the negative

electrostatic potential is greater in A-T minor groove,[109] thus the positively charged molecules have a higher affinity.

3.2.2.1 Netropsin and Distamycin A

Two closely related antibiotics, netropsin and distamycin A represent classical examples of minor groove binders (**Figure 3.8**).

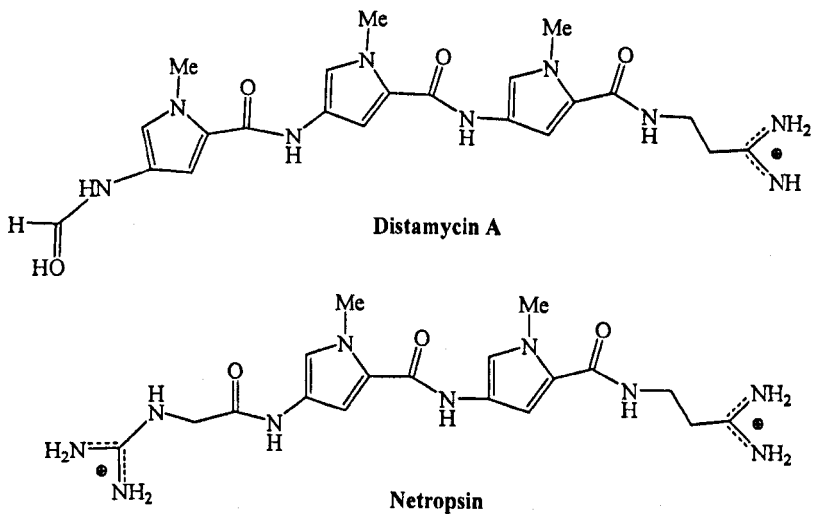

Figure 3.8: Structure of netropsin and distamycin A.

These molecules form non-covalent complexes with duplex DNA in the minor groove, making van der Waals contacts with both sides of the groove and forming hydrogen bonds between amides of the ligand and the acceptor groups of the bases.[110] Binding of netropsin appears to cause a slight widening of the minor groove at the entry point and a bending of the helix axis away from the site of binding. The positively charged end groups of the ligands are positioned to favorably interact with the electrostatic potential of the DNA. All of these factors contribute to the high affinity of these molecules for DNA. These oligopeptides also exhibit considerable preference for A-T rich sequence. NMR[111] and X-ray[107, 112, 113] studies indicate that tight binding of these drugs requires a site size of four (5'-AATT-3') and five (5'-AAATT-3') A·T base pairs within the

narrow minor groove for netropsin and distamycin A, respectively. The difference is associated with the additional pyrrole amide group in the distamycin A molecule and also the different terminal residues.[113]

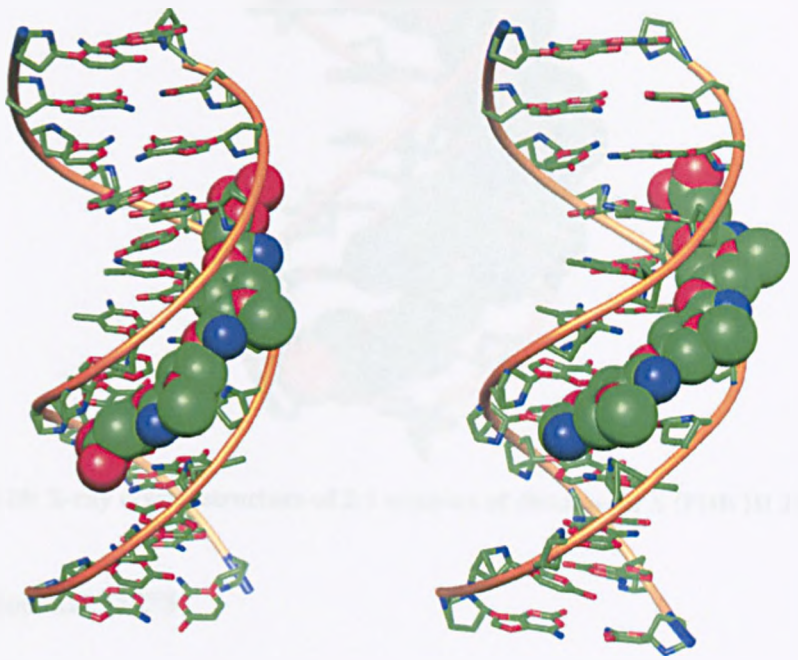

Figure 3.9: X-ray crystal structures of netropsin bound to d(CGCGAATTCGCG)$_2$, (PDB ID: 101D)[111] and distamycin A bound to d(CGCAAATTTGCG)$_2$, (PDB ID: 2DND).[113]

Most interestingly, NMR studies have further indicated that binding sites of at least five base pairs in length can accommodate two distamycin A molecules side-by-side in an antiparallel orientation[114, 115] (**Figure 3.10**). In this 2:1 complex, each ligand preserves all the molecular recognition elements of minor groove binders. The preference for the 2:1 over the 1:1 complex of distamycin A-DNA depends strongly on the DNA sequence. For example, when distamycin A is titrated into a sample containing a narrow groove poly(A) sequences, 1:1 binding mode is favoured and 2:1 binding only occurs after the saturation of 1:1 binding sites; while 2:1 binding motif is favoured with a wider or more flexible groove of an alternating 5'-ATATA-3'. In contrast to distamycin A, the dication netropsin binds only as a single molecule per binding site, suggesting that electrostatic repulsion between the charged ends of netropsin

inhibit the side-by-side arrangement of two netropsin molecules in the minor groove.

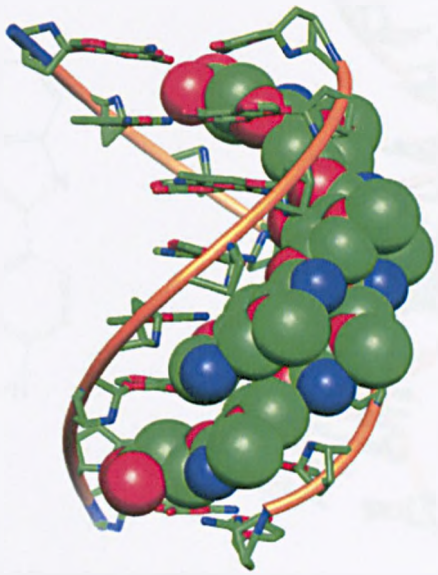

Figure 3.10: X-ray crystal structure of 2:1 complex of distamycin A (PDB ID 378D).[116]

3.2.2.2 Hoechst 33258

Hoechst 33258 (H33258), (**Figure 3.11**) like the other groove binders, binds with an affinity of ~ 5 x 10^8 M^{-1} to minor groove sites that have at least four A-T pairs.[117] It is similar in structure to netropsin and distamycin A, but shows some significant differences. In contrast to distamycin and netropsin, H33258 has a stronger affinity for AATT than for TATA and higher binding to AATT than to AAAA.[118] The binding of H33258 to DNA involves hydrogen-bonds from the benzimidazole-NH groups to O2 of thymine and N3 of adenine.

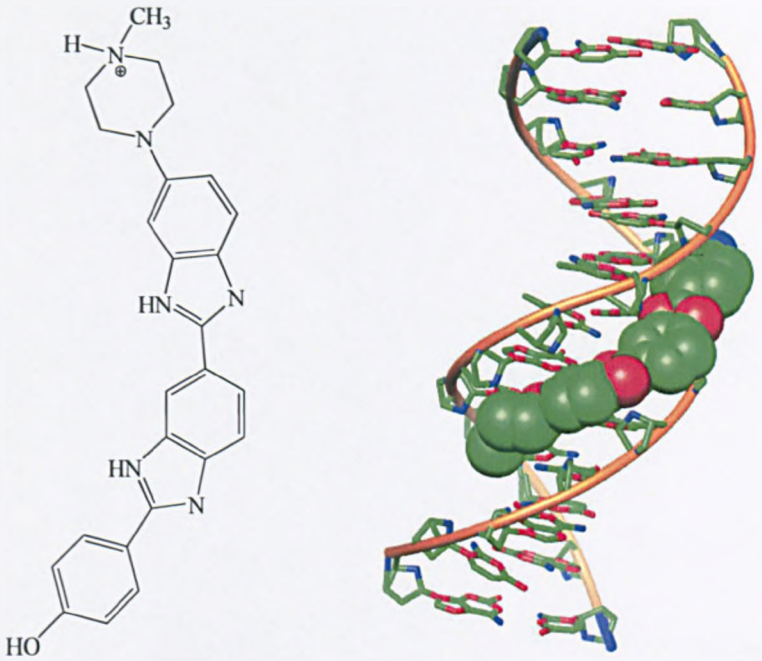

Figure 3.11: Structure of Hoechst 33258 (left) and X-ray crystal structure of H33258 binding to DNA (PDB ID 1DNH)[119] (right).

3.2.3 Intercalation

In the early 1960s, Lerman[120] presented a number of physical studies on the interaction of DNA with planar heteroaromatic moiety. In his work, he concluded that planar aromatic molecules can insert and stack between the DNA base pair by a process called intercalation. This process typically results in a substantial change in DNA structure, causes lengthening, unwinding and stiffening of the DNA helix as a result of rotation about torsional bonds in the DNA backbone in order to accommodate the intercalator.[120, 121, 122] The intercalator and adjacent base pairs are sandwiched tightly on the intercalating surface and the intercalator is stabilised electronically in the helix by a π-π stacking and dipole-dipole interactions. A number of physical methods are well established to determine intercalative binding;[65, 123, 124] for example hypochromism and red shift of the UV-Visible absorption spectrum of the ligand, quenching/enhancement of the steady-state emission for substrates that luminesce and also an increase in length of the base pair which can be monitored by hydrodynamic methods such as viscosity and sedimentation measurement. In

general, drugs such as proflavine[120] and ethidium bromide[125, 126, 127] are well known to be intercalators (**Figure 3.12**).

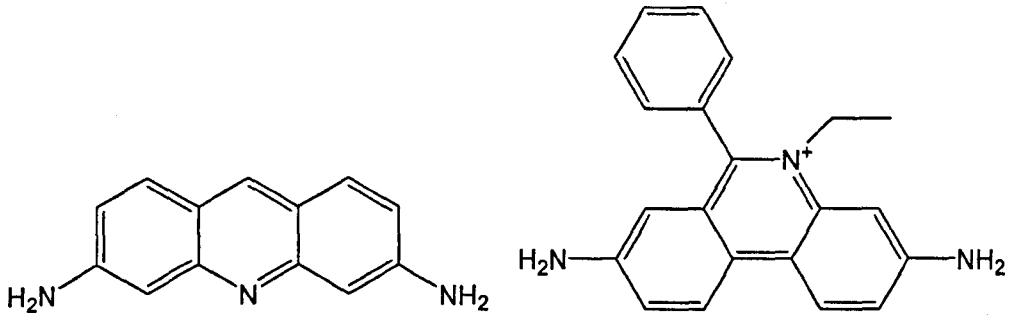

Proflavine Ethidium Bromide

Figure 3.12: Structures of proflavine and ethidium bromide.

3.2.3.1 Organic Intercalators

Daunomycin (**Figure 3.13**) is an anthracycline antibiotic which commonly used in the treatment of cancer, particularly for leukaemia. This compound is a typical example of an organic intercalator and is one of the best characterised. Work by Chaires *et al.* in 1983 explored the sequence specifity of daunomycin.[128] In the study, they found that daunomycin shows a preference for alternating purine-pyrimidine tracks, binding best to alternating A-T sequences. Further studies showed that daunomycin shows a moderate preference for G-C rich sequence DNA that also contains A-T base pairs.[129] X-ray crystal structure[130] of daunomycin bound to d(CGTACG) showed intercalation of the chromophore between the C-G base pair, while the daunomycin amino sugar lies in the minor groove.

Actinomycin D (**Figure 3.13**) is a very potent antitumor drug that has been used for treating certain types of cancers. This compound forms a tightly bound, noncovalent, reversible complex with duplex DNA, preferentially binding at 5'-GpC-3' sites. It was not until 1992 when Kamitori[131] determined a crystal structure of actinomycin D with a DNA oligomer duplex ($d(GAAGCTTC)_2$).

The crystal structure indicates that the mode of binding involves full penetration of the phenoxazone ring between the base pairs, while the two cyclic side chain moieties (denoted as R in **Figure 3.13**) lie in the minor groove and the complex is stabilised by base-peptide and chromophore hydrogen bonds.

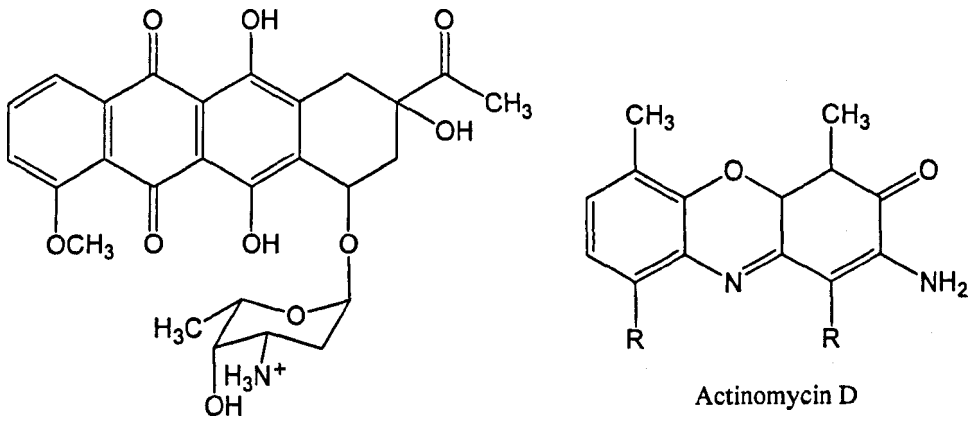

Daunomycin

Actinomycin D

Figure 3.13: Structure of daunomycin and actinomycin D.

Recently, Thomas *et al.* have reported another class of organic intercalators somewhat related to actinomycin D based on organic derivatives of dipyrido [3,2-*a*:2',3'-*c*] phenazine (dppz)[132, 133] (**Figure 3.14**). All compounds bind to DNA *via* intercalation with moderate affinities ($\geq 10^5$ M^{-1}); however **2** binds to DNA with a magnitude higher than that obtained for the rest of the series and are comparable to that of mononuclear [Ru^{II}(dppz)] metal complexes. It has been suggested that compound **1** intercalates to the DNA through the minor groove, like actinomycin D. This is due to the structural similarities between **1** and the intercalative unit of actinomycin D, and the consistency of selectivity of **1** towards poly(dG).poly(dC) with actinomycin D[134] which also binds preferentially to specific G-C rich sequence. Indeed, compound **2** displays more pronounced sequence selectivity for G-C regions over A-T steps.

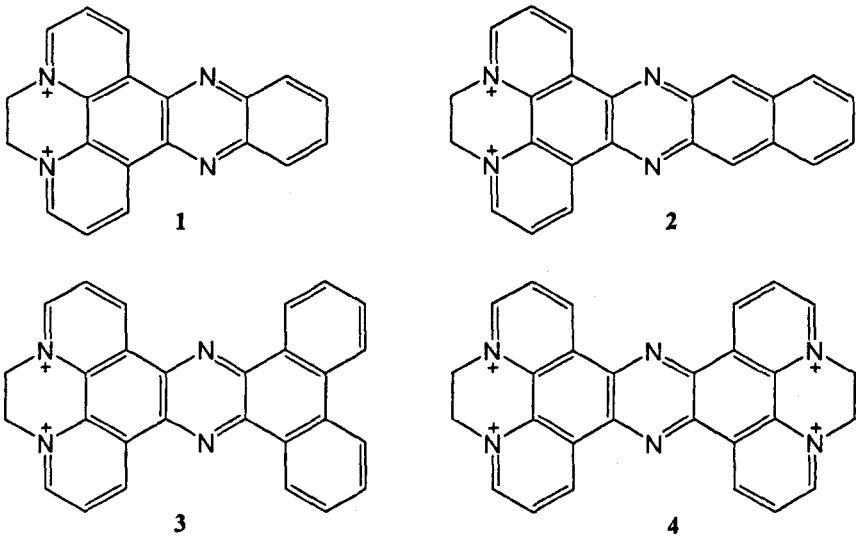

Figure 3.14: Thomas's organic intercalators.

3.2.3.2 Metallo-Intercalators

The study of transition metal complexes that reversibly bind to DNA has been a burgeoning area. Complexes that primarily bind to DNA through intercalation have become known as metallo-intercalators. This growth of interest has been due in large part to the useful properties of transition metal complexes, which possess rich photophysical and electrochemical properties and allow for extensive utility in a wide range of capacities, from fluorescent markers to DNA foot-printing agents and electrochemical probes.[65] It has also been shown that a plethora in choice of metal ions and ligands offers the possibility to tune their DNA binding and recognition properties.

3.2.3.2.1 Monometallic Complexes

It was not until the mid-1970s when Lippard and co-workers[135] first introduced a monocationic square planar Pt(II) complexes containing 2,2':6',2"-terpyridine (tpy) ligand, that complexes which could bind to duplex DNA through intercalation were known. Since then, a variety of new systems based on metal centres have been reported.

3.2.3.2.1.1 Tris(phenanthroline) ruthenium(II)

The earliest work on DNA binding of octahedral metal centers focused on tris(phenanthroline) complexes of ruthenium. There are extensive studies on this complex; however there have been a number of conflicting arguments on the exact mode of binding. Barton *et al.*[136, 137] initially proposed that there are two distinct modes of binding on the basis of fluorescence and unwinding result; it was suggested that $[Ru(phen)_3]^{2+}$ (**Figure 3.15**) interacted with duplex DNA *via* hydrophobic interactions in the minor groove, the other mode being a partial intercalation of a phenanthroline ligand into the DNA base stack. More importantly the study suggested the importance of chirality in DNA binding.[138] It was suggested that the Δ-enantiomer preferred intercalative binding, while the Λ-enantiomer favoured minor groove binding.

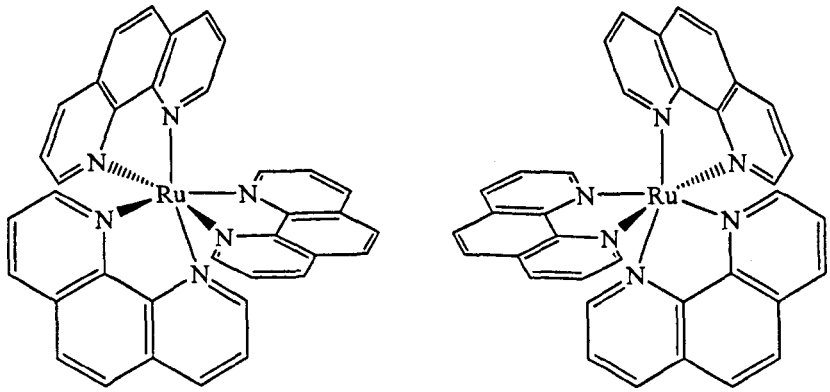

Figure 3.15: Structure of Λ-$[Ru(phen)_3]^{2+}$ (left) and Δ-$[Ru(phen)_3]^{2+}$ (right).

In subsequent work, Hiort *et al.*[139] concluded that neither isomer is bound through intercalation to DNA. Indeed, each enantiomer had only one mode of binding, but these differed between enantiomers. They proposed that the Λ-enantiomer favoured binding with one of the ligand points into the major groove while the Δ-enantiomer favours two. Later, the issue of intercalation was clarified when Chaires *et al.*[140] who revealed that there was relatively small change in viscosity upon $[Ru(phen)_3]^{2+}$ complexation with DNA, compared to

that for classical intercalator. Then in 1999, Rodger *et al.*[141] reported detailed spectroscopic and modelling studies on the binding mode of these enantiomers. In their report, they showed that there are three modes of binding, which depends on the degree of saturation of the DNA by the drug complex. In particular, at all mixing ratios, Λ-$[Ru(phen)_3]^{2+}$ binds in the major groove, with a single phen ligand approximately parallel to the base pairs plane. On the other hand, at low ratios Δ-$[Ru(phen)_3]^{2+}$ binds in the minor groove, with two of phen ligands inserted into the groove (**Figure 3.16**). While at higher mixing ratios, Δ-$[Ru(phen)_3]^{2+}$ binds *via* insertion of a single chelate into both major and minor grooves. Clearly then, neither enantiomer is an intercalator.

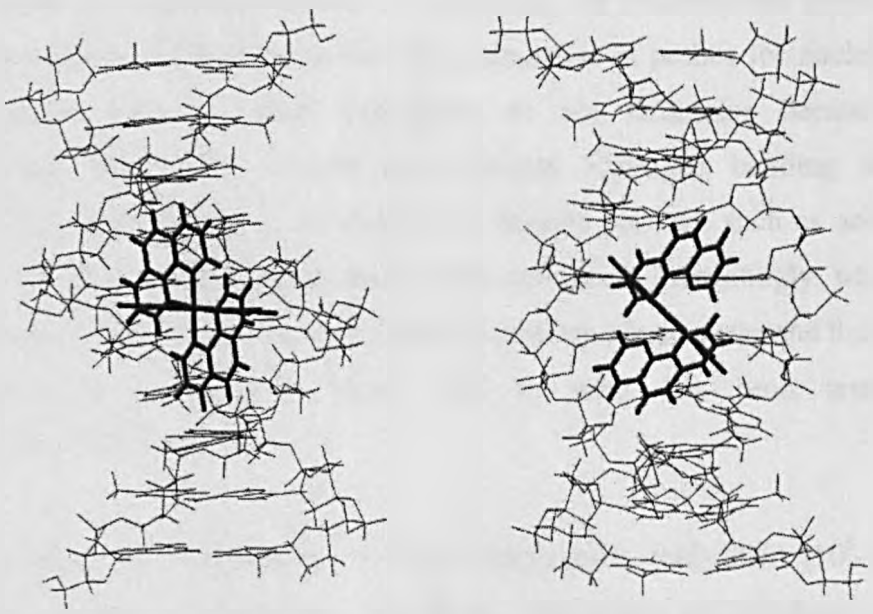

Figure 3.16: The "partially inserted" of Λ-$[Ru(phen)_3]^{2+}$ (left) and the minor groove facial complex of Δ-$[Ru(phen)_3]^{2+}$, at low mixing ratios (right).[141]

3.2.3.2.1.2 Ruthenium Dipyridophenazine Complexes

Barton *et al.*[83] were the first to report on the so called "molecular light switch" intercalator. They realised that to make a true intercalating binding agents, an increase in the surface of the putative intercalative ligand is of importance. Subsequently, the interaction of $[Ru(bpy)_2(dppz)]^{2+}$ and $[Ru(phen)_2(dppz)]^{2+}$ (**Figure 3.17**) with DNA have been extensively studied.[83, 84]

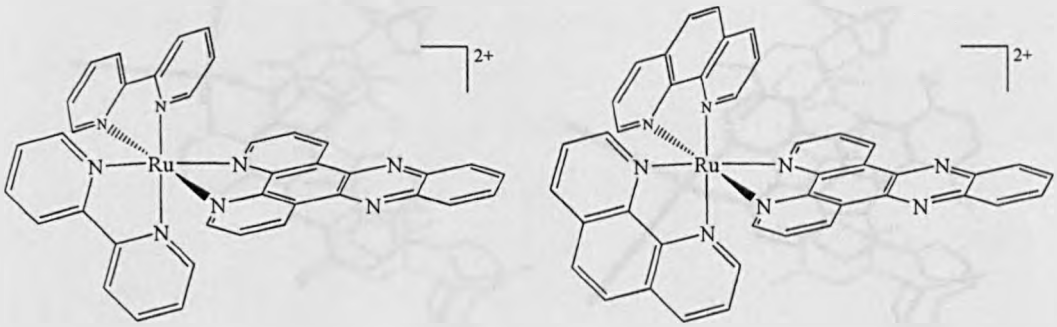

Figure 3.17: Structures of $[Ru(bpy)_2(dppz)]^{2+}$ (left) and $[Ru(phen)_2(dppz)]^{2+}$ (right).

The extension to a dppz unit not only results in better binding characteristics but also leads to complexes where the sensitivity of excited-state properties to microenvironment has promise for the construction of probes for nucleic acids. In aqueous solutions, these complexes do not luminesce because water deactivates the MLCT excited state through hydrogen bonding with the phenazine nitrogen atoms. In contrast, in organic solvents such as acetonitrile these complexes exhibit strong steady state emission. Interestingly, when these complexes bind to DNA, the dppz ligand is protected from water and thus intense luminescence is observed which lead to what has been termed the "light switch effect".

Despite the high affinity shown by these complexes towards DNA (10^6-10^7 M^{-1}), there has been some debate over the binding orientation of $[Ru(phen)_2(dppz)]^{2+}$. Photophysical studies show that both enantiomers of $[Ru(phen)_2(dppz)]^{2+}$ display biexponential decay of luminescence lifetime when bound to DNA. This observation suggested $[Ru(phen)_2(dppz)]^{2+}$ possesses two binding modes. Barton *et al.*[84] have proposed that both binding modes are intercalative in nature; the difference between the two being due to the alignment of intercalated complexes along the DNA helix. In one mode, the dppz ligand is parallel to the DNA dyad axis while in the other mode it is perpendicular (**Figure 3.18**).

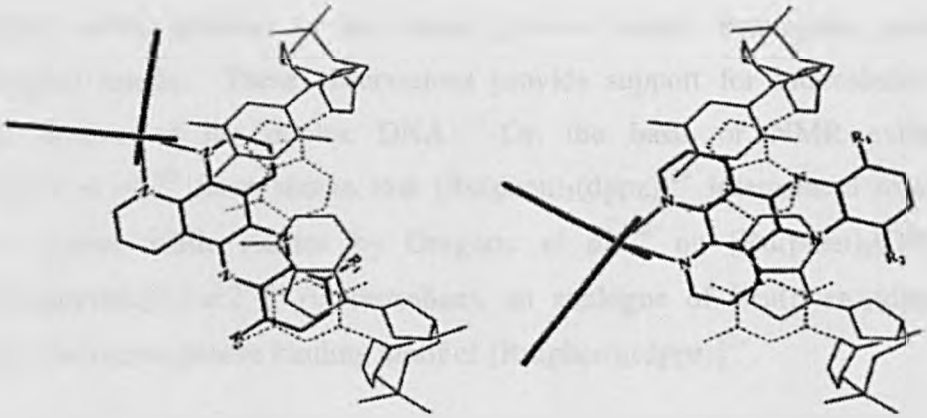

Figure 3.18: Side on (left) and perpendicular (right) modes of intercalation of [Ru^{II}(dppz)] complex into B-DNA.

Another interpretation has been proposed by Nordén *et al.*[142] based on linear dichroism results, which are consistent with only one binding geometry of $[Ru(phen)_2(dppz)]^{2+}$. They concluded that both enantiomers bind to DNA *via* intercalation of the dppz unit between the base pair. In contrast, Nordén also observed a biexponential decay of the DNA-bound complex, but reported this depended on the binding ratio. The former observation and the suggestion one binding mode for $[Ru(phen)_2(dppz)]^{2+}$ was also later presented by Tuite *et al.*[143] They employed T4-DNA to investigate the binding mode of this complex. T4-DNA is 100 % glycosylated (addition of a saccharide) at the cytosine 5-CH_2-OH position in the major groove, therefore providing a significant steric obstacle to any binding into this groove. From the studies, they reported that binding of both enantiomers to T4-DNA is not hindered in any way and indeed the binding stoichiometries are similar. These results strongly inferred that $[Ru(phen)_2(dppz)]^{2+}$ binds *via* minor groove, and it is thus difficult to envisage the intercalation of $[Ru(phen)_2(dppz)]^{2+}$ *via* two distinct orientations.

In 1998, Holmlin *et al.*[144] investigated the competition binding interaction of $[Ru(phen)_2(dppz)]^{2+}$ with a known major groove intercalator (Δ-α-[Rh[(*R*,*R*)-Me_2trien]phi]$^{3+}$) and a minor (distamycin) groove binding agents. It was found that $[Ru(phen)_2(dppz)]^{2+}$ was displaced upon titration of the rhodium

complex, while addition of the minor groove binder distamycin produces contrasting results. These observations provide support for intercalation *via* major groove of the duplex DNA. On the basis of NMR evidence, Dupureur *et al.*[145] have shown that $[Ru(phen)_2(dppz)]^{2+}$ intercalated from the major groove while studies by Greguric *et al.*[146] on $[Ru(phen)_2(DPQ)]^{2+}$ (DPQ=dipyrido[2,2-*d*:2',3'-*f*]quinoxaline), an analogue of $[Ru(phen)_2(dppz)]^{2+}$ support the minor groove binding motif of $[Ru(phen)_2(dppz)]^{2+}$.

Recently, Biver *et al.*[147] have investigated the binding mode of $[Ru(phen)_2(dppz)]^{2+}$ with DNA using stop-flow and spectrophotometric methods. In their studies, they discussed a second non-intercalative binding mode when $[Ru(phen)_2(dppz)]^{2+}$ bind to DNA. They believed that the phen moieties reside in the grooves allowing the dppz ligand to partially intercalate between the base pair. Thus, this results in partial unwinding of the helix and when sufficient unwinding has been achieved, the duplex is able to accommodate the $[Ru(phen)_2(dppz)]^{2+}$ according to an ordinary intercalation mode.

3.2.3.2.1.3 Rhenium Complexes

While most of metallo-intercalators reported to-date are based on ruthenium and dppz-based complexes, comparatively little attention has been focused on luminescent Re^I compound.[148] However, this family of complexes has shown promise as nucleic acid probes due to their attractive spectroscopic characteristics.[149] In 1995, both the Schanze and Yam groups reported intercalative Re^I complex of dppz, $[Re(dppz)(CO)_3(py)][O_3SCF_3]$ and dppn, $[Re(dppn)(CO)_3(py)][O_3SCF_3]$ (dppn = benzo[*i*]dipyrido[3,2-*a*:2',3'-*c*] phenazine, py = pyridine)[150, 151] (**Figure 3.19**)

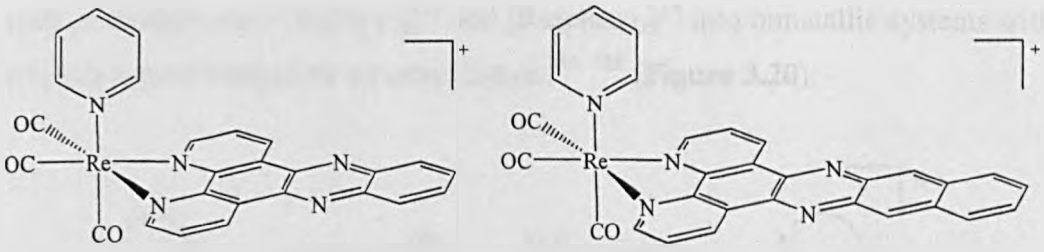

Figure 3.19: Rhenium(I) intercalators based upon dppz and dppn ligands.

All the complexes showed hypochromicity in the UV-Visible spectra, with a small bathochromic shift upon binding to CT-DNA. As well as the changes in the absorbance spectrum, the Re^{I} dppz complex also shows a DNA light switch effect, with a dramatic enhancement in the steady-state emission upon titration of DNA. In contrast, the luminescent enhancement for Re^{I} dppn complex is much lower, with a significant drop in intensity at low [DNA]/Re^{I} dppn ratios. However, both complexes result in similar binding affinities with CT-DNA, being 4.2 x 10^{4} M^{-1} and 6.4 x 10^{4} M^{-1},[152] respectively. Compared to that of $[Ru(bpy)_2(dppz)]^{2+}$, these values are two orders of magnitude lower. The lower binding constants can be attributed to the charge difference between these monocationic complexes of Re(I) and the dicationic complexes of other Ru(II) complexes such as $[Ru(bpy)_2(dppz)]^{2+}$. Yam and coworkers also explored the binding properties of these complexes with poly(dA).poly(dT) and poly(dG).poly(dC) DNA. They found that both the dppz and dppn complexes show preference for AT sites with enhancement in luminescence.

3.2.3.3 Bimetallic Complexes

Research on the use of complexes as nucleic acids probes have explored the use of extended aromatic ligands, such as dppn to enhance the binding affinities, especially through intercalation. However, some research groups have started to look into the possibility of improving DNA interaction by preparing covalently linked bifunctional compounds.[153] In 1996, Kelly and co-workers reported early examples of bimetallic complexes by tethering relatively weak binding systems

such as mononuclear $[Ru(bpy)_3]^{2+}$ and $[Ru(phen)_3]^{2+}$ into bimetallic systems with one bpy ligand bridged by a carbon linker.[154, 155] (**Figure 3.20**).

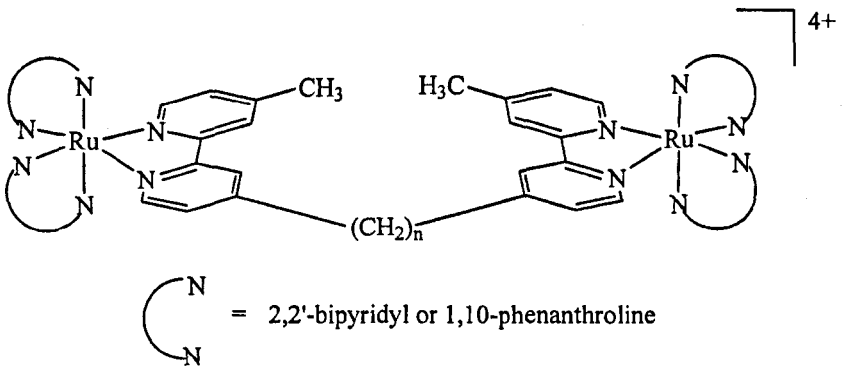

Figure 3.20: $[L_2Ru^{II}(Mebpy)\text{-}(CH_2)_n\text{-}(bpyMe)Ru^{II}L_2)$, with L = 2,2'-bpy or 1,10-phen.

Analysis of the DNA binding interactions of these complexes with salmon sperm DNA showed that they exhibit higher binding affinities, approximately two orders of magnitude higher than their monometallic analogues. Nordén *et al.*[156, 157] have also reported on another bimetallic complexes, in which ruthenium centres are linked by a semi-rigid dppz units (**Figure 3.21**).

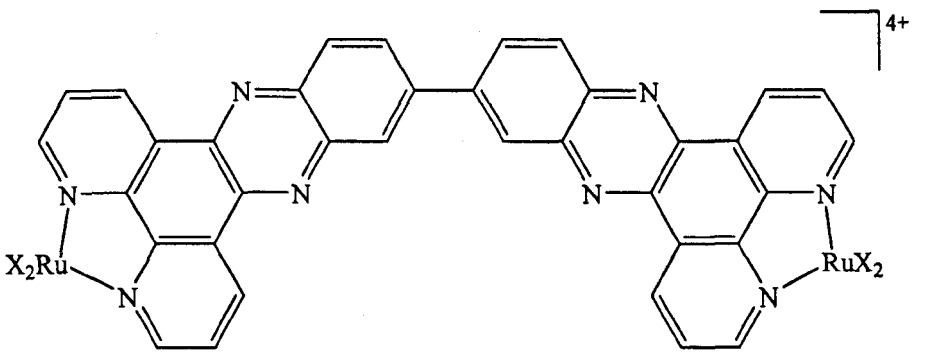

Figure 3.21: Structure of $[\mu\text{-}(11,11'\text{-bidppz})(X)_4Ru_2]^{4+}$; where X = 1,10-phen or 2,2'-bpy and 11,11'-bidppz = 11,11'-bi(dipyrido[3,2-a:2',3'-c]phenazinyl.

Initial linear dichroism (LD) measurement and luminescence spectroscopy studies revealed that both complexes bind to DNA with extremely high affinity ($K_b = 10^{12}$ M^{-1}); however neither ΔΔ- nor the ΛΛ-enantiomers seemed to

intercalate into DNA but bound in the grooves. Interestingly, striking different behaviour was observed for ΔΔ- and ΛΛ- enantiomers of the phen complex. Later work revealed that the initial groove bound geometry switched to the intercalative mode, by threading one of the $Ru(phen)_2$ units through the core of the DNA, leaving one metal centre in each groove. Later work by the same group resulted in a true bis-intercalating system, where $[Ru(phen)_2(dppz)]^{2+}$ units are conjoined by a more flexible aliphatic diamide linker[158] (**Figure 3.22**).

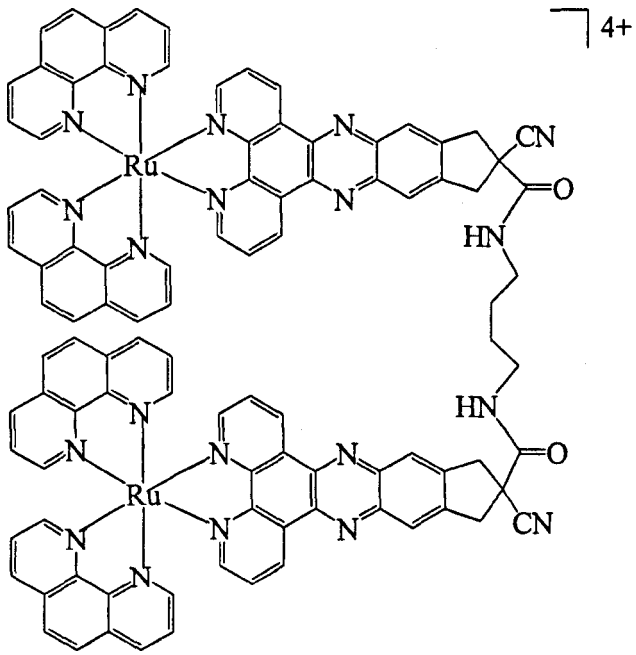

Figure 3.22: Structure of the threading $[\mu\text{-c4(cpdppz)}_2\text{-(phen)}_4Ru_2]^{4+}$ dimer.

This complex is known as a DNA staple due to the binding mode that this complex exhibits. The tethering infers that the complex can only interact with DNA *via* a threading process (**Figure 3.23**), with the intercalating ligands separating by two base pairs.

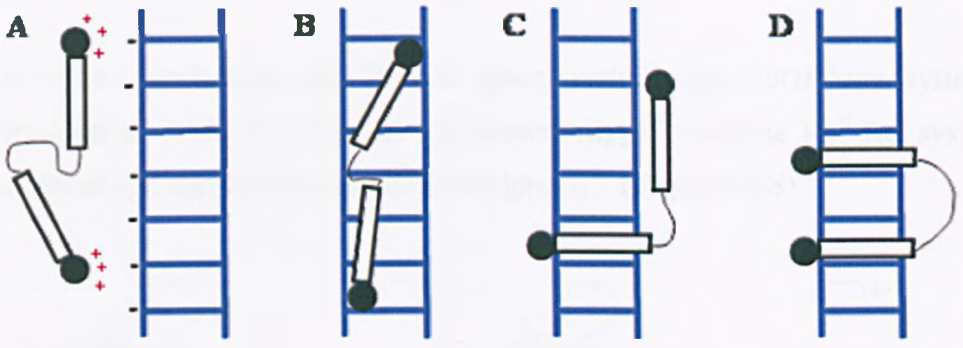

Figure 3.23: Schematic DNA interaction modes of Nordén's dimer: A) External binding, B) Groove binding, C) Mono-intercalation, D) Bis-intercalation.

Initial work in the Thomas group include the synthesis of an achiral bimetallic complex, $[\{(CO)_3Redppz\}_2dpp[3]]^{2+}$ (**Figure 3.24**).[159] While such a system was expected to exhibit straightforward intercalation insertion, and not threading, the DNA binding interaction is far more interesting. Initally, the DNA titration observed by UV-Visible appears to approach saturation; however further addition of DNA results in a much more shallow binding curve which does not reach saturation, even at higher [DNA]/[complex] ratios. Estimated binding constant from the initial titration data reveals a similar magnitude with the monometallic complexes, $[(CO)_3PyRedppz]^+$ and $[(CO)_3MeCNdppz]^+$. Perhaps more important than the interesting behaviour observed for the bimetallic rhenium complex, was the revelation that the propane tether is insufficiently long for both rhenium centres to intercalate into the same duplex.

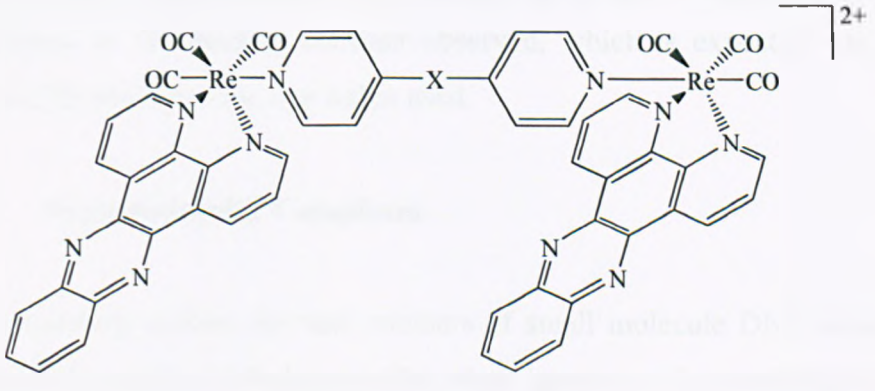

Figure 3.24: Structure of Thomas bimetallic complex, $[\{(CO)_3Redppz\}_2dpp[3]]^{2+}$ (dpp = 4,4'-dipyridyl-1,5-pentane).

More recent work from the Thomas group include tpm-Ru(II)dppz systems linked together with 4,4'-dipyridyl-1,5-pentane (dpp)[160] and the Ru^{II}-Re^{I} system $[(Ru(tpm)(dppz))(\mu\text{-dpp}[5])(fac\text{-}(CO)_3Re(dppz))]^{3+}$ (**Figure 3.25**).[161]

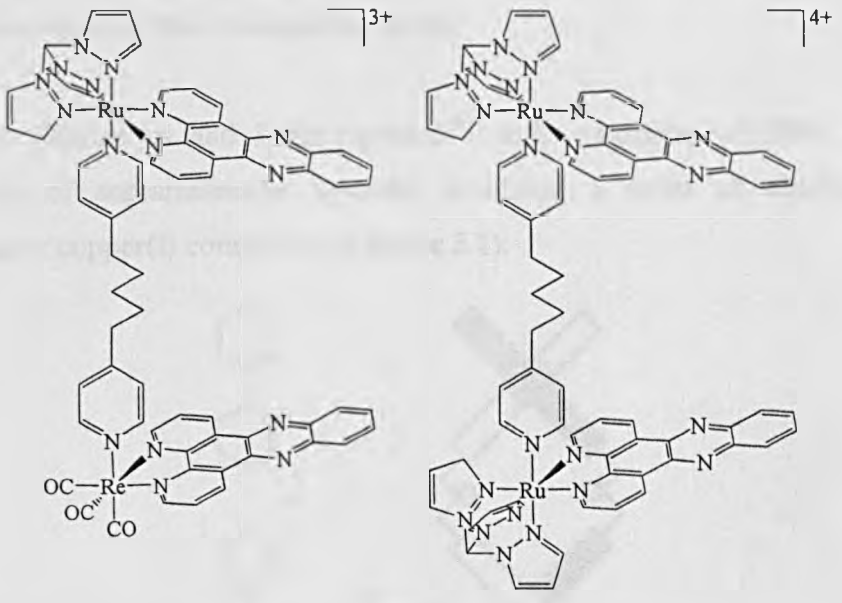

Figure 3.25: Structures of $[(Ru(tpm)(dppz))(\mu\text{-dpp}[5])(fac\text{-}(CO)_3Re(dppz))]^{3+}$ (left) and tpm-Ru(II)dppz bimetallic (right).

Interestingly, the mixed Ru-Re system demonstrated similar binding affinity to the dinuclear, tetracation Ru-Ru system, $K_b \approx 10^5\ M^{-1}$. The complex also displays two order of magnitude enhancement in binding affinity relative to the mononuclear Re^{I} starting material. In contrast, the Ru-Ru complex gave no great enhancement to the binding constant observed, which is expected due to the length and flexibility of the dpp linker used.

3.2.4 Supramolecular Complexes

In the preceding section, the vast numbers of small molecule DNA recognition agents which usually bind through the minor groove or by intercalative mode have briefly reviewed. In contrast, supramolecular architectures could possibly

interact with DNA in somewhat different binding modes, especially by binding in or around the major groove.[162] Despite the lack of supramolecular DNA binding agents reported to-date, metallo-supramolecular assemblies are particularly attractive for the design of non-covalent DNA probes; as such systems would allow the chemists to bridge the size gap between traditional small molecule and larger biomolecule DNA recognition motifs.

In 1995, Schoentjes and Lehn reported[163] early examples of DNA binding properties of supramolecular systems, involving a series of double-helical polynuclear copper(I) complexes (**Scheme 3.1**).

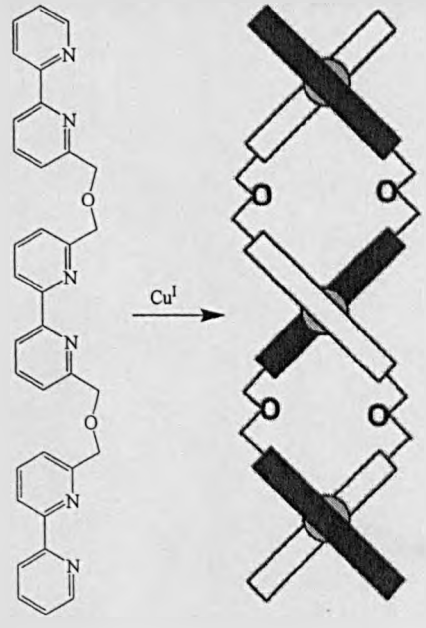

Scheme 3.1: Copper(I) double helicates by Schoentjes and Lehn. Ligands shown as black and white strands; shaded circle represent Cu^{I}.

It was postulated that these complexes bind to duplex DNA through the major groove of DNA although there are also possibilities of multiple binding sites at higher concentration. This could be reasoned by the size compatibility between the complexes (17 Å by 6 Å) and the major groove of B-DNA. DNA melting experiments demonstrated that the binding affinity increases as a function of the helicate length and that GC rich sequences are preferentially bound. This is due

to a better fit of these helicates into the major groove GC rich duplexes. These complexes were also found to be capable of inhibiting the cleavage of DNA.

In 2001, Hannon and co-workers[162] reported preliminary DNA binding studies on a racemic mixture a cylindrical tetracationic dimetallo triple-helicate, $[Fe_2L_3]^{4+}$ (**Scheme 3.2**). Modeling studies suggested that this cylinder was too large to fit into the minor groove of B-DNA, but is the correct size and shape to fit into the major groove. The circular dichroism (CD) and linear dichroism (LD) studies reveal that the cylinder does bind to DNA, with a high affinity ($K_b \approx 10^7$ M^{-1}). The most striking effect revealed by atomic force microscopy (AFM) was that, even at moderate cylinder loading, DNA undergoes intramolecular coiling.

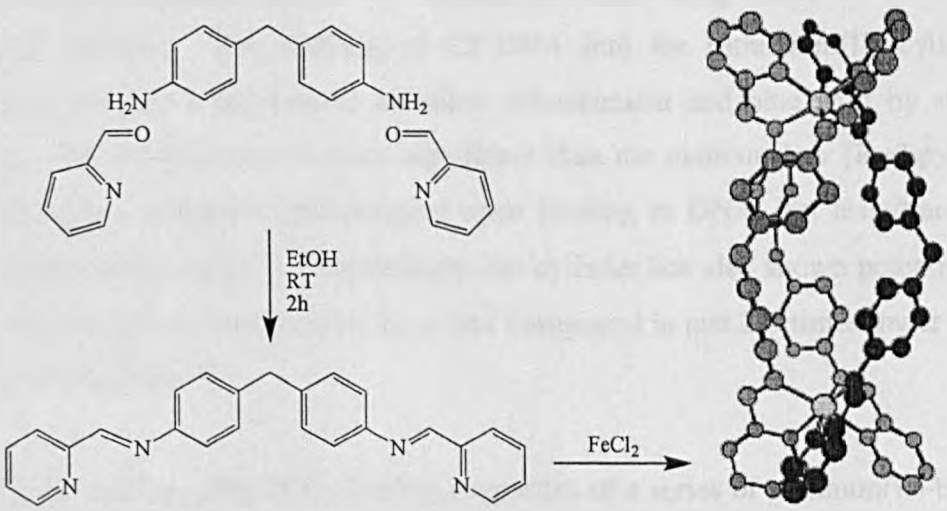

Scheme 3.2: The molecular structure of the ligand and the tetracationic triple helical supramolecular cylinder $[Fe_2(C_{25}H_{20}N_4)_3]Cl_4$.

Hannon *et al.*[164] further investigated the enantioselectivity of binding for this complex. It was concluded that the resolved enantiomers of the iron(II) cyclinder display different binding modes. While the M-enantiomer preferentially lies in the major groove, the P-enantiomer lies along the surface of the minor groove, perhaps spanning the two phosphate backbones.

In 2007, once again Hannon *et al.*[165] reported the luminescent ruthenium(II) triple-stranded helicate of ligand L (**Figure 3.26**).

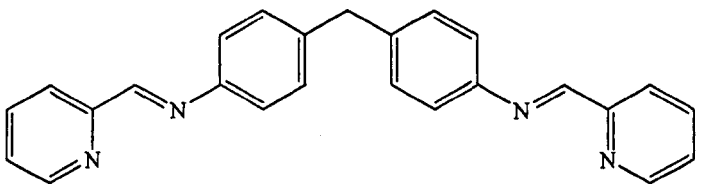

Figure 3.26: Ligand L.

The presence of ruthenium metal centre facilitates the potential use of these systems as luminescent DNA probes and enhances stability due to the inert nature of ruthenium(II). From CD and LD studies, it was concluded that the ruthenium(II) cylinder has a very similar bending/coiling effect on DNA, as iron(II) cylinder. The addition of CT-DNA into the ruthenium(II) cylinder solution induced a progressive emission enhancement and blue shift by about 8 nm. The enhancement is more significant than the mononuclear $[Ru(bpy)_3]^{2+}$ which shows negligible enhancement upon binding to DNA, but less dramatic than $[Ru(phen)_2(dppz)]^{2+}$. Interestingly, the cylinder has also shown potential as anti-cancer agents; the cytotoxicity of this compound is just 2-5 times lower than those of cisplatin.[165]

Later, the non-covalent DNA binding properties of a series of platinum(II)-based metallacalix[4]arenes with formula $[\{Pt(en)(5\text{-}X\text{-}Hpymo)\}_4]^{4+}$ (en = ethylenediamine; X = H, Cl, Br or I; Hpymo = hydroxypyrimidine) were also reported.[166] Fluorescence competitive binding experiments were carried out for this series of metallacalix[4]arenes with ethidium bromide (EB). It was found that, the first two complexes in the series with (X = H and Cl), respectively were not able to displace EB, thus indicating that the complexes bind with somewhat weaker affinity to CT-DNA. However, the bromide and iodide analogues interact strongly with CT-DNA, and thus displace the EB. The difference in binding strength was explained by the different conformation that these complexes possess. AFM studies were also carried out and reveal that at low complex

loadings, these complexes only cause small amounts of kinking/coiling. In contrast, these complexes induce the formation of flexible CT-DNA filaments at higher loading.

Recently, Sleiman *et al.*[167] have reported another class of supramolecular assemblies, platinum molecular square which display high binding affinity to quadruplex DNA, and indeed efficient telomerase inhibition (**Figure 3.27**). Molecular modeling suggested that this square is complementary in size with the G-quadruplex.

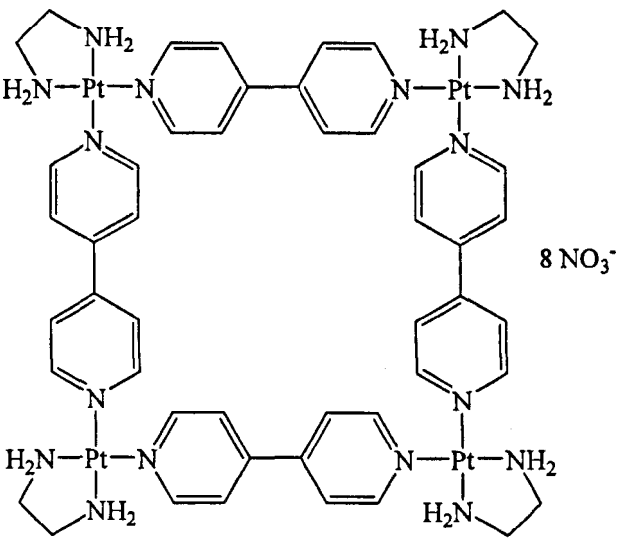

Figure 3.27: Structure of the platinum molecular square.

The Thomas group has also reported[168] a self-assembled kinetically locked, tetranuclear metallomacrocycle which interacts with duplex DNA (**Figure 1.18** - Chapter 1). Binding to CT-DNA results in hypochromicity of the absorption spectra and quenching of the emission intensity, which contrast with negligible change in the emission of the mononuclear building block. Estimates for binding constant obtained from the titration experiments reveal in high affinity, K_b = 10^6 M^{-1}, which is several orders of magnitude higher than its mononuclear building blocks. Interestingly, the viscosity experiment carried out reveal that initially, the macrocycle induced very large decreases in the relative

viscosity, suggesting some kind of bending/kinking in the duplex conformation. In contrast, these changes reverse at high [ligand]/[DNA] ratios. Given all these observations, it can be concluded that the complex bind in a novel external binding mode, but clearly more work is needed to fully delineate the nature of binding.

3.3 Analytical Techniques Used

Several different techniques were used to study the interactions of ligands with DNA. In the following section, a brief introduction of each of these techniques is described.

3.3.1 Viscosity

Viscosity describes a fluid's internal resistance to flow; an increase in the viscosity implies more resistance to flow. Hence, viscosity has become one of the essential methods to monitor the interaction of ligand with DNA. Relative viscosity is defined as the relation between the viscosity of the solution and the viscosity of the pure solvent. This can be calculated from the formula given below:

$$\eta = \left(\frac{t - t_0}{t_0} \right) \qquad (3.1)$$

where t is the observed flow time of the DNA and t_0 is the flow time of the buffer alone. Viscosity data is usually presented as a graph of $(\eta/\eta_0)^{1/3}$ *vs.* 1/R where R = [DNA]/[ligand].

There are several effects on DNA viscosity that can describe the binding modes of a DNA-ligand. Typically, intercalators such as ethidium bromide and $[Ru(phen)_2(dppz)]^{2+}$ result in an increase in the relative viscosity of the

DNA.[123, 169] However, a partial and/or non-classical intercalation process may results in bending/kinking of the DNA helix, with usually less dramatic (positive or negative) or negligible changes in the relative DNA viscosity.[139] On the other hand, a groove binder which binds in the DNA grooves does not lengthen the DNA helix and thus should not increase viscosity.[139]

3.3.2 Continuous Variation Analysis (Job Plots)

The method of continuous variation designed by Job *et al.*[170] uses a range of ligand-DNA ratios. This method accurately determines the number of drug(s) that bind to DNA or the number of base pairs required for drug binding (i.e. stoichiometry). The concentration of both reactants is varied, while the sum of their concentrations remains constant. Samples were prepared to give varying mole ratios from 0:1 to 1:0. The fluorescence intensities of these samples were recorded at 25°C using a HORIBA Jobin Yvon FluoroMax-3 spectrometer. The change in fluorescence intensity is plotted against mole fraction of ligand and inflection points yield the stoichiometry of the interaction.[171]

3.3.3 UV-Visible and Luminescence Titrations

A complex will be subjected to change in its microenvironment when interacting with DNA; from complete solvation in aqueous solution to a hydrophobic environment situated within the base pairs stack of the DNA grooves. One of the most common approaches to monitor the changes in microenvironment is by following the perturbations that occur in the UV-Visible spectrum of the complex upon binding to DNA. Typically, the hypochromic (decrease in absorption) and bathochromic (shift to longer wavelength) effects are seen during the binding process which is due to the perturbation of the metal centred MLCT band and the ligand centred $\pi \rightarrow \pi^*$ band of the UV-Visible spectrum of the complexes.[172] These effects are rationalised by stabilisation or destabilisation of the HOMO/LUMO orbitals involved in the binding process which triggered the alteration of the transition energy.

Alternatively, luminescence emission from molecules can also quantify the interaction of DNA-ligand. The excited state luminescence emission spectra (both intensity and wavelength) are also sensitive to the microenvironment of the molecule. It is well known that polar water molecules can be efficient quenchers of excited state, particularly when they hydrogen bond to nitrogen donor sites of the complexes. Hence, binding to the hydrophobic interior of the grooves and the base stack serve as protection of the nitrogen atoms from bulk water molecules which results in enhancement of the emission intensity.[83]

3.3.3.1 Binding Curves and Models

When DNA is titrated into a solution of ligand with a known concentration, the change in absorption/emission intensity in the UV-Visible or luminescence spectrum is proportional to the fraction of drug bound to the DNA. The fraction of ligand bound (χ) can be estimated from equation: $\chi = \frac{(A_u - A_{obs})}{(A_u - A_b)}$ where A_u is the absorbance of the free unbound ligand, A_b is absorbance of the fully bound ligand at saturation binding and A_{obs} is the observed absorbance at a given point. Similarly, for luminescence titration where the emission intensity of the ligands increase upon binding to DNA, the fraction bound is given by: $\chi = \frac{(I_{obs} - I_u)}{(I_b - I_u)}$ where I_{obs}, I_u and I_b are the emission intensities of the observed, free and fully bound ligand respectively.

In 1949, George Scatchard[173] constructed a linear binding isotherm from the hyperbolic binding data that fits with a least-squares regression analysis. Knowing the initial concentration of ligand, C_i and the fraction of bound ligand at any given point, the concentration of bound ligand (C_b) can be calculated as $C_b = \chi C_i$. By simply rearrange equation $C_i = C_b + C_f$, the concentration of free ligand (C_f) can be calculated as $C_f = C_i - C_b$.

Thus, the binding ratio r, where r is the ratio of bound complex to total concentration of DNA in base pairs can be determined as: $r = \frac{C_b}{[DNA]}$. Binding data can be fitted to a simple binding model, first proposed by Scatchard,[173] plotting the ratio of binding (r) against the ratio of binding to free ligand (r/C_f) using the equation: $\frac{r}{C_f} = K_i(n-r)$, where K_i is the intrinsic equilibrium constant and n the number of DNA binding sites occupied by the bound ligand. This model works well for small ligands bound to non-interacting isolated binding sites on proteins. However, for more complicated systems, such as when using calf thymus DNA where potentially thousands of overlapping sites are available for a ligand molecule to bind, the binding isotherm deviates from linearity. Clearly, another model is needed for this kind of system. It was not until 1974 when McGhee and von Hippel[174] proposed a non-linear model of Scatchard plots which accurately determining the binding constant and site size. However, this model works with a few assumptions. First, the model assumes that the binding sites on the lattice are isotropic which give equal probability of the ligand molecule to choose any given site. It also assumed that there is no cooperativity between the lattice and the ligand. This indicates that a ligand has no preference for choosing free binding sites over one next to an already bound site. This non-cooperative form can be demonstrated as $\frac{r}{C_f} = K.(1-nr)\left(\frac{1-nr}{1-(n-1)r}\right)^{n-1}$ where K is the intrinsic binding constant and n is the binding site size in base pairs.

3.3.4 Isothermal Titration Calorimetry (ITC)

Isothermal titration calorimetry (ITC)[175] is a titration technique used to determine the thermodynamic parameters of biochemical interactions.[176, 177] ITC is the only quantitative technique that can directly measure the binding constant, enthalpy changes and binding stoichiometry of the interaction between two or more

components without the partitioning of the components and subsequent spectroscopic determination of bound and free ligand concentration.[178]

3.3.4.1 ITC Experiment

The instrument is composed of two identical cells contained inside an isothermal jacket. Both cells are constantly held at a chosen experimental temperature throughout the duration of the experiment. One cell, the reference cell is filled with water (for aqueous experiment), while the other cell is filled with host for the interaction (DNA) and the syringe is filled with the guest (ligand). A schematic of a modern micro-calorimeter is shown in **Figure 3.28.**

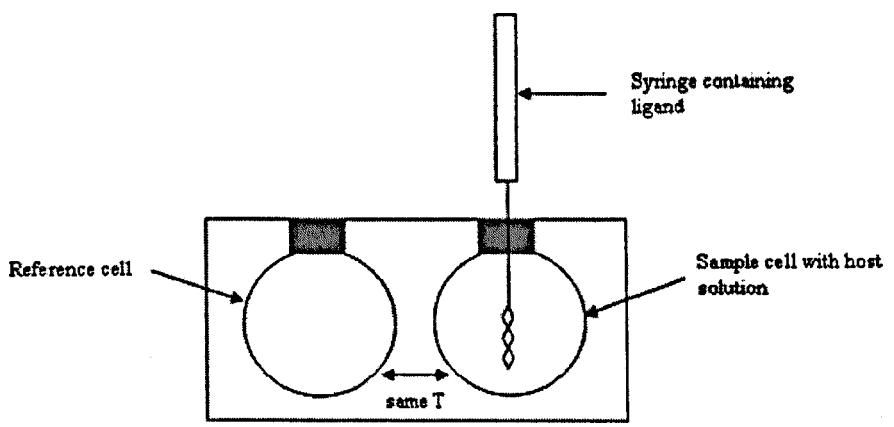

Figure 3.28: Schematic of a modern micro-calorimeter.

The cells are left to equilibrate at a desired experimental temperature before the syringe injects a certain volume of guest solution into the host solution at regular intervals. The host-guest interaction causes heat to be released or absorbed; producing a difference in temperature between the cells, and the heat energy which required to keep the cells in thermal equilibrium is measured. The raw power output which required for this thermal equilibrium between both cells is plotted versus time. The heat output is calculated by intergrating the peaks with respect to time and is then plotted against the molar ratio of the interacting compounds.

3.3.4.2 ITC Experiment Analysis

For a general bimolecular reaction, the association constant for the reaction is (where A is sample and B is the injectant):[175]

$$A + B \leftrightarrow AB \qquad K_a = \frac{[AB]}{[A][B]} \qquad (3.2)$$

$$[A]_{tot} = [A] + [AB] \qquad (3.3)$$

$$[B]_{tot} = [B] + [AB] \qquad (3.4)$$

Substituting equation (3.3) and (3.4) into equation (3.2) will give:

$$K = \frac{[AB]}{[A]_{tot}[B]_{tot} - [AB]([B]_{tot} + [A]_{tot}) + [AB]^2} \qquad (3.5)$$

$$[AB] = \frac{[B]_{tot} + [A]_{tot} + \frac{1}{K} - \sqrt{\left([B]_{tot} + [A]_{tot} + \frac{1}{K}\right)^2 - 4[A]_{tot}[B]_{tot}}}{2} \qquad (3.6)$$

Differentiation and rearrangement of (3.6) leads to:

$$\frac{d[AB]}{d[B]_{tot}} = \frac{1}{2} + \frac{[A]_{tot} - \left(\frac{[B]_{tot} + [A]_{tot} + \frac{1}{K}}{2}\right)}{\sqrt{([B]_{tot} + [A]_{tot} + \frac{1}{K})^2 - 4[B]_{tot}[A]_{tot}}} \qquad (3.7)$$

Since for each injection the heat absorbed or released is proportional to the change in [AB]:

$$dq = V \cdot \Delta H^0 \cdot d[AB] \qquad (3.8)$$

where V is the volume in sample cell and ΔH^0 is the enthalpy of binding.

Therefore substituting into equation (3.7):

$$\frac{1}{V_0}(dq/d[B]_{tot}) = \Delta H^0{}_{bind} \cdot \left\{ \frac{1}{2} + \frac{[A]_{tot} - \left(\frac{[B]_{tot} + [A]_{tot} + \frac{1}{K}}{2} \right)}{\sqrt{([B]_{tot} + [A]_{tot} + \frac{1}{K})^2 - 4[B]_{tot}[A]_{tot}}} \right\} \qquad (3.9)$$

Binding curves can be generated from equation (3.9),[175] and therefore the binding constant and enthalpies for the interaction can be calculated.

The free energy change for a reaction can be calculated from the equilibrium binding constant:

$$\Delta G^0 = -RT\ln K \qquad (3.10)$$

where ΔG^0 is the Gibbs free energy, T the temperature in Kelvin and R is the gas constant (1.98×10^3 kcal mol^{-1} K^{-1}). Knowing ΔG^0 and ΔH^0 we can then calculate the entropy of the interaction, ΔS^0:

$$\Delta G^0 = \Delta H^0 - T\Delta S^0 \qquad (3.11)$$

3.4 DNA Binding Results of Ruthenium(II) Complexes

As a reminder, complexes discussed in this study are shown in **Figure 3.29**.

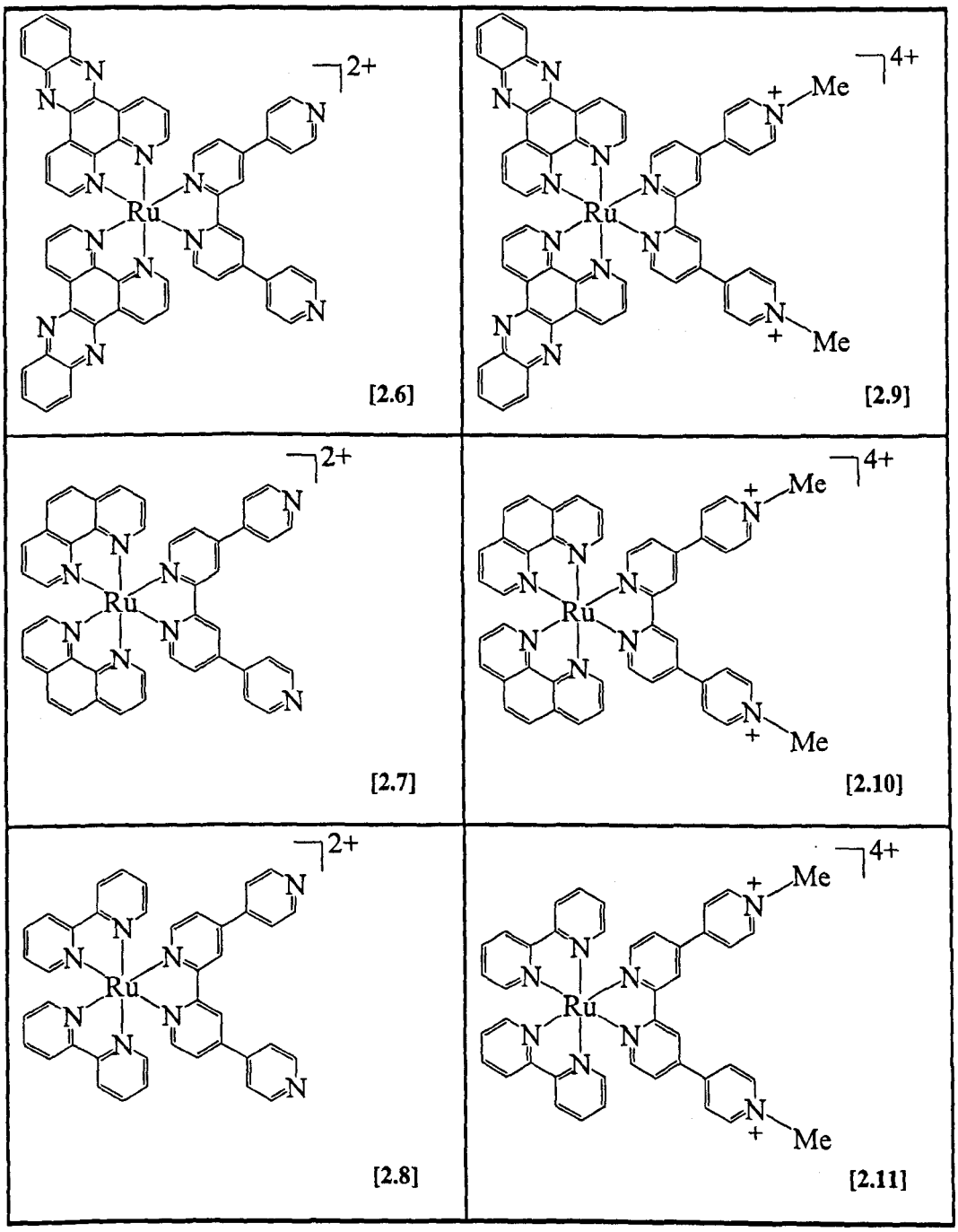

Figure 3.29: Complexes discussed in this study.

3.4.1 Viscosity

A classical intercalation model results in lengthening in the DNA helix, as base pairs are separated to accommodate the binding ligand, leading to the increase of DNA viscosity. However, a partial and/or nonclassical intercalation of complex, such as $[Ru(phen)_3]^{2+}$, may bend DNA helix, reduce its effective length and, concomitantly, its viscosity.[122, 140] In addition, some complexes such as $[Ru(bpy)_3]^{2+}$, which interacts with DNA by an electrostatic binding mode, have no influence on DNA viscosity.[179] The effects of ruthenium(II) polypyridyl complexes on the viscosity of CT-DNA are showed in **Figure 3.30**.

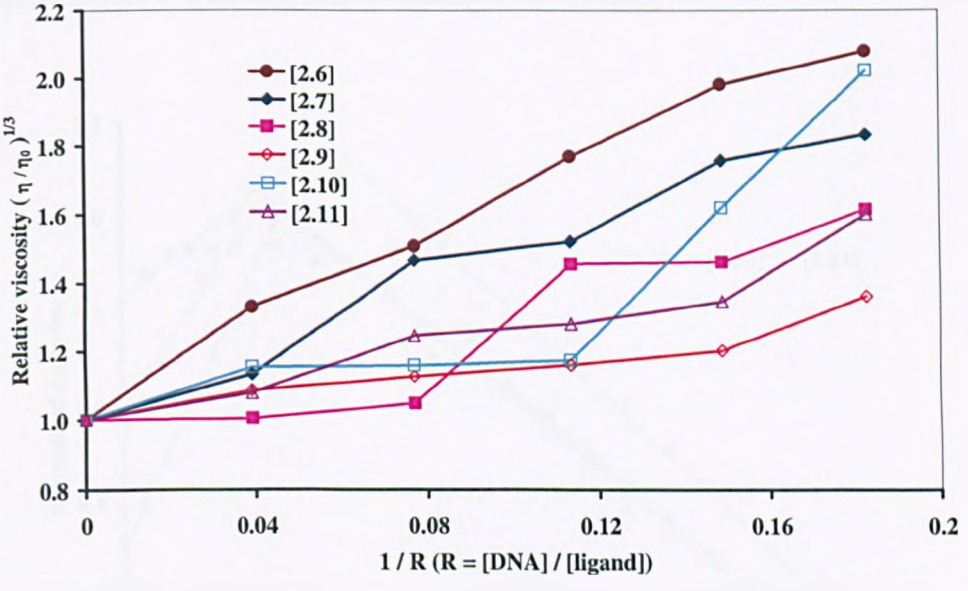

Figure 3.30: Relative viscosity of CT-DNA upon addition of [2.6], [2.7], [2.8], [2.9], [2.10] and [2.11] (27 °C, 5 mM Tris buffer, 25 mM NaCl, pH 7.0; viscosity of [2.6] was performed in 5 % methanolic buffer due to limited solubility).

On increasing the amounts of **[2.6]**, **[2.7]**, **[2.8]**, **[2.9]**, **[2.10]** and **[2.11]**, the relative viscosity of DNA increases, indicating that all these complexes interact with CT-DNA *via* intercalation. A similar complex to **[2.6]**, $[Ru(L)(dppz)_2](PF_6)_4$ (L = 5,5'-di(1-(trimethylammonio)methyl)-2,2'-dipyridyl) was also reported by Mao *et al.*,[180] which indeed showing an intercalative mode

of binding to CT-DNA. The difference in viscosity changes probably being caused by the different ancillary ligands incorporated in the series. Compound **[2.6]** produces large increases in the relative viscosity when bound to CT-DNA. The steric demand of the dppz complex causes the greatest DNA lengthening.

3.4.2 Continuous Variation Analysis (Job Plots)

The continuous variation analysis (Job Plots) method can be used to estimate the binding stoichiometries between the interactions of compound with DNA. This was done by following the changes in emission intensities of the mixtures upon excitation at the wavelength characteristic of the MLCT band of the compound. **Figure 3.31** shows the Job plots for the interaction of **[2.6]**, **[2.10]** and **[2.11]** complexes with CT-DNA (data is normalised for clarity).

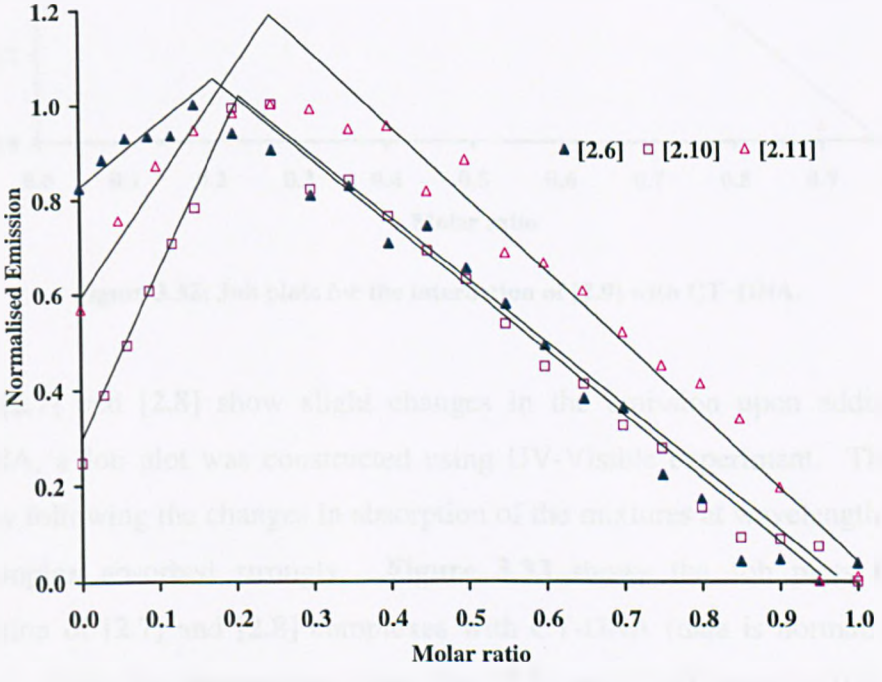

Figure 3.31: Job plots for the interaction of [2.6], [2.10] and [2.11] with CT-DNA.

Figure 3.31 shows the intersection point for **[2.6]** was at 0.18 which is equivalent to stoichiometry of 4.6 mol of base pair per mol of complex. While the inflection point for **[2.10]** was 0.22 and for **[2.11]** was 0.25, being equivalent to a

stoichiometry of 3.5 and 3 mol of base pair per mol of complex respectively (data are summarised in **Table 3.2**). However, complex **[2.9]** consistently gave more than two binding stoichiometries (**Figure 3.32**). This result is consistent with the binding isotherms produced from the Isothermal Titration Calorimetry experiment of this complex which showed three modes of binding - *vide infra* in Section 3.3.5.

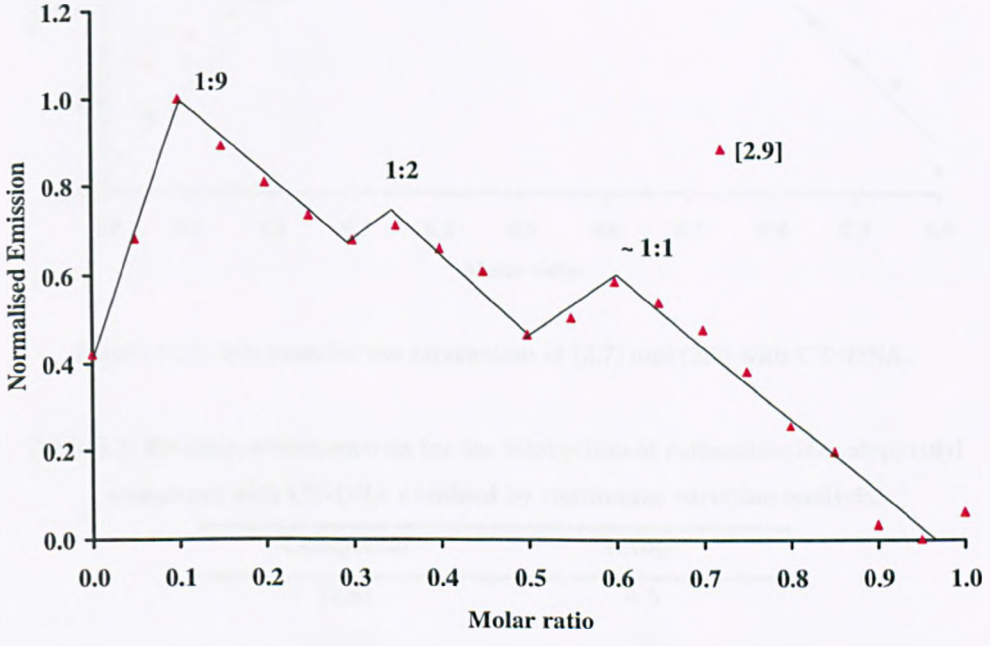

Figure 3.32: Job plots for the interaction of [2.9] with CT-DNA.

Since **[2.7]** and **[2.8]** show slight changes in the emission upon addition of CT-DNA, a Job plot was constructed using UV-Visible experiment. This was done by following the changes in absorption of the mixtures at wavelength where the complex absorbed strongly. **Figure 3.33** shows the Job plots for the interaction of **[2.7]** and **[2.8]** complexes with CT-DNA (data is normalised for clarity). Both the intersection point for **[2.7]** and **[2.8]** were at 0.5, being equivalent to a stoichiometry of 1 mol of base pair per mol of complex.

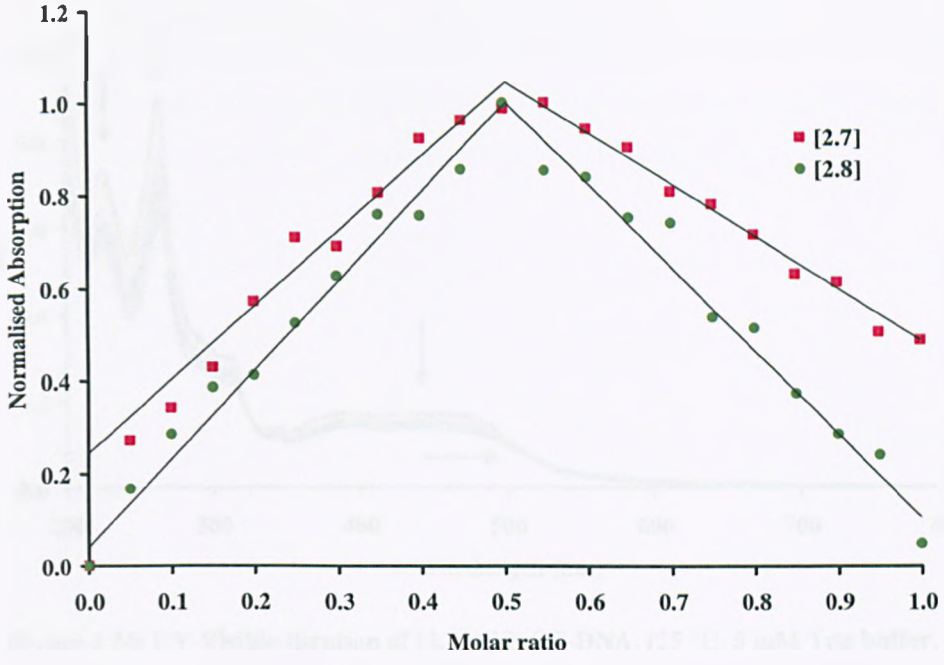

Figure 3.33: Job plots for the interaction of [2.7] and [2.8] with CT-DNA.

Table 3.2: Binding stoichiometries for the interaction of ruthenium(II) polypyridyl complexes with CT-DNA obtained by continuous variation analysis.

Compound	N (bp)
[2.6]	4.6
[2.7]	3.5
[2.8]	3.0
[2.9]	1.0, 2.0, 9.0
[2.10]	1.0
[2.11]	1.0

3.4.3 UV-Visible Titrations

The interaction of the ruthenium(II) complexes with CT-DNA were studied using UV-Visible spectroscopy. Upon increasing concentrations of DNA, all of the absorption bands of the complexes displayed clear hypochromicities although no large red shift was observed. As an example, the spectral changes of **[2.7]** upon addition of CT-DNA are shown in **Figure 3.34**.

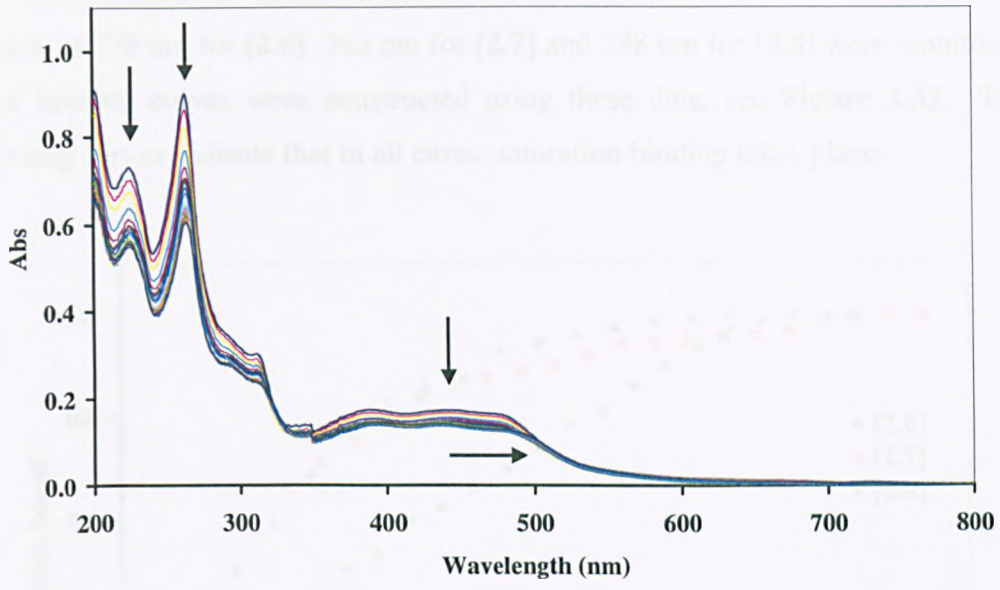

Figure 3.34: UV-Visible titration of [2.7] with CT-DNA. (25 °C, 5 mM Tris buffer, 25 mM NaCl, pH 7.0).

The addition of CT-DNA resulted in hypochromism for the absorptions at 225 nm, 263 nm and 474 nm for complex **[2.7]** and when saturation is close, the band at 474 nm also showed a small bathochromic shift. Hypochromicity and bathochromic effects are typically observed when aromatic chromophores stack between the DNA base pairs, and are indicative of the interaction between the π-orbitals of the ligand and the DNA base pairs.[181, 182] Nair *et al.*[183] have also postulated that the extent of hypochromism is relative to intercalative binding strength.

As the concentration of CT-DNA is increased, hypochromism at 278 nm and 468 nm is observed for complex **[2.6]**. The lower energy band also displays a bathochromic shift on approaching binding saturation. Addition of CT-DNA to **[2.8]** leads to similar changes to **[2.6]** and **[2.7]**, with the bands at 246 nm, 288 nm and 463 nm showing a high degree of hypochromicity. However, there is only small red shift for the lower energy band upon saturation.

To study further the interaction of these molecules with DNA, changes in the bands at 278 nm for **[2.6]**, 263 nm for **[2.7]** and 288 nm for **[2.8]** were monitored and binding curves were constructed using these data, see **Figure 3.35**. The binding curves indicate that in all cases, saturation binding takes place.

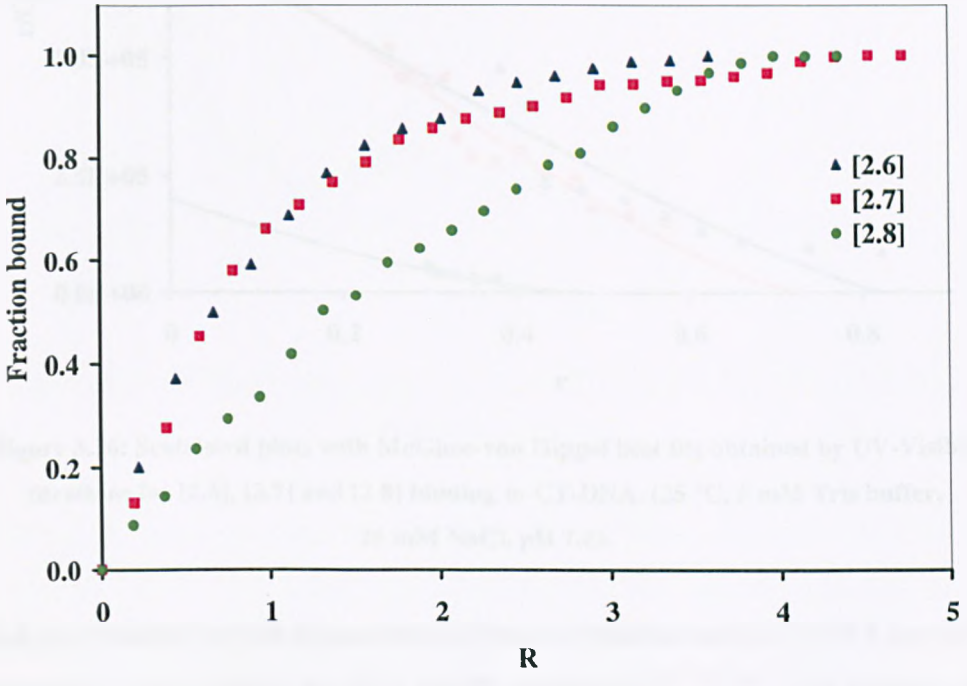

Figure 3.35: Binding curves obtained by UV-Visible titrations for [2.6], [2.7] and [2.8] binding to CT- DNA (25 °C, 5 mM Tris buffer, 25 mM NaCl, pH 7.0).

The hypochromisms of **[2.6]**, **[2.7]** and **[2.8]** on addition of CT-DNA were used to construct a Scatchard plot, which was then fitted to the McGhee-von Hippel model,[174] **Figure 3.36**. The Scatchard plots were constructed from the binding data between 30 % and 95 % fraction bound. The model fitted the data well in all cases and the R^2 value for the non-linear least squares fit was > 0.95. The data are summarised in **Table 3.3**.

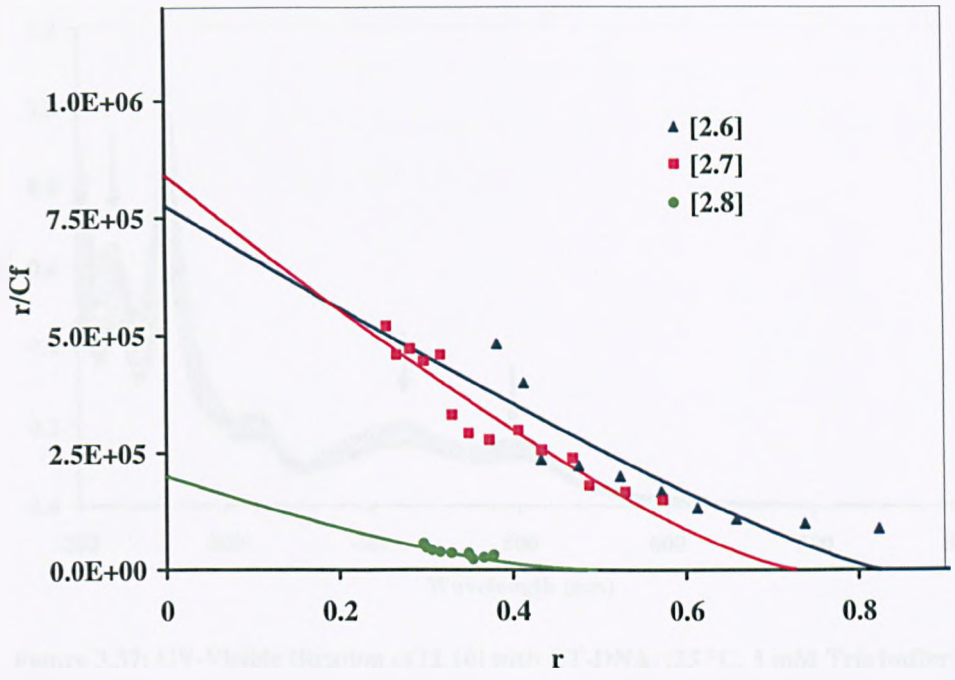

Figure 3.36: Scatchard plots with McGhee-von Hippel best fits obtained by UV-Visible titrations for [2.6], [2.7] and [2.8] binding to CT-DNA. (25 °C, 5 mM Tris buffer, 25 mM NaCl, pH 7.0).

Binding constants for the interaction of these complexes with CT-DNA are in the micromolar range similar to other Ru(II) complexes.[83, 139, 184] The binding sites sizes for the interaction of these complexes with CT-DNA are between 1 and 2 mol of base pair per mol of complex.

We have also investigated the interaction of the pyridinium complexes with CT-DNA by following changes in the UV-Vis spectra. **Figure 3.37** shows a typical titration of **[2.10]** with CT-DNA.

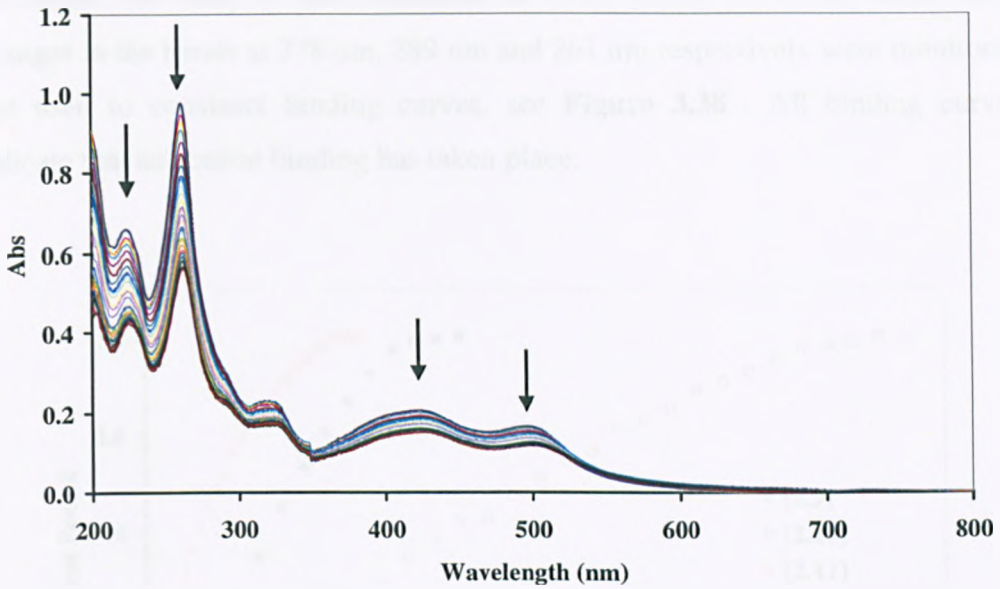

Figure 3.37: UV-Visible titration of [2.10] with CT-DNA. (25 °C, 5 mM Tris buffer, 25 mM NaCl, pH 7.0).

Figure 3.37 shows a decrease in absorption for **[2.10]** upon addition of CT-DNA in aqueous buffer. There are distinctive bands at 243 nm, 289 nm, 429 nm and 496 nm, which all reduce in absorbance.

The addition of CT-DNA to **[2.9]** also resulted in changes in the UV-Vis spectrum, with hypochromicity being observed at 278 nm, 365 nm and 490 nm. Addition of CT-DNA to **[2.11]** leads to similar changes, with the bands at 222 nm, 261 nm, 422 nm and 495 nm showing a high degree of hypochromicity. Previously, Baker *et al.* have reported[185] that **[2.11]** shows hyperchromic effect on the MLCT band upon binding with CT-DNA. In contrast, on our hand we observed a hypochromic effect on the MLCT band upon titration with CT-DNA. Presumably this is due to different salt concentration used in both experiments; however our result is consistent with the other complexes in the series. As mentioned earlier, all these hypochromicity and bathochromic effects are typically observed when aromatic ligands stack between the DNA base pairs.

To further the study of the interaction of **[2.9]**, **[2.10]** and **[2.11]** with DNA, changes in the bands at 278 nm, 289 nm and 261 nm respectively were monitored and used to construct binding curves, see **Figure 3.38**. All binding curves indicate that saturation binding has taken place.

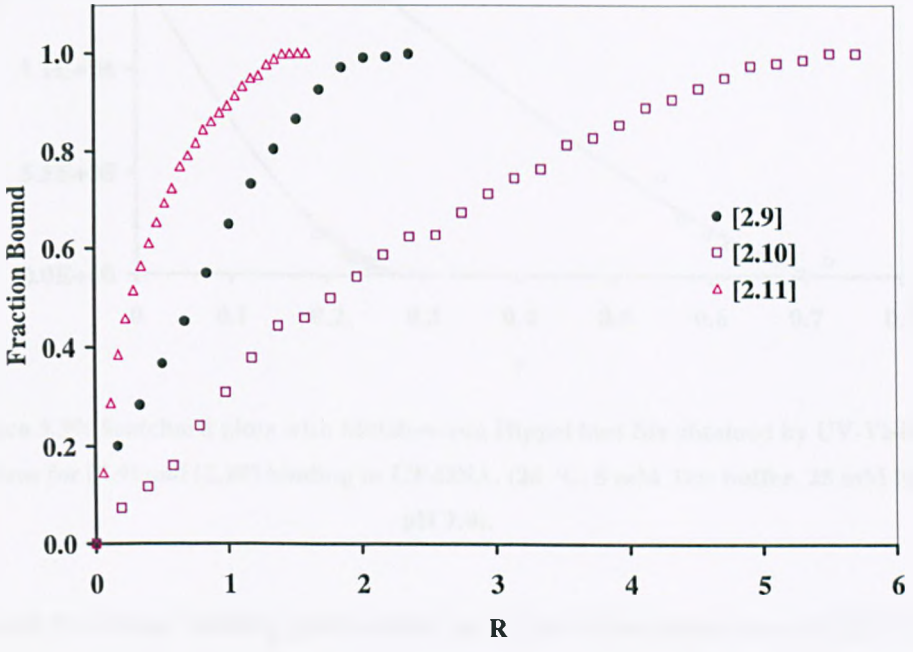

Figure 3.38: Binding curves obtained by UV-Visible titrations for [2.9], [2.10] and [2.11] binding to CT-DNA. (25 °C, 5 mM Tris buffer, 25 mM NaCl, pH 7.0).

Fitting of the titration data into the McGhee-von Hippel model[174] produces a non-linear Scatchard plots, **Figure 3.39**. The Scatchard plots were constructed from the binding data between 30 % and 95 % fraction bound. The model fitted the data well in all cases and the R^2 value for the non-linear least squares fit was > 0.95. The data are summarised in **Table 3.3**.

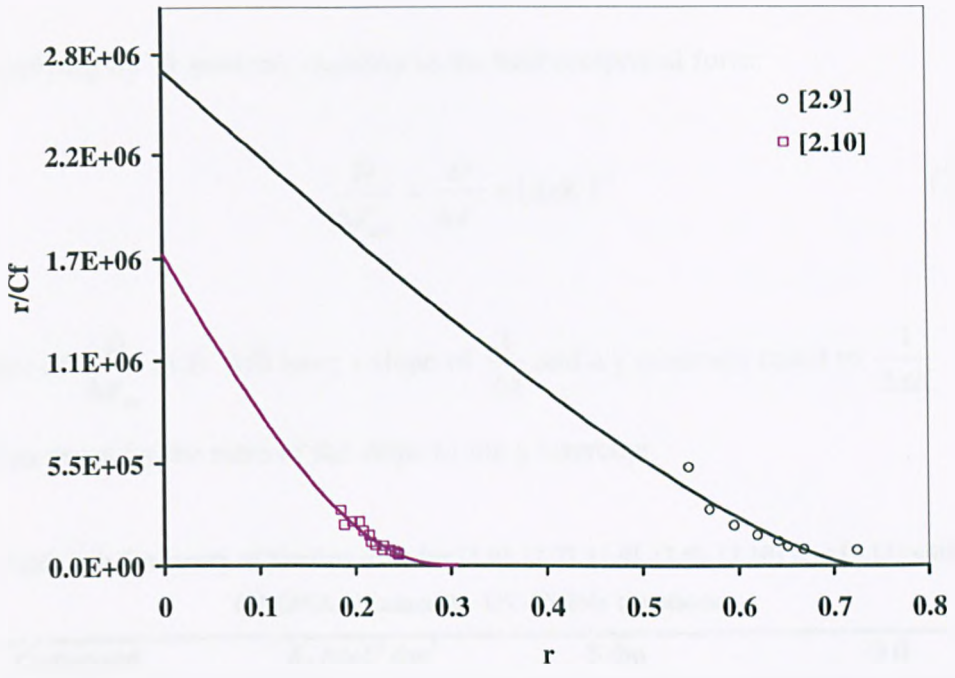

Figure 3.39: Scatchard plots with McGhee-von Hippel best fits obtained by UV-Visible titrations for [2.9] and [2.10] binding to CT-DNA. (25 °C, 5 mM Tris buffer, 25 mM NaCl, pH 7.0).

Attempts to obtain binding parameters using the absorption data of **[2.11]** and McGhee-von Hippel model produced poor fits. Thus, binding constant was determined from equation (2) through a double-reciprocal plot of the change in the apparent extinction coefficient of the ligand *vs.* DNA concentration. The equilibrium binding constant, K_b can be determined from this plot[186] when r, the ratio of bound ligand to DNA base pairs, is near zero. This is represented by the equation:

$$\frac{1}{\Delta\varepsilon_{ap}} = \frac{1}{\Delta\varepsilon\ KD} + \frac{1}{\Delta\varepsilon} \qquad (1)$$

Where $\Delta\varepsilon_{ap} = (\varepsilon_a - \varepsilon_f)$, $\Delta\varepsilon = (\varepsilon_b - \varepsilon_f)$, and ε_a, ε_f and ε_b are the apparent, free and bound ligand extinctions, respectively. D is the DNA concentration in base pairs for native DNA and in potential base pairs (half the concentration of bases) for denaturated DNA.

Multiplying by D puts the equation in the half-reciprocal form:

$$\frac{D}{\Delta\varepsilon_{ap}} = \frac{D}{\Delta\varepsilon} + (\Delta\varepsilon K)^{-1} \qquad (2)$$

A plot of $\frac{D}{\Delta\varepsilon_{ap}} vs.D$ will have a slope of $\frac{1}{\Delta\varepsilon}$ and a y intercept equal to $\frac{1}{\Delta\varepsilon K}$. K is then given by the ratio of the slope to the y intercept.

Table 3.3: Summary of binding data for [2.6], [2.7], [2.8], [2.9], [2.10] and [2.11] with CT-DNA obtained by UV-Visible titrations.

Compound	K_b /mol^{-1} dm^3	S /bp	%H
[2.6][(a)]	7.75 ± 1.52 x 10^5	1.21 ± 0.09	40.4
[2.7]	8.40 ± 0.60 x 10^5	1.37 ± 0.05	32.9
[2.8]	2.00± 0.30 x 10^5	2.00 ± 0.08	15.1
[2.9]	2.66 ± 0.80 x 10^6	1.38 ± 0.05	40.0
[2.10]	1.67 ± 0.20 x 10^6	3.26 ± 0.07	42.6
[2.11]	1.00 x 10^6	-	27.0

(Where % H is the percent of the hypochromism, % H=[($A_\lambda^{[DNA]=0}$-$A_\lambda^{[DNA]=SAT}$)/ $A_\lambda^{[DNA]=0}$] x 100).
[(a)] Titration perfomed in 5 % methanolic buffer due to limited solubility.

Analysis of the Scatchard plot shows that the binding affinity of the *N*-methylated complexes is about 2 - 5 fold higher than those non-methylated complexes. This clearly shows that the binding affinity of the complexes increased upon changing the charge of the complex from +2 to +4, thus indicates that there is a contribution of electrostatic interactions for the pyridinium complexes with CT-DNA. Indeed, the binding affinity for the pyridinium complexes are comparable[142, 187] to that reported for $[Ru(phen)_2(dppz)]^{2+}$ and other Ru(II)-dppz and Ru(II)-dppn complexes. The site sizes obtained are 1.38 bp and 3.26 bp per ligand for **[2.9]** and **[2.10]**, respectively.

Previously, Baker *et al.*[185] reported that the binding constant for similar compound **[2.8]** and **[2.11]** with CT-DNA in 5 mM TRIS buffer, 50 mM NaCl, pH 7.4 were (1.3 ± 0.2) x 10^4 and (2.8 ± 0.6) x 10^4, respectively. However, we observed that the binding constant for these complexes in 5 mM TRIS buffer, 25 mM NaCl, pH 7.0 were higher than those observed by Baker *et al.* Presumably this is due to low salt concentrations used in our studies, the salt concentration dependence experiments were carried out for further investigations (see Section 3.3.5). The site size reported[185] for **[2.8]** is consistent with ours, which is 2 - 3 base pairs per ligand.

3.4.4 Luminescence Titrations

The luminescence has been examined previously in water and in acetonitrile. All of the complexes luminesce brightly in acetonitrile but weakly in water especially **[2.6]** and **[2.9]** with dppz units as the ancillary ligands. The changes in luminescence emission intensity were apparent on binding the **[2.6]**, **[2.9]**, **[2.10]** and **[2.11]** to CT-DNA. Luminescence titrations were carried out using excitation wavelengths into the MLCT band of the molecules. The emission of **[2.6]** increased upon addition of CT-DNA. **Figure 3.40** shows a typical titration of **[2.6]** with CT-DNA, with emission blue shifts about 26 nm compared to the unbound cation.

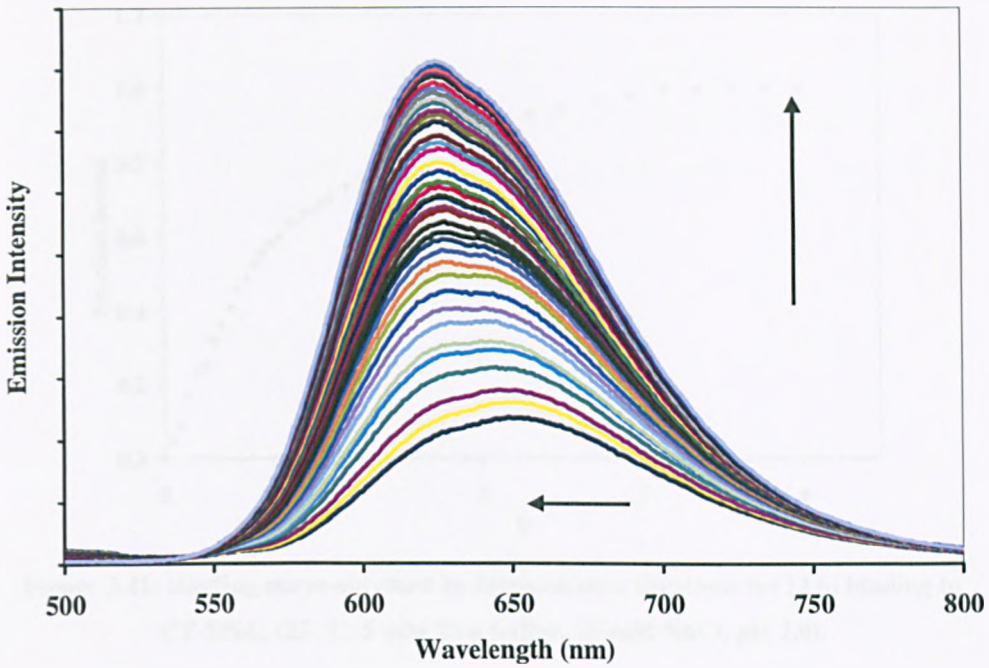

Figure 3.40: Luminescence titration of [2.6] with CT-DNA. (25 °C, 5 mM Tris buffer, 25 mM NaCl, pH 7.0).

Emission intensities are essentially unchanged for **[2.8]**. This result is consistent with report by Baker *et al.*[185] which observed no emission change upon titration of CT-DNA into the solution of **[2.8]**. The analogous titration involving **[2.7]** results in a similar observation, with slight changes in the emission intensity. This observation suggests that **[2.7]** and **[2.8]** complexes interact with CT-DNA in a somewhat similar way. Space filling studies[185] on **[2.8]** have shown that this ligand would not be accommodated symmetrically within the major groove of DNA due to the size of the ligand. The exposure to solvent might explain the lack of change in emission of **[2.7]** and **[2.8]**.

The binding curve derived from the luminescence data for the interaction of **[2.6]** with CT-DNA is shown in **Figure 3.41**. Once again, it shows that saturation binding has taken place. The data was then fitted to the McGhee-von Hippel model[174] (**Figure 3.42**). Binding parameters obtained from fits of the raw data are summarised in **Table 3.4**.

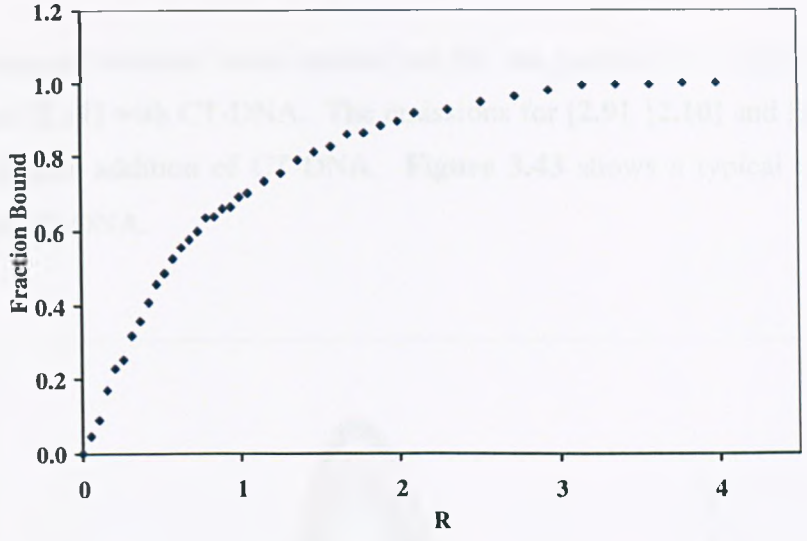

Figure 3.41: Binding curve obtained by luminescence titrations for [2.6] binding to CT-DNA. (25 °C, 5 mM Tris buffer, 25 mM NaCl, pH 7.0).

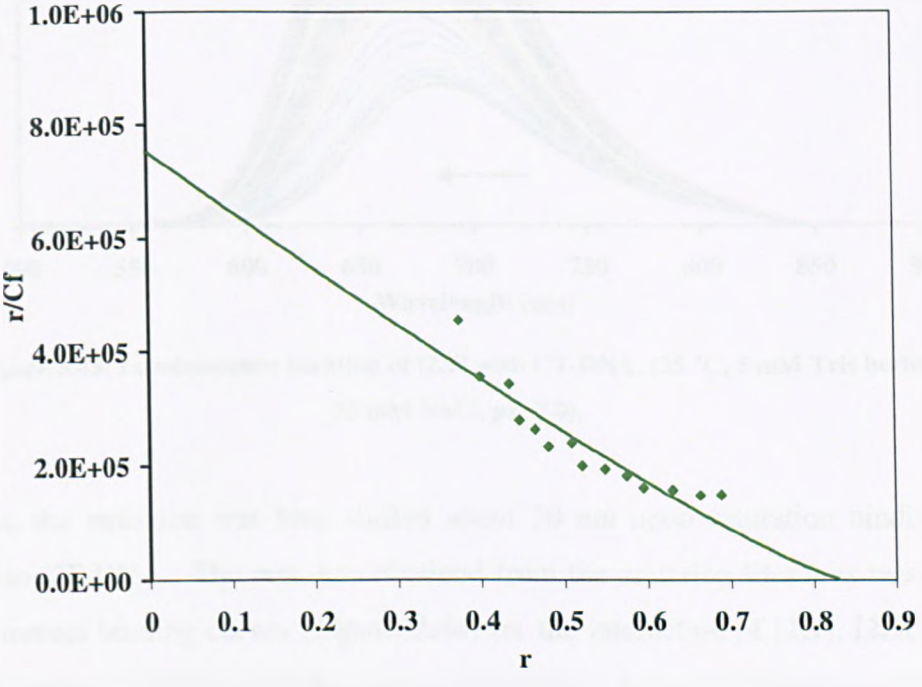

Figure 3.42: Scatchard plots with McGhee-von Hippel best fits obtained by luminescence titrations for [2.6] binding to CT-DNA. (25 °C, 5 mM Tris buffer, 25 mM NaCl, pH 7.0).

The binding constant and the site size obtained from luminescence titration is in good agreement with those obtained from UV-Visible absorption experiments. This confirm that **[2.6]** binds to DNA with reasonably high affinity ($\geq 10^5$ mol^{-1} dm^3).

The analogous titrations were carried out for the pyridinium complexes **[2.9]**, **[2.10]** and **[2.11]** with CT-DNA. The emissions for **[2.9]**, **[2.10]** and **[2.11]** were increased upon addition of CT-DNA. **Figure 3.43** shows a typical titration of **[2.9]** with CT-DNA.

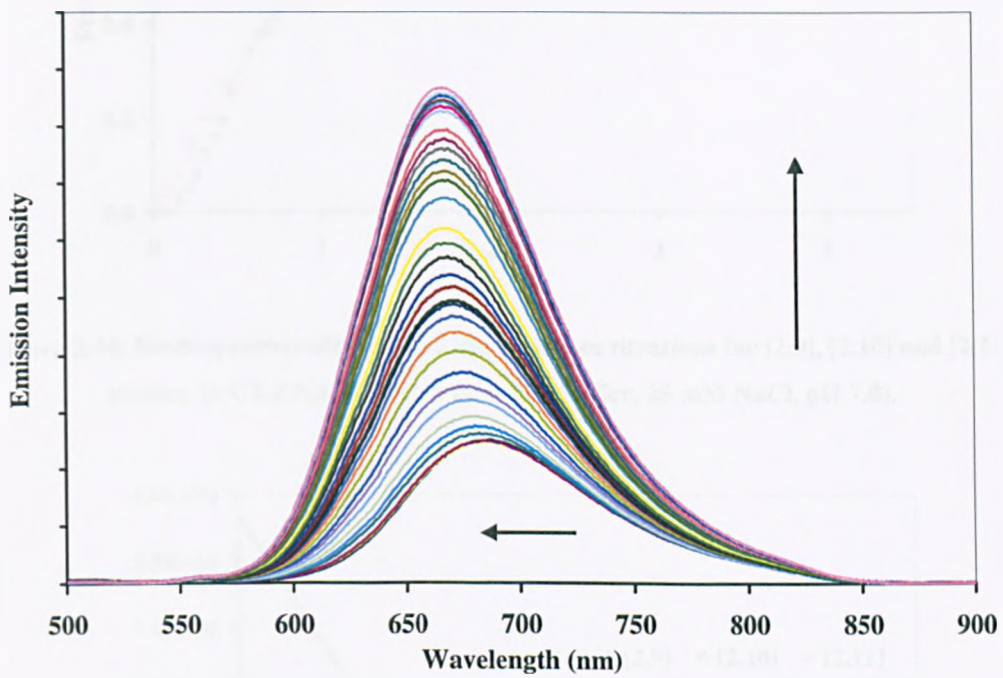

Figure 3.43: Luminescence titration of [2.9] with CT-DNA. (25 °C, 5 mM Tris buffer, 25 mM NaCl, pH 7.0).

Again, the emission was blue shifted about 20 nm upon saturation binding of **[2.9]** to CT-DNA. The raw data obtained from the emission titrations was used to construct binding curves (**Figure 3.44**) for the interaction of **[2.9]**, **[2.10]** and **[2.11]** with CT-DNA, which were in turn fitted to the McGhee-von Hippel model[174] (**Figure 3.45**).

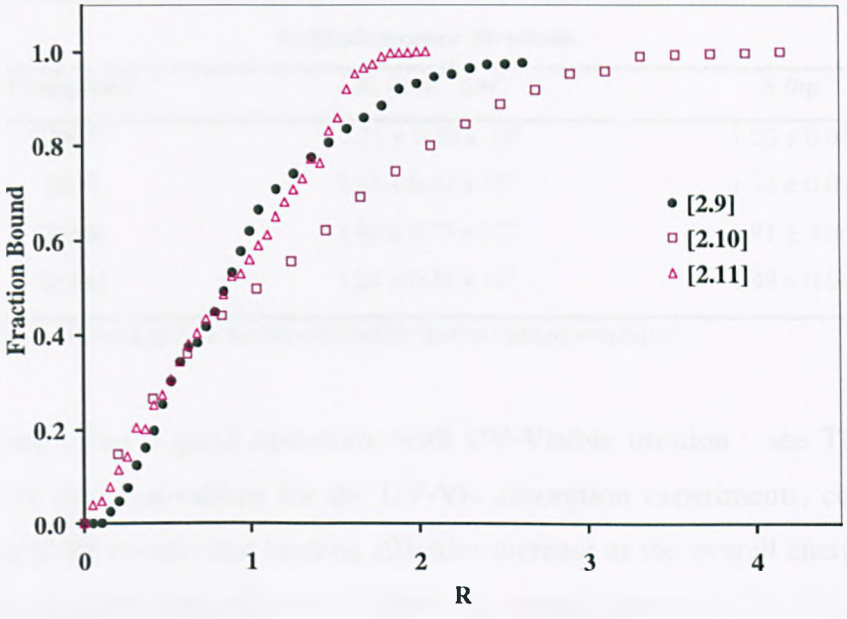

Figure 3.44: Binding curves obtained by luminescence titrations for [2.9], [2.10] and [2.11] binding to CT-DNA. (25 °C, 5 mM Tris buffer, 25 mM NaCl, pH 7.0).

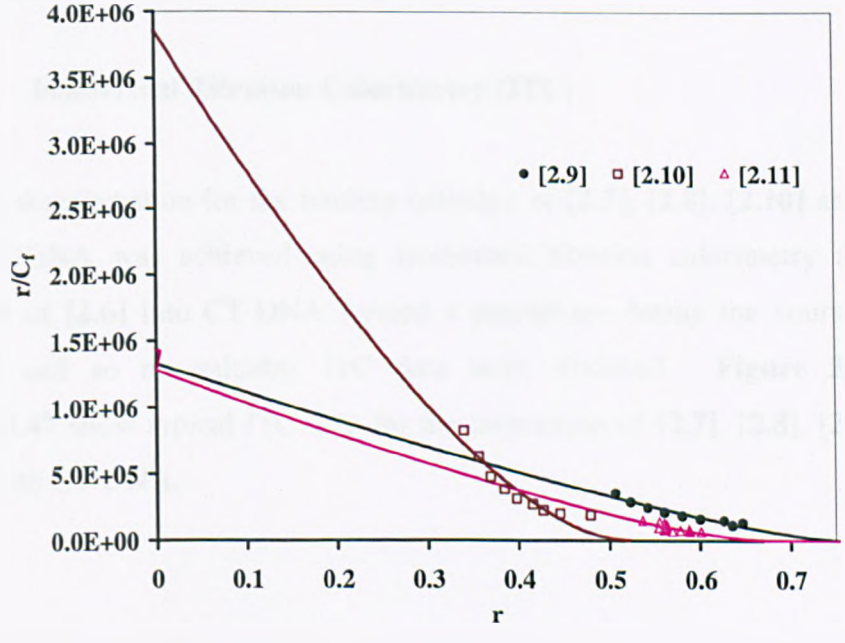

Figure 3.45: Scatchard plots with McGhee-von Hippel best fits obtained by luminescence titrations for [2.9], [2.10] and [2.11] binding to CT-DNA. (25 °C, 5 mM Tris buffer, 25 mM NaCl, pH 7.0).

Table 3.4: Summary of binding data for [2.6], [2.9], [2.10] and [2.11] with CT-DNA obtained by luminescence titrations.

Compound	K_b /mol^{-1} dm^3	S /bp
[2.6][(a)]	7.51 ± 0.70 x 10^5	1.20 ± 0.04
[2.9]	1.33 ± 0.10 x 10^6	1.33 ± 0.03
[2.10]	3.86 ± 0.73 x 10^6	1.91 ± 0.06
[2.11]	1.28 ± 0.36 x 10^6	1.49 ± 0.04

[(a)] Titration performed in 5 % methanolic buffer due to limited solubility.

The fitting offers a good agreement with UV-Visible titration - see **Table 3.3**. Similar to the observations for the UV-Vis absorption experiments, comparing **[2.6]** and **[2.9]**, reveals that binding affinities increase as the overall charge on the complex ion rises from +2 to +4. Since the overall charge on **[2.11]** increases, Baker *et al.*[185] suggested that the interaction is no longer intercalative, but is based on electrostatic mode. However, viscosity studies obtained for **[2.11]** give evidence of intercalative interaction for this type of complex.

3.4.5 Isothermal Titration Calorimetry (ITC)

A direct determination for the binding enthalpy of **[2.7]**, **[2.8]**, **[2.10]** and **[2.11]** with CT-DNA was achieved using isothermal titration calorimetry at 25°C. Titration of **[2.6]** into CT-DNA formed a precipitate during the course of the titration and so no valuable ITC data were obtained. **Figure 3.46** and **Figure 3.47** show typical ITC data for the interaction of **[2.7]**, **[2.8]**, **[2.10]** and **[2.11]** with CT-DNA.

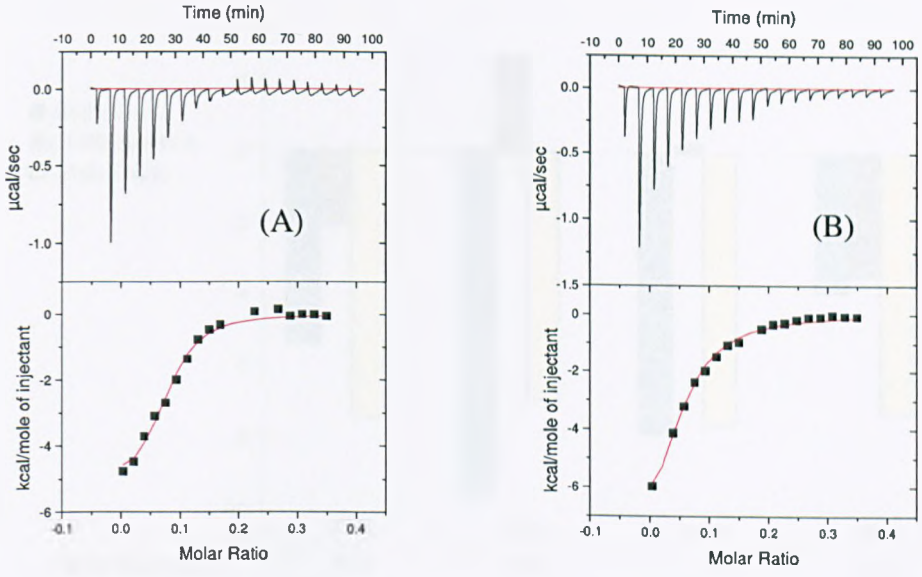

Figure 3.46: ITC raw data for the interaction of CT-DNA with; (A) [2.7] and (B) [2.8] in 5 mM Tris, 25 mM NaCl, pH 7.0 at 25°C.

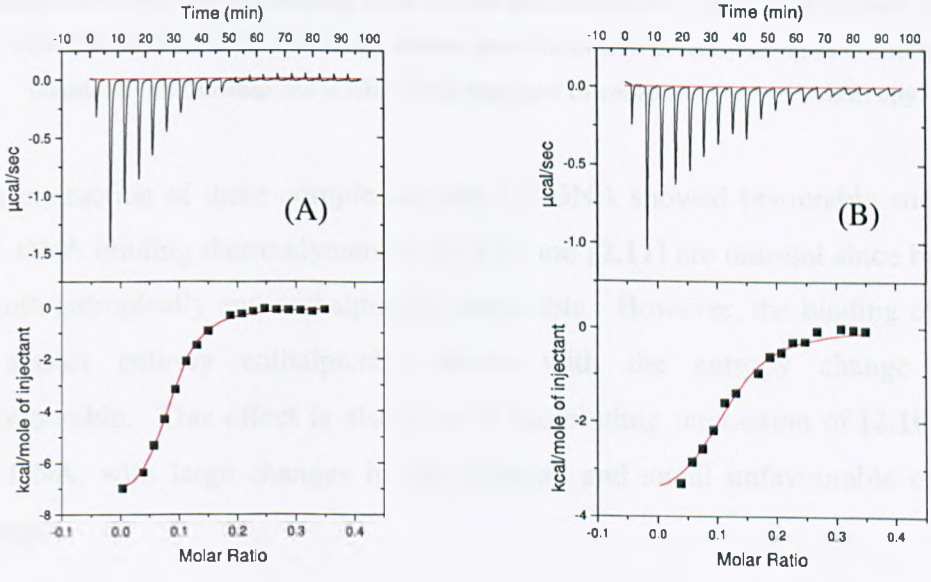

Figure 3.47: ITC raw data for the interaction of CT-DNA with; (A) [2.10] and (B) [2.11] in 5 mM Tris, 25 mM NaCl, pH 7.0 at 25°C.

These data were best fit using a single set of identical binding sites model. A comparison of the enthalpic and entropic contributions to the binding of **[2.7]**, **[2.8]**, **[2.10]** and **[2.11]** with CT-DNA is summarised in **Figure 3.48**.

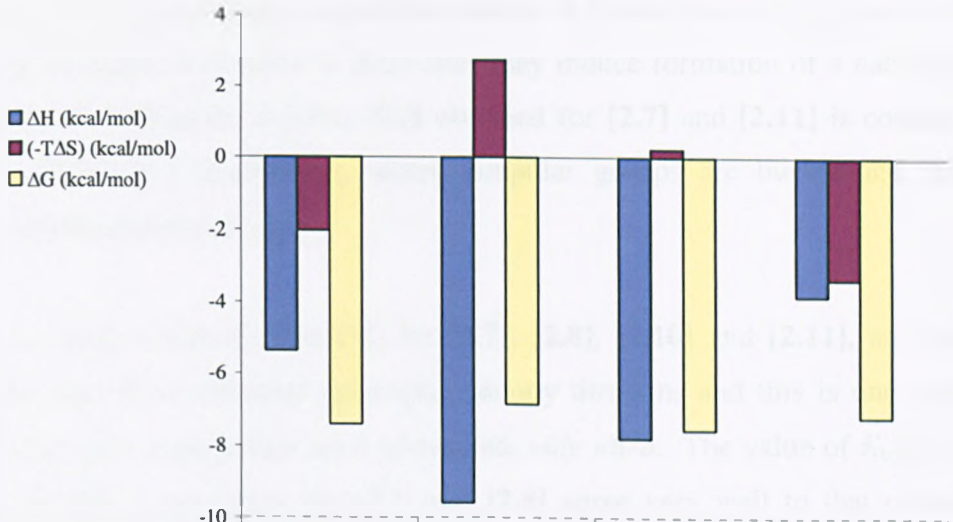

	[2.7]	[2.8]	[2.10]	[2.11]
ΔH (kcal/mol)	-5.37	-9.59	-7.80	-3.86
(-TΔS) (kcal/mol)	-2.04	2.73	0.23	-3.37
ΔG (kcal/mol)	-7.41	-6.86	-7.57	-7.23
Kb, (X10E+05) M-1	2.69	1.06	3.59	2.00

Figure 3.48: ITC thermodynamic data for the interaction of [2.7], [2.8], [2.10] and [2.11] with CT-DNA at 25°C. (Enthalpy values were measured directly using ITC and the standard relationship ΔG = ΔH - TΔS was used to compute changes in entropy).

The interaction of these complexes with CT-DNA showed favourable enthalpy. The DNA binding thermodynamics of **[2.7]** and **[2.11]** are unusual since binding is both entropically and enthalpically favourable. However, the binding of **[2.8]** is almost entirely enthalpically driven with the entropy change being unfavourable. This effect is also seen in the binding interaction of **[2.10]** with CT-DNA, with large changes in the enthalpy and small unfavourable entropy change.

In all cases, negative ΔH were obtained which is likely if the complex is stabilised by hydrogen bonding as well as van der Waals interactions.[184] The negative ΔH is also typical for intercalation where stacking interactions with DNA base pairs stabilise the ligand-DNA complex. For example, enthalpy value of -10.4 and -8.8 kcal/mol has been determined for daunomycin and ethidium bound to DNA, respectively.[188, 189] There is also a possibility that there may be some fraying of the duplex structure, specifically at the very ends of the helix

which in turn representing a significant source of favourable enthalpy due to the binding of ligand molecules at these sites may induce formation of a native-like structure.[184] While the positive TΔS obtained for **[2.7]** and **[2.11]** is consistent with hydrophobic interactions, where nonpolar groups are buried and made inaccessible to polar solvent.

The site size, obtained from ITC for **[2.7]**, **[2.8]**, **[2.10]** and **[2.11]**, are much smaller than those obtained from spectroscopy titrations and this is one reason why a Job plot experiments were conducted, *vide ultra*. The value of K_b derived from the ITC experiments for **[2.7]** and **[2.8]** agree very well to that obtained from spectroscopic titrations. However, the K_b value derived from the ITC experiments for **[2.10]** and **[2.11]** are five fold lower than those obtained from spectroscopy titrations. There are several explainations for this observation.

The discrepancy between ITC and spectroscopic obtained binding parameters is because data are fitted to different binding models. For absorption/luminescence titration, the binding isotherms are fitted by using the neighbour exclusion model, which assumes DNA is a lattice of identical and non-interacting potential binding sites where ligand binding to any sites excludes neighbour sites. However, the ITC model uses a single set of identical binding sites. This means that generally the ITC estimates of K_b are lower than the more accurate figures obtained by spectroscopic titrations. However, the aim of conducting ITC experiments was not to obtain another estimate of binding affinity, but to allow the enthalpic and entropic components to the free energy of binding to be determined.

Figure 3.49 shows two experiments merged together to complete the binding isotherm for **[2.9]** with CT-DNA. The titrations were not able to be completed in one experiment. Thus, the syringe was reloaded with ligand and the titration immediately continued after the first nineteen injections. This is due to the limited solubility of the ligand and the fact the syringe can only hold a fixed volume of liquid. The data were then combined using ConCat32, a program specifically designed by Microcal for this purpose.

The binding of **[2.9]** to CT-DNA showed three modes of binding (**Figure 3.49**). This is consistent with more than two binding stoichiometries observed from the Job plots experiment. It is impossible to fit data for such a situation using commercially available software, because it only allows us two sets of binding.

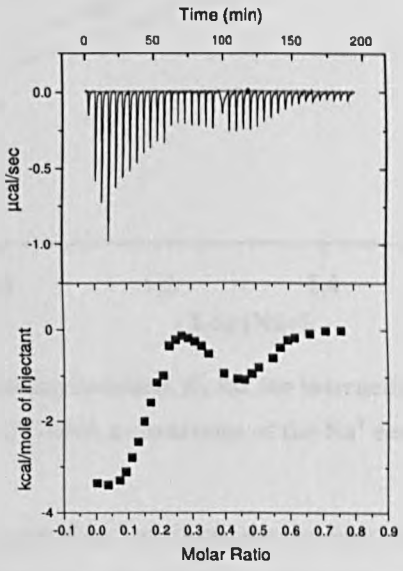

Figure 3.49: ITC raw data for the interaction of CT-DNA with [2.9].

Salt concentration dependence experiments were conducted using ITC with different salt concentrations ranging from 25 - 100 mM NaCl at 25°C. **Figure 3.50** shows that for this system, log K_b is a linear function of log $[Na^+]$.

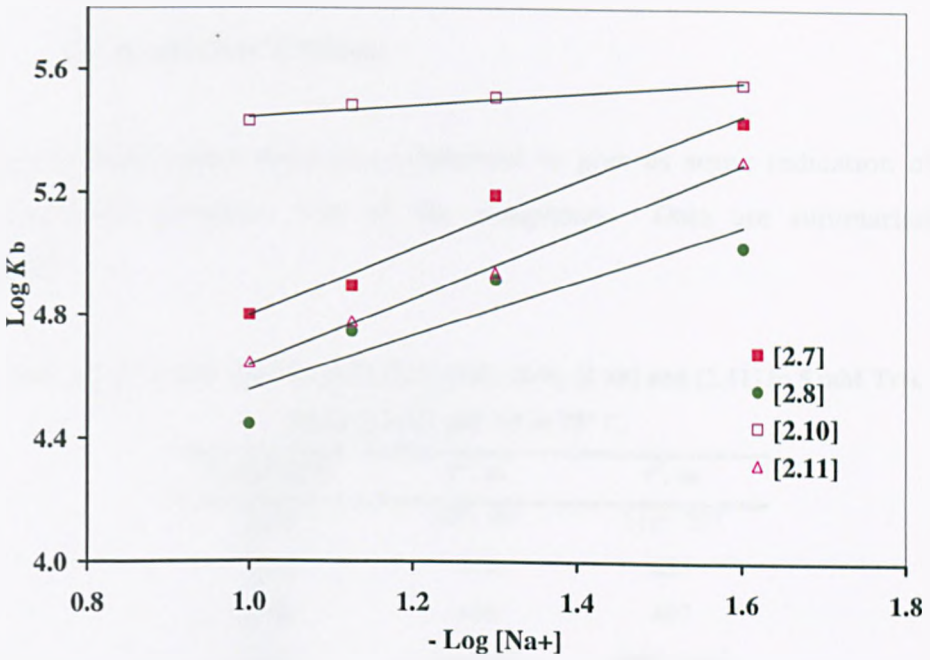

Figure 3.50: Log plot of binding constant, K_b for the interaction of [2.7], [2.8], [2.10] and [2.11] with CT-DNA as functions of the Na^+ concentration.

Clearly, **Figure 3.50** shows that an increase in salt concentration reduces the binding constant of **[2.7]**, **[2.8]**, **[2.10]** and **[2.11]** to CT-DNA. This correlates well with the polyelectrolyte theory; that is the binding constant is sensitive to ionic strength. Work by Record and Manning have shown that the higher the salt concentration the lower the binding constant.[184, 190, 191] This is exactly what we observed. Upon increasing the salt concentrations, there is concomitant decrease in the binding constant, K_b. From the relationship between the binding constant, K_b and the salt concentrations, we can see that the electrostatic interaction does not contribute much in the binding interaction of **[2.10]** with CT-DNA.

Duplex DNA comprises highly negatively charged lattices, which in the presence of cations, will be neutralised. The cations are condensed around the DNA and are non-specifically bound to DNA. This means that the positively charge ligand will have to compete with the cations for a site on the DNA. Thus the cations and ligand binding are thermodynamically linked, and the binding of one influences the binding of the other.[188]

3.4.6 Luminescence Lifetime

Lifetime measurements were also performed to give us some indication of the DNA binding interaction with all the complexes. Data are summarised in **Table 3.5**.

Table 3.5: Lifetime data for [2.6], [2.7], [2.8], [2.9], [2.10] and [2.11] in 5 mM Tris, 25 mM NaCl, pH 7.0 at 25° C.

Compound	τ^a, ns	τ^b, ns
[2.6]	60[c]; 10[d]	118[c]; 23[d]
[2.7]	716	657
[2.8]	413	497
[2.9]	224[c]; 63[d]	868[c]; 347[d]
[2.10]	68	208
[2.11]	61	196

[a]Lifetime at binding ratio of [CT-DNA bp]/[Ru] 0:1. [b]Lifetime at binding ratio of [CT-DNA(bp)]/[Ru] saturated:1. [c]First component. [d]Second component. (All solutions are degassed unless otherwise stated)

For all complexes, the lifetimes were recorded in the absence of CT-DNA and in the presence of saturated CT-DNA (saturation points were determined from the luminescence titration experiments). The decay profiles for both dppz complexes fitted well to a biexponential curve corresponding to two lifetimes for **[2.6]** and **[2.9]**. When the binding ratio of [CT-DNA(bp)]/[Ru] varied from 0:1 to saturated:1, the excited lifetime increased from 60 ns and 10 ns to 118 ns and 23 ns for **[2.6]** and from 224 ns and 63 ns to 868 ns and 347 ns for **[2.9]**. The trace obtained for **[2.7]**, **[2.8]**, **[2.10]** and **[2.11]** fitted well to a monoexponential curve corresponding to one lifetime for these complexes. Both compounds **[2.7]** and **[2.8]** show slight changes in the luminescence lifetimes as observed from the luminescence titrations. On the other hand, when the binding ratio of [CT-DNA(bp)]/[Ru] varied from 0:1 to saturated:1, the excited lifetime increased from 68 ns to 208 ns for **[2.10]** and from 61 ns to 196 ns for **[2.11]**. It is clearly shown that upon binding with CT-DNA, the excited-state lifetimes were

increased for **[2.6]**, **[2.9]**, **[2.10]** and **[2.11]**, consistent with the observed enhancement in emission upon binding. However, there is no distinct changes in the lifetime of **[2.7]** and **[2.8]** upon binding with CT-DNA and this is also consistent with the steady state studies.

3.5 DNA Binding Results of Rhenium(I) Complexes

We were interested in investigating the DNA binding properties of the rhenium(I) qtpy-based complexes with CT-DNA due to the fact that they only contain a single "chromophoric" diimine ligand and thus there is no ambiguity with respect to the acceptor ligand that is involved in the interaction with DNA. However, only two of the rhenium complexes, **[2.14]** and **[2.15]** have been studied due to poor solubility of the neutral **[2.12]** and +1 charge **[2.13]** species in buffer. As a reminder, complexes discussed in this study are shown in **Figure 3.51**.

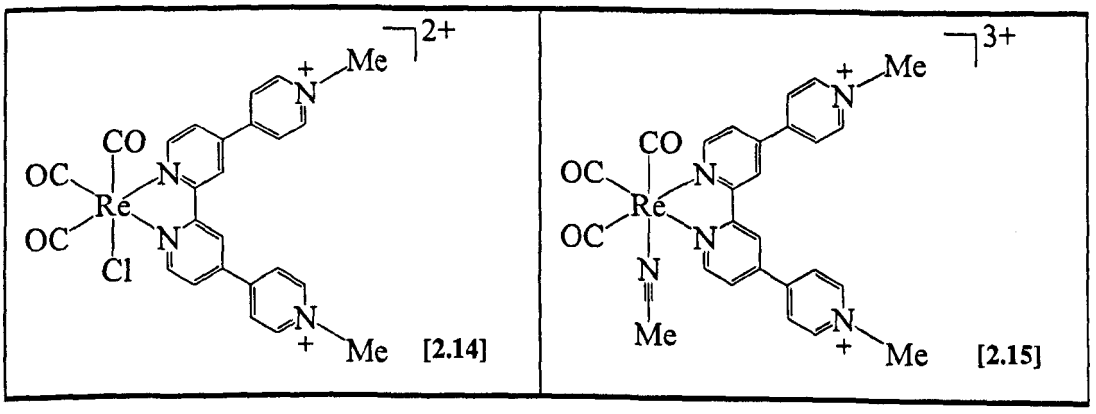

Figure 3.51: Rhenium(I) complexes discussed in this study.

3.5.1 Viscosity

As previously mentioned a major feature of intercalating ligands is the lengthening of the DNA helix which ultimately increases the viscosity of DNA. The mode of binding for **[2.14]** and **[2.15]** to CT-DNA was studied using viscometry. **Figure 3.52** shows that the relative viscosity of CT-DNA increases with increasing amounts of **[2.14]** and **[2.15]**. This provides strong evidence that these ligands bind to DNA by intercalation.

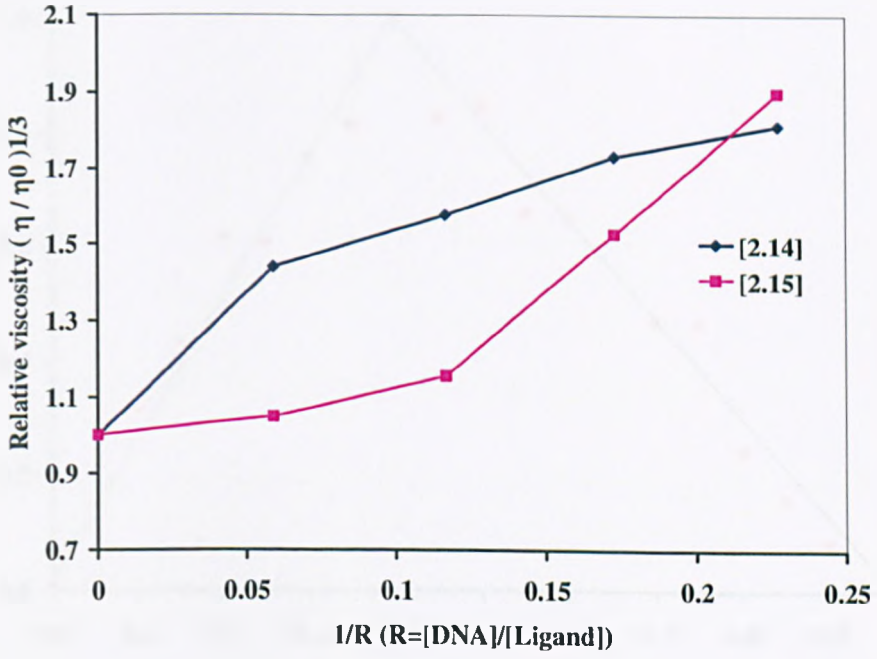

Figure 3.52: Relative viscosity of CT-DNA upon addition of [2.14] and [2.15] to CT-DNA using 5 mM TRIS, 25 mM NaCl, pH 7.0 at 27°C.

These results are very interesting as they indicate that the qtpy ligand is intercalated between the base pairs. Previous work by Barton *et al.*[192] has proposed a plausible model for partially intercalated diphenylphenanthroline (DIP) groups. Due to the structure similarity between DIP ligand and qtpy ligand, we believed that the qtpy ligand is bound to CT-DNA in a similar way to the DIP moiety.

3.5.2 Continuous Variation Analysis (Job Plots)

The continuous variation analysis (Job plots) experiments were carried out to determine the binding stoichiometries between the interactions of **[2.14]** and **[2.15]** with CT-DNA. Data are summarised in **Table 3.6**. This was done by following the changes in emission intensities of the mixtures upon excitation at the wavelength characteristic of the MLCT band of **[2.15]**. **Figure 3.53** shows the Job plots for the interaction of **[2.15]** with CT-DNA (data is normalised for clarity).

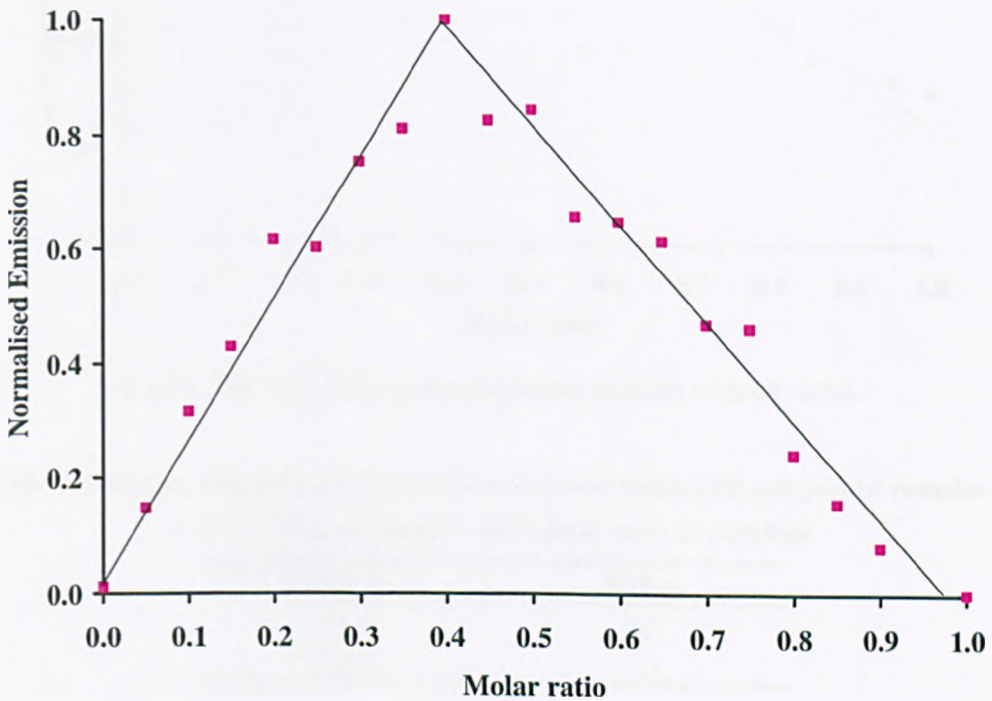

Figure 3.53: Job plots for the interaction of [2.15] with CT-DNA.

Figure 3.53 shows the intersection point for **[2.15]** was at 0.4 which is equivalent to stoichiometry of 1.5 mol of base pair per mol of complex. Since the complex **[2.14]** gives no emission enhancement upon addition of CT-DNA, a Job plot was constructed using UV-Visible experiment. This was done by following the changes in absorption of the mixtures at wavelength where the complex absorbed strongly. **Figure 3.54** shows the Job plots for the interaction of **[2.14]** with

CT-DNA (data is normalised for clarity). The intersection point for **[2.14]** was at 0.25, being equivalent to a stoichiometry of 3 mol of base pairs per mol of complex.

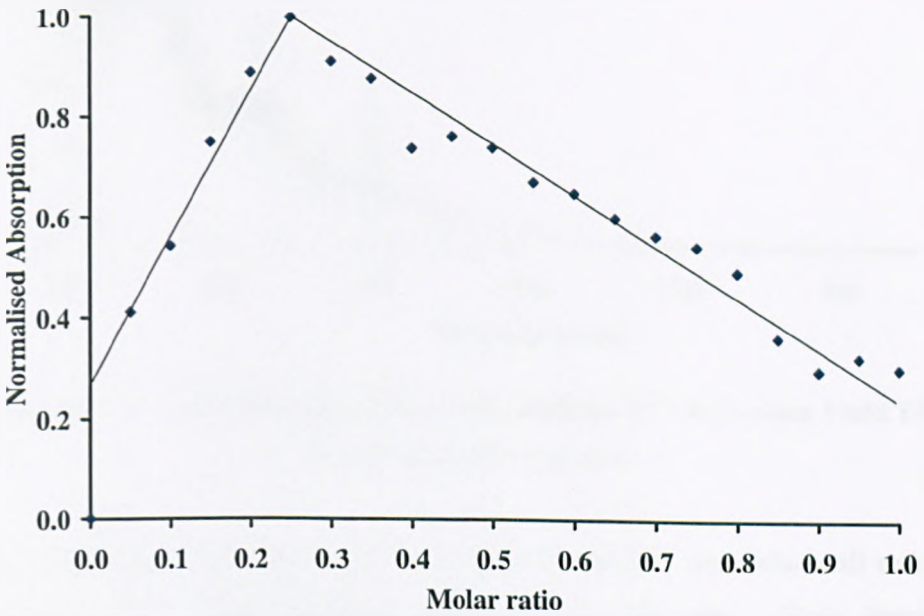

Figure 3.54: Job plots for the interaction of [2.14] with CT−DNA.

Table 3.6: Binding stoichiometries for the interaction of rhenium(I) polypyridyl complexes with CT-DNA obtained by continuous variation analysis.

Compound	N (bp)
[2.14]	3.0
[2.15]	1.5

3.5.3 UV-Visible Titrations

The interaction for **[2.14]** and **[2.15]** with CT-DNA has been analysed using absorption spectroscopy. **Figure 3.55** displayed clear hypochromicities in the absorption bands for **[2.14]** upon addition of CT-DNA in aqueous buffer.

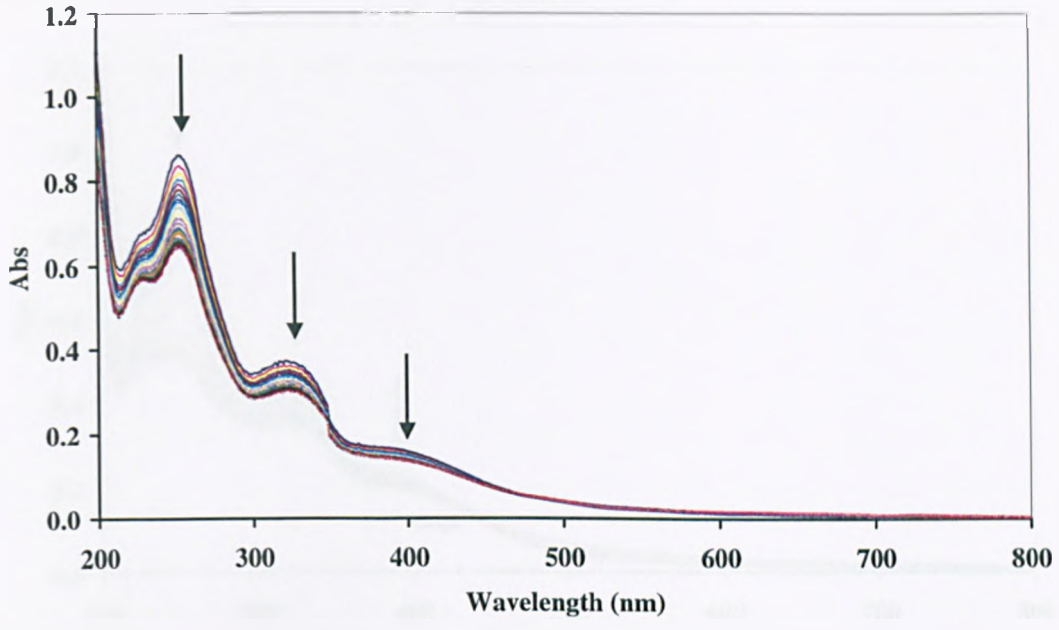

Figure 3.55: UV-Visible titration of [2.14] with addition of CT-DNA using 5 mM TRIS, 25 mM NaCl, pH 7.0 at 25°C.

There are distinctive bands at 253 nm, 322 nm and 391 nm, which all reduce in absorbance, with hypochromism (24.9 %) at 253 nm. This feature is characteristic of **[2.14]** – CT-DNA binding interactions.

The absorption bands for **[2.15]** decreases with increasing concentrations of CT-DNA (**Figure 3.56**). Again, there are distinctive bands at 252 nm, 323 nm and 389 nm which all reduce in absorbance. The wavelength band at 389 nm displays a bathochromic shift approaching binding saturation. All these features are indicative of **[2.15]** – CT-DNA binding interactions. With *prior* evidence from viscosity, these spectral changes illustrate an intercalative mode of binding.

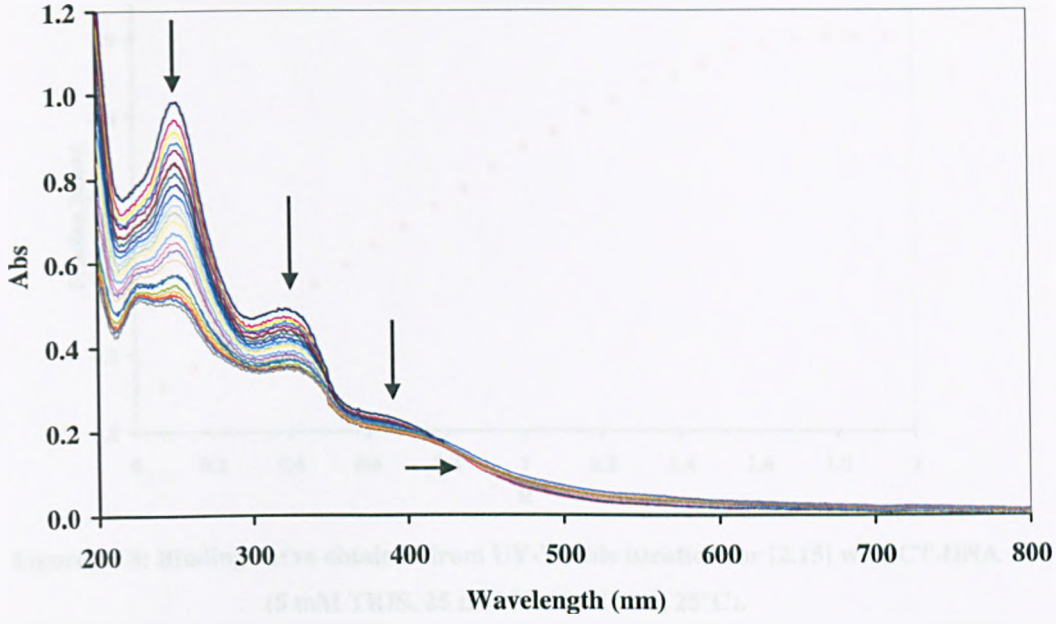

Figure 3.56: UV-Visible titration of [2.15] with addition of CT-DNA using 5 mM TRIS, 25 mM NaCl, pH 7.0 at 25°C.

The changes in the band at 253 nm for **[2.14]** and at 252 nm for **[2.15]** were monitored and binding curves were constructed using these data, see **Figure 3.57** and **Figure 3.58**. The binding curves indicate that in all cases, saturation binding had taken place.

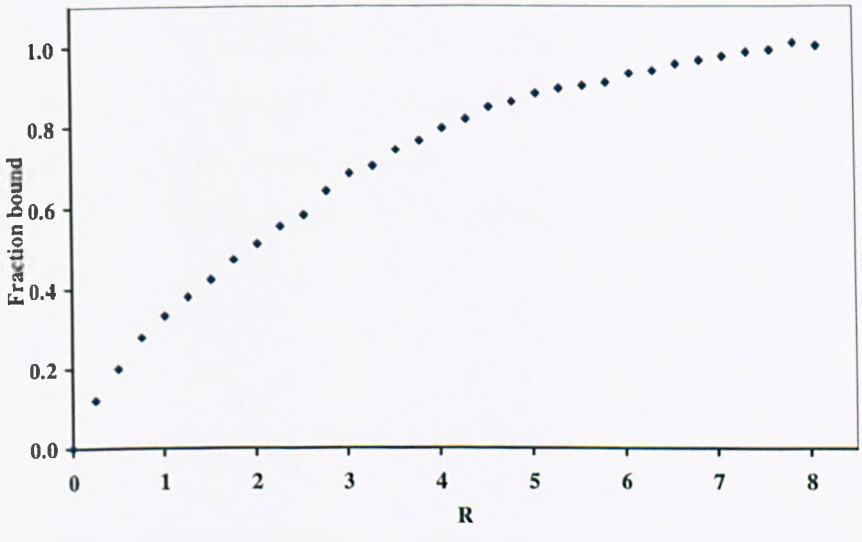

Figure 3.57: Binding curve obtained from UV-Visible titration for [2.14] with CT-DNA (5 mM TRIS, 25 mM NaCl, pH 7.0, 25°C).

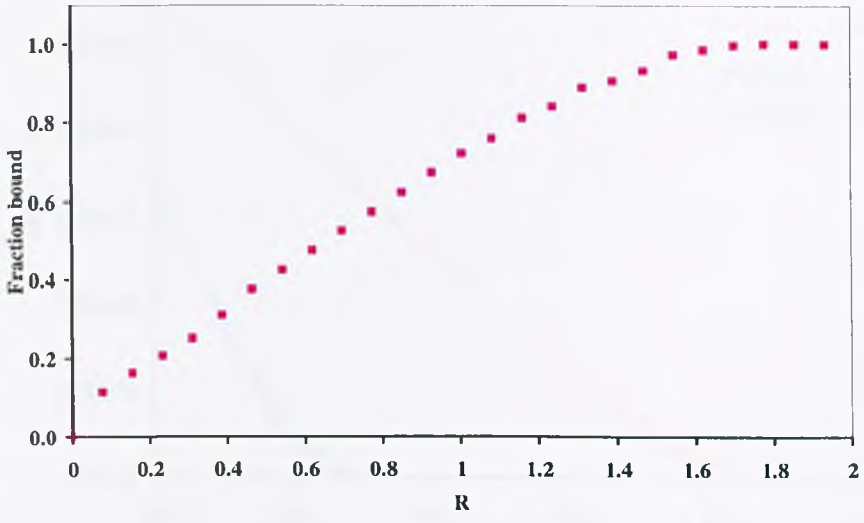

Figure 3.58: Binding curve obtained from UV-Visible titration for [2.15] with CT-DNA (5 mM TRIS, 25 mM NaCl, pH 7.0, 25°C).

The hypochromisms of **[2.14]** and **[2.15]** on addition of CT-DNA were used to construct a Scatchard plot, which was then fitted to the McGhee-von Hippel model,[174] **Figure 3.59**. The Scatchard plots were constructed from the binding data between 30 % and 95 % fraction bound. The model fitted the data well in all cases and the R^2 value for the non-linear least squares fit was > 0.95. The data are summarised in **Table 3.6**.

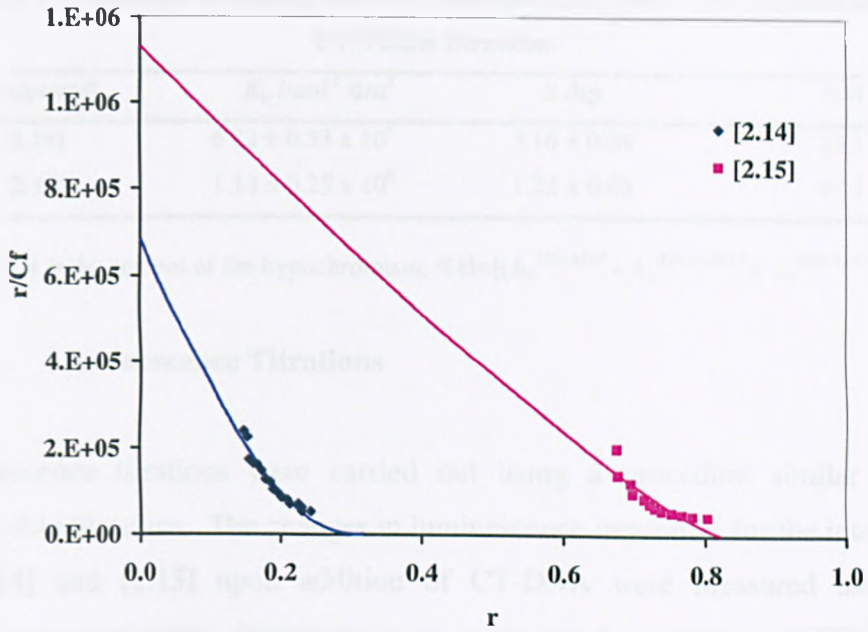

Figure 3.59: Scatchard plots fitted to the McGhee-von Hippel model using UV-Visible titration data from [2.14] and [2.15] binding to CT-DNA in 5 mM TRIS, 25 mM NaCl, pH 7.0.

Analysis of the Scatchard plot shows that **[2.14]** binds to CT-DNA with a binding constant of 6.82 x 10^5 M^{-1} and a stoichiometry of 3.16 bp per ligand, whereas **[2.15]** has a higher binding constant of 1.13 x 10^6 M^{-1} and a lower stoichiometry of 1.2 bp per ligand. The stoichiometries obtained for both **[2.14]** and **[2.15]** are in good agreement with those obtained from Job plots experiments. Re^I complexes **[2.14]** and **[2.15]** bind with affinities that are comparable, if not higher than that of $[Ru^{II}(qtpy)]^{2+}$ analogues and the ancillary ligands of the Re^I centre present the least steric demand of all. Indeed, previous studies[193] on $[(CO)_3MeCNRe]^+$ extended terpyridyl complexes indicate binding affinity in the 10^5 M^{-1} range.

Table 3.7: Summary of binding data for [2.14] and [2.15] with CT-DNA obtained by UV-Visible titrations.

Compound	K_b /mol^{-1} dm^3	S /bp	%H
[2.14]	$6.82 \pm 0.53 \times 10^5$	3.16 ± 0.08	24.9
[2.15]	$1.13 \pm 0.25 \times 10^6$	1.22 ± 0.03	47.1

(Where %H is the percent of the hypochromism, $\%H=[(A_\lambda^{[DNA]=0} - A_\lambda^{[DNA]=SAT})/ A_\lambda^{[DNA]=0}] \times 100$).

3.5.4 Luminescence Titrations

Luminescence titrations were carried out using a procedure similar to the UV-Visible titrations. The changes in luminescence intensities for the interaction of **[2.14]** and **[2.15]** upon addition of CT-DNA were measured using the excitation wavelength characteristic of each metal complex at 25°C. The emission of **[2.15]** was found to be enhanced upon addition of CT-DNA and no shifting of emission wavelength upon saturation binding. **Figure 3.60** shows typical luminescence titrations of **[2.15]** with CT-DNA.

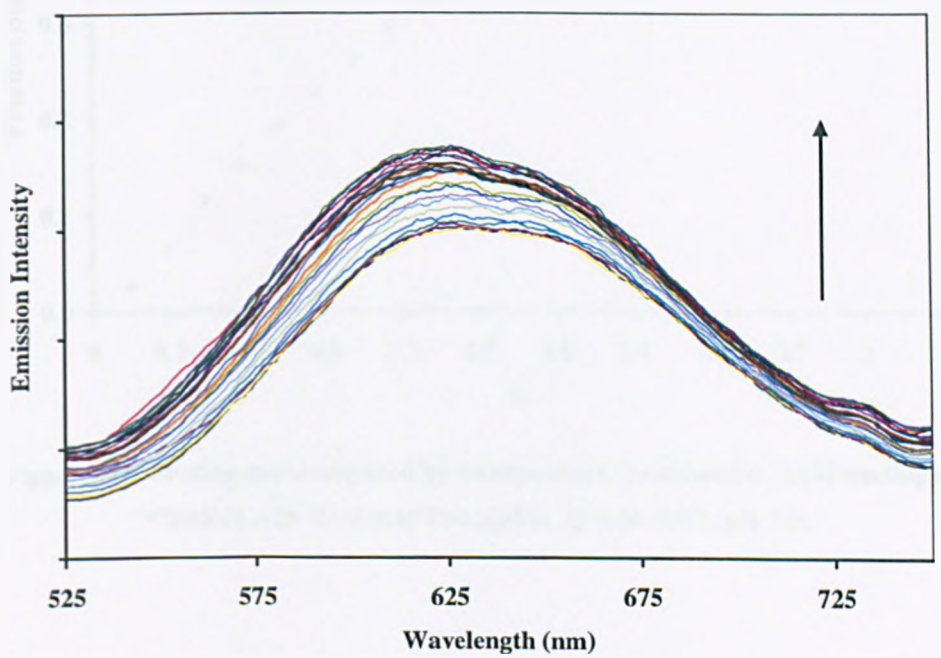

Figure 3.60: Luminescence titration of [2.15] with CT-DNA. (25 °C, 5 mM Tris buffer, 25 mM NaCl, pH 7.0).

Surprisingly, there is no emission for **[2.14]** in buffer solution and the emission was not switched on upon addition of CT-DNA. However, viscosity measurements established that this complex intercalates between the base pair of DNA and UV-Visible titrations indicate an affinity in the range of 10^5 M^{-1}.

The binding curve for the interaction of **[2.15]** with CT-DNA is shown in **Figure 3.61**. Once again, it shows that saturation binding has taken place. Binding parameters obtained from fits to the McGhee-von Hippel model[174] are summarised in **Table 3.8**. The Scatchard plot was constructed from the binding data between 30 % and 95 % fraction bound (**Figure 3.62**). The model fitted the data well and the R^2 value for the non-linear least squares fit was > 0.95.

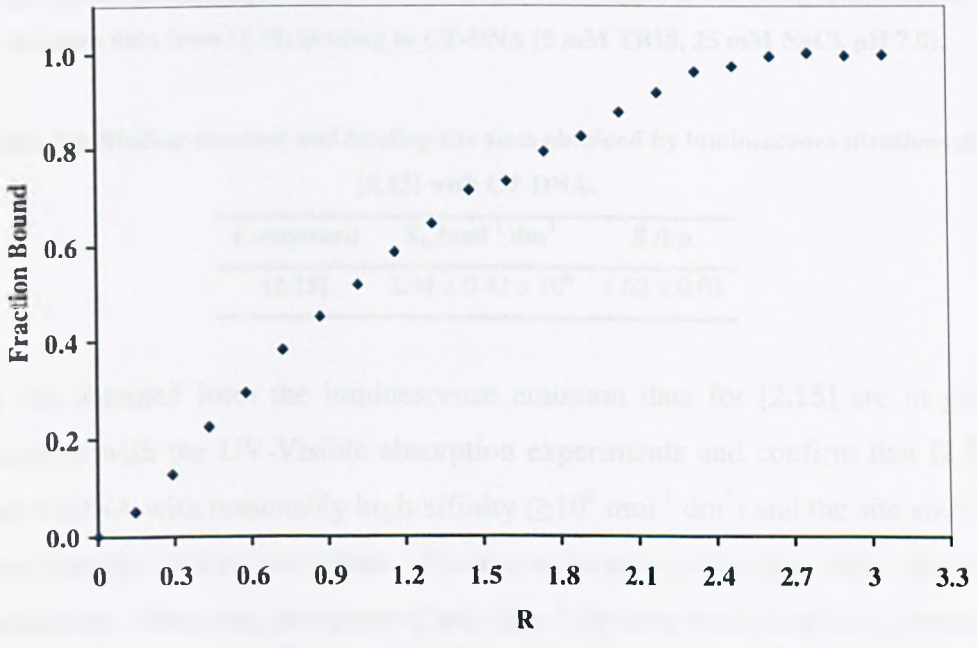

Figure 3.61: Binding curve obtained by luminescence titrations for [2.15] binding to CT-DNA. (25 °C, 5 mM Tris buffer, 25 mM NaCl, pH 7.0).

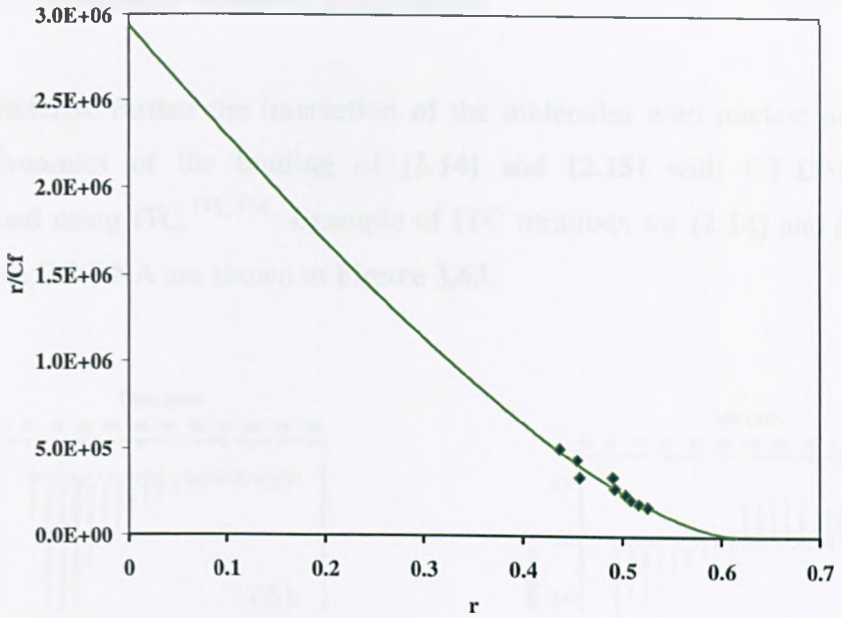

Figure 3.62: Scatchard plot fitted to the McGhee-von Hippel model using luminescence titration data from [2.15] binding to CT-DNA (5 mM TRIS, 25 mM NaCl, pH 7.0).

Table 3.8: Binding constant and binding site sizes obtained by luminescence titrations of [2.15] with CT-DNA.

Compound	K_b /mol^{-1} dm^3	S /bp
[2.15]	$2.94 \pm 0.42 \times 10^6$	1.62 ± 0.03

The fits obtained from the luminescence emission data for **[2.15]** are in good agreement with the UV-Visible absorption experiments and confirm that **[2.15]** binds to DNA with reasonably high affinity ($\geq 10^6$ mol^{-1} dm^3) and the site sizes of approximately 1.62 bp per ligand. The site sizes are smaller than those classical intercalators. However, site sizes of less than 1 bp have been frequently reported for other intercalators. This could results from some stacking of these complexes on the DNA surface.[194, 195]

3.5.5 Isothermal Titration Calorimetry

To characterise further the interaction of the molecules with nucleic acids, the thermodynamics of the binding of **[2.14]** and **[2.15]** with CT-DNA were determined using ITC.[175, 176] Example of ITC titrations for **[2.14]** and **[2.15]** at 25°C with CT-DNA are shown in **Figure 3.63**.

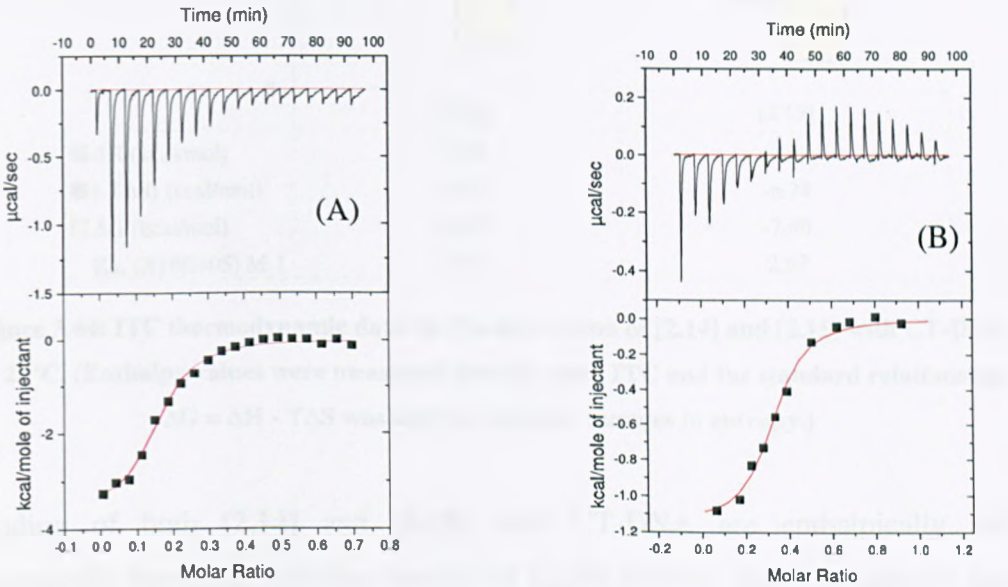

Figure 3.63: ITC raw data for the interaction of CT-DNA with; (A) [2.14] and (B) [2.15] in 5 mM Tris, 25 mM NaCl, pH 7.0 at 25°C.

The titration data for **[2.14]** and **[2.15]** were fitted to a one set of sites model, indicating one binding event. A comparison of the enthalpic and entropic contributions is summarised in **Figure 3.64**.

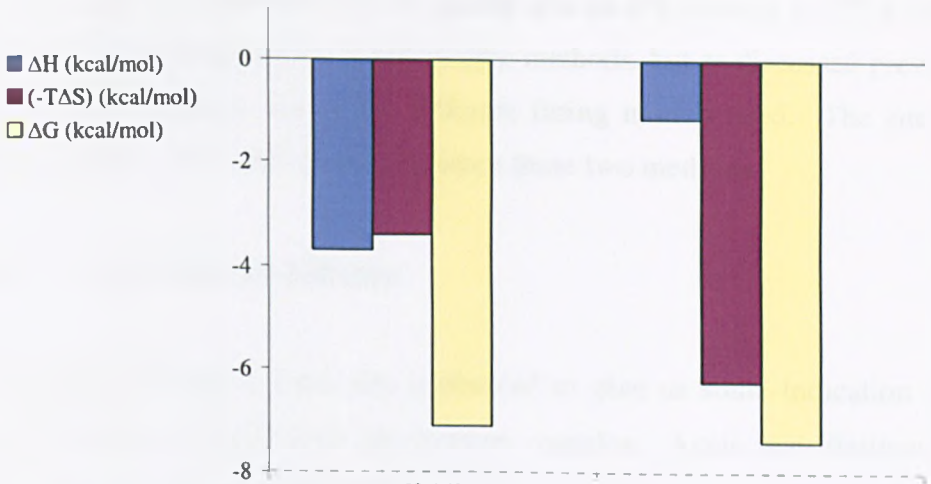

	[2.14]	[2.15]
ΔH (kcal/mol)	-3.70	-1.15
(-TΔS) (kcal/mol)	-3.40	-6.24
ΔG (kcal/mol)	-7.10	-7.40
Ka, (X10E+05) M-1	1.59	2.67

Figure 3.64: ITC thermodynamic data for the interaction of [2.14] and [2.15] with CT-DNA at 25°C. (Enthalpy values were measured directly using ITC and the standard relationship $\Delta G = \Delta H - T\Delta S$ was used to compute changes in entropy.)

Binding of both **[2.14]** and **[2.15]** with CT-DNA are enthalpically and entropically favoured, with the binding of **[2.14]** showing that the enthalpy and entropy is balanced. As mentioned previously, the negative ΔH obtained indicates that the complex is stabilised by hydrogen bonding as well as van der Waals interactions.[184] It is also typical for intercalation where stacking interactions with DNA base pairs stabilise the ligand-DNA complex. However, binding of **[2.15]** is dominated by the entropy term with a small (negative) favourable enthalpy terms. A favourable entropy term observed has probably resulted from changes in the hydration state of both the ligand and the DNA. Disruption of bound water from the ligand or the DNA binding site would result in an unfavourable enthalpy term but favourable entropy term. This may be one of the reasons why the net enthalpy change is smaller in magnitude than what might be otherwise expected for intercalators.

The K_bs obtained from the ITC for **[2.14]** and **[2.15]** binding to CT-DNA are lower than those obtained *via* spectroscopic methods, but as discussed previously this is to be expected, due to the different fitting models used. The site sizes unfortunately do not agree so well between these two methods.

3.5.6 Luminescence Lifetime

Lifetime measurements were also performed to give us some indication of the DNA binding interaction with the rhenium complex. Again, the lifetimes were recorded in the absence of CT-DNA and in the presence of saturated CT-DNA (saturation points were determined from the luminescence titration experiments). From the luminescence titration, we observed that the emission of **[2.14]** was not switched on upon titration with CT-DNA. Thus no luminescence lifetime with CT-DNA reported for this compound. On the other hand, the decay profiles for **[2.15]** fitted well to a monoexponential curve corresponding to one lifetime for this complex. When the binding ratio of [CT-DNA(bp)]/[Ru] varied from 0:1 to saturated:1, the excited-state lifetime increased from 20 ns to 142 ns. This different in the excited-state lifetime is visible in the emission intensity upon titration with DNA. The intercalation of the rhenium complex protects the excited state from a deactivating water protonation process, thus inducing emission.

3.6 Conclusions

This chapter reported studies on the interactions of **[2.6]**, **[2.7]**, **[2.8]**, **[2.9]**, **[2.10]**, **[2.11]**, **[2.14]** and **[2.15]** with duplex DNA. All complexes have been proven to bind to DNA *via* intercalation, which might be surprising because of the deceived lack of coplanarity of the qtpy ligand. Indeed, the binding affinities for these complexes are relatively high and comparable to those observed for many metallo-intercalators.

The binding thermodynamics of these complexes with DNA is different to the usual binding characteristics of metal complexes with DNA which are almost entirely entropically driven. The interactions of **[2.7]**, **[2.11]**, **[2.14]** and **[2.15]** with CT-DNA are unusual since binding is both entropically and enthalpically favourable. However, the binding of **[2.8]** is almost entirely enthalpically driven with the entropy change being unfavourable. This effect is also seen in the binding interaction of **[2.10]** with CT-DNA, with large changes in the enthalpy and small unfavourable entropy change. These observations can be exploited in the construction of future DNA binding systems and these studies also allow us to compare the binding characteristic of macrocyclic systems based on these building blocks.

4 Heterometallic Macrocycles

As outlined in Chapter 1, many research groups are currently studying the self-assembly of 2D and 3D geometrical structures such as squares, triangles *etc.* This chapter is concerned with the chemistry of self-assembled, kinetically locked metallomacrocycles based on precursor complexes that have been synthesised and characterised as described in the Chapter 2.

4.1 Synthetic Studies

4.1.1 RubpyRe macrocycle [4.1]

The RubpyRe macrocycle **[4.1]** (**Figure 4.1**) was prepared by refluxing equimolar amounts of $[Ru(bpy)_2(qtpy)][PF_6]_2$ **[2.8]** and $Re(CO)_5Cl$ in a 1:1 acetonitrile:THF solution for 48 hours. After this time, excess THF was added and the product precipitated out of solution as a red solid. This solid was collected *via* filtration, washed successively with THF and diethyl ether, then dried *in vacuo*. The red solid obtained was purified on a silica column, eluting with a 0.1:1:9 KNO_3:water:acetonitrile mixture. The product was obtained in 30 % yield and characterised by ^1H NMR, ES-MS spectroscopy and elemental analysis.

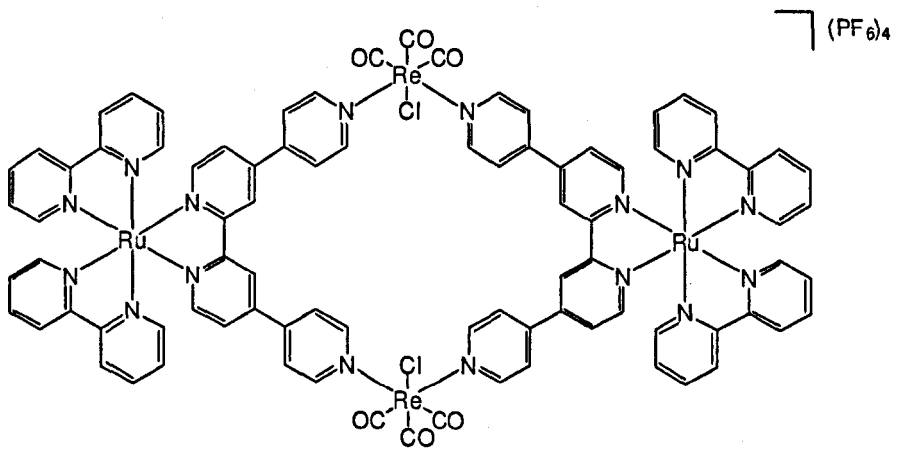

Figure 4.1: RubpyRe [4.1].

4.1.2 RuphenRe macrocycle [4.2]

RuphenRe **[4.2]** (**Figure 4.2**) was prepared in an analogous manner to **[4.1]**, except using $[Ru(phen)_2(qtpy)][PF_6]_2$ **[2.7]** in place of **[2.8]**. The crude product was purified by column chromatography on silica column, eluting with a 0.1:1:9 KNO_3:water:acetonitrile mixture to yield pure red coloured solid. The product was obtained in 45 % yield and characterised by ^1H NMR, ES-MS spectroscopy and elemental analysis.

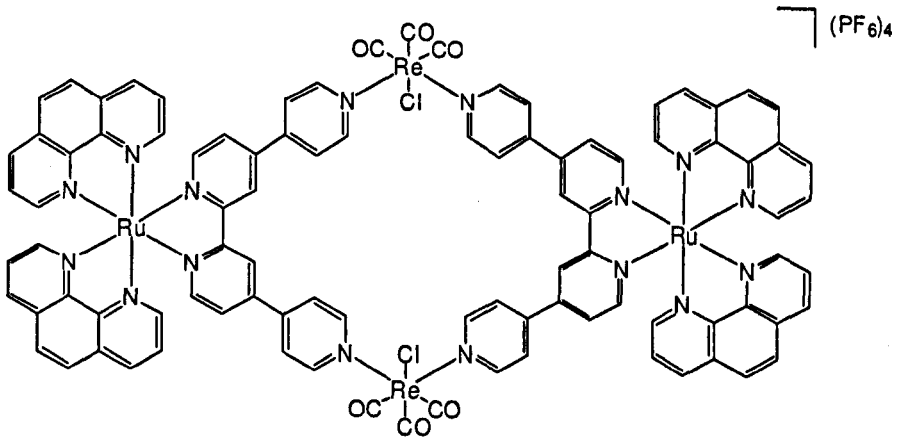

Figure 4.2: RuphenRe [4.2].

4.1.3 RudppzRe macrocycle [4.3]

RudppzRe **[4.3]** (**Figure 4.3**) was prepared in an analogous manner to **[4.1]**, except using $[Ru(dppz)_2(qtpy)][PF_6]_2$ **[2.6]** in place of **[2.8]**. The crude product was purified by column chromatography on silica column, eluting with a 0.1:1:9 KNO_3:water:acetonitrile mixture to yield pure red coloured solid. The product was obtained in 35 % yield and characterised by ^1H NMR, ES-MS spectroscopy and elemental analysis.

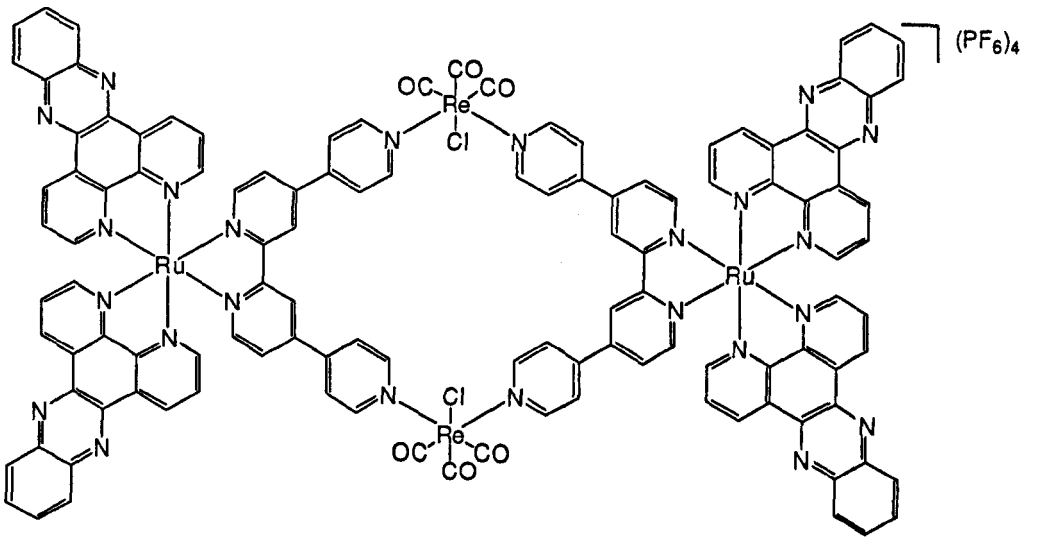

Figure 4.3: RudppzRe [4.3].

4.2 ^{1}H NMR Spectroscopic Studies

4.2.1 RubpyRe macrocycle [4.1]

Complex **[4.1]** have been characterised and were found to be consistent with previous report.[27, 28]

4.2.2 RuphenRe macrocycle [4.2]

The ^{1}H NMR spectrum of the RuphenRe macrocycle **[4.2]** in d^3-acetonitrile showed only the signals associated with the complex and no impurities. The downfield, aromatic region (**Figure 4.4**) is integrates to a total of 60 protons, which is consistent with the proposed structure **[4.2]**. The peak assignment was made with the aid of a ^{1}H-COSY NMR spectrum (**Figure 4.5**).

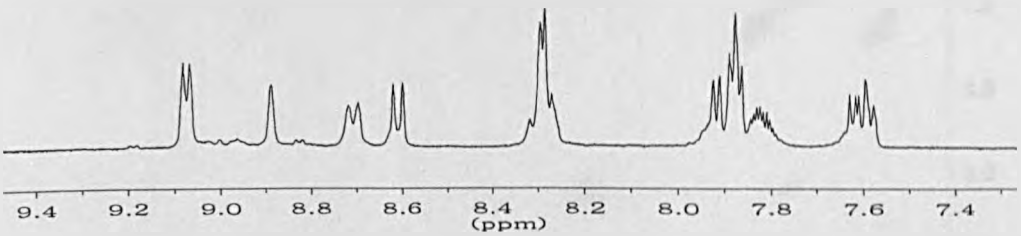

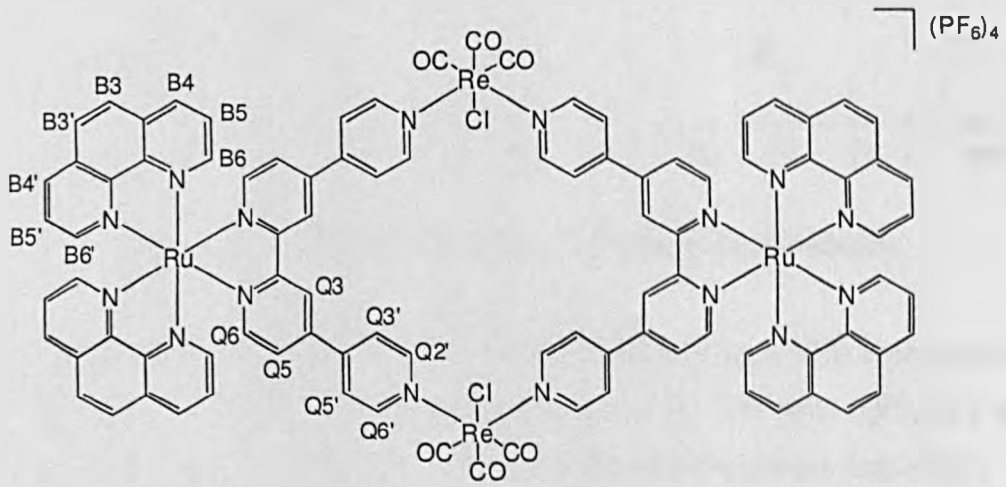

Figure 4.4: Downfield region of ^{1}H NMR spectrum of RuphenRe macrocycle in CD_3CN and proton labeling scheme.

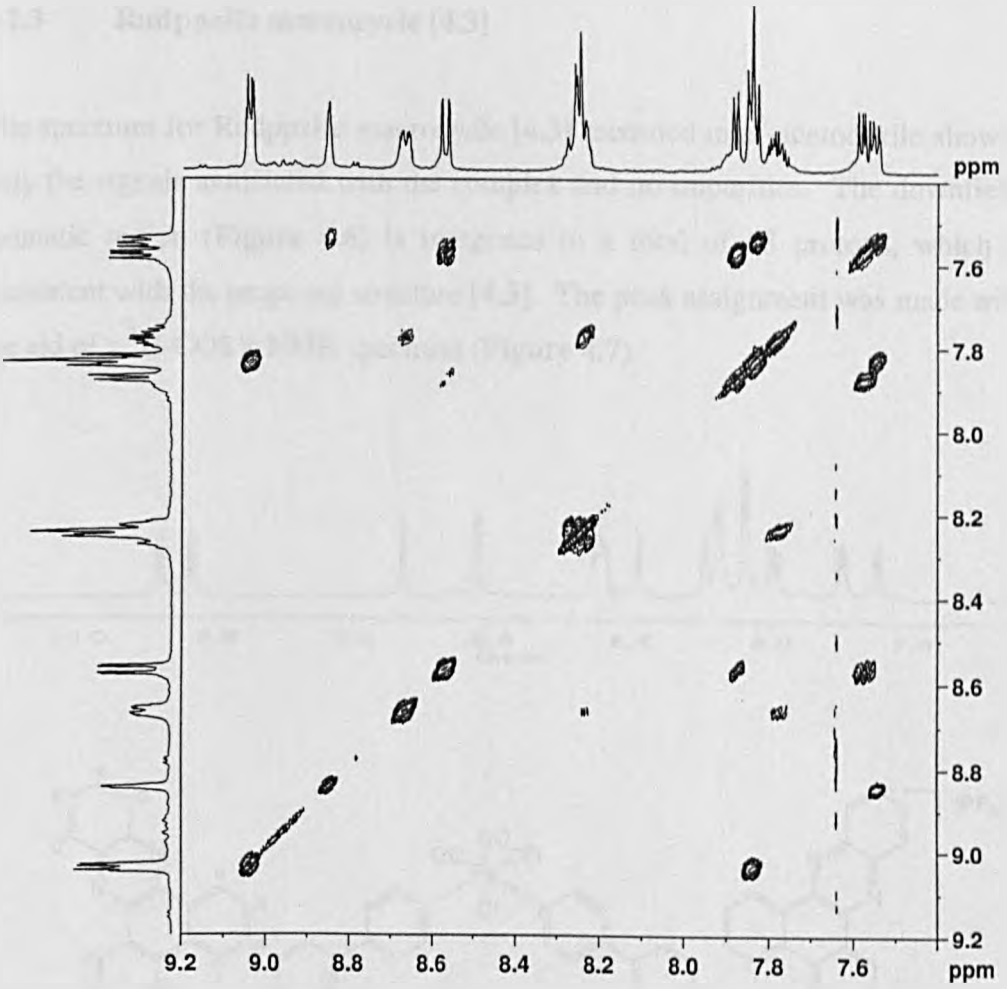

Figure 4.5: ^{1}H-COSY NMR spectrum of RuphenRe [4.2] in CD_3CN.

The signals at 7.59 ppm (Q5), 7.87 ppm (Q6) and 8.88 ppm (Q3) correspond to the protons on the inner qtpy rings, while those at 7.89 ppm (Q2',Q6') and 9.07 ppm (Q3',Q5') correspond to protons on the pendant pyridyl ring of qtpy.

As observed in the monomer, the signal for B3,B3' is split into two peaks with (B3) at 8.70 ppm while (B3') at 8.60 ppm. Protons corresponding to the protons of (B6), (B6'), (B5,B5'), (B4,B4') are located at 7.92 ppm, 7.61 ppm, 7.82 ppm and 8.28 ppm, respectively.

4.2.3 RudppzRe macrocycle [4.3]

The spectrum for RudppzRe macrocycle **[4.3]** recorded in d^3-acetonitrile showed only the signals associated with the complex and no impurities. The downfield, aromatic region (**Figure 4.6**) is integrates to a total of 68 protons, which is consistent with the proposed structure **[4.3]**. The peak assignment was made with the aid of a ^{1}H-COSY NMR spectrum (**Figure 4.7**).

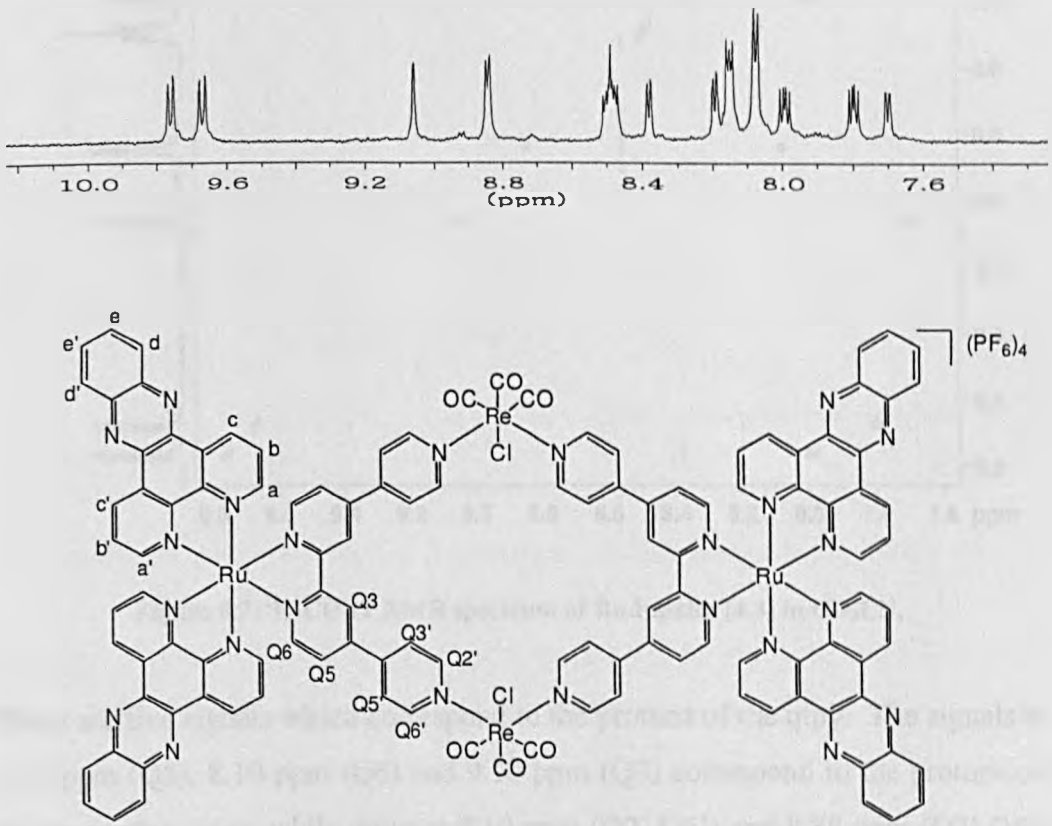

Figure 4.6: Downfield region of ^{1}H NMR spectrum of RudppzRe macrocycle in CD_3CN and proton labeling scheme.

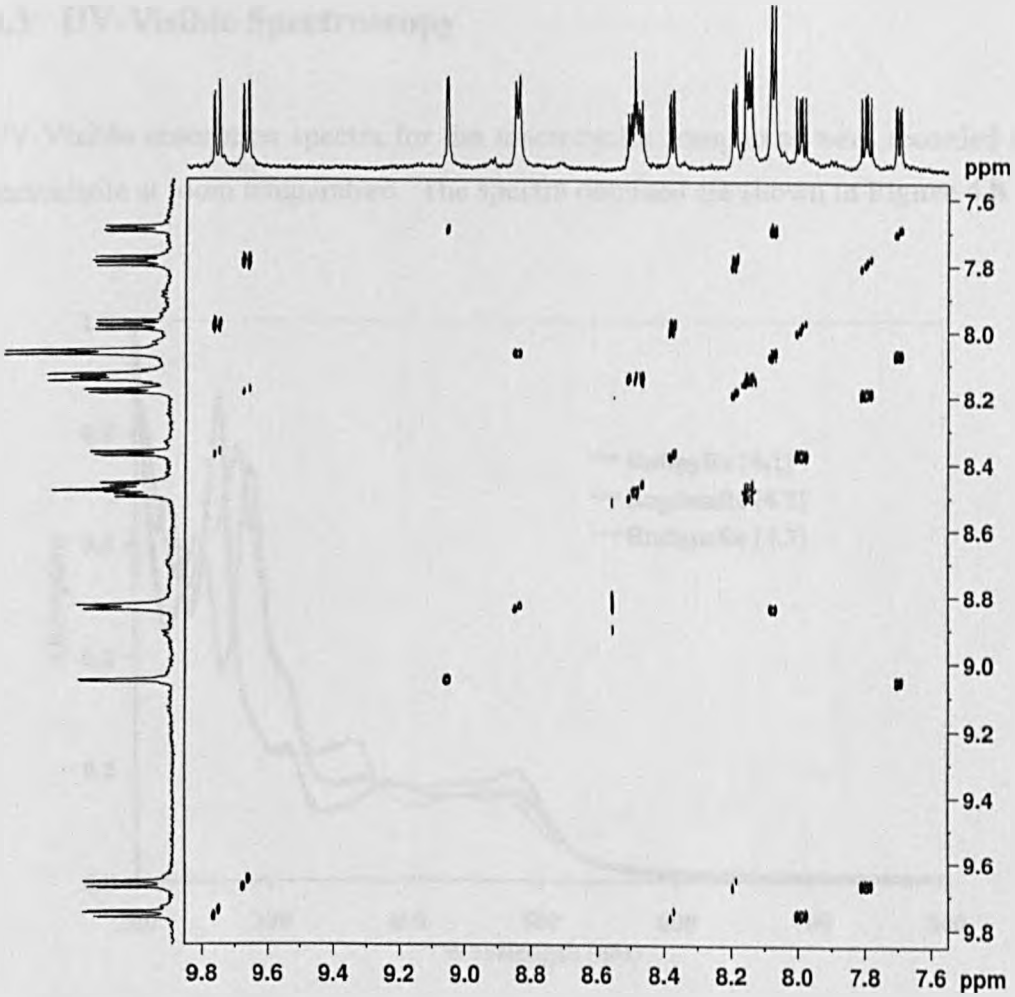

Figure 4.7: ^{1}H-COSY NMR spectrum of RudppzRe [4.3] in CD_3CN.

There are five signals which correspond to the protons of the qtpy. The signals at 7.74 ppm (Q5), 8.10 ppm (Q6) and 9.10 ppm (Q3) correspond to the protons on the inner qtpy rings, while those at 8.10 ppm (Q2',Q6') and 8.88 ppm (Q3',Q5') correspond to protons on the pendant pyridyl ring of qtpy. The signals correspond to dppz unit are quite complicated due to the inequivalence of the dppz units. The signals at 7.82 ppm (e'), 8.03 ppm (e), 8.19 ppm (b,b'), 8.23 ppm (d'), 8.40 ppm (d), 8.53 ppm (c,c'), 9.70 ppm (a') and 9.79 ppm (a) are assigned as dppz protons.

4.3 UV-Visible Spectroscopy

UV-Visible absorption spectra for the macrocyclic complexes were recorded in acetonitrile at room temperature. The spectra obtained are shown in **Figure 4.8**.

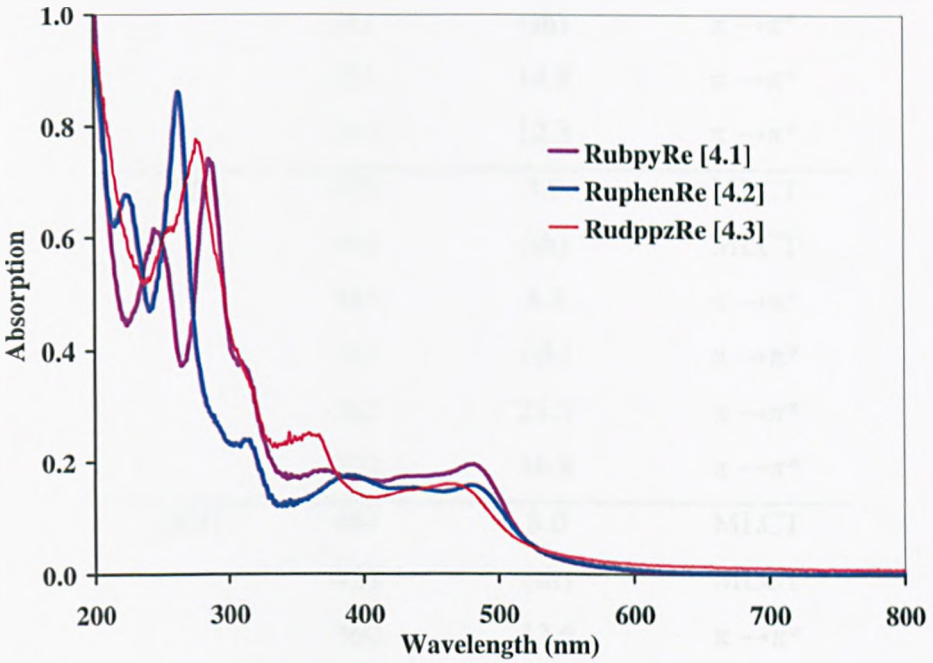

Figure 4.8: UV-Visible spectra of macrocyclic complexes recorded in acetonitrile.

The absorption spectra for **[4.1]** - **[4.3]** show high intensity, high energy bands around 200 - 350 nm which are consistent with intraligand $\pi \rightarrow \pi^*$ transitions, while the less intense bands between 350 and 550 nm are due to metal-to-ligand charge transfer (MLCT). These values are typical of other metal polypyridyl systems (**Table 4.1**).

Table 4.1: UV-Visible data for macrocyclic complexes.

Compound	λ_{max} (nm)	ε (10^4 $M^{-1}cm^{-1}$)	Assignation
[4.1]	480	3.9	MLCT
	425	(sh)	MLCT
	364	3.6	$\pi \rightarrow \pi^*$
	311	(sh)	$\pi \rightarrow \pi^*$
	285	14.8	$\pi \rightarrow \pi^*$
	244	12.3	$\pi \rightarrow \pi^*$
[4.2]	480	3.9	MLCT
	439	(sh)	MLCT
	385	4.3	$\pi \rightarrow \pi^*$
	311	(sh)	$\pi \rightarrow \pi^*$
	262	21.5	$\pi \rightarrow \pi^*$
	222	16.8	$\pi \rightarrow \pi^*$
[4.3]	467	8.0	MLCT
	432	(sh)	MLCT
	360	12.6	$\pi \rightarrow \pi^*$
	306	(sh)	$\pi \rightarrow \pi^*$
	277	38.5	$\pi \rightarrow \pi^*$
	253	30.5	$\pi \rightarrow \pi^*$

4.4 Luminescence Studies

Emission spectra for **[4.1] - [4.3]** complexes were recorded in acetonitrile and water at room temperature. **Figure 4.9** shows the emission spectra of macrocyclic complexes in acetonitrile. Both organic and aqueous solutions of these macrocyclic complexes display luminescence. Emission data are summarised in **Table 4.2**. Depending on the complex, excitation into the ^{1}MLCT at 480 nm results in ^{3}MLCT-based emission between 600 to 700 nm. While a comparison with analogous systems suggests that the emission is assigned from the Ru-MLCT manifold.[27]

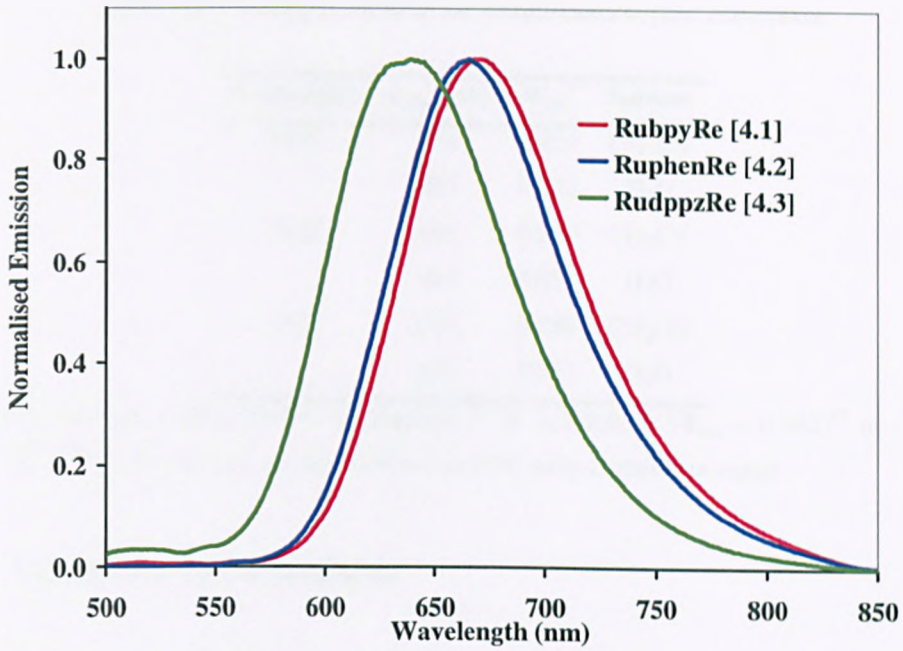

Figure 4.9: Emission spectra of macrocyclic complexes recorded in acetonitrile.

The emission for all the macrocyclic complexes in acetonitrile appears at substantially lower in energy compared to the mononuclear building blocks. Moreover, the quantum yields are also somewhat lower. The observed difference in excited-state energy can be readily attributed to the perturbation in the π^* orbital energy on the bridging ligand by the attachment of the second metal centers.

Earlier in this report, we observed that the building blocks for these macrocycles display weak emissions in water. Similarly, we observed that the emissions of the macrocycles **[4.1]**, **[4.2]** and **[4.3]** in water are weaker (Φ_{em} = 0.022, Φ_{em} = 0.021 and Φ_{em} = 0.001), respectively relative to $[Ru(bpy)_3]^{2+}$ (Φ_{em} = 0.042).[89] The luminescence characteristic of **[4.3]** depends significantly on the solvents. The emission is red shifted by about 11 nm upon changing the solvent from acetonitrile to water. The lower quantum yield and red shift in the emission of **[4.3]** upon changing the solvents indicate some participation of dppz located excited state.

Table 4.2: Luminescence data for metallomacrocyclic complexes.

Compound	λ_{max} (nm)	Φ_{em}[a]	Solvent
[4.1]	670	0.059	CH_3CN
	667	0.022	H_2O
[4.2]	666	0.050	CH_3CN
	664	0.021	H_2O
[4.3]	639	0.060	CH_3CN
	650	0.001	H_2O

[a]Emission quantum yields relative to $[Ru(bpy)_3]^{2+}$ in acetonitrile (Φ_{em} = 0.062)[87] or in water (Φ_{em} = 0.042).[89] All solutions are degassed and at 25°C unless otherwise stated.

4.5 Luminescence Lifetimes

Luminescence lifetimes for all the macrocyclic compounds were carried out in acetonitrile and water. Data are summarised in **Table 4.3**. RudppzRe **[4.3]** gave the longest lived lifetime (698 ns) in acetonitrile among the macrocyclic complexes, while the luminescence lifetime for **[4.1]** and **[4.2]** are 595 ns and 510 ns, respectively. In contrast to its Ru(II) building block, the trace obtained for **[4.3]** is monoexponential in both acetonitrile and water, suggesting that the nature of excited state differs from the monomer, **[2.6]**. Previously, we postulated that the excited states of **[2.6]** are at least partially localised on the dppz ligands. However, for **[4.3]** the excited state is presumably on the qtpy. Indeed, other reports suggest that the decrease in energy of the π^* orbital on the bridging ligand upon attachment of the second metal.[196, 197] This would indicate that the $Ru^{II} \rightarrow$ qtpy ^{3}MLCT is now at a lower energy compared to the alternative $Ru^{II} \rightarrow$ dppz-based excited state.

In all cases, the luminescence lifetimes obtained for the macrocyclic complexes in acetonitrile are shorter than the monomers. These observations correlate well with the substantial decrease in the quantum yields and the lower energy emission observed. This is consistent with either some quenching of the ^{3}MLCT excited state by Re(I) centre or the lower energy gap or both. On the other hand, the

lifetimes obtained for all the complexes in water were shorter. The fact that it is postulated that the lowest energy excited state is mainly located on the qtpy ligand is consistent with this observation: as the lifetime for the dppz containing macrocycle **[4.3]** is so not dramatically affected as happens to the monomer upon changing the solvent to water.

The radiative rate constants obtained for these complexes are in the range of 10^4 s^{-1} which is typical for Ru(II) or Re(I) polypyridyl complexes. The Energy Gap Law (EGL) for the non-radiative decay of excited state indicates that the non-radiative decay rate constant should decay exponentially with the increasing difference in energy between the emitting and ground state levels for a series of complexes in which the luminescent chromophore remains unchanged.[198] Our observations on this series of complexes correlate well with the EGL. Complex **[4.3]** has the smallest k_{nr}, consistent with the longest lifetimes, highest energy emission and highest emission quantum yields in acetonitrile within the series; while **[4.1]** and **[4.2]** have larger k_{nr}, with shorter lifetimes and lower energy emission and slightly lower emission quantum yields. We observed that the radiative rate constants for **[4.1]** and **[4.2]** are similar in both organic and aqueous solutions while the radiative rate constant for **[4.3]** is slightly lower, especially in water indicating some participation of excited state located on the dppz ligand.

Table 4.3: Luminescence lifetime data for macrocyclic complexes.

Compound	τ, ns	10^4 s^{-1}, k_r	10^4 s^{-1}, k_{nr}	Conditions[a]
[4.1]	595	9.9	158.2	CH_3CN
	491	4.5	199.2	H_2O
[4.2]	510	9.8	186.3	CH_3CN
	470	4.5	208.3	H_2O
[4.3]	698	8.6	134.7	CH_3CN
	170	1.2	587.0	H_2O

[a]All solutions are degassed and at 25 °C unless otherwise stated.

4.6 Electrochemistry Studies

The electrochemical properties of the hexafluorophosphate salts of **[4.1] - [4.3]** in acetonitrile were studied by cyclic voltammetry at a scan rate 100 mVs^{-1}, and all data were corrected for internal resistance using the AG&G Electrochemistry Power Suite software package. Data are summarised in **Table 4.4**.

Table 4.4: Electrochemical data for the metallomacrocyclic complexes.

Complex	Oxidation (V)	ΔE_p (mV)	Reduction (V)	ΔE_p (mV)
[4.1]	+1.51	70	-0.85[a]	-
	+1.65	80	-1.10	80
			-1.37	110
[4.2]	+1.50	70	-0.90[a]	-
	+1.63	80	-1.10	80
			-1.69[a]	-
[4.3]	+1.52	80	-0.89[a]	-
	+1.64	70	-1.20[a]	-

[a]Peak not fully chemically reversible, therefore only E_p is quoted.

Characteristic ligand-centered reductions were observed for each of the macrocycles. In all three complexes, the first reductions are chemically irreversible. Coordination of the rhenium metal centers results in a slight decrease in the energy of the LUMOs, as evidenced by the 200 - 260 mV shift of the first reduction of **[4.1]** and **[4.2]** to more positive potentials compared to the monomers. Such effect is likely to be absence for **[4.3]**. As mentioned previously, the first wave for **[2.6]**, which is the building block for **[4.3]** is presumably corresponds to the reduction of the dppz ligand. This might be the reason for the non-shifting of the first wave of **[4.3]**. Additionally, complexes **[4.1]** and **[4.2]** display a third reduction within the MeCN voltage window, which is chemically irreversible for **[4.2]**. No comparable reduction is observed for **[4.3]**. The cyclic voltammetric data suggest that the lack of reversibility for **[4.3]** may be caused by an increased tendency for adsorption owing to the large planar aromatic character of the dppz ligand.

All the macrocycles also display two close-lying chemically reversible oxidations at approximately 1.5 V and 1.6 V (**Figure 4.10**). The first waves are consistent with Ru(III)/Ru(II)-based couples, while the second waves observed for these complexes attributed to the simultaneous oxidation of the rhenium(I) centers. It is postulated that the interaction between the adjacent redox active metal centers results a separation between Ru(III)/Ru(II) and Re(II)/Re(I) couples.[27] In all cases, the signals for Ru-based couples are anodically shifted by > 100 mV with respect to the Ru(III)/(II) couple for the ruthenium building blocks.

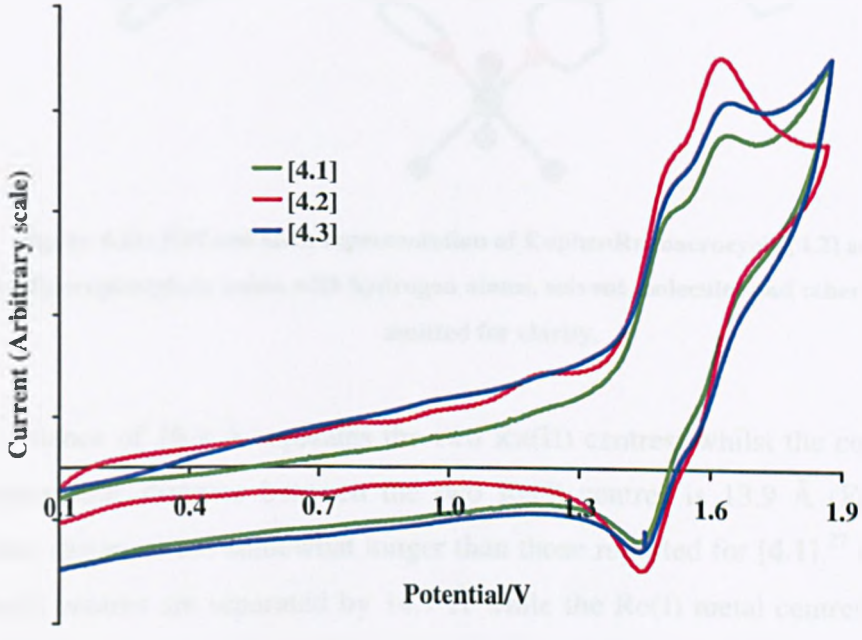

Figure 4.10: Electrochemical cyclic voltammogram for the oxidations of metallomacrocycles [4.1], [4.2] and [4.3].

4.7 X-Ray Crystallography Studies

The structure of **[4.1]** has been reported[27] previously. X-ray quality crystals of RuphenRe macrocycle **[4.2]** were grown *via* vapour diffusion of benzene into a nitromethane solution of the complex. Although the refinement is not of sufficient quality to determine bond lengths and angles with accuracy, it confirms

the connectivity and overall geometry of the macrocycle. The crystal structure (**Figure 4.11**) shows that all metal centres possess octahedral geometries with the quaterpyridyl ligand binding in a bidentate fashion to the Ru(II) metal centres and in a monodentate fashion to the Re(I) metal centres.

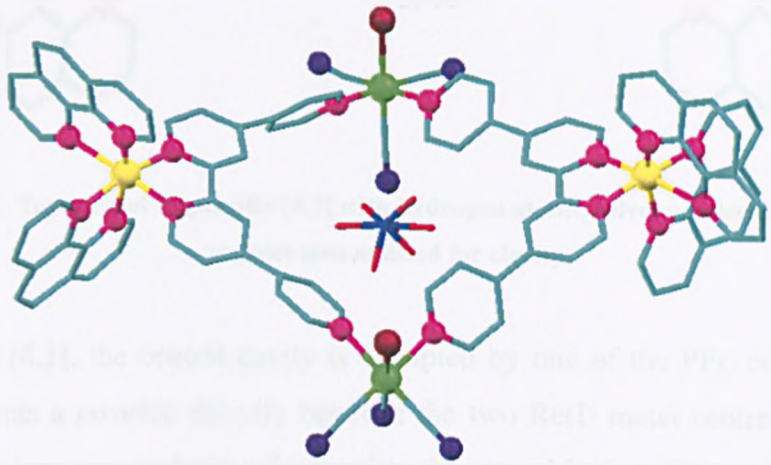

Figure 4.11: Ball and stick representation of RuphenRe macrocycle [4.2] and bound hexafluorophosphate anion with hydrogen atoms, solvent molecules and other counter ions omitted for clarity.

A distance of 16.9 Å separates the two Ru(II) centres, whilst the corresponding intermetallic distance between the two Re(I) centres is 13.9 Å (**Figure 4.12**). These distances are somewhat longer than those reported for **[4.1]**,[27] with the two Ru(II) centres are separated by 14.7 Å while the Re(I) metal centres are located 13.1 Å from one another. This is interesting as it suggests a few possibilities for inducing a bigger separation between the Ru(II) metal centres. One possible explaination is due to bulkier phen ligand compare to bpy in **[4.1]**, thus resulting flexibility in the structure which induce that conformation obtained for **[4.2]**. Besides, it could be due to steric repulsion between hydrogen atoms on neighbouring pyridine rings of the qtpy. The pyridine rings will also twist slightly out of plane to limit this repulsion.

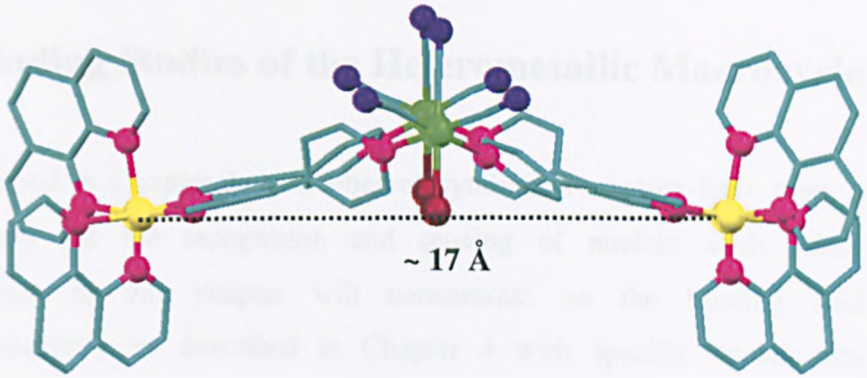

Figure 4.12: Top view of RuphenRe [4.2] with hydrogen atoms, solvent molecules and other counter ions omitted for clarity.

Similar to **[4.1]**, the central cavity is occupied by one of the PF_6^- counter ions, which adopts a position directly between the two Re(I) metal centres while the other three ions are randomly displaced in the crystal lattice (**Figure 4.11**). This is of interest as energy may be needed to displace the ion in order to allow binding processes with other anions.

4.8 Conclusions

The spectroscopic and photophysical behavior of this series of metallomacrocycles complexes differs significantly from that of their monometallic counterparts (Chapter 2). As expected, much of the difference results from the perturbation of the π^* orbital energy on the bridging ligand by attachment of the second metal center. Following initial studies into the synthesis and coordination of the metallomacrocycles, further work in this area will be exploring their properties as devices such as hosts and sensors for a variety of biomolecules in aqueous environment. Specific nucleic acids will also be investigated.

5 Binding Studies of the Heterometallic Macrocycles

As outlined in Chapter 1, a number of synthetic receptors have been reported previously for the recognition and sensing of nucleic acids constituents. Discussion in this chapter will concentrate on the binding studies of metallomacrocycles described in Chapter 4 with specific nucleic acids and nucleosides.

5.1 Anion Binding Studies

Previous work with **[4.1]** has revealed that titration of polyaromatic molecules such as 1,4-dimethoxybenzene and 1-naphthol into aqueous solutions of **[4.1]** results in large changes in the absorption spectra of the macrocycle.[28] Whilst the recognition process in water has no effect on the luminescence output of the macrocycle, anion binding in organic solvents results in enhancements of ^{3}MLCT emission, with binding constants in the range of 10^3 M^{-1}.[27] Given these facts, we decided to investigate the interaction of **[4.1]** - **[4.3]** with selected biological anions in water.

5.1.1 Materials and Methods

The heterometallic macrocycles referred to in this section were studied as their chloride salts.

Adenine, adenosine-5'-triphosphate (ATP), guanosine-5'-triphosphate (GTP), cyclic guanosine-3',5'-monophosphate (cGMP) and uridine were purchased from Sigma-Aldrich and used without further purification. Water was doubly distilled before use.

5.1.2 Luminescence Titration Protocol

A stock solution of appropriate macrocyclic host was prepared in doubly distilled water such that its concentration was approximately 10^{-6} M. A stock solution of the appropriate guest was also prepared in doubly distilled water such that its concentration was approximately 10^{-3} M. The luminescence spectra were recorded ranging from 0 M concentration of guest until saturation binding takes place (no more changes in the integrated intensity of host + guest). The solution was left to equilibrate for 10 minutes before each spectrum was recorded.

5.1.3 UV-Visible Titration Protocol

A stock solution of appropriate macrocyclic host was prepared in doubly distilled water such that its concentration was approximately 10^{-6} M. The solution was left to equilibrate for 10 minutes before a spectrum was recorded. During the titration, an equimolar host containing guest at a known concentration of approximately 10^{-3} M was added to the sample cell. In the reference cuvette, an equivalent titre of a solution containing guest at an equimolar concentration was added. The absorption spectra were recorded ranging from 0 M concentration of guest until saturation binding takes place (no more changes in the absorption spectra of host + guest).

5.1.4 Results and Discussion

5.1.4.1 UV-Visible Titrations

The binding and sensing properties of **[4.1]**, **[4.2]** and **[4.3]** with various biological anions were investigated by UV-Visible titrations. Example of systematic changes in the electronic spectra upon the addition of aqueous adenine solution to the aqueous solution of **[4.2]** is shown in **Figure 5.1.**

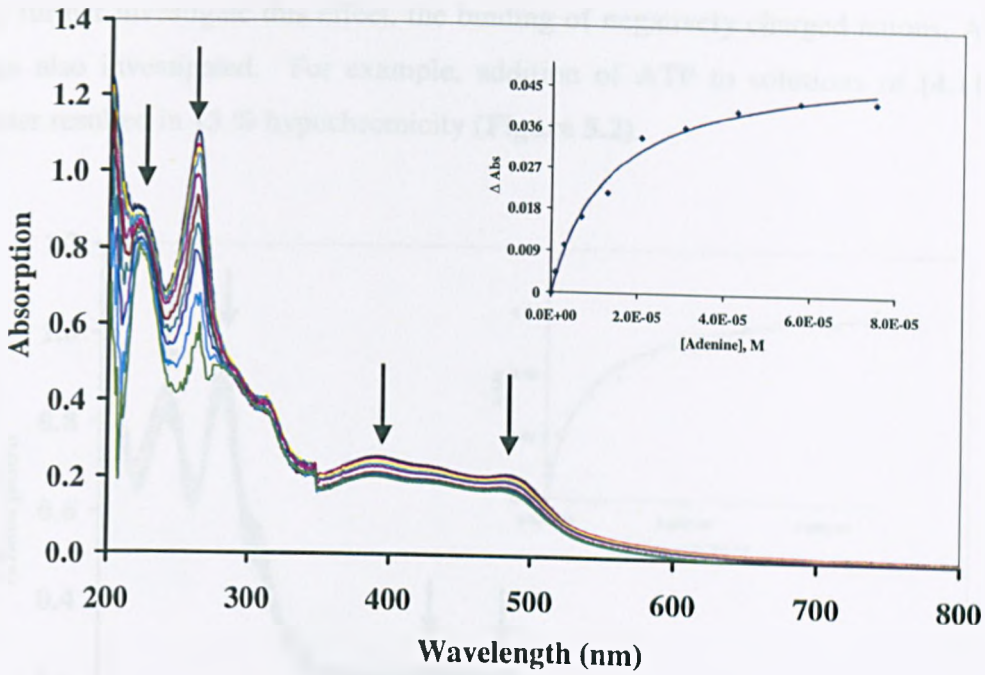

Figure 5.1: UV-Vis titration of [4.2] (5.0×10^{-6} M) in aqueous solution with adenine. Inset: Corresponding titration profile.

It was found that, although there was no red shift, titration of adenine into aqueous solution of **[4.1]**, **[4.2]** and **[4.3]** led to a progressive hypochromicity in absorptions of the host macrocycles. Estimates of binding affinities were obtained through fits of the changes in absorption to a 1:1 binding model (**Table 5.1**). Macrocycles **[4.1]**, **[4.2]** and **[4.3]** show binding affinities of 4.6×10^4 M^{-1}, 7.1×10^4 M^{-1} and 1.57×10^5 M^{-1}, respectively towards adenine. The observed binding affinity of **[4.1]**, **[4.2]** and **[4.3]** with adenine in pure water is comparable with a receptor[57] that selectively discriminates adenine over other nucleobases in CH_3CN/H_2O (95:5, v/v) solution. This receptor binds adenine through a complementary hydrogen bonding between the receptor and adenine, which is absence in our systems. In addition, most of receptors[199] reported for adenine sensing are restricted in the recognition of adenine in non-polar organic solvents due to limited solubility of adenine in water. Interestingly, the macrocycles **[4.1]**, **[4.2]** and **[4.3]** have demonstrated the capability to recognise this nucleobase in the range of micromolar in aqueous solution.

To further investigate this effect, the binding of negatively charged anions, ATP was also investigated. For example, addition of ATP to solutions of **[4.1]** in water resulted in 13 % hypochromicity (**Figure 5.2**).

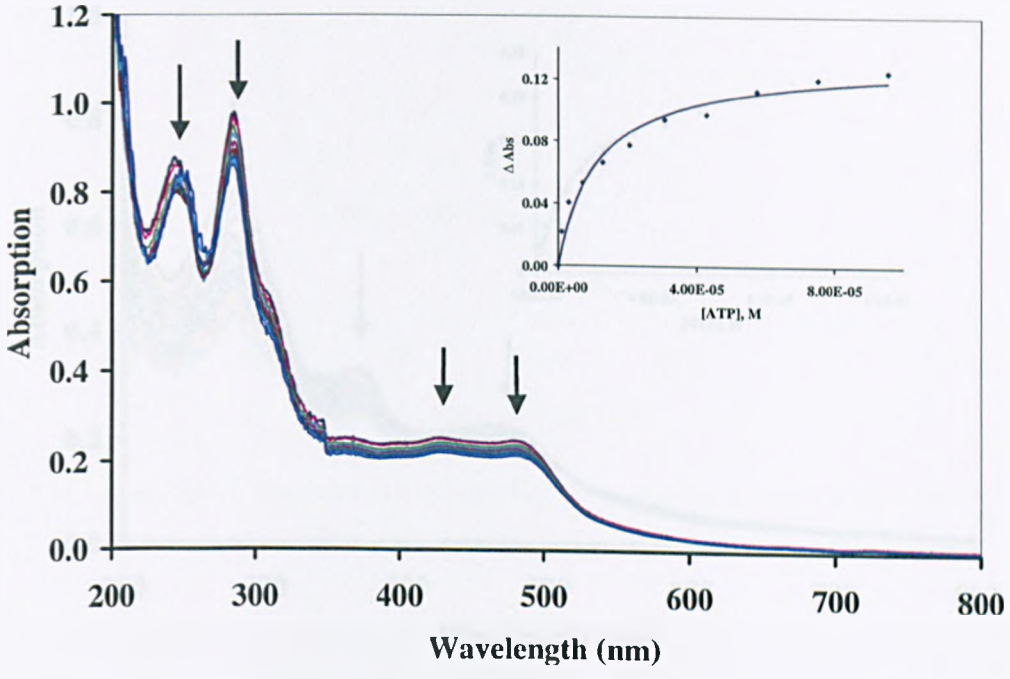

Figure 5.2: UV-Vis titration of [4.1] (5.0×10^{-6} M) in aqueous solution with ATP. Inset: Corresponding titration profile.

Addition of ATP to aqueous solutions of **[4.1]**, **[4.2]** and **[4.3]** also result in hypochromicity in the absorption of the host macrocycles. The binding constants obtained for **[4.1]**, **[4.2]** and **[4.3]** are 8.9×10^4 M^{-1}, 1.32×10^5 M^{-1} and 1.32×10^5 M^{-1}, respectively. These results suggest no discrimination between neutral nucleobase (adenine) with the negatively charge nucleotide (ATP). However, these values are comparable to other receptors reported for the recognition of ATP, binding through electrostatic, π-stacking or metal-ligand interactions with the binding affinity on the order of 10^5 M^{-1} in water.[43, 44, 45]

We also investigated the host-guest interaction of these macrocycles with GTP. For example, titration of GTP to aqueous solutions of **[4.3]** resulted in a more pronounced hypochromicity (41%) in the UV-Visible spectra of the host

(**Figure 5.3**). The binding constants for **[4.1]**, **[4.2]** and **[4.3]** are 3.7 x 10^4 M^{-1}, 6.2 x 10^4 M^{-1} and 5.9 x 10^4 M^{-1}, respectively; in the range of those observed in literature for other hosts.[49, 50]

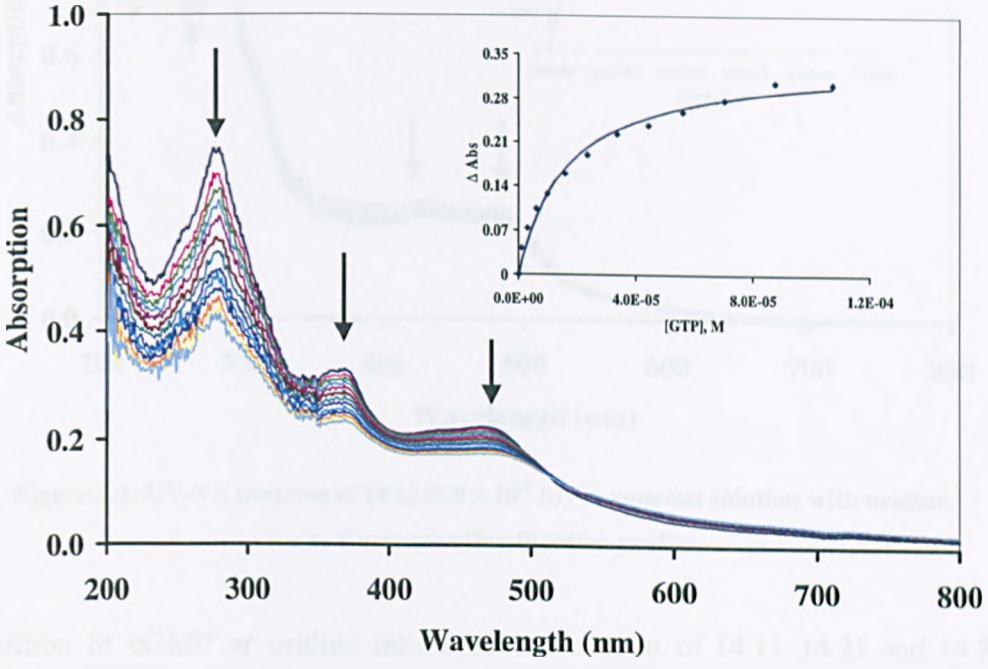

Figure 5.3: UV-Vis titration of [4.3] (4.0 x 10^{-6} M) in aqueous solution with GTP. Inset: Corresponding titration profile.

Spectrophotometric titrations were also carried out for **[4.1]** - **[4.3]** using cGMP and uridine as the anionic analytes. Example of titration profile of **[4.1]** with uridine is shown in **Figure 5.4**.

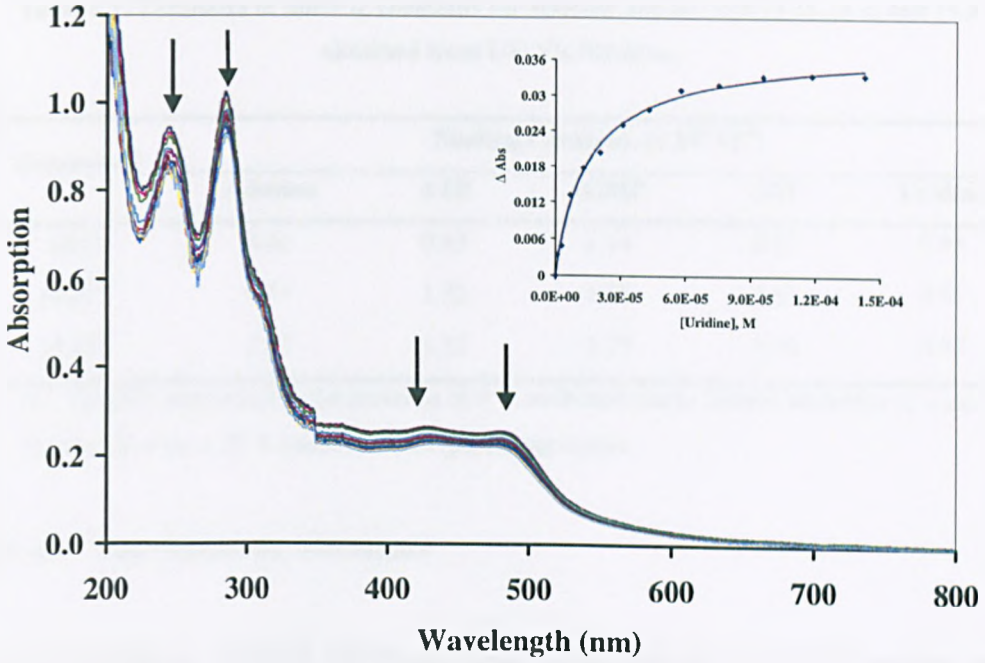

Figure 5.4: UV-Vis titration of [4.1] (5.0×10^{-6} M) in aqueous solution with uridine. Inset: Corresponding titration profile.

Addition of cGMP or uridine into aqueous solution of **[4.1]**, **[4.2]** and **[4.3]**, respectively also results in similar changes, with band around 200 nm to 550 nm showing a high degree of hypochromicity. The binding constants for the interactions of these macrocycles with cGMP are found to be 1.14×10^5 M^{-1}, 1.06×10^5 M^{-1} and 1.75×10^5 M^{-1}, respectively. These values show that binding of a cyclic nucleotide monophosphate are generally of the same order to that of the nucleotides triphosphates, ATP and GTP. On the other hand, titrations of host complexes **[4.1]**, **[4.2]** and **[4.3]** with uridine revealed the binding constants of 6.5×10^4 M^{-1}, 9.1×10^4 M^{-1} and 8.2×10^4 M^{-1}, respectively. The strikingly small affinity differences observed between neutral adenine to nucleoside (uridine), cyclic nucleotide monophosphate (cGMP) and the nucleotides triphosphates (ATP and GTP) emphasise the paramount importance of stacking forces over electrostatic contribution.

Table 5.1: Estimates of binding constants for selected anions with [4.1], [4.2] and [4.3] obtained from UV-Vis titration.

Compound	Binding Constant, (x 10^5 M^{-1})				
	Adenine	ATP	cGMP	GTP	Uridine
[4.1]	0.46	0.89	1.14	0.37	0.65
[4.2][(a)]	0.71	1.32	1.06	0.62	0.91
[4.3][(a)]	1.57	1.32	1.75	0.59	0.82

(a) Titration performed in the presence of 5 % methanol due to limited solubility in water. Estimated error ± 20 % based on five repeat experiments.

5.1.4.2 Luminescence Titrations

The interactions of **[4.1]**, **[4.2]** and **[4.3]** with various biological anions were further investigated by luminescence spectroscopy in aqueous solutions. Data are summarised in **Table 5.2.**

Gradual addition of cGMP into host solution of **[4.1]** resulting in 53 % quenching of the emission intensity of the respective host (**Figure 5.5**). The quenching mechanism of this guanine nucleotide is most probably based on photoinduced electron transfer.[200] However, titration of **[4.1]** with adenine did not give rise to significant progressive emission enhancement/quenching. Job plot analyses using luminescence spectroscopy showed that **[4.1]** formed 1:1 stoichiometric complexes with ATP, GTP, cGMP and uridine, respectively. Since **[4.1]** did not give a significant emission enhancement/quenching response with adenine, the Job plot was carried out using UV-Visible spectroscopy. This Job plot indicates that the host complex **[4.1]** also formed 1:1 stoichiometric complexes with adenine.

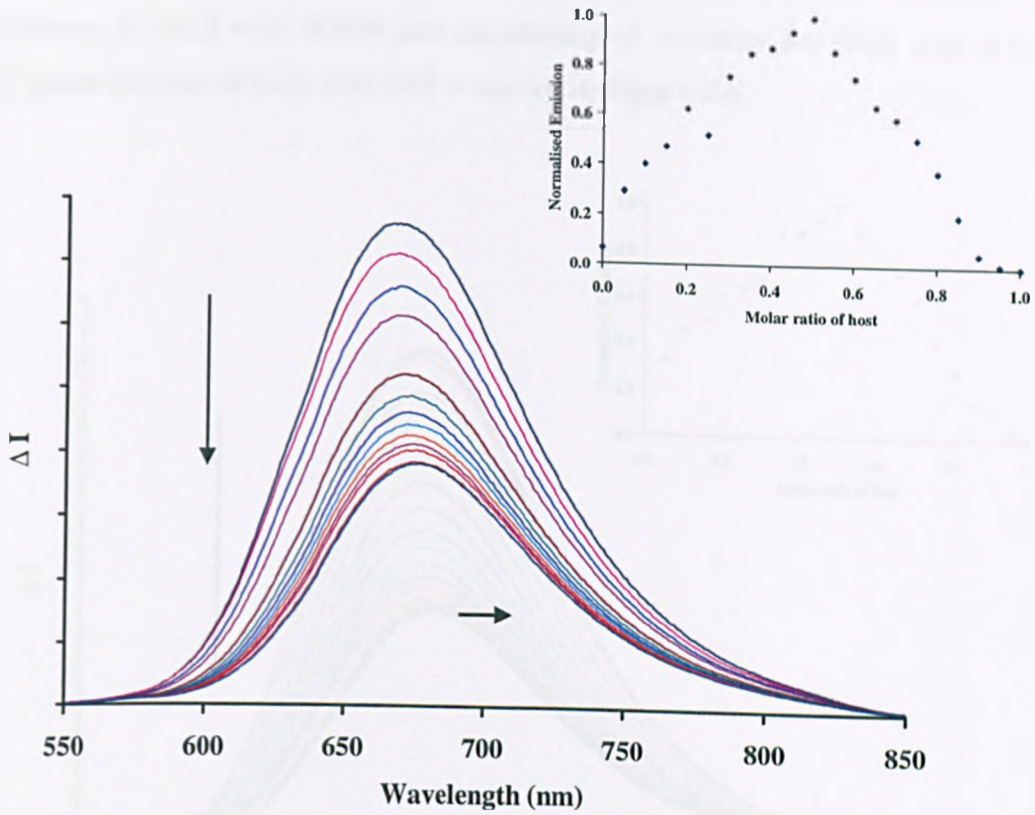

Figure 5.5: Luminescence titration of [4.1] (5.0×10^{-6} M) in aqueous solution with cGMP. The inset shows the Job plot of [4.1] and cGMP.

The binding constants of **[4.1]** with ATP, GTP, cGMP and uridine as determined by fitting the titration data into 1:1 binding model using luminescence data are 6.18×10^3 M^{-1}, 4.87×10^3 M^{-1}, 2.08×10^3 M^{-1} and 3.66×10^3 M^{-1}, respectively. These values were 15 - 20 times lower than those obtained from absorption titrations. Upon saturation binding, the emission wavelength of **[4.1]** is red shift by about 7 nm for the interaction of **[4.1]** with ATP and cGMP, respectively. In contrast, a 7 nm blue shift is observed for the interaction of **[4.1]** with uridine and no shifting for the interaction of **[4.1]** with GTP.

Emission quenching was also observed upon titration of the metallomacrocycle **[4.2]** with various anions. Similar to **[4.1]**, titration of **[4.2]** with adenine did not give rise to significant progressive emission enhancement/quenching. Titrations

of aqueous solutions of GTP and uridine results in blue-shifted of the λ_{em} of **[4.2]** by about 6 nm upon saturation binding; while red-shifted of 5 nm is observed for titration of **[4.2]** with cGMP and no shifting of emission for **[4.2]** with ATP. Typical titration of **[4.2]** with ATP is shown in **Figure 5.6**.

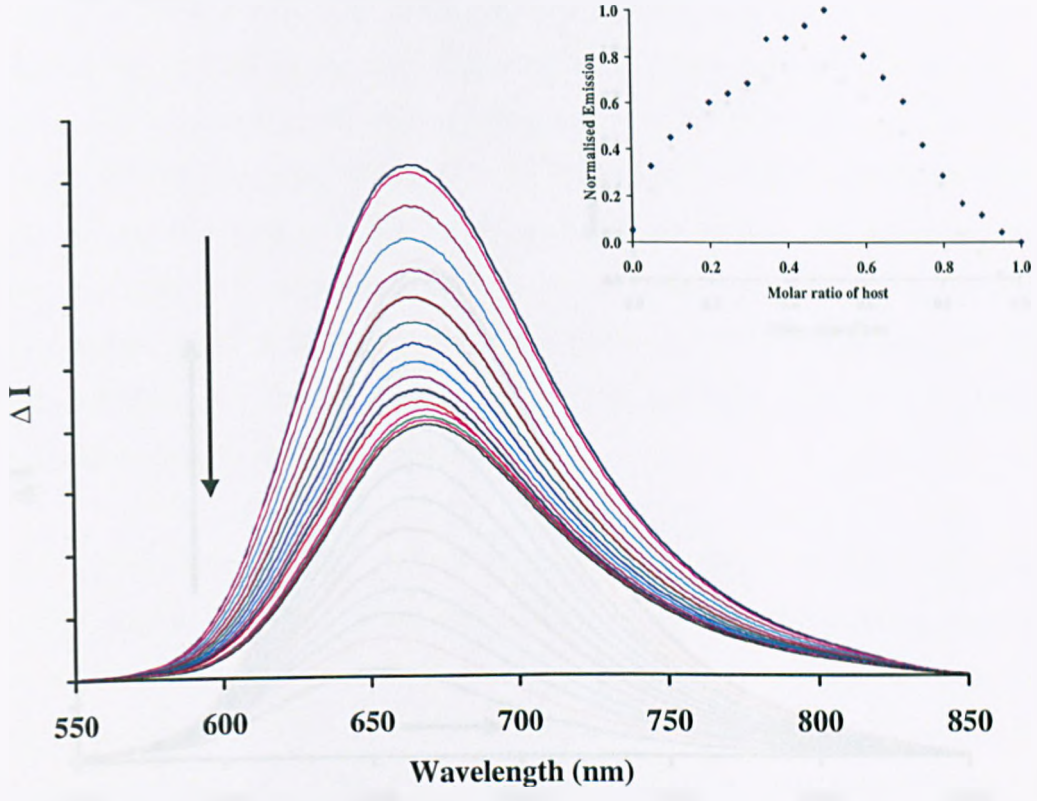

Figure 5.6: Luminescence titration of [4.2] (5.0 x 10^{-6} M) in aqueous solution with ATP. The inset shows the Job plot of [4.2] and ATP.

The binding affinities of **[4.2]** towards all the anions are similar to those obtained for **[4.1]**. The binding constants between **[4.2]** with uridine, ATP, GTP and cGMP are found to be 1.16 x 10^4 M^{-1}, 1.04 x 10^4 M^{-1}, 8.64 x 10^3 M^{-1} and 7.60 x 10^3 M^{-1}, respectively. These values were 7 - 17 times lower than those obtained from absorption titrations; however in each case the titrations reach saturation. Job plots experiments carried out using luminescence spectroscopy (except for **[4.2]**-adenine by UV-Vis spectroscopy) indicate that in all cases, **[4.2]** formed 1:1 complexes with the guests.

On the other hand, upon titration of **[4.3]** with the various biological anions, only ATP, cGMP and uridine gave rise to significant emission enhancement. Also, only titrations of ATP and cGMP into solutions of **[4.3]** result in a red-shift of emission wavelength by about 19 nm and 14 nm, respectively. A typical titration of **[4.3]** with cGMP is shown in **Figure 5.7**.

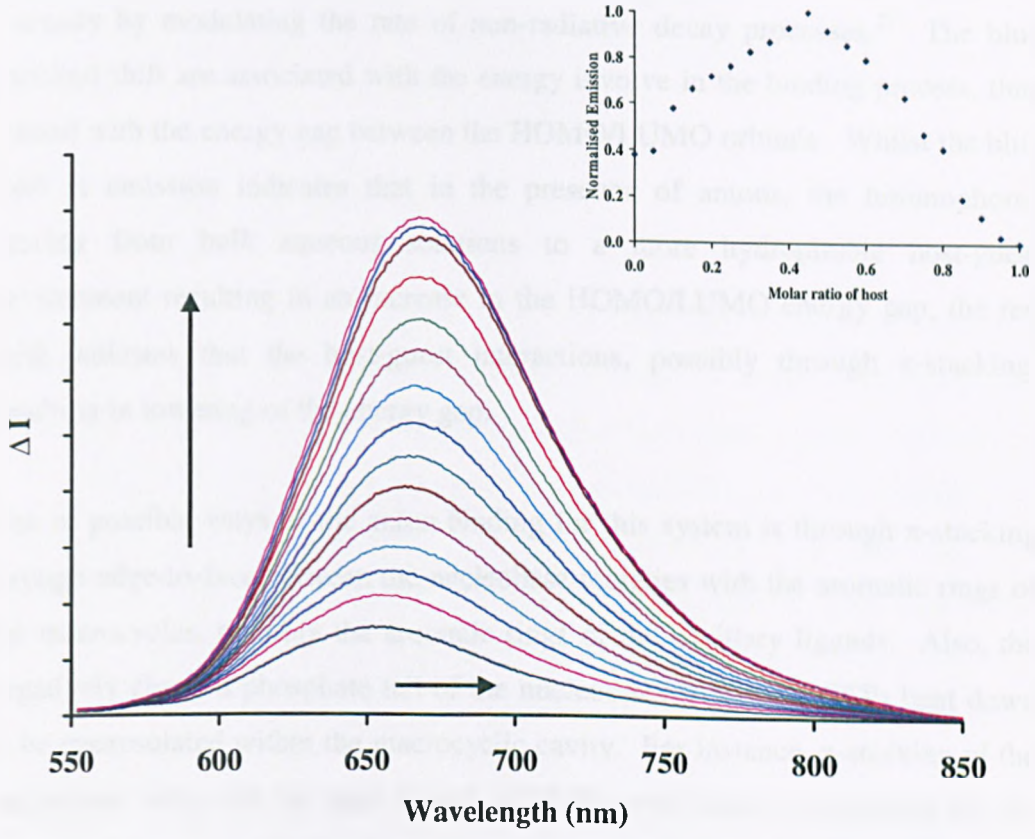

Figure 5.7: Luminescence titration of [4.3] (5.0×10^{-6} M) in aqueous solution with cGMP. The inset shows the Job plot of [4.3] and cGMP.

The binding constants for ATP, cGMP and uridine in a 1:1 binding stoichiometry (which were further confirmed by the Job plots) are 9.58×10^3 M^{-1}, 1.22×10^3 M^{-1} and 2.67×10^3 M^{-1}, respectively, as estimated by a 1:1 binding model. Since **[4.3]** did not give significant emission enhancement/quenching with adenine and GTP, the Job plots were carried out using UV-Visible spectroscopy and indicated that the host complex **[4.3]** formed 1:1 stoichiometric complexes with both bases.

The emission changes observed during the host-guest interactions involving the metallomacrocycles **[4.1]** - **[4.3]** and the selected biological anions are postulated to be due to modulations in the torsion angles between aromatic rings in the bridging ligand, qtpy. The accommodation of guests within the macrocycles binding pockets results in a conformational change, thus affect the emission intensity by modulating the rate of non-radiative decay processes.[27] The blue shift/red shift are associated with the energy involve in the binding process, thus related with the energy gap between the HOMO/LUMO orbitals. Whilst the blue shift in emission indicates that in the presence of anions, the luminophores moving from bulk aqueous solutions to a more hydrophobic host-guest environment resulting in an increase in the HOMO/LUMO energy gap, the red shift indicates that the host-guest interactions, possibly through π-stacking, resulting in lowering of the energy gap.

One of possible ways of the anion binding for this system is through π-stacking through edge-to-face between the nucleobase moieties with the aromatic rings of the macrocycles, possibly the aromatic rings of the ancillary ligands. Also, the negatively charged phosphate tail of the nucleotides (ATP and GTP) bent down to be encapsulated within the macrocyclic cavity. For instance, π-stacking of the nucleobase units with the dppz ligands of **[4.3]** would serve as protection for the phenazine nitrogen of the dppz ligands from hydrogen bonded with water molecules, thus resulting in enhancement of the emission intensity of **[4.3]**, as what being observed in the luminescence titrations of **[4.3]** with ATP, cGMP and uridine. Besides, there might be some other non-specific interactions, for example electrostatic charge-charge attractions involve in the host-guest system.

Table 5.2: Estimates of binding constants for selected anions with [4.1], [4.2] and [4.3] obtained from luminescence titration.

Compound	Binding Constant, (x 10^3 M^{-1})				
	Adenine	ATP	cGMP	GTP	Uridine
[4.1]	-	6.18	4.87	2.08	3.66
[4.2][(a)]	-	10.4	7.60	8.64	11.6
[4.3][(a)]	-	9.58	1.22	-	2.67

(a) Titration performed in the presence of 5 % methanol due to limited solubility in water. Estimated error ± 20 % based on five repeat experiments.

5.2 DNA Binding Studies

Macrocycles **[4.1]** - **[4.3]** have shown that they are capable of binding to biological anions with considerably high affinities in water. While previous chapter has proven that the building blocks for these macrocycles could bind to DNA; indeed the binding affinities for these complexes are relatively high and are typical of those observed for metallo-intercalators. It has also been demonstrated that supramolecular architectures are capable of binding to duplex DNA; for example metallo-supramolecular cylinder with similar dimensions to zinc fingers can interact with B-DNA through its major groove.[162, 164, 165] X-ray studies on **[4.1]** reveal a relatively large (≈ 15 Å in width), highly structured, palm-like binding cavity composed of hydrophobic aromatic residues[27] which maybe suitable for binding on the outside of DNA. Recently, we have reported[168] a preliminary study on the DNA binding interaction of RubpyRe **[4.1]**. These previous results have prompted us to further investigate the possible use of the heterometallic macrocycles as DNA binding substrates.

5.2.1 Viscosity

To provide insight into the binding mode of these macrocycles with CT-DNA, viscosity experiments were carried out. The viscosity of CT-DNA in the presence of the macrocyclic molecules is shown in **Figure 5.8**.

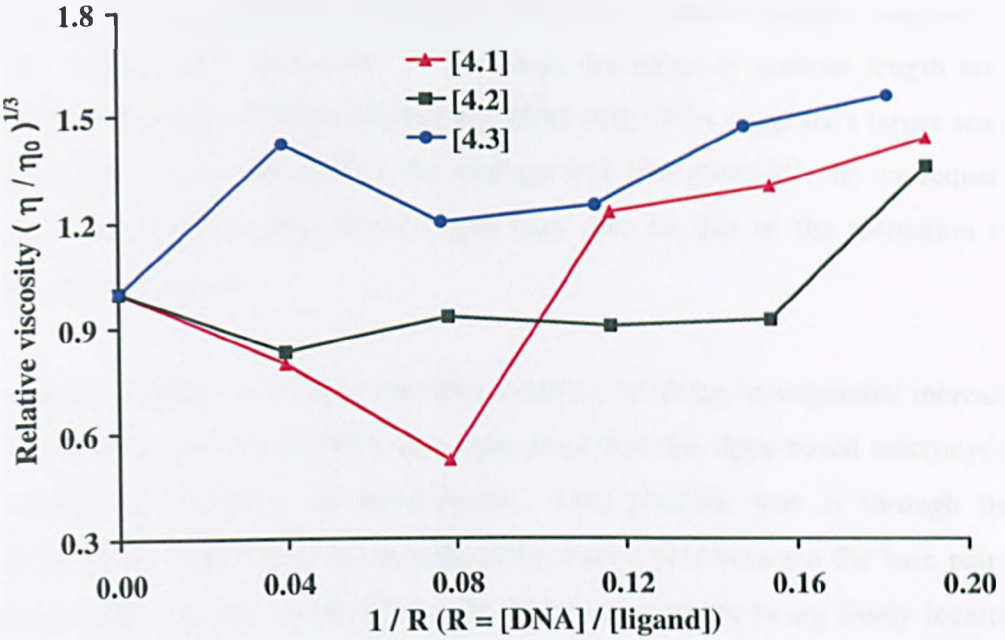

Figure 5.8: Relative viscosity of CT-DNA upon addition of [4.1], [4.2] and [4.3] (27 °C, 5 mM Tris buffer, 25 mM NaCl, pH 7.0; viscosity of CT-DNA with [4.2] and [4.3] was performed in 5 % methanolic buffer due to limited solubility in aqueous solutions).

From **Figure 5.8**, it can be concluded that there are at least two modes of binding for this series of metallomacrocycles; **[4.1]** and **[4.2]** display fairly similar mode of binding, while **[4.3]** binds differently from those two complexes.

When DNA sequences below its persistence length are used in such experiments, it behaves as a rod-like polymer and thus changes in the viscosity of aqueous solutions can be related to the average contour length of the dissolved duplex.[201] It is clear that the initial titre of **[4.1]** results in a dramatic decrease in viscosity of DNA, while **[4.2]** producing about 20 % decreases in viscosity of DNA. These changes reverse on further addition of **[4.1]** and **[4.2]** respectively, resulting in a final relative viscosity that is higher than that of the original solutions. A number of previous studies on DNA binding substrates have demonstrated a similar - *albeit less intense* - viscosity change; for example, Δ-$[Ru(phen)_3]^{2+}$ initially induces a ~7% decrease in hydrodynamic length.[122] In this latter case, it has been proposed that this preliminarily decrease is due to substrate-induced DNA kinking, is followed by the introduction of further unphased kinks that

produce rod like superhelical structures with hydrodynamic lengths comparable to the starting DNA molecules.[168] The large decreases in contour length seen during the initial interactions of **[4.1]** and **[4.2]** with DNA suggests a larger scale of bending mode for the duplex. By analogy with $[Ru(phen)_3]^{2+}$, the consequent increases in hydrodynamic DNA length may also be due to the formation of supercoiled structures.

In contrast, addition of **[4.3]** to the DNA solution, resulting in sequential increase in the relative viscosity of DNA, thus indicating that this dppz-based macrocycle is binding to CT-DNA *via* intercalation. One possible way is through the insertion of the dppz units on one side of the macrocycle between the base pairs, with the dppz ligands on the other side of the macrocycle being freely located outside of the helix. It is clear that changing the ancillary ligands of the macrocycles results in modulation of the binding modes of this system.

More excitingly, there are striking different results between macrocycles **[4.1]** and **[4.2]** and their respective building blocks. In order to provide a clear comparison between the viscosity changes of CT-DNA upon addition of the macrocycles and the monomers respectively, all the results are plotted in the same graph (**Figure 5.9**).

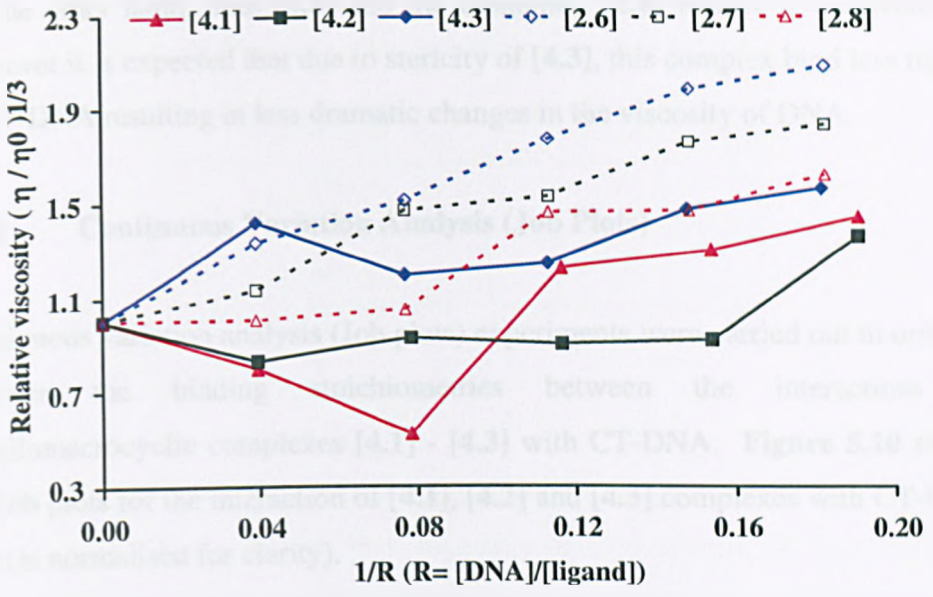

Figure 5.9: Relative viscosity of CT-DNA upon addition of [2.6], [2.7], [2.8], [4.1], [4.2] and [4.3]. (Viscosity of CT-DNA with [2.6], [4.2] and [4.3] was performed in 5 % methanolic buffer due to limited solubility in aqueous solutions).

It was found that the building blocks for these macrocycles **[2.6]** - **[2.8]** behaved as a typical intercalator;[159, 160, 161, 193, 194] addition of the complex produced sequential increases in relative specific viscosity due to the expected increase in duplex contour length.[122, 140, 201] Clearly, **[4.1]** and **[4.2]** bind to CT-DNA in a different mode compared to the building blocks.

Furthermore, the crystallographic data[27] on **[4.1]** reveals a cupped palm structure of the macrocycle (approximate space filling dimensions = 22 Å x 17 Å x 9 Å) is too large for conventional binding within the minor or major groove (width ≈ 6 and 12 Å, respectively). Similarly, crystal structure for **[4.2]** reveals more or less similar dimension to that of **[4.1]**, thus is too large for conventional binding within the minor or major groove as well. Given this, it seems likely that the DNA bending induced by **[4.1]** and **[4.2]** is due to a novel external binding mode. More experimental and theoretical studies clearly need to be done to further investigate the nature of this novel interaction and probe for any evidence of binding selectivity.

On the other hand, both **[4.3]** and the monomer, **[2.6]** behave as intercalators. However it is expected that due to stericity of **[4.3]**, this complex bind less tightly to CT-DNA resulting in less dramatic changes in the viscosity of DNA.

5.2.2 Continuous Variation Analysis (Job Plots)

Continuous variation analysis (Job plots) experiments were carried out in order to estimate the binding stoichiometries between the interactions of metallomacrocyclic complexes **[4.1]** - **[4.3]** with CT-DNA. **Figure 5.10** shows the Job plots for the interaction of **[4.1]**, **[4.2]** and **[4.3]** complexes with CT-DNA (data is normalised for clarity).

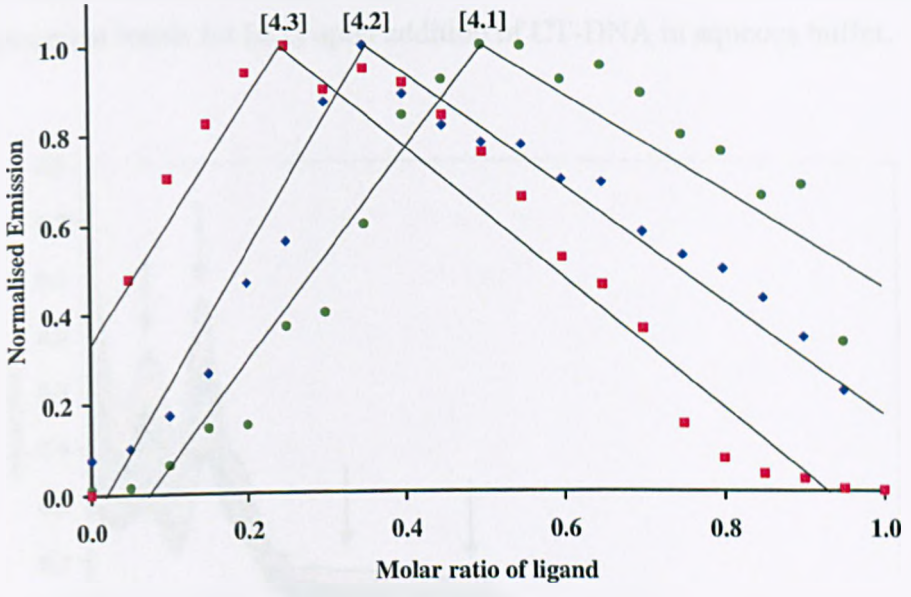

Figure 5.10: Job plots for the interactions of [4.1], [4.2] and [4.3] with CT-DNA.

Figure 5.10 shows the intersection point for **[4.1]** was at 0.5 which is equivalent to stoichiometry of 1.0 mol of base pair per mol of complex. While the inflection point for **[4.2]** was 0.35 and for **[4.3]** was 0.25, being equivalent to a stoichiometry of 1.9 and 3.0 mol of base pair per mol of complex respectively (data are summarised in **Table 5.3**).

Table 5.3: Binding stoichiometries for the interactions of macrocyclic complexes with CT-DNA obtained by continuous variation analysis.

Compound	N (bp)
[4.1]	1.0
[4.2]	1.9
[4.3]	3.0

5.2.3 UV-Visible Titrations

As outlined previously, the UV-Visible absorption spectra of binding substrates change upon interaction with DNA due to the changes in their microenvironment. The interaction of **[4.1]**, **[4.2]** and **[4.3]** with CT-DNA has also been analysed using absorption spectroscopy. **Figure 5.11** displayed clear hypochromicities in the absorption bands for **[4.1]** upon addition of CT-DNA in aqueous buffer.

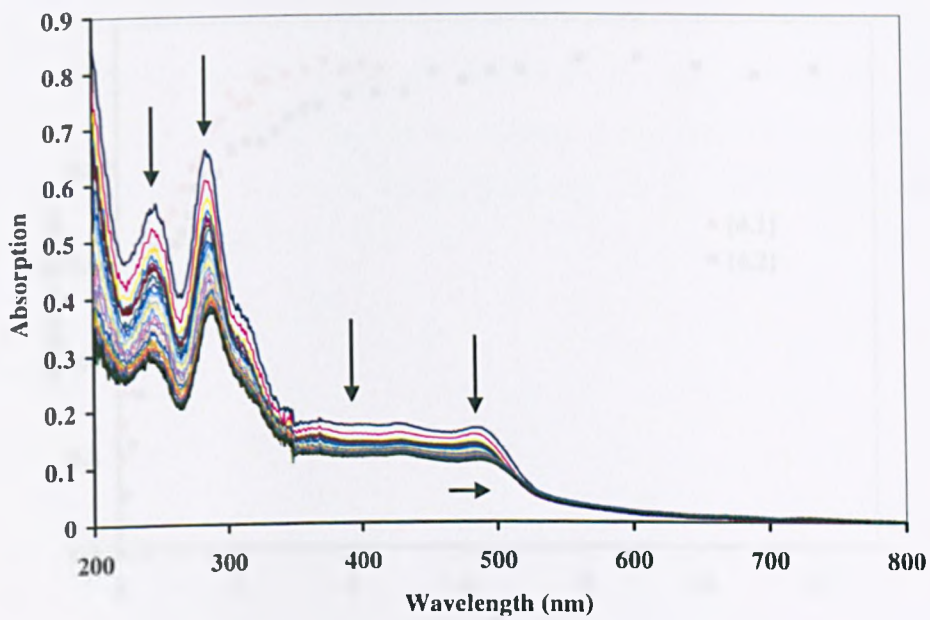

Figure 5.11: UV-Visible titration of [4.1] with addition of CT-DNA (5 mM TRIS, 25 mM NaCl, pH 7.0 at 25°C).

There are distinctive bands at 245 nm, 286 nm and 480 nm, which all reduce in absorbance, with hypochromism of 43.6 % at 286 nm. There is also a small bathochromic shift upon binding saturation.

Addition of CT-DNA to **[4.2]** and **[4.3]** leads to similar changes, with the bands between 200 nm and 550 nm showing a high degree of hypochromicity. Similar to **[4.1]**, the higher wavelength band for both complexes displays a bathochromic shift upon approaching binding saturation.

To study further the interaction of these molecules with DNA, changes in the bands at 286 nm for **[4.1]**, 261 nm for **[4.2]** and 277 nm for **[4.3]** were monitored and binding curves were constructed using these data, see **Figure 5.12** and **Figure 5.13**. The binding curves indicate that in all cases, saturation binding has taken place.

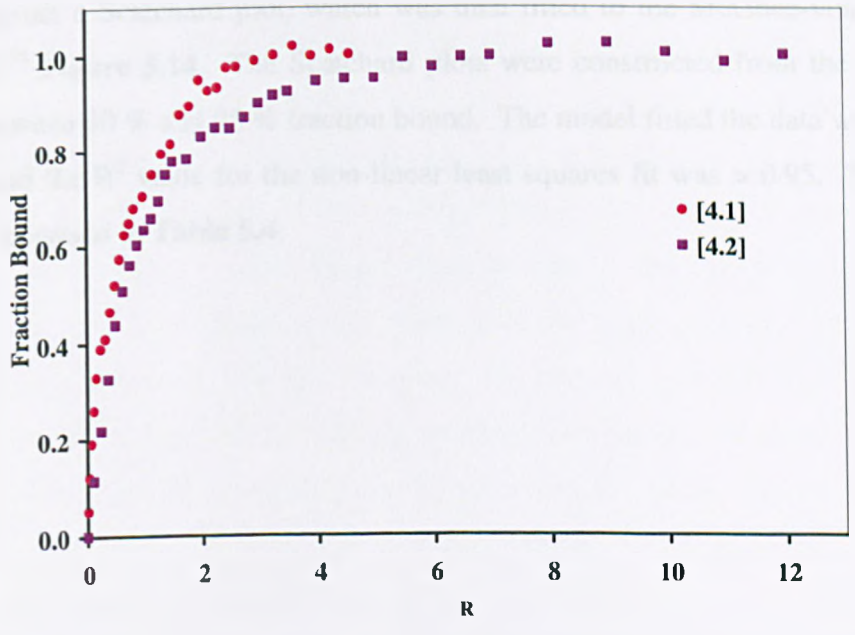

Figure 5.12: Binding curves obtained by UV-Visible titrations for [4.1] and [4.2] binding to CT- DNA (25 °C, 5 mM Tris buffer, 25 mM NaCl, pH 7.0).

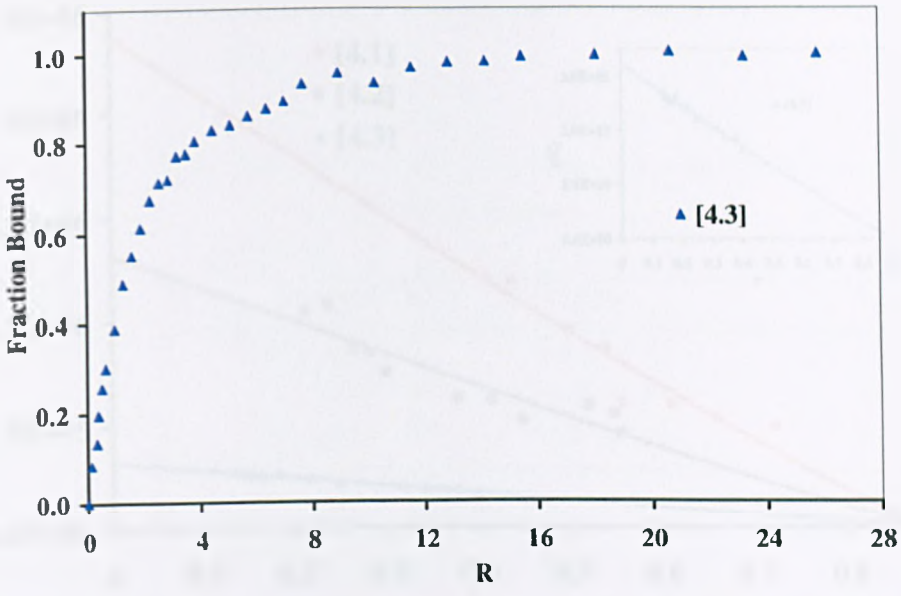

Figure 5.13: Binding curve obtained by UV-Visible titrations for [4.3] binding to CT-DNA (25 °C, 5 mM Tris buffer, 25 mM NaCl, pH 7.0).

The hypochromisms of **[4.1]**, **[4.2]** and **[4.3]** on addition of CT-DNA were used to construct a Scatchard plot, which was then fitted to the McGhee-von Hippel model,[174] **Figure 5.14**. The Scatchard plots were constructed from the binding data between 30 % and 95 % fraction bound. The model fitted the data well in all cases and the R^2 value for the non-linear least squares fit was > 0.95. The data are summarised in **Table 5.4**.

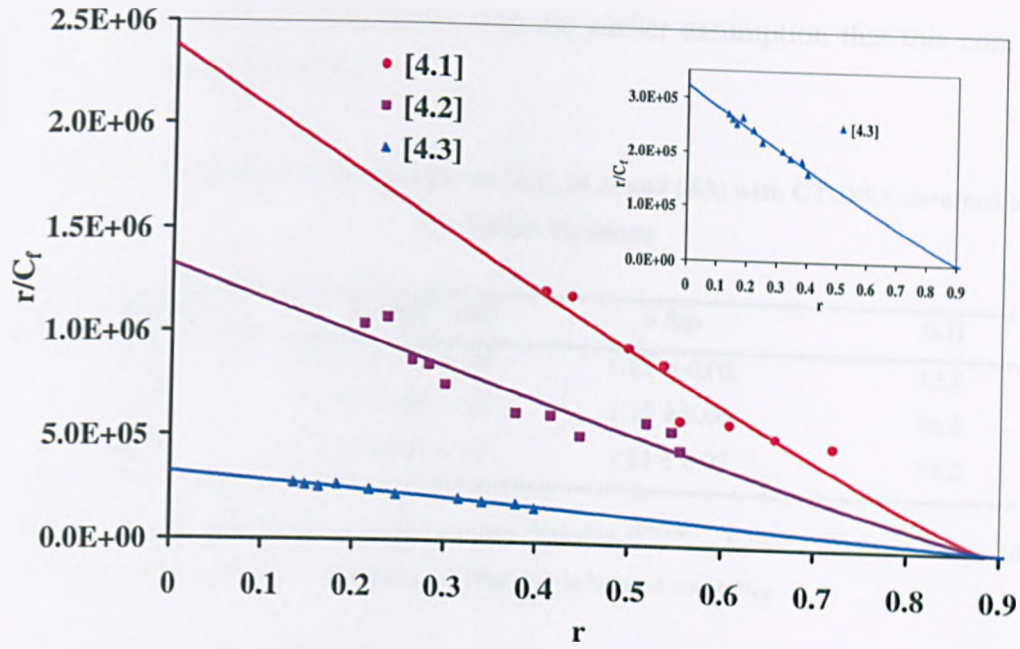

Figure 5.14: Scatchard plots fitted to the McGhee-von Hippel model using UV-Visible titrations data from [4.1], [4.2] and [4.3] binding to CT-DNA in 5 mM TRIS, 25 mM NaCl, pH 7.0.

Analysis of the Scatchard plot shows that, **[4.1]** shows the strongest binding to CT-DNA, having a 2-fold and 7-fold increase in affinity compared to that of **[4.2]** and **[4.3]**, respectively. In addition, the binding affinity of **[4.1]** is about a magnitude higher than that of the building block **[2.8]**. However, the site sizes obtained are similar, being 1 bp for each complex. The site size for **[4.1]** is consistent with the stoichiometry obtained from the continuous variation analysis (Job Plots) experiment. On the other hand, the binding interaction of **[4.2]**-DNA is about twice of **[2.7]**-DNA, with the binding constant of 1.33 x 10^6 M^{-1}. The site sizes for both **[4.2]** and **[2.7]** are more or less the same. Macrocycle **[4.3]** binds less tightly to CT-DNA with a binding affinity of 3.32 x 10^5 M^{-1}. Indeed, this macrocycle shows weaker affinity towards CT-DNA than the monomer **[2.6]**, which could be reasoned by the steric demand of this macrocycle. Although the changes in the relative viscosity has suggested that this complex binds through intercalation mode, the site size obtained from UV-Visible titration is low; however the stoichiometry obtained from the Job Plots experiment for **[4.3]** is

3.0 bp per ligand and this agrees with the earlier assumption that this complex binds through intercalation.

Table 5.4: Summary of binding data for [4.1], [4.2] and [4.3] with CT-DNA obtained by UV-Visible titrations.

Compound	K_b /mol^{-1} dm^3	S /bp	%H
[4.1]	2.38 ± 0.26 x 10^6	1.13 ± 0.05	43.6
[4.2][a]	1.33 ± 0.96 x 10^6	1.12 ± 0.06	46.8
[4.3][a]	3.32 ± 0.71 x 10^5	1.11 ± 0.03	54.2

(Where %H is the percent of the hypochromism, $\%H=[(A_\lambda^{[DNA]=0} - A_\lambda^{[DNA]=SAT})/ A_\lambda^{[DNA]=0}] \times 100$).
[a] Titration performed in 5 % methanolic buffer due to limited solubility.

5.2.4 Luminescence Titrations

Luminescence titrations were carried out using a procedure similar to the UV-Vis titrations. To reinterate, in previous host-guest studies, we have found that binding to polyaromatic molecules in water has no effect on luminescent output of **[4.1]**,[28] whilst anion binding in non-aqueous solutions results in enhancements of steady state emission, but no shift in λ_{em}.[27] Earlier in this report, we have found that binding of somewhat bigger biological anions to **[4.1]**, **[4.2]** and **[4.3]** in water have resulted in changes of the luminescence output (either increase or decrease). **Figure 5.15** shows typical luminescence titrations **[4.1]** with CT-DNA.

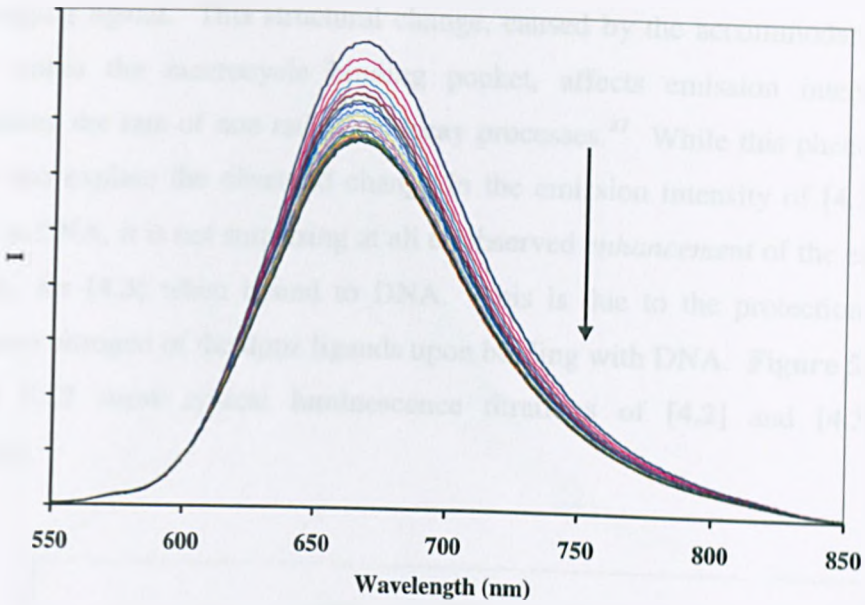

Figure 5.15: Luminescence titration of [4.1] with CT-DNA. (25 °C, 5 mM Tris buffer, 25 mM NaCl, pH 7.0).

Interestingly, the emission of **[4.1]** is quenched upon addition of CT-DNA. However, even at saturation binding **[4.1]** still displays significant residual luminescence in aqueous solution. There is no shifting of emission wavelength upon saturation binding. Reduced luminescence from substrate bound to DNA is often associated with redox quenching involving oxidation of G-sites.[65, 132, 133, 202] However, this mechanism is unlikely as, once the initial minimum is obtained, no further decrease in luminescence is observed even in the presence of a large excess of DNA.

In contrast to the former observation, analogous titration involving **[4.2]** and **[4.3]** results in a progressive enhancement in the emission intensity of both molecules. Again, no shifting in the emission wavelength upon saturation binding was observed. It is somewhat surprising that the emission intensity for **[4.2]** is increased upon titration with CT-DNA although **[4.1]** and **[4.2]** show a high degree of similarity in the viscosity experiments. We have previously suggested that emission changes caused by host-guest interactions involving the macrocycles are due to alterations in the torsion angles between aromatic rings in

the bridging ligand. This structural change, caused by the accommodation of a guest within the macrocycle binding pocket, affects emission intensity by modulating the rate of non radiative decay processes.[27] While this phenomenon might also explain the observed change in the emission intensity of **[4.2]** upon bound to DNA, it is not surprising at all to observed *enhancement* of the emission intensity for **[4.3]** when bound to DNA. This is due to the protection of the phenazine nitrogen of the dppz ligands upon binding with DNA. **Figure 5.16** and **Figure 5.17** show typical luminescence titrations of **[4.2]** and **[4.3]** with CT-DNA.

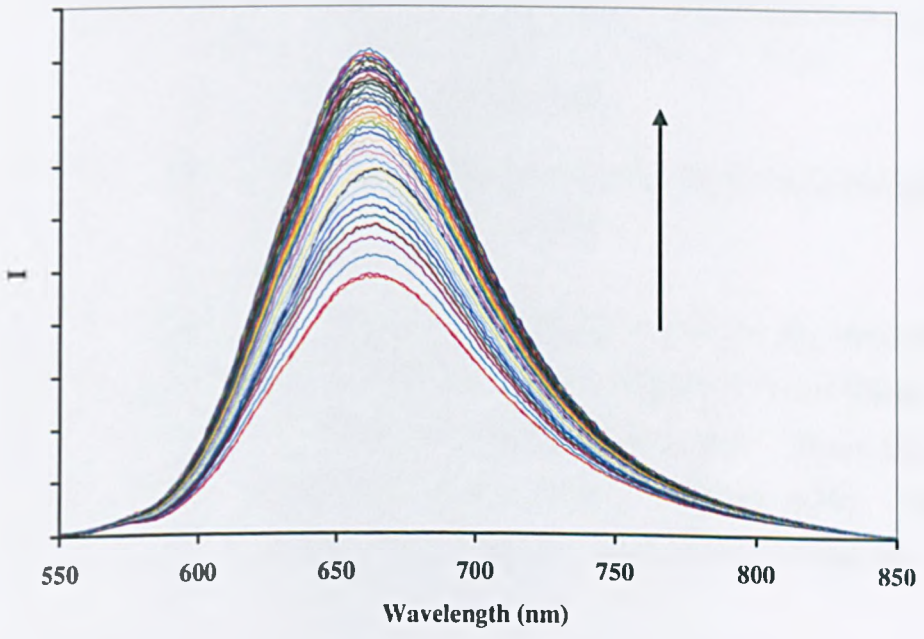

Figure 5.16: Luminescence titration of [4.2] with CT-DNA. (25 °C, 5 mM Tris buffer, 25 mM NaCl, pH 7.0).

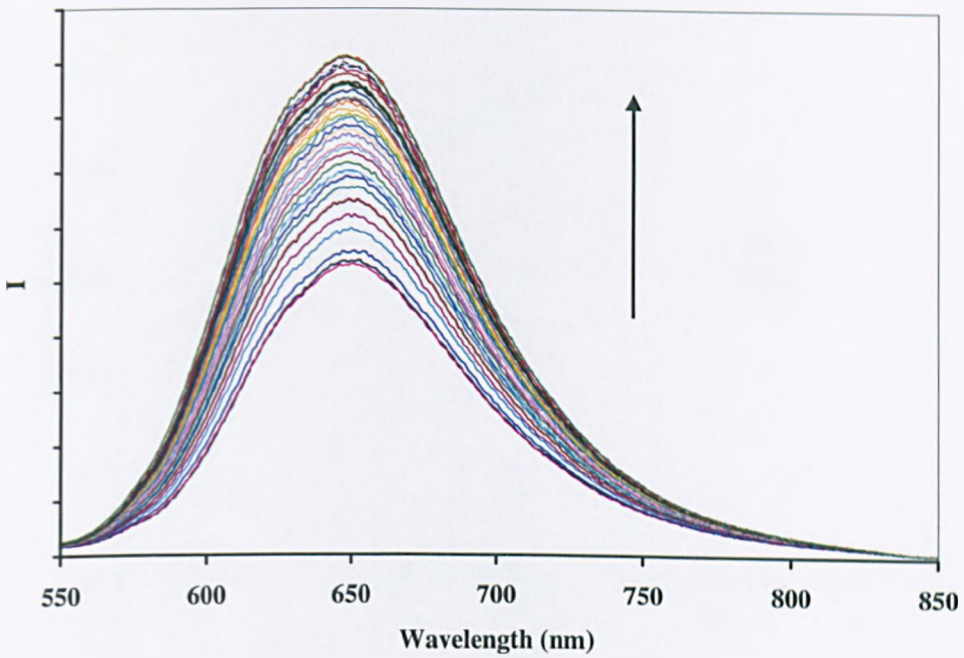

Figure 5.17: Luminescence titration of [4.3] with CT-DNA. (25 °C, 5 mM Tris buffer, 25 mM NaCl, pH 7.0).

The binding curves derived from the luminescence data for the interaction of **[4.1]**, **[4.2]** and **[4.3]** with CT-DNA are shown in **Figure 5.18** and **Figure 5.19**. Once again it shows that saturation binding has taken place. These data were then fitted to the McGhee-von Hippel model[174] (**Figure 5.20**). Binding parameters obtained from fits of the raw data are summarised in **Table 5.5**.

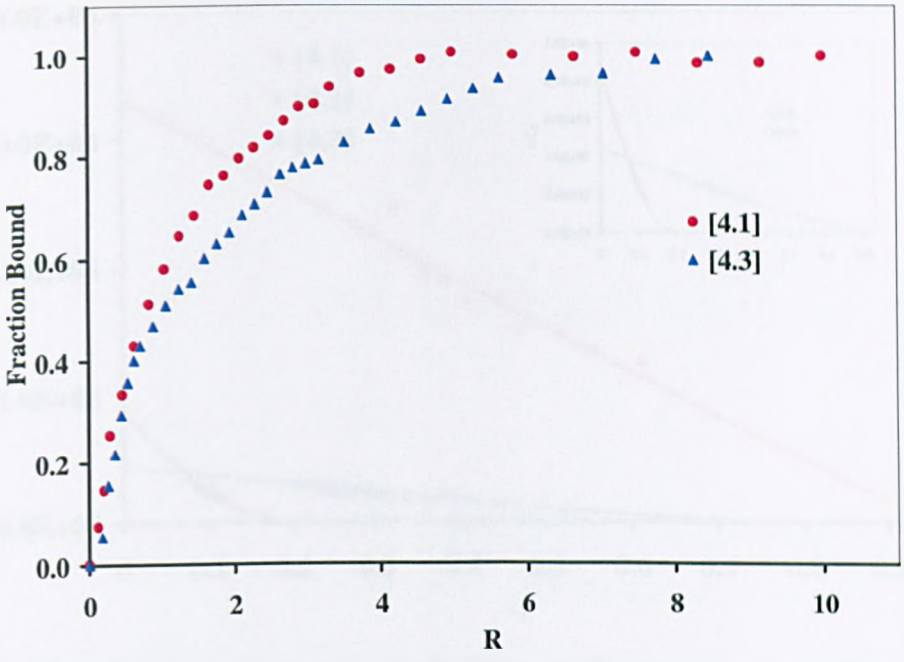

Figure 5.18: Binding curves obtained by luminescence titrations for [4.1] and [4.3] binding to CT-DNA (25 °C, 5 mM Tris buffer, 25 mM NaCl, pH 7.0).

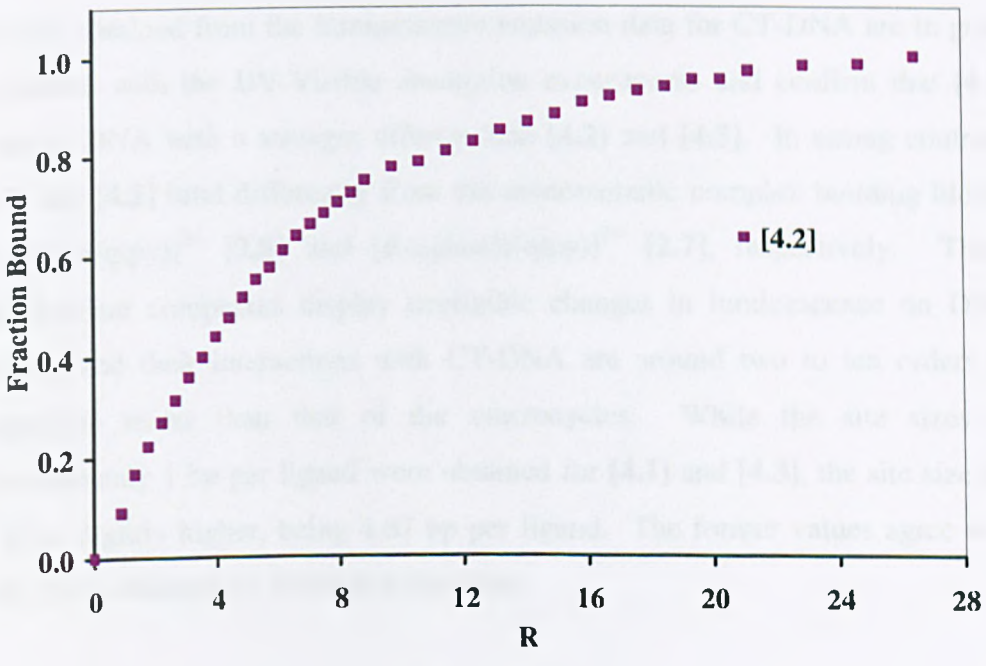

Figure 5.19: Binding curve obtained by luminescence titrations for [4.2] binding to CT-DNA (25 °C, 5 mM Tris buffer, 25 mM NaCl, pH 7.0).

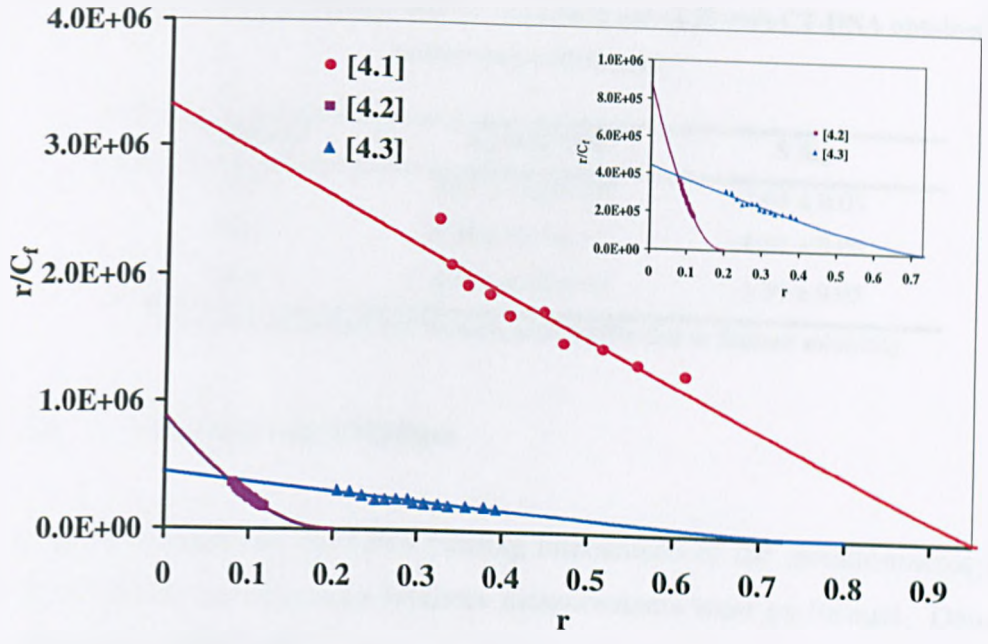

Figure 5.20: Scatchard plots fitted to the McGhee-von Hippel model using luminescence titrations data from [4.1], [4.2] and [4.3] binding to CT-DNA in 5 mM TRIS, 25 mM NaCl, pH 7.0.

The fits obtained from the luminescence emission data for CT-DNA are in good agreement with the UV-Visible absorption experiments and confirm that **[4.1]** binds to DNA with a stronger affinity than **[4.2]** and **[4.3]**. In strong contrast, **[4.1]** and **[4.2]** bind differently from the monometallic complex building blocks $[Ru(bpy)_2(qtpy)]^{2+}$ **[2.8]** and $[Ru(phen)_2(qtpy)]^{2+}$ **[2.7]**, respectively. These mononuclear complexes display negligible changes in luminescence on DNA binding and their interactions with CT-DNA are around two to ten orders of magnitude lower than that of the macrocycles. While the site sizes of approximately 1 bp per ligand were obtained for **[4.1]** and **[4.3]**, the site size for **[4.2]** is slightly higher, being 4.67 bp per ligand. The former values agree well with those obtained by absorption titrations.

Table 5.5: Summary of binding data for [4.1], [4.2] and [4.3] with CT-DNA obtained by luminescence titrations.

Compound	K_b /mol^{-1} dm^3	S /bp
[4.1]	3.32 ± 0.25 x 10^6	1.05 ± 0.05
[4.2][(a)]	8.75 ± 0.19 x 10^5	4.67 ± 0.05
[4.3][(a)]	4.42 ± 0.22 x 10^5	1.36 ± 0.05

[(a)] Titration performed in 5 % methanolic buffer due to limited solubility.

5.2.5 Luminescence Lifetimes

For further insight into the DNA binding interactions of the metallomacrocycles with CT-DNA, luminescence lifetimes measurements were performed. Data are summarised in **Table 5.6**.

Table 5.6: Lifetime data for [4.1], [4.2] and [4.3] in 5 mM Tris, 25 mM NaCl, pH 7.0 at 25°C.

Compound	τ^a, ns	τ^b, ns
[4.1]	463	430
[4.2]	427	474
[4.3]	173	276[c]; 46[d]

[a]Lifetime at a binding ratio of [CT-DNA(bp)]/[Ru] 0:1. [b]Lifetime at a binding ratio of [CT-DNA(bp)]/[Ru] saturated:1. [c]First component. [d]Second component. (All solutions are degassed unless otherwise stated)

The lifetimes were recorded in the absence of CT-DNA and in the presence of saturated CT-DNA (saturation points were determined from the luminescence titration experiments). Both **[4.1]** and **[4.2]** gave shorter luminescence lifetimes compared to the respective building blocks upon binding to CT-DNA. On the other hand, the lifetime obtained for **[4.3]**-DNA is about two fold longer than **[2.6]**-DNA.

Interestingly, the decay profile for **[4.3]** fitted well to a biexponential curve upon binding with CT-DNA rather than a monoexponential curve before binding. This observation supports the earlier assumption that the dppz ligands are involved in

the DNA binding interaction, most probably through intercalation, thus indicate that when binding to DNA, the lowest excited states for **[4.3]** are at least partially localised on the dppz ligands. Two lifetimes can be attributed to the different distribution of the intercalated complex along the DNA helix, as such proposed by Barton *et al.*[84] for $[Ru(phen)_2(dppz)]^{2+}$. In one mode, the dppz ligand is parallel to the DNA dyad axis, while in other mode it is perpendicular.

When the binding ratio of [CT-DNA(bp)]/[Ru] varied from 0:1 to saturated:1, the excited lifetime increased from 427 ns to 474 ns for **[4.2]** and from a monoexponential lifetime of 173 ns to biexponential lifetimes of 276 ns and 46 ns for **[4.3]**. The increments are consistent with the observed progressive emission enhancement of **[4.2]** and **[4.3]** upon binding to CT-DNA. The trace obtained for **[4.1]** is slightly decreased from 463 ns to 430 ns when the binding ratio of [CT-DNA(bp)]/[Ru] varied from 0:1 to saturated:1; this is also consistent with the quenched emission of **[4.1]** upon binding with CT-DNA.

5.3 Conclusions

In conclusion, we have found that these large, photoactive, kinetically inert, tetranuclear metallomacrocycles can function as hosts for biological anions in aqueous environment. However, there is no selectivity observed between the macrocycles and the biomolecules. Thus, macrocycles **[4.1]**, **[4.2]** and **[4.3]** may serve as a starting point for the development of more sensitive and specific probes for nucleic acid constituents in water.

In fact, these macrocycles have demonstrated the capability of binding large polyanions such as duplex DNA with affinities that are comparable with other DNA binding substrates. Interestingly, the binding affinities and binding modes are modulated upon changing the ancillary ligands of the macrocycles.

6 Future Work

Future work in this area may concentrate on fabrication of macrocycles which are tailored to function as specific sensing systems. By changing the bridging ligand, the size of the host cavity can be tuned (**Figure 6.1**), while changing the overall charge of the structure, the selectivity for ions or hydrophobic aromatic molecules can be adjusted (**Figure 6.2**).

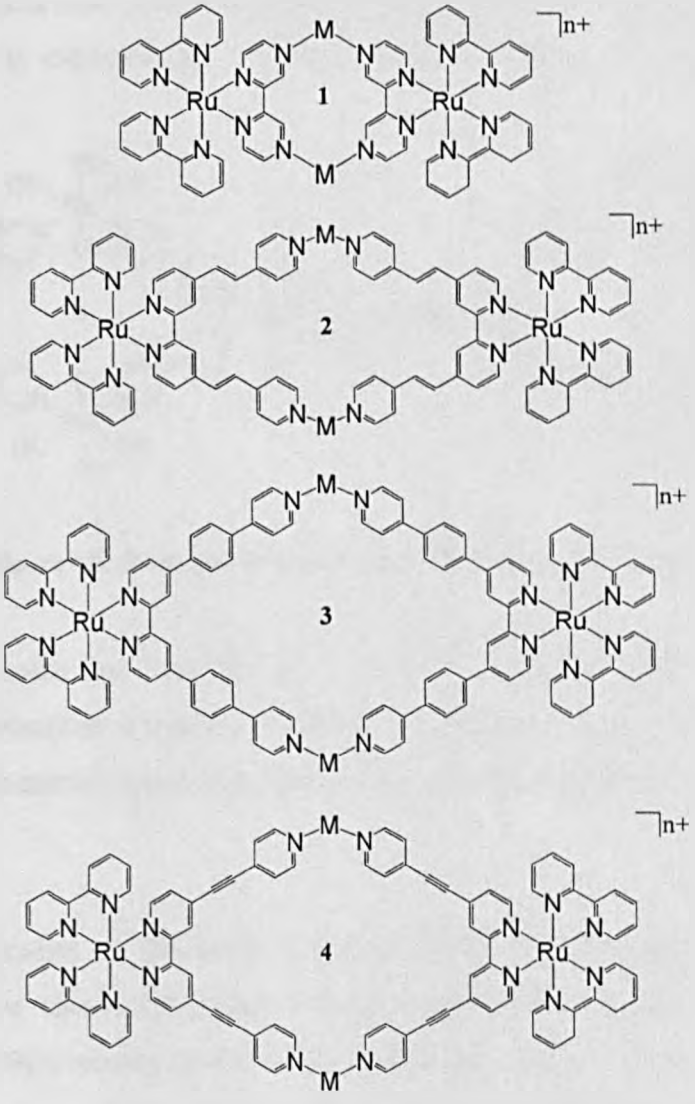

Figure 6.1: Analogous macrocycles with different bridging ligands.

For these hosts to function as sensors, an output that is modulated by guest binding is required. In our macrocycles RubpyRe **[4.1]**, RuphenRe **[4.2]** and RudppzRe **[4.3]**, energy transfer process within these systems mean that this signal is always supplied by a change in the metal-to-ligand charge transfer (MLCT), luminescence from the Ru^{II}-center situated at the coordination site which is exterior to the binding pocket. However, other output signals could be investigated, for example for complex **5,** the output is supplied by a Re^{I} MLCT from the same site, while in complex **6**, since the exterior coordination site is occupied by a non-emissive center, emission from the Re^{I} center that forms part of the macrocycle will occur. As this metal center is close to any guest bound in the pocket it is expected that emission changes in this sensor will be greatly modulated.

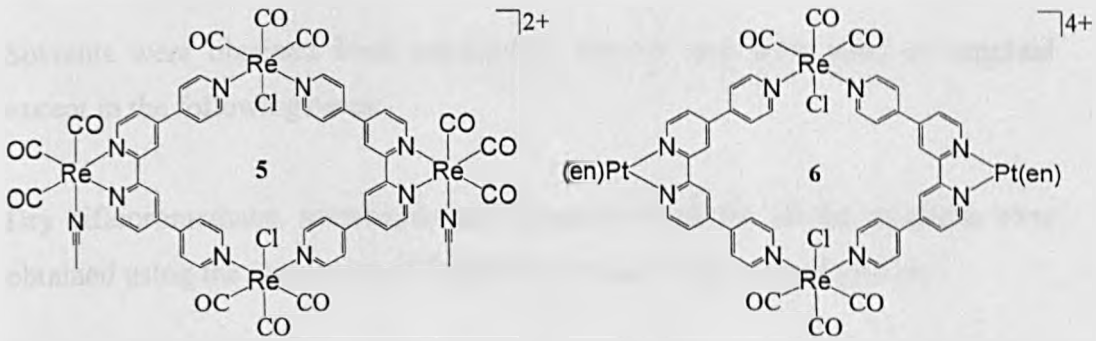

Figure 6.2: Analogous structures with different overall charges.

It should be noted that both Ru^{II} and Re^{I} are electroactive metal centers, with distinctive reversible oxidation couples. Therefore the possibility that the complexes discussed above function as electrochemical sensors could also be investigated.

Preliminary studies on the binding interactions of the prototype systems with CT-DNA have shown the promise these heterometallic macrocycles have as luminescent DNA binding probe. In the longer term, we would like to investigate whether these types of complexes show any sequence preferences in binding to DNA. This work may lead to sensors for specific genetic sequences and DNA structures involved in diseases such as cancer.

7 Experimental Techniques and Synthetic Procedures

7.1 Materials and Equipment

7.1.1 Chemicals

All chemicals were purchased from commercial sources and used as supplied unless otherwise stated.

7.1.2 Solvents

Solvents were obtained from commercial sources and were used as supplied except in the following cases:-

Dry difluoromethane, acetonitrile and tetrahydrofuran for all the reactions were obtained using the University of Sheffield Grubbs^{TM} dry solvent system.

7.1.3 Reaction Conditions

All reactions were carried out under an oxygen free nitrogen atmosphere, unless otherwise stated.

7.1.4 Chromatography

Alumina column chromatography was carried out on Brockmann grade I.

All alumina and silica column sizes were approximately 150 x 30 mm unless otherwise stated. Sephadex column sizes were approximately 500 x 10 mm.

7.1.5 Nuclear Magnetic Resonance Spectra

Standard ^{1}H NMR spectra were recorded on a Bruker AM250 or AV400 machine, working in Fourier transform mode.

More complex ^{1}H NMR experiments including 2D-COSY experiments were performed by Sue Bradshaw of the University of Sheffield. The spectra were recorded on a Bruker DRX500 machine.

The following abbreviations are used in the annotation of ^{1}H NMR spectra:

br – broad, s – singlet, d – doublet, dd – double doublet, td –triple doublet, t – triplet, q – quartet, m – multiplet.

7.1.6 Mass Spectra

FAB mass spectra were recorded on a Kratos MS80 machine in positive ion mode with a *m*-nitrobenzyl alcohol matrix. ES mass spectra were recorded on a Micromass LCT ES-TOF machine.

All spectra were run by Mr. Simon Thorpe, Ms. Jane Stanbra or Ms. Sharon Spey of the University of Sheffield Mass Spectrometry Service.

7.1.7 Electrochemistry Studies

Cyclic voltammograms were recorded using an EG&G model Versastat II potentiostat and either CONDECON 310 hardware/software package or the EG&G electrochemistry powersuite software package.

Experiments were performed in freshly distilled acetonitrile with 0.1 M NBu_4PF_6 as support electrolyte.

Potentials were measured against a Ag/AgCl reference electrode and ferrocene was used as an internal standard. All cyclic voltammograms were software corrected for internal resistance.

7.1.8 UV-Visible Absorption Spectra

UV-Vis spectra were recorded on a Cary 500 spectrometer in double beam mode, using quartz cells of 10 mm path length. Spectra were measured in acetonitrile unless otherwise stated, and were baseline corrected.

7.1.9 Emission Spectra

Emission spectra were recorded on a Jobin-Yvon FluoroMax-3 spectrophotometer operating in luminescence wave scan mode. The photomultiplier tube was set to a potential of 700 V, the excitation and emission slit widths were 5 nm, the scan speed was 240 nms^{-1} and the response time was set to 0.05 s.

7.1.10 Luminescence Lifetime Studies

The luminescence lifetime studies were determined using the Mini-τ Fluorescence Lifetime Spectrometer operating under single photon counting conditions and collected by a Hamamatsu H5773-03 single photon counting detector. Data analysis was performed using Marquadt-Levenberg Algorithm. The goodness of fit was assessed by minimising the reduced chi squared function (χ^2) and visual inspection of the weighted residuals. Oxygen-free samples were prepared by degassing three times with freeze-pump-thaw cycles on a high-vacuum line with liquid nitrogen.

7.1.11 Quantum Yield Measurements

Quantum yields were measured at excitation wavelength and compared to reference emitters by the following equation:[203]

$$\Phi_x = \Phi_r \left[\frac{A_R}{A_x}\right]\left[\frac{E_x}{E_R}\right]\left[\frac{I_R}{I_x}\right]\left[\frac{n_x^2}{n_R^2}\right]$$

where A is the absorbance at the excitation wavelength (λ), E is the corrected emission intensity of the excitation light at the excitation wavelength (λ), n is the refractive index of the solvent, I is the relative intensity of the exciting light, and Φ is the emission quantum yield. The subscript r and x refer to the reference and the sample, respectively. All quantum yields were performed at an identical excitation wavelength for the samples and reference, canceling the $(I_R)/(I_x)$ term in the equation. All complexes were measured against $[Ru(bpy)_3]^{2+}$ in acetonitrile ($\Phi = 0.062$)[87] and in water ($\Phi = 0.042$)[89] as reference, respectively. Experiments were performed in freshly distilled acetonitrile or double distilled water.

7.1.12 X-Ray Diffraction

Structures were solved by Harry Adams in the department's X-ray structure determination service on a Bruker Smart CCD area detector with Oxford Cryosystems low temperature system and complex scattering factors from the SHELXTL program package.

7.1.13 Spectroelectrochemistry

UV/Vis/NIR spectroelectrochemical measurements were performed in acetonitrile using an OTTLE cell, path length 0.4 mm, at 253 K unless stated otherwise. Hardware used comprised a Cary 5000 UV/Vis/NIR spectrometer and

an EG+G 273A Potentiostat. The electrodes used were a platinum gauze working electrode, platinum wire counter electrode, and silver pseudo-reference electrode. Experiments were performed in acetonitrile, dried as before, with 0.1 M NBu_4PF_6 as base electrolyte.

7.2 DNA Binding Study Protocols

7.2.1 Preparation of Calf Thymus DNA

Calf thymus DNA (CT-DNA) was purchased from Sigma as a solid sodium salt and dissolved in buffer (5 mM Tris, 25 mM NaCl, pH 7.0). An average chain length[128] of 150-200 base pairs (bp) was achieved by subjecting the CT-DNA solution to 30 minutes of discontinuous sonication using a Sanyo Soniprep 150 ultrasonic disintegrator, fitted with a 19 mm diameter probe. It was then dialysed[204] in 2 litres of Tris buffer for 24 h at 4 °C using dialysis tubing with a MWCO of 3,500 Daltons.

Purity of the sample was determined by UV-Visible spectroscopy, with $\frac{A_{260}}{A_{280}} > 1.9$ indicating a protein free sample. DNA concentration was also determined by UV-Visible spectroscopy using ε_{260} = 13200 M^{-1} cm^{-1} for concentration analysis.

7.2.2 Viscosity

Viscosity experiments were carried out on a Cannon-Manning semi-micro viscometer (size 50) immersed in a thermostated water bath maintained at 27 ± 1 °C. The concentration of CT-DNA was kept between 0.5 – 1 mM bp^{-1}, and approximately 200 bp in length, as described in section 7.2.1, to minimise complexities rising from DNA flexibility.[124, 183] The different samples were prepared by adding ligand to the DNA solution to give an increase in the ligand/bp ratio. (Solutions were made up so that values of 1/R

(R=[DNA]/[ligand]) were between 0 and 0.2). The flow times (time taken for the solution to pass through the capillary tube) were recorded in triplicate and the average calculated after thermal equilibration of 20 minutes. Estimated error ± 10 % based on five repeat experiments.

7.2.3 Continuous variation analysis (Job plots)

Continuous variation analyses were carried out in a HORIBA Jobin Yvon FluoroMax-3 spectrometer or a Varian-Cary 3-Bio UV-Visible spectrometer. The sum of the concentrations of CT-DNA and metal complex was kept constant at 20 μM, and the concentration of DNA and metal complex was varied. The fluorescence intensities of these mixtures were measured using the excitation wavelength characteristic of each metal complex at 25 °C. While for those complexes that gave slight changes in the emission, the Job plots were done by following the changes in absorption of the mixtures at wavelength where the complex absorbed strongly and the concentration of DNA and metal complex was kept constant at 5 μM. Estimated error ± 20 % based on five repeat experiments.

7.2.4 UV-Visible Titrations

UV-Visible titrations were performed on a Varian-Cary 3-Bio UV-Visible spectrometer. 3 mL of buffer was loaded into two identical 1 cm path length optical quartz cuvettes. To the first cuvette, a volume of buffer was removed with a Gilson pipette and replaced with the same volume of stock solution of drug. This first cuvette was placed into the sample cell and the second into the reference cell of the spectrometer and maintained at 25 °C. Both cuvettes were mixed 15 times with a Gilson 1000 μL pipette and all bubbles removed.

After equilibration, a spectrum between 200 – 600 nm was recorded. 1 – 5 μL of a concentrated stock CT-DNA was added to both cuvettes and mixed 15 times. The spectrum was recorded after equilibration and checking that no bubbles were

present. This procedure was continued until the absorbance became constant, indicating saturation binding had occurred. Figures are quoted as the average from a number of repeat experiments and the standard deviation.

7.2.5 Luminescence Titrations

Luminescence titrations were performed on a HORIBA Jobin Yvon FluoroMax-3 spectrometer. 3 mL of buffer was loaded into a 1 cm path length optical quartz cuvette. A volume of buffer was removed with a Gilson pipette and replaced with the same volume of stock solution of drug. This cuvette was placed into the sample cell of the spectrometer, mixed 15 times with a Gilson 1000 μL pipette, all bubbles removed and maintained at 25 °C. After equilibration, the emission spectrum was recorded using the excitation wavelength characteristic of the compound. A small volume of concentrated stock DNA solution was added to the cuvette and mixed, and then the emission was recorded. This procedure was continued until the emission became constant. Figures are quoted as the average from a number of repeat experiments and the standard deviation.

7.2.6 Isothermal Titration Calorimetry (ITC)

ITC experiments were conducted using a VP-ITC from MicroCal LLC (Northampton MA, USA) interfaced to a Gateway PIII PC. Data acquisition and analysis was performed using Origin 5.0 (MicroCal LLC) and all titrations were performed at 25 °C in the 5 mM Tris, 25 mM NaCl, pH 7.0 buffer, unless otherwise stated. The reference cell was filled with distilled water. The sample cell was filled with DNA (typical concentration of around 0.1 - 0.3 mM) and approximately 290 μL of the ligand (concentration between 0.5 - 1.5 mM) was loaded into the syringe and titrated into the DNA solution. After an initial injection of 3 μL, 18 injections of 15 μL each performed with a separation of 300 – 800 seconds depending on the rate with which the experiment returned to the baseline. The DNA solution was stirred continuously at 300 rpm throughout the experiments, which were maintained at 25 °C (unless is specified). Heats of

dilution for each compound were determined by titrating the complex into the buffer solution. These dilution heats were subtracted from the $\Delta H°$ value for DNA-complex titration to give a corrected heat effect. Each titration was repeated at least two times and the average of $\Delta H°$ was calculated.

The ITC technique was also used to perform salt concentration dependence experiments. Four difference ITC experiments were carried out for each compound in 5 mM TRIS buffer, pH 7.0 and with a salt concentration of 25 mM, 50 mM, 75 mM and 100 mM, respectively. It is then possible to determine the salt concentration dependence of the binding constant by plotting the log K against -log $[Na^+]$.

7.3 Synthetic Procedures

7.3.1 Preparation of 2,2':4,4'':4',4'''-Quaterpyridyl [2.1]

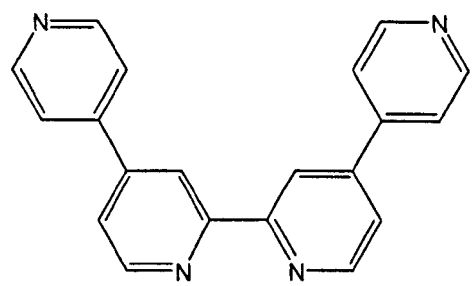

Figure 7.1: 2,2':4,4'':4',4'''-Quaterpyridyl.

4,4'-bipyridine (80 g, 0.51 mol) and 10 % palladium on carbon (16 g) were heated in a sealed bomb at 230^{0}C for 2 days. Chloroform (150 mL) was added and the mixture was refluxed for a further 30 minutes. Following filtration, to remove the Pd/C, acetone (150 mL) was added to the resulting solids and the mixture was stirred. The resulting slurry was filtered, yielding a crop of crude quaterpyridine. The volume of the filtrate was reduced *in vacuo* by approximately 50 ml to yield more solid, which was again collected. The batches of crude quaterpyridine were then combined and recrystallised from hot ethanol giving a cream solid.

Yield: 14.63 g (9.25 %).

FAB-MS: m/z = 310 [M^+].

^{1}H NMR ($CDCl_3$): δ_H = 8.82-8.68 (m, 8H), 7.65 (d, 4H, J_{HH} = 4.4 Hz, 1.7 Hz), 7.60 (d, 2H, J_{HH} = 4.9 Hz, 1.8 Hz).

7.3.2 Preparation of 1,10-phenanthroline-5,6-dione (dpq)

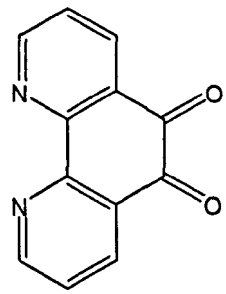

Figure 7.2: 1,10-phenanthroline-5,6-dione.

Concentrated sulphuric acid (60 ml) and concentrated nitric acid (30 ml) were mixed slowly in an ice bucket. 1,10-phenanthroline (8 g, 44.4 mmol) and sodium bromide (8 g, 77.6 mmol) were added to the acid mixture and refluxed heavily for 3h. After cooling the deep orange mixture was poured over ice (1 L) and neutralised to pH 7.0 with the addition of sodium hydrogen carbonate. The product was extracted with chloroform (4 x 150 ml) and dried over $MgSO_4$. The solvent was removed *in vacuo* and the yellow product was recrystallised from 1:1 methanol:water.

Yield: 3.50 g (37.50 %).

FAB-MS; m/z (%): 211 [M^+].

^1H NMR ($CDCl_3$): δ_H = 7.56 (dd, 2H, J_{HH} = 4.6 Hz, 2.0 Hz), 8.47 (dd, 2H, J_{HH} = 7.8 Hz, 2.0 Hz), 9.07 (dd, 2H, J_{HH} = 7.8 Hz, 4.6 Hz).

7.3.3 Preparation of Dipyrido [3,2-a:2',3'-c] phenazine (dppz) [2.2]

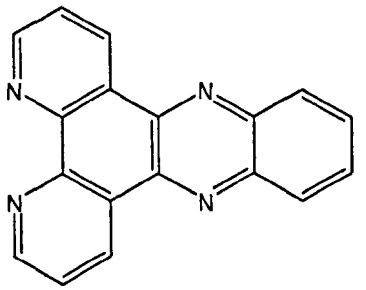

Figure 7.3: Dipyrido [3,2-a:2',3'-c] phenazine (dppz).

1,10-phenanthroline-5,6-dione (3.47 g, 16.5 mmol) and *o*-phenylene-diamine (1.78 g, 16.5 mmol) were refluxed in EtOH (100 ml) for 2h, during this period solution turned from dark brown to deep red). After cooling the solvent was removed *in vacuo* and the resulting solid was recrystallised with 1:1 EtOH/water. The recrystallised orange needles were collected by filtration, washed subsequently with ice cold water (50 ml) and ethanol (50 ml) and dried *in vacuo.*

Yield: 2.60 g (55.82 %).

FAB-MS; m/z (%): 283 [MH^+].

^{1}H NMR (d^6-$CDCl_3$): δ_H = 9.65 (dd, 2H, J_{HH} = 8.2 Hz, 1.6 Hz), 9.27 (dd, 2H, J_{HH} = 4.6 Hz, 1.7 Hz), 8.36 (dd, 2H, J_{HH} = 5.2 Hz, 3.5 Hz), 7.93 (dd, 2H, J_{HH} = 5.3 Hz, 3.5 Hz), 7.80 (dd, 2H, J_{HH} = 8.2 Hz, 4.4 Hz).

7.3.4 Preparation of $Ru(dppz)_2Cl_2$ [2.3]

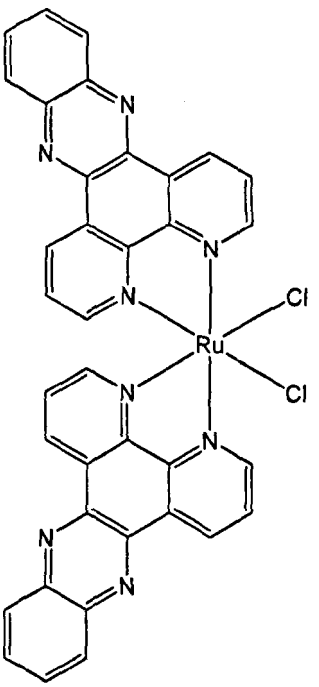

Figure 7.4: $Ru(dppz)_2Cl_2$.

Typically, ruthenium(III) chloride trihydrate (0.96 g, 3.82 mmol), dppz (2.08 g, 7.64 mmol) and LiCl (1.1 g) were dissolved in fresh DMF (10 ml) and heated to reflux for 8 hours. The purple solution was then cooled and poured into stirred acetone (50 ml) and cooled to 4^0C for 18 hours. The dark brown solid was collected by filtration and washed with water (3 x 25 ml), then dried *in vacuo*.

Yield: 1.83 g (62.01 %).

FAB-MS; m/z (%): 701 [M^+-Cl].

7.3.5 Preparation of $Ru(phen)_2Cl_2$ [2.4]

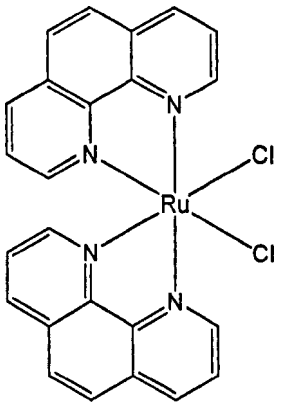

Figure 7.5: $Ru(phen)_2Cl_2$.

Typically, ruthenium(III) chloride trihydrate (10 g, 38.2 mmol), 1,10-phenanthroline (13.8 g, 76.6 mmol) and LiCl (11 g) were dissolved in fresh DMF (60 ml) and heated to reflux for 8 hours. The dark-brown solution was then cooled and poured into stirred acetone (200 ml) and cooled to 4^0C for 18 hours. The dark brown solid was collected by filtration and washed with water (3 x 25 ml), then dried *in vacuo*.

Yield: 10.73 g (49.40 %).

FAB-MS: $m/z = 497$ $[M^+-Cl]$, 462 $[M^{2+}-2Cl]$.

7.3.6 Preparation of $Ru(bpy)_2Cl_2$ [2.5]

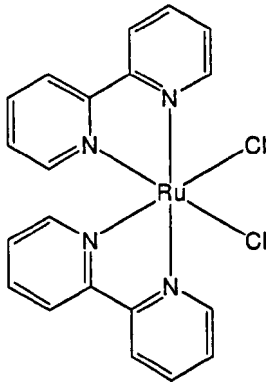

Figure 7.6: $Ru(bpy)_2Cl_2$.

Typically, ruthenium(III) chloride trihydrate (10 g, 38.2 mmol), 2,2'-bipyridine (12 g, 76.9 mmol) and LiCl (11 g) were dissolved in fresh DMF (60 ml) and heated to reflux for 8 hours. The purple solution was then cooled and poured into stirred acetone (200 ml) and cooled to 4^0C for 18 hours. The dark brown-purple solid was collected by filtration and washed with water (3 x 25 ml), then dried *in vacuo*.

Yield: 12.30 g (61.92 %).

FAB-MS: m/z = 484 [M^+], 449 [M^+-Cl].

7.3.7 Preparation of $[Ru(dppz)_2(qtpy)](PF_6)_2$ [2.6]

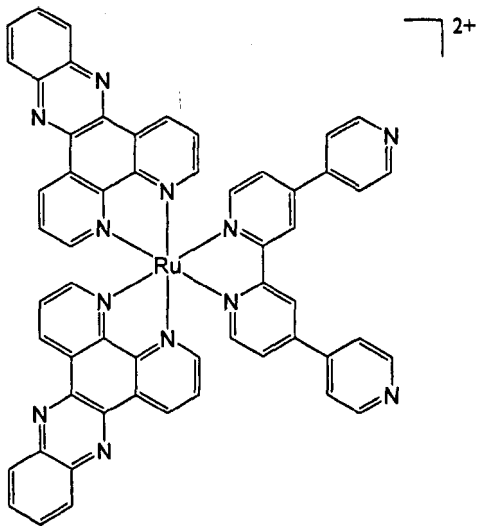

Figure 7.7: $[Ru(dppz)_2(qtpy)](PF_6)_2$.

Typically $Ru(dppz)_2Cl_2$ (0.5 g, 0.647 mmol) and qtpy (0.2 g, 0.645 mmol) were heated to reflux in freshly distilled, dry ethylene glycol for 1 hour. Upon cooling, the red-orange product was isolated by addition of solid NH_4PF_6, filtered, washed successively with water (2 x 10 ml), ethanol (2 x 10 ml) and diethyl ether (2 x 10 ml), then dried *in vacuo*. This crude product was purified by column chromatography on grade 1, neutral alumina, eluting with a 1:1:9 KNO_3:water:acetonitrile mixture.

Yield: 0.61 g (75 %).

ES-MS; m/z (%): 1121 $[M^+-PF_6]$, 488 $[M^{2+}-2PF_6]$.

Accurate Mass: Calculated for $RuC_{56}H_{34}N_{12}F_6P$. $[M^+-PF_6]$: 1121.1715.
Observed: 1121.1752 ± 3.3 PPM.

^1H NMR (d^3-acetonitrile): δ_H = 9.79 (dd, 2H, J_{HH} = 8.3 Hz, 1.2 Hz), 9.68 (dd, 2H, J_{HH} = 8.2 Hz, 1.3 Hz), 9.10 (s, 2H), 8.85 (dd, 4H, J_{HH} = 4.6 Hz, 1.7 Hz), 8.54 (m, 4H), 8.44 (dd, 2H, J_{HH} = 5.4 Hz, 1.5 Hz), 8.23 (dd, 2H, J_{HH} = 5.4 Hz, 1.5 Hz), 8.19 (m, 4H), 8.07 (d, 2H, J_{HH} = 5.9 Hz), 8.03 (dd, 2H, J_{HH} = 8.1 Hz, 5.4 Hz), 7.91 (dd, 4H, J_{HH} = 4.6 Hz, 1.7 Hz), 7.83 (dd, 2H, J_{HH} = 8.1 Hz, 5.4 Hz), 7.71(dd, 2H, J_{HH} = 6.0 Hz, 1.9 Hz).

Elemental analysis calculated for $C_{56}H_{34}F_{12}N_{12}P_2Ru.H_2O$: C, 52.38; H, 2.83; N, 13.09. Found: C, 52.25; H, 2.72; N, 12.93.

7.3.8 Preparation of $[Ru(phen)_2(qtpy)](PF_6)_2$ [2.7]

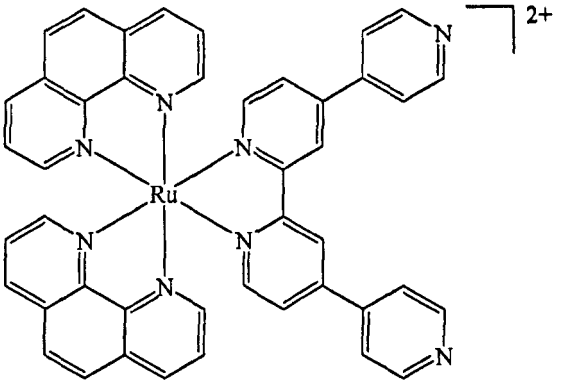

Figure 7.8: $[Ru(phen)_2(qtpy)](PF_6)_2$.

Typically $Ru(phen)_2Cl_2$ (0.74 g, 1.288 mmol) and qtpy (0.4 g, 1.288 mmol) were heated to reflux in freshly distilled, dry ethylene glycol for 1 hour. Upon cooling, the red-orange product was isolated by addition of solid NH_4PF_6, filtered, washed successively with water (2 x 10 ml), ethanol (2 x 10 ml) and diethyl ether (2 x 10 ml), then dried *in vacuo*. This crude product was purified by column chromatography on grade 1, neutral alumina, eluting with a acetonitrile.

Yield: 1.21 g (88.41 %).

ES-MS; m/z (%): 917 $[M^+-PF_6]$, 386 $[M^{2+}-2PF_6]$.

Accurate Mass: Calculated for $RuC_{44}H_{30}N_8$. $[M^{2+}-2PF_6]$: 386.0819.
Observed: 386.0833 ± 3.6 PPM.

^1H NMR (d^3-acetonitrile): δ_H = 9.02 (s, 2H), 8.83 (dd, 4H, J_{HH} = 4.7 Hz, 1.7 Hz), 8.71 (dd, 2H, J_{HH} = 8.2 Hz, 1.1 Hz), 8.61 (dd, 2H, J_{HH} = 8.2 Hz, 1.1 Hz), 8.32 (dd, 2H, J_{HH} = 5.3 Hz, 1.1 Hz), 8.30 (m, 4H), 7.94 (dd, 2H, J_{HH} = 5.1 Hz, 1.2 Hz), 7.87 (dd, 4H, J_{HH} = 4.7 Hz, 1.7 Hz), 7.83 (m, 2H), 7.62 – 7.58 (m, 6H).

Elemental analysis calculated for $C_{44}H_{30}F_{12}N_8P_2Ru.3H_2O$: C, 47.36; H, 3.25; N, 10.04. Found: C, 47.31; H, 2.71; N, 9.86.

7.3.9 Preparation of $[Ru(bpy)_2(qtpy)](PF_6)_2$ [2.8]

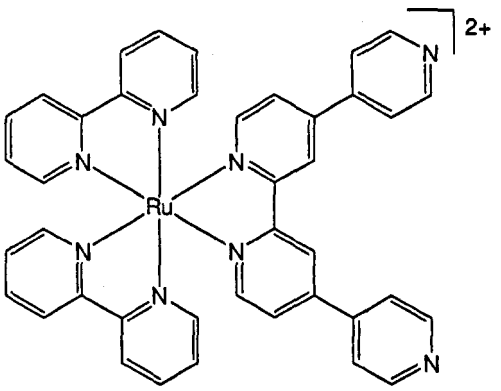

Figure 7.9: $[Ru(bpy)_2(qtpy)](PF_6)_2$.

Typically $Ru(bpy)_2Cl_2$ (0.2 g, 3.85 mmol) and qtpy (0.119 g, 3.87 mmol) were heated to reflux in freshly distilled, dry ethylene glycol for 1 hour. Upon cooling, the red-orange product was isolated by addition of solid NH_4PF_6, filtered, washed successively with water (2 x 10 ml), ethanol (2 x 10 ml) and diethyl ether (2 x 10 ml), then dried *in vacuo*. This crude product was purified by column chromatography on grade 1, neutral alumina, eluting with a 1:1 acetonitrile:toluene mixture.

Yield: 0.351 g (89.93 %).

ES-MS; m/z (%): 869 $[M^+-PF_6]$, 362 $[M^{2+}-2PF_6]$.

^1H NMR (d^3-acetonitrile): δ_H = 8.90 (s, 2H), 8.83 (dd, 4H, J_{HH} = 4.5 Hz, 1.6 Hz), 8.56 (d, 4H, J_{HH} = 8.1 Hz), 8.11 (m, 4H), 7.89 (d, 2H, J_{HH} = 6.1 Hz), 7.86 (dd, 4H, J_{HH} = 4.5 Hz, 1.6 Hz), 7.84 (d, 2H, J_{HH} = 5.6 Hz), 7.79 (d, 2H, J_{HH} = 5.1 Hz), 7.75 (dd, 2H, J_{HH} = 6.0 Hz, 1.8 Hz), 7.45 (m, 4H).

7.3.10 Preparation of $[Ru(dppz)_2(qtpyMe_2)][PF_6]_4$ [2.9]

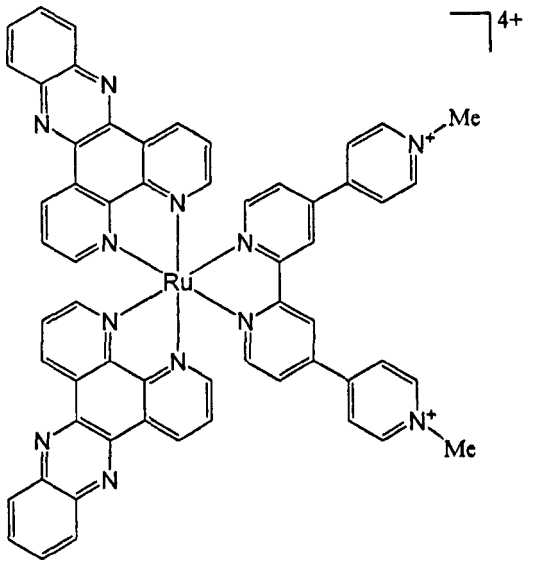

Figure 7.10: $[Ru(dppz)_2(qtpyMe_2)](PF_6)_4$.

A mixture of the $[Ru(dppz)_2(qtpy)](PF_6)_2$ (0.2 g, 0.158 mmol) and a fifteen-fold molar excess of methyl iodide (0.098 ml, 1.58 mmol) in acetonitrile was stirred at 50°C for two days. The solvent was removed on a rotary evaporator. The red-orange residue was redissolved in aqueous methanol (1:1) and KPF_6, added to precipitate the product, which was collected by filtration and dried.

Yield: 0.176 g (70.23 %).

FAB-MS; m/z (%): 1441 $[M^+-PF_6]$, 1296 $[M^{2+}-2PF_6]$, 1151 $[M^{3+}-3PF_6]$, 648 $[M^{2+}-2PF_6]$.

Accurate Mass: Calculated for $RuC_{58}H_{40}N_{12}F_{18}P_3$. $[M^+ -PF_6]$: 1441.1468.
Observed: 1441.1399 ± 4.8 PPM.

^1H NMR (d^3-acetonitrile): δ_H = 9.81 (dd, 2H, J_{HH} = 8.2 Hz, 1.1 Hz), 9.72 (dd, 2H, J_{HH} = 8.2 Hz, 1.2 Hz), 9.13 (s, 2H), 8.83 (d, 4H, J_{HH} = 6.9 Hz), 8.54 (m, 4H), 8.45 (d, 4H, J_{HH} = 6.9 Hz), 8.42 (dd, 2H, J_{HH} = 5.3 Hz, 1.1 Hz), 8.23 (d, 2H, J_{HH} = 1.2 Hz), 8.21 (m, 4H), 8.19 (s, 2H), 8.03 (dd, 2H, J_{HH} = 8.2 Hz, 5.3 Hz), 7.85 (dd, 2H, J_{HH} = 8.3 Hz, 5.4 Hz), 7.79 (dd, 2H, J_{HH} = 6.0 Hz, 1.8 Hz), 4.44 (s, 6H).

Elemental analysis calculated for $C_{58}H_{40}F_{24}N_{12}P_4Ru.3H_2O$: C, 42.48; H, 2.83; N, 10.25. Found: C, 41.98; H, 2.58; N, 9.97.

7.3.11 Preparation of $[Ru(phen)_2(qtpyMe_2)](PF_6)_4$ [2.10]

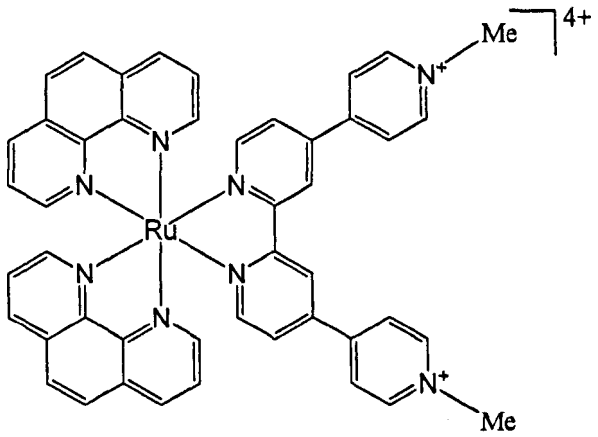

Figure 7.11: $[Ru(phen)_2(qtpyMe_2)](PF_6)_4$.

A mixture of the $[Ru(phen)_2(qtpy)](PF_6)_2$ (0.1 g, 0.094 mmol) and a fifteen-fold molar excess of methyl iodide (0.088 ml, 1.41 mmol) in acetonitrile was stirred at 50°C for two days. The solvent was removed on a rotary evaporator. The red-orange residue was redissolved in aqueous methanol (1:1) and KPF_6, added to precipitate the product, which was collected by filtration and dried.

Yield: 0.100 g (76.86 %).

ES-MS; m/z (%): 1238 $[M^+-PF_6]$, 546 $[M^{2+}-2PF_6]$.

Accurate Mass: Calculated for $RuC_{46}H_{37}N_8F_{18}P_3$. $[M^+ -PF_6]$: 1238.1110.
Observed: 1238.1051± 4.8 PPM.

^1H NMR (d^3-acetonitrile): δ_H = 9.22 (s, 2H), 8.82 (d, 4H, J_{HH} = 6.9 Hz), 8.73 (dd, 2H, J_{HH} = 8.3 Hz, 1.2 Hz), 8.63 (dd, 2H, J_{HH} = 8.3 Hz, 1.2 Hz), 8.55 (d, 4H, J_{HH} = 6.9 Hz), 8.31 (m, 4H), 8.01 (d, 2H, J_{HH} = 5.9 Hz), 7.93 (dd, 2H, J_{HH} = 5.1 Hz, 1.2 Hz), 7.84 (dd, 2H, J_{HH} = 8.3 Hz, 5.1 Hz), 7.73 (dd, 2H, J_{HH} = 5.9 Hz, 1.8 Hz), 7.63 (dd, 4H, J_{HH} = 8.3 Hz, 5.1 Hz), 4.34 (s, 6H).

Elemental analysis calculated for $C_{46}H_{36}F_{24}N_8P_4Ru.4H_2O$: C, 38.00; H, 3.05; N, 7.71. Found: C, 37.45; H, 2.65; N, 7.51.

7.3.12 Preparation of $[Ru(bpy)_2(qtpyMe_2)](PF_6)_4$ [2.11]

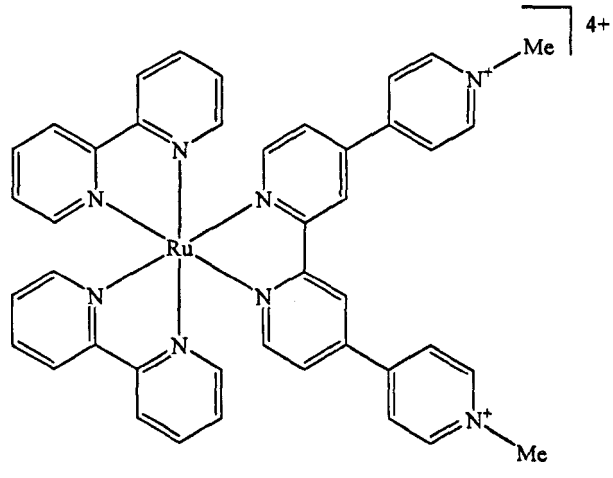

Figure 7.12: $[Ru(bpy)_2(qtpyMe_2)](PF_6)_4$.

A mixture of the $[Ru(bpy)_2(qtpy)](PF_6)_2$ (0.2 g, 0.197 mmol) and a fifteen-fold molar excess of methyl iodide (0.184 mL, 2.96 mmol) in acetonitrile was stirred at 50°C for two days. The solvent was removed on a rotary evaporator. The red-orange residue was redissolved in aqueous methanol (1:1) and KPF_6, added to precipitate the red-orange product, which was collected by filtration and dried.

Yield: 0.223 g (43.43 %).

ES-MS; m/z (%): 1189 $[M^+-PF_6]$, 522 $[M^{2+}-2PF_6]$.

^1H NMR (d^3-acetonitrile): δ_H = 9.07 (s, 2H), 8.84 (d, 4H, J_{HH} = 6.8 Hz), 8.57 (d, 4H, J_{HH} = 7.8 Hz), 8.46 (d, 4H, J_{HH} = 6.8 Hz), 8.13 (m, 4H), 8.05 (d, 2H, J_{HH} = 5.9 Hz), 7.84 (dd, 2H, J_{HH} = 6.1 Hz, 2.0 Hz), 7.80 (d, 2H, J_{HH} = 5.6 Hz), 7.76 (d, 2H, J_{HH} = 5.9 Hz), 7.46 (m, 4H), 4.40 (s, 6H).

7.3.13 Preparation of $Re(qtpy)(CO)_3Cl$ [2.12]

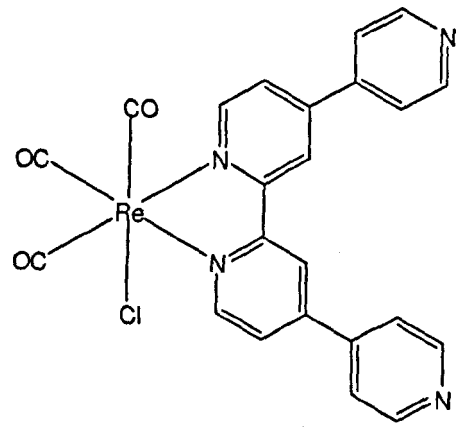

Figure 7.13: $Re(qtpy)(CO)_3Cl$.

$[Re(CO)_5Cl]$ (0.5 g, 1.38 mmol) and qtpy (0.45 g, 1.45 mmol) were heated to reflux for 8 hours in a 2:1 toluene:THF mixture (100 ml). Upon cooling to room temperature the orange solids precipitated out of solution and was collected by centrifugation, washed with $CHCl_3$, and dried *in vacuo*.

Yield: 0.47 g (55.29 %).

FAB-MS; m/z (%): 617 $[MH^+]$, 616 $[M^+]$ 581 $[MH^+ Cl]$.

^1H NMR (d^6-DMSO): δ_H = 9.33 (s, 2H), 9.15 (d, 2H, J_{HH} = 5.8 Hz), 8.89 (d, 4H, J_{HH} = 5.8 Hz), 8.20 (d, 2H, J_{HH} = 4.3 Hz), 8.10 (d, 4H, J_{HH} = 5.8 Hz).

7.3.14 Preparation of [Re(qtpy)(CO)$_3$(NCMe)][OTf] [2.13]

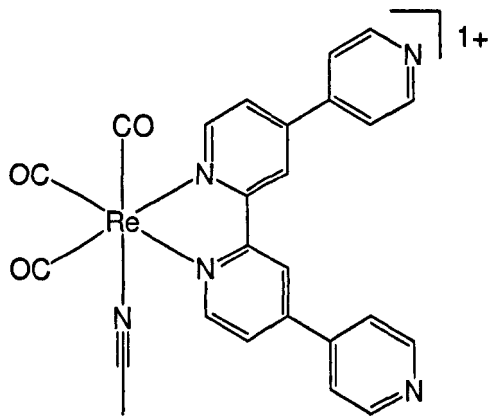

Figure 7.14: [Re(CO)$_3$(qtpy)(NCMe)][OTf].

Re(CO)$_3$(qtpy)Cl (0.8 g, 1.30 mmol) and AgOTf (0.36 g, 1.38 mmol) were heated to reflux in freshly distilled acetonitrile (50 ml) for 10 hours. The AgCl produced was removed by filtration through Celite. The mixture was added to excess diethyl ether and the yellow solids precipitated out as the OTf$^-$ salt, separated by centrifugation, and dried *in vacuo*.

Yield: 0.77 g (76.90 %).

FAB-MS; m/z (%): 622 [MH$^+$-OTf], 581[M$^+$-OTf-MeCN].

^{1}H NMR (d^3-acetonitrile): δ_H = 9.17 (d, 2H, J_{HH} = 5.9 Hz), 8.96 (d, 2H, J_{HH} = 2.0 Hz), 8.89 (dd, 4H, J_{HH} = 4.6 Hz, 1.7 Hz), 8.08 (dd, 2H, J_{HH} = 5.9 Hz, 2.0 Hz), 7.97 (dd, 4H, J_{HH} = 4.6 Hz, 1.7 Hz), 2.04 (s, 3H).

7.3.15 Preparation of $[Re(qtpyMe_2)(CO)_3Cl][PF_6]_2$ [2.14]

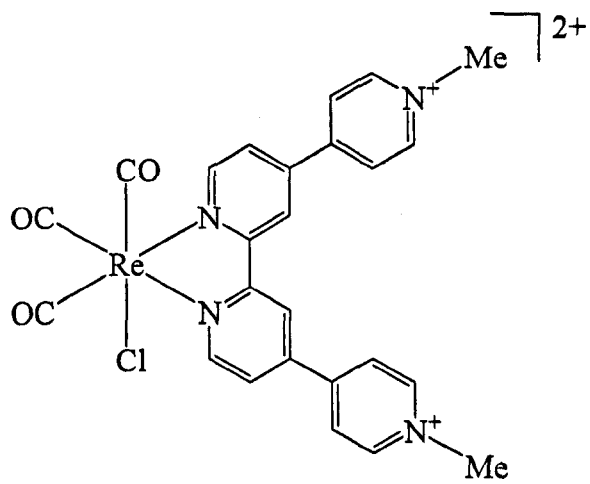

Figure 7.15: Preparation of $[Re(qtpyMe_2)(CO)_3Cl][PF_6]_2$

A mixture of the $[Re(qtpy)(CO)_3Cl]$ (0.3 g , 0.487 mmol) and a fifteen-fold molar excess of methyl iodide (0.45 ml, 7.31 mmol) in acetonitrile was stirred at 50°C for two days. The solvent was removed on a rotary evaporator. The red-orange residue was redissolved in aqueous methanol (1:1) and KPF_6, added to precipitate the product, which was collected by filtration and dried.

Yield: 0.148 g (32.47 %).

ES-MS; m/z (%): 791 $[M^+-PF_6]$, 756 $[M^+-PF_6-Cl]$.

Accurate Mass: Calculated for $ReC_{25}H_{20}N_4F_6O_3P_1Cl$ $[M^+ -PF_6]$: 791.0423

Observed: 791.0419 ± 0.6 PPM.

^1H NMR (d^6-DMSO): δ_H = 9.47 (s, 2H), 9.39 (d, 2H, J_{HH} = 5.8 Hz), 9.31 (d, 4H, J_{HH} = 6.1 Hz), 8.82 (d, 4H, J_{HH} = 6.1 Hz), 8.37 (d, 2H, J_{HH} = 5.8 Hz), 4.46 (s, 6H).

Elemental analysis calculated for $C_{25}H_{20}F_{12}N_4P_2O_3Re.4H_2O$: C, 29.79; H, 2.80; N, 5.56. Found: C, 29.26; H, 2.27; N, 5.42.

7.3.16 Preparation of $[Re(qtpyMe_2)(CO)_3(NCMe)][PF_6]_3$ [2.15]

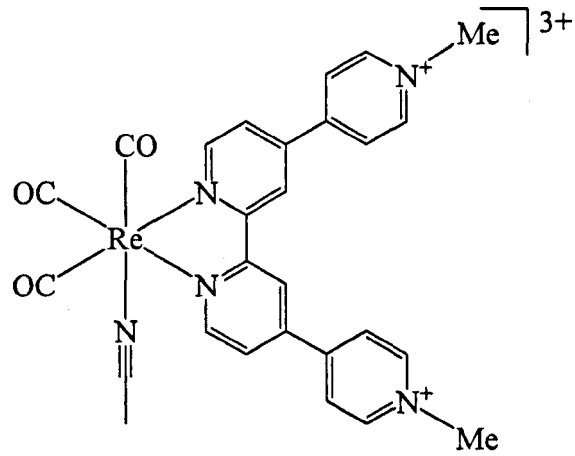

Figure 7.16: Preparation of $[Re(qtpyMe_2)(CO)_3(NCMe)][PF_6]_3$.

A mixture of the $[Re(qtpy)(CO)_3(NCMe)][OTf]$ (0.1 g, 0.13 mmol) and a fifteen-fold molar excess of methyl iodide (0.121 ml, 1.95 mmol) in acetonitrile was stirred at 50°C for two days. The solvent was removed on a rotary evaporator. The red-orange residue was redissolved in aqueous methanol (1:1) and KPF_6, added to precipitate the product, which was collected by filtration and dried.

Yield: 0.068 g (48.17 %).

ES-MS; m/z (%): 399 $[M^{2+}\text{-}2PF_6]$.

Accurate Mass: Calculated for $ReC_{27}H_{23}N_5F_6O_3P_1Cl$ $[M^{2+}\text{-}2PF_6]$:398.5500.
Observed: 398.5481 ± 4.8 PPM.

^1H NMR (d^3-acetonitrile): δ_H = 9.39 (d, 2H, J_{HH} = 5.6 Hz), 8.98 (s, 2H), 8.87 (d, 4H, J_{HH} = 6.6 Hz), 8.52 (d, 4H, J_{HH} = 6.6 Hz), 8.08 (dd, 2H, J_{HH} = 5.9 Hz, 2.0 Hz), 4.42 (s, 6H), 2.11 (s, 3H).

Elemental analysis calculated for $C_{27}H_{23}F_{18}N_5P_3O_3Re.2(CH_3OH)$: C, 30.27; H, 2.72; N, 6.09. Found: C, 30.79; H, 2.23; N, 5.96.

7.3.17 Preparation of RubpyRe Macrocycle [4.1]

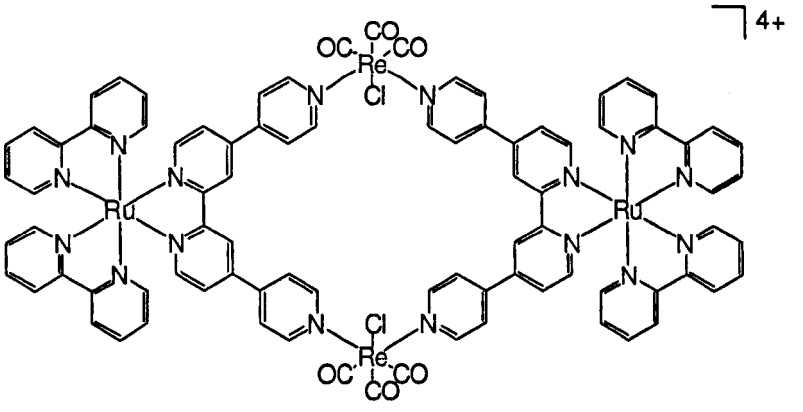

Figure 7.17: RubpyRe Macrocycle.

$[Ru(bpy)_2(qtpy)](PF_6)_2$ (0.200 g, 0.2 mmol) and $Re(CO)_5Cl$ (0.071 g, 0.2 mmol) in 30 ml 1:1 MeCN:THF solution were heated to reflux for 2 days. After this time excess THF was added and a red solid precipitated out. The precipitate was collected by filtration and washed successively with 2 x 25 ml THF and 3 x 25 ml diethyl ether, then dried *in vacuo*. The deep red solid obtained was purified on a silica column, eluting with a 0.1:1:9 KNO_3:water:acetonitrile mixture.

Yield: 0.148 g (30 %).

ES-MS; m/z (%): 1175 $[M^{2+} - 2PF_6]$, 1139 $[M^{4+} - 2PF_6 - 2Cl]$, 735 $[M^{3+} - 3PF_6]$.

^1H NMR (d^3-acetonitrile): δ_H = 9.09 (d, 8H, J_{HH} = 5.4 Hz), 8.85 (s, 4H), 8.54 (d, 8H, J_{HH} = 8.1 Hz), 8.11 (m, 8H), 7.92 - 7.90 (m, 12H), 7.78 (d, 4H, J_{HH} = 4.9 Hz), 7.75 (d, 4H, J_{HH} = 5.4 Hz), 7.70 (d, 4H, J_{HH} = 5.9 Hz), 7.45 (m, 8H).

Elemental analysis calculated for $C_{86}H_{60}Cl_2F_{24}N_{16}O_6P_4Re_2Ru_2.3H_2O$: C, 38.36; H, 2.47; N, 8.32. Found: C, 38.04; H, 2.48; N, 8.01.

7.3.18 Preparation of RuphenRe Macrocycle [4.2]

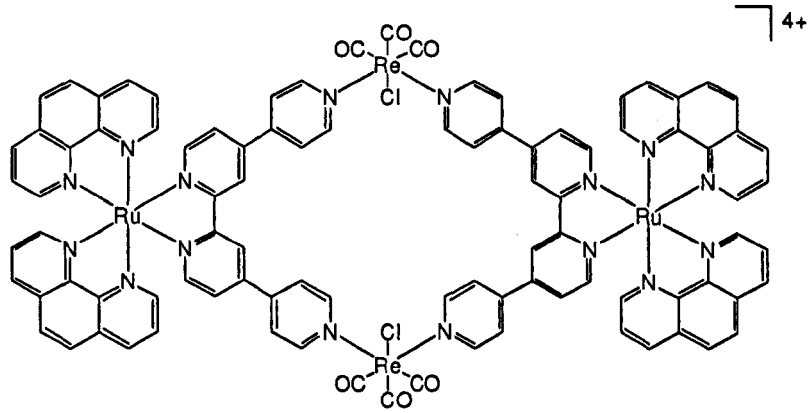

Figure 7.18: RuphenRe Macrocycle.

$[Ru(phen)_2(qtpy)](PF_6)_2$ (0.253g, 0.24mmol) and $Re(CO)_5Cl$ (0.086g, 0.24 mmol) in 30 ml 1:1 MeCN:THF solution were heated to reflux for 2 days. After this time excess THF was added and a red solid precipitated out. The precipitate was collected by filtration and washed successively with 2 x 25 ml THF and 3 x 25 ml diethyl ether, then dried *in vacuo*. The red solid obtained was purified on a silica column, eluting with a 0.1:1:9 KNO_3:water:acetonitrile mixture.

Yield: 0.295 g (45 %).

ES-MS; m/z (%): 1223 $[M^{2+} - 2PF_6]$, 767 $[M^{3+} - 3PF_6]$.

^1H NMR (d^3-acetonitrile): δ_H = 9.07 (d, 8H, J_{HH} = 5.4 Hz), 8.88 (s, 4H), 8.70 (d, 4H, J_{HH} = 8.3 Hz), 8.60 (d, 4H, J_{HH} = 8.3 Hz), 8.28 (m, 8H), 7.92 (d, 4H, J_{HH} = 5.4 Hz), 7.89 - 7.87 (m, 12H), 7.82 (m, 8H), 7.61 (dd, 4H, J_{HH} = 8.3 Hz, 5.4 Hz), 7.59 (d, 4H, J_{HH} = 7.1 Hz).

Elemental analysis calculated for $C_{94}H_{60}Cl_2F_{24}N_{16}O_6P_4Re_2Ru_2.6H_2O$: C, 39.71; H, 2.55; N, 7.88. Found: C, 39.18; H, 2.04; N, 7.59.

7.3.19 Preparation of RudppzRe Macrocycle [4.3]

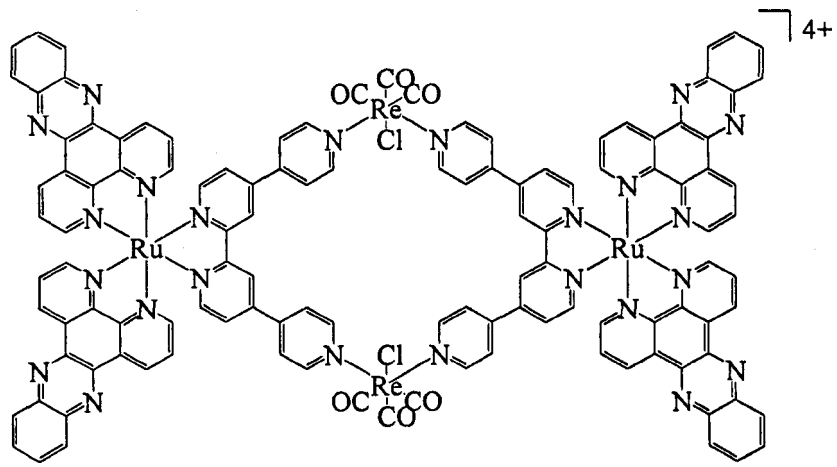

Figure 7.19: RudppzRe Macrocycle.

$[Ru(dppz)_2(qtpy)](PF_6)_2$ (0.256 g, 0.2 mmol) and $Re(CO)_5Cl$ (0.073 g, 0.2 mmol) in 30 ml 1:1 MeCN:THF solution were heated to reflux for 2 days. After this time excess THF was added and a red solid precipitated out. The precipitate was collected by filtration and washed successively with 2 x 25 ml THF and 3 x 25 ml diethyl ether, then dried *in vacuo*. This crude product was purified by column chromatography on silica, eluting with a 0.1:1:9 KNO_3:water:acetonitrile mixture.

Yield: 0.220 g (35 %).

ES-MS; m/z (%): 1427 $[M^{2+} - 2PF_6]$, 903 $[M^{3+} - 3PF_6]$.

^1H NMR (d^3-acetonitrile): δ_H = 9.79 (dd, 4H, J_{HH} = 8.3 Hz, 1.2 Hz), 9.70 (dd, 4H, J_{HH} = 8.3 Hz, 1.2 Hz), 9.10 (s, 4H), 8.84 (d, 8H, J_{HH} = 6.1 Hz), 8.53 (m, 8H), 8.40 (dd, 4H, J_{HH} = 5.4 Hz, 1.2 Hz), 8.23 (dd, 4H, J_{HH} = 5.4 Hz, 1.2 Hz), 8.19 (m, 8H), 8.10 (d, 12H, J_{HH} = 6.0 Hz), 8.03 (dd, 4H, J_{HH} = 8.3 Hz, 5.4 Hz), 7.82 (dd, 4H, J_{HH} = 8.3 Hz, 5.4 Hz), 7.74 (dd, 4H, J_{HH} = 5.9 Hz, 2.0 Hz).

Elemental analysis calculated for $C_{118}H_{68}Cl_2F_{24}N_{24}O_6P_4Re_2Ru_2.4H_2O$: C, 44.08; H, 2.38; N, 10.45. Found: C, 43.72; H, 2.22; N, 10.06.

8 Appendix

8.1 Crystallographic Data

Summary of crystallographic data for **[2.6]**$[(PF_6)_2]$, **[2.7]**$[(PF_6)_2].C_6H_6$ and **[2.8]**$[(PF_6)_2].MeNO_3$.

	[2.6]$[(PF_6)_2]^a$	**[2.7]**$[(PF_6)_2].C_6H_6{}^b$	**[2.8]**$[(PF_6)_2].MeNO_3{}^c$
Empirical formula	$C_{56}H_{34}F_{7.50}N_{12}P_{1.25}Ru$	$C_{50}H_{36}F_{12}N_8P_2Ru$	$C_{41}H_{33}F_{12}N_9O_2P_2Ru$
f_w	1157.23	1139.88	1074.77
Crystal System	Monoclinic	Orthorhombic	Monoclinic
Space group	$P2_1/c$	Pbcn	$P2_1/c$
Crystal dimensions (mm)	0.09 x 0.07 x 0.03	0.21 x 0.11 x 0.10	0.10 x 0.01 x 0.01
A (Å)	20.502(4)	19.924(5)	21.011(4)
b (Å)	13.933(2)	13.886(3)	14.830(3)
c (Å)	42.078(8)	17.850(5)	14.319(3)
α (deg)	90	90	90
β (deg)	103.286(3)	90	93.83(3)
γ (deg)	90	90	90
U (Å^3)	11698(3)	4939(2)	4451.8(16)
Z	8	4	4
D_c (mg/m^3)	1.314	1.533	1.604
F(000)	4674	2296	2160
μ(Mo-Kα) (mm^{-1})	0.372	0.472	0.522
Final R1 (on F)[a]	0.3013	0.1018	0.1665
Final wR2 (on F)[a]	0.5532	0.2569	0.4770

[a]A weighting scheme $w = 1/[\sigma^2(Fo^2) + (0.2000*P)^2+0.00*P]$ where $P=(Fo^2+ 2 * Fc^2)/3$ was used in the latter stages of refinement. [b]A weighting scheme $w = 1/[\sigma^2(Fo^2) + (0.1230*P)^2+103.1388*P]$ where $P=(Fo^2+ 2 * Fc^2)/3$ was used in the latter stages of refinement. [c]A weighting scheme $w = 1/[\sigma^2(Fo^2) + (0.2000*P)^2+0.00*P]$ where $P=(Fo^2+ 2 * Fc^2)/3$ was used in the latter stages of refinement.

9 References

[1] P. A. Gale, *Phil. Trans. R. Soc. Lond. A*, **2000**, *358*, 431-453.

[2] Steed, J. W.; Atwood, J. L. Supramolecular Chemistry, John Wiley & Sons, Ltd: New York, **2000**.

[3] M. M. Conn, J. Rebek Jr., *Chem. Rev.* **1997**, *97*, 1647.

[4] H. Ogino, *J. Am. Chem. Soc.*, **1981**, *103*, 1303; *New J. Chem.*, **1993**, *17*, 683.

[5] (a) C. O. D.-Buchecker, J.-P. Sauvage, J. P. Kintzinger, *Tetrahedron Lett.*, **1983**, *24*. 5095. (b) C. O. D.-Buchecker, J.-P. Sauvage, *Chem. Rev.*, **1987**, *87*, 795. (c) J.-P. Sauvage, *Acc. Chem. Res.*, **1990**, *23*, 319.

[6] P. N. W. Baxter, J.-M. Lehn, J. Fischer, M.-T. Youinou, *Angew. Chem. Int. Ed. Engl.*, **1994**, *33*, 2284.

[7] Sleiman, H.; Baxter, P.; Lehn, J.-M.; Rissanenb, K. *J. Chem. Soc., Chem. Commun.*, **1995**, 715.

[8] (a) M. Fujita, J. Yazaki, K. Ogura. *J. Am. Chem. Soc.*, **1990**, *112*, 5645; (b) M. Fujita, F. Ibukuro, K. Yamaguchi, K. Ogura, *J. Am. Chem. Soc.*, **1995**, *117*, 4175.

[9] M. Fujita, O. Sasaki, T. Mitsuhashi, T. Fujita, J. Yazaki, K. Yamaguchi and K. Ogura, *Chem. Commun.*, **1996**, 1535.

[10] S. B. Lee, S. Hwang, D. S. Chung, H. Yun and J. -I. Hong, *Tetrahedron Lett.*, **1998**, *39*, 873-876.

[11] P. J. Stang, D. H. Cao, *J. Am. Chem. Soc.*, **1994**, *116*, 4981.

[12] P. J. Stang, B. Olenyuk, J. Fan, A. M. Arif. *Organometallics*, **1996**, *15*, 904.

[13] R.V. Slone, J. T. Hupp, C. L. Stern, T. E. Albrecht-Schmitt. *Inorg. Chem.*, **1996**, *35*, 4096.

[14] J. A. Thomas, *Chem. Soc. Rev.*, **2007**, *36*, 856–868.

[15] S. S. Sun, A. J. Lees. *Inorg. Chem.* **2001**, *40*, 3154.

[16] V. C. Lau, L. A. Berben and J. R. Long, *J. Am. Chem. Soc.*, **2002**, *124*, 9042-9043.

[17] N. Shan, J. D. Ingram, T. L. Easun, S. J. Vickers, H. Adams, M. D. Ward and J. A. Thomas, *Dalton Trans.*, **2006**, 2900–2906.

[18] S. Roche, C. Haslam, H. Adams, S. L. Heath, J. A. Thomas, *Chem. Commun.*, **1998**, 1681.

[19] M. Tominaga, K. Suzuki, M. Kawano, T. Kusukawa, T. Ozeki, S. Sakamoto, K. Yamaguchi and M. Fujita, *Angew. Chem. Int. Ed.*, **2004**, *43*, 5621 –5625.

[20] S. P. Argent, H. Adams, T. R.-Johannessen, J. C. Jeffery, L. P. Harding and M. D. Ward, *J. Am. Chem. Soc.*, **2006**, *128*, 72-73.

[21] P. H. Dinolfo, J. T. Hupp, *Chem. Mater.* **2001**, *13*, 3113.

[22] G. F. Swiegers, T. J. Malefetse, *Coord. Chem. Rev.*, **2002**, *225*, 91.

[23] A. Hamilton, J.-M. Lehn, J. L. Sessler, *J. Am. Chem. Soc.* **1986**, *108*, 5158.

[24] C. A. Hunter. *Chem. Commun.* **1991**, 749.

[25] P. D. Beer and P. A. Gale, *Angew. Chem. Int. Ed.*, **2001**, *40*, 486 - 516.

[26] R. V. Slone, D. I. Yoon, R. M. Calhoun, J. T. Hupp. *J. Am. Chem. Soc.* **1995**, *117*, 11813.

[27] P. de Wolf, P. Waywell, M. Hanson, S. L Heath, A. J. H. M. Meijer, S. J Teat, J. A. Thomas, *Chem. Eur. J.*, **2006**, *12*, 2188 – 2195.

[28] P. De Wolf, S. L. Heath, J. A. Thomas, *Chem. Commun.*, **2002**, 2540.

[29] P. De Wolf, Ph. D Thesis, University of Sheffield, **2002**.

[30] a) S. Leininger, B. Olenyuk, P. J. Stang, *Chem. Rev. 2000*, 100, 853 ;b) G. F. Swiegers, T. J. Malefetse, *Chem. Rev.*, **2000**, *100*, 3483.

[31] F. Ibukuro, T. Kusukawa, M. Fujita, *J. Am.Chem. Soc.*, **1998**, *120*, 8561.

[32] a) J. Edwards, R. Sprung, R. Sprague, D. Spence, *Analyst*, **2001**, *126*, 1257; b) T. Sakakibara, S. Murakami, N. Hattori, M. Nakajima, K. Imai, *Anal. Biochem.*, **1997**, *250*, 157; c) T. Kamidate, S. Niwa, N. Nakata, *Anal. Chim. Acta*, **2000**, *424*, 169; d) P. Ronner, E. Friel, K. Czerniawski, S. Fraenkle, *Anal. Biochem.*, **1999**, *275*, 208; e) F. Dai, J. A. Kelley, H. P. Zhang, N. Malinowski, M. F. Kavlick, J. Lietzau, L. Welles, R. Yarchoan, H. Ford Jr., *Anal. Biochem.*, **2001**, *288*, 52.

[33] a) A. D. Hamilton, D. V. Engen, *J. Am. Chem. Soc.*, **1987**, *109*, 5035; b) M. W. Hosseini, J. -M. Lehn, M. P. Mertes, *Helv. Chim. Acta*, **1983**, *66*, 2454; c) M. Shionaya, T. Ikeda, E. Kimura, S. Motoo, *J. Am. Chem. Soc.*, **1994**, *116*, 3848.

[34] S. E. Schneider, S. N. O'Nei and E. V. Anslyn, *J. Am. Chem. Soc.*, **2000**, *122*, 542-543.

[35] a) S. M. Butterfield and M. L. Waters, *J. Am. Chem. Soc.*, **2003**, *125*, 9580-9581; b) Z. Kejík, K. Záruba, D. Michalík, J. Sěbek, J. Dian, S. Pataridis, K. Volka and V. Král, *Chem. Commun.*, **2006**, 1533-1535.

[36] M. Sirish and H.-J. Schneider, *J. Am. Chem. Soc.*, **2000**, *122*, 5881.

[37] M. Shionoya, E. Kimura, M. Shiro, *J. Am. Chem. Soc.*, **1993**, *115*, 6730-6737.

[38] a) E. Kimura, M. Kikuchi, H. Kitamura and T. Koike, *Chem. Eur. J.*, **1999**, *5*, 3113; b) E. Kikuta, S. Aoki and E. Kimura, *J. Am. Chem. Soc.*, **2001**, *123*, 7911-7912.

[39] M. Morikawa, M. Yoshihara, T. Endo and N. Kimizuka, *J. Am. Chem. Soc.*, **2005**, *127*, 1358-1359.

[40] a) J. A. Aguilar, E. García-España, J. A. Guerrero, S. V. Luis, J. M. Llinares, J. A. Ramírez, C. Soriano, *J. Chem. Soc., Chem. Commun.* **1995**, 2237; b) J. A. Aguilar, E. García-España, J. A. Guerrero, S. V. Luis, J. M. Llinares, J. A. Ramírez, C. Soriano, *Inorg. Chim. Acta*, **1996**, *246*, 287.

[41] a) K. Niikura, A. Metzger, E. V. Anslyn, *J.Am. Chem. Soc.*, **1998**, *120*, 8533 - 8534; b) Z. Zhong, E. V. Anslyn, *J. Am. Chem. Soc.*, **2002**, *124*, 9014 – 9015; c) D. H. Lee, S. Y. Kim, and J.-I Hong, *Angew. Chem. Int. Ed.*, **2004**, *43*, 4777 –4780.

[42] a) F. Zapata, A. Caballero, A. Espinosa, A. Tárraga and P. Molina, *J. Org. Chem.*, **2008**, *73*, 4034 – 4044; b) C. Li, M. Numata, M. Takeuchi and S. Shinkai, *Angew. Chem. Int. Ed.*, **2005**, *44*, 6371 – 6374.

[43] C. Bazzicalupi, S. Biagini, A. Bencini, E. Faggi, C. Giorgi, I. Matera and B. Valtancoli, *Chem. Commun.*, **2006**, 4087–4089.

[44] A. Ojida, S.-K. Park, Y. Mito-oka and I. Hamachi, *Tetrahedron Lett.*, **2002**, *43*, 6193 - 6195.

[45] A. Ojida, I. Takashima, T. Kohira, H. Nonaka and I. Hamachi, *J. Am. Chem. Soc.*, **2008**, *130*, 12095 - 12101.

[46] F. Sancenón, A. B. Descalzo, R. M.- Máñez, M. A. Miranda and J. Soto, *Angew. Chem. Int. Ed.*, **2001**, *40*, 2640.

[47] a) R. M.- Máñez and F. Sancenón, *Chem. Rev.*, **2003**, *103*, 4419-4476; b) E. J. Cho, J. W. Moon, S. W. Ko, J. Y. Lee, S. K. Kim, J. Yoon, K. C. Nam, *J. Am. Chem. Soc.* **2003**, *125*, 12376.

[48] B. Alberts, A. Johnson, J. Lewis, M. Raff, K. Roberts, P. Walter. *Molecular Biology of the Cell*, **2002**, Garland Science: New York.

[49] J. Y. Kwon, N. J. Singh, H. N. Kim, S. K. Kim, K. S. Kim and J. Yoon, *J. Am. Chem. Soc.*, **2004**, 126, 8892-8893.

[50] P. P. Neelakandan, M. Hariharan and D. Ramaiah, *J. Am. Chem. Soc.*, **2006**, *128*, 11334-11335.

[51] R. Seifert, G. Schultz, *Trends Pharmacol.*, **1989**, *10*, 365.

[52] T. Page, A. Yu, J. Fontanesi, W. L. Nyhan, *Proc. Natl. Acad. Sci. U.S.A.*, **1997**, *94*, 11601.

[53] F. J. Gonzalez, P. Fernandez-Salguero, *Trends Pharmacol. Sci.*, **1995**, *16*, 325.

[54] G. P. Connolly, H. A. Simmonds, J. A. Duley, *Trends Pharmacol. Sci.*, **1996**, *17*, 107.

[55] W. Tan, Z. Wang, D. Zhang and D. Zhu, *Sensors*, **2006**, *6*, 954-961.

[56] C. Bazzicalupi, A. Bencini, L. Bussotti, E. Berni, S. Biagini, E. Faggi, P. Foggi, C. Giorgi, A. Lapini, A. Marcelli and B. Valtancoli, *Chem. Commun.*, **2007**, 1230–1232.

[57] N. Singh, G. W. Lee and D. O. Jang, *Tetrahedron Lett.*, **2008**, *49*, 44-47.

[58] P. Turkewitsch, B. Wandelt, R. R. Ganju, G. D. Darling, W. S. Powell, *Chem. Phys. Lett.*, **1996**, *260*, 142-146.

[59] G. Zubay, Biochemistry, 2nd Ed., **1988**, Macmillan, New York.

[60] V. Balzani, S. Campagna, G. Denti, A. Juris, S. Serroni and M. Venturi, *Acc. Chem. Res.* , **1998**, *31*, 26-34.

[61] V. Balzani, P. Ceroni, A. Juris, M. Venturi, S. Campagna, F. Puntoriero and S. Serroni, *Coord. Chem. Rev.*, **2001**, *219*, 545-572.

[62] V. Balzani and A. Juris, *Coord. Chem. Rev.*, **2001**, *211*, 97-115.

[63] S. Di Bella, *Chem. Soc. Rev.*, **2001**, *30*, 355-366.

[64] P. G. Lacroix, *Eur. J. Inorg. Chem.*, **2001**, 339-348.

[65] K. E. Erkkila, D. T. Odom and J. K. Barton, *Chem. Rev.*, **1999**, *99*, 2777-2795.

[66] C. Creutz and H. Taube, *J. Am. Chem. Soc.*, **1969**, *91*, 3988.

[67] J. P. Paris and W. W. Brandt, *J. Am. Chem. Soc.*, **1959**, *81*, 5001.

[68] S. Serroni, S. Campagna, F. Punteriero, C. Di Pietro, N. D. McClenaghan and F. Loiseau, *Chem. Soc. Rev.*, **2001**, *30*, 367.

[69] M. Wrighton, D. L. Morse, *J. Am. Chem. Soc.*, 1974, *96*, 998.

[70] J. A. Baiano, R. J. Kessler, R. S. Lumpkin, M. J. Munley and W. R. Murphy, Jr., *J. Phys. Chem.* , **1995**, *99*, 17680.

[71] J. A. Baiano and W. R. Murphy, Jr., *Inorg. Chem.*, **1991**, *30*, 4594.

[72] J. V. Caspar and T. J. Meyer, *J. Phys. Chem.*, **1983**, *87*, 952.

[73] A. Juris, S. Campagna, I. Bidd, J.-M. Lehn and R. Ziessel, *Inorg. Chem.*, **1988**, *27*, 4007.

[74] K. Bierig, R. J. Morgan, S. Tysoe, H. D. Gafney, T. C. Strekas and A. D. Baker, *Inorg. Chem.*, **1991**, *30*, 4898.

[75] M. A. Hayes, C. Meckel, E. Schatz and M. D. Ward, *J. Chem. Soc. Dalton Trans.*, **1992**, 703.

[76] P. De Wolf, S. L. Heath and J. A. Thomas, *Inorg. Chim. Acta.*, **2003**, *355*, 280.

[77] F. H. Burstall, *J. Chem. Soc., Dalton Trans.*, **1938**, 1662.

[78] R. J. Forster and T. E. Keyes, *J. Phys. Chem. B*, **1998**, *102*, 10004-10012.

[79] R. J. Forster, T. E. Keyes and M. Majda, *Phys. Chem. B*, **2000**, *104*, 4424.

[80] R. J. Morgan and A. D. Baker, *J. Org. Chem.*, **1990**, *55*, 1986.

[81] J. E. Dickeson and L. A. Summers, *Aust. J. Chem.*, **1970**, *23*, 1023-1027.

[82] W. Paw and R. Eisenberg, *Inorg. Chem.*, **1997**, *36*, 2287.

[83] A. E. Friedman, J. -C. Chambron, J. -P. Sauvage, N. J. Turro and J. K. Barton, *J. Am. Chem. Soc.*, **1990**, *112*, 4960.

[84] R. M. Hartshorn, J. K. Barton, *J. Am. Chem. Soc.* **1992**, *114*, 5919 - 5925.

[85] M. Atsumi, L. González and C. Daniel, *J. Photochem. Photobiol., A.*, **2007**, *190*, 310.

[86] B. P. Sullivan, D. J. Salmon and T. J. Meyer, *Inorg. Chem.*, **1978**, *17*, 3334.

[87] E. M. Kober, J. L. Marshall, W. J. Dressick, B. P. Sullivan, J. V. Caspar and T. J. Meyer, *Inorg. Chem.*, **1985**, 2755-2763.

[88] B. P. Sullivan, H. Abruna, H. O. Finklea, D. J. Salmon, J. K. Nagle, T. J. Meyer and H. Sprintschnik, *Chem. Phys. Lett.*, **1978**, *58*, 389.

[89] L. J. Henderson, Jr. and W. R. Cherry, *J. Photochem.*, **1985**, *28*, 143-151.

[90] B. J. Yoblinski, M. Stathis and T. F. Guarr, *Inorg. Chem.*, **1992**, *31*, 5.

[91] J. A. Baiano, R. J. Kessler, R. S. Lumpkin, M. J. Munley and W. R. Murphy, Jr., *J. Phys. Chem.*, **1995**, *99*, 17680.

[92] Verónica González González, University of Sheffield, **2006**.

[93] S. L. W. McWhinnie, S. M. Charsley, C. J. Jones, J. A. McCleverty, L. J. Yellowlees, *Dalton Trans.*, **1993**, 413-16.

[94] J. Fees, W. Kaim, M. Moscherosch, W. Matheis, J. Klíma, M. Krejčík and S. Záliš, *Inorg. Chem.*, **1993**, *32*, 166-174.

[95] D. Voet and J. G. Voet, *Biochemistry*, 2nd ed., **1995**, John Wiley & Sons, New York.

[96] C. R. Calladine and H. R. Drew, *Understanding DNA: The Molecule & How It Works*, **1992**, Academic Press, Cambridge.

[97] S. Doonan, *Nucleic Acids*, **2004**, the Royal Society of Chemistry, Cambridge.

[98] G. M. Blackburn, M. J. Gait, D. Loakes and D. M. Williams, *Nucleic Acids in Chemistry and Biology*, 3rd ed., **2006**, RSC, Cambridge.

[99] P. Belmont, J. -F. Constant and M. Demeunynck, *Chem. Soc. Rev.*, **2001**, *30*, 70-81.

[100] C. C. Sines, L. McFail-Isom, S. B. Howerton, D. VanDerveer and L. D. Williams, *J. Am. Chem. Soc.*, **2000**, *122*, 11048-11056.

[101] S. E. Franklin and R. G. Gosling, *Nature*, **1953**, *171*, 740-741.

[102] Y.-G. Gao, H. Robinson and A. H. J. Wang, *Eur. J. Biochem.*, **1999**, *261*, 413-420.

[103] R. E. Dickerson, H. R. Drew, B. N. Conner, R. M. Wing, A. V. Fratini and M. L. Kopka, *Science*, **1982**, *216*, 475-485.

[104] T. J. Thomas, U. B. Gunnia and T. Thomas, *J. Biol. Chem.*, **1991**, *266*, 6137-6141.

[105] H. S. Basu and L. J. Marton, *Biochem. J.*, **1987**, *244*, 243-6.

[106] W. Goddard, K. Plaxco, *Biochemistry*, **1994**, *33*, 3050.

[107] D. S. Goodsell, M. L. Kopka and R. E. Dickerson, *Biochemistry*, **1995**, *34*, 4983-4993.

[108] R. M. Wartell, J. E. Larson and R. D. Wells, *J. Biol. Chem.*, **1974**, *249*, 6719-6731.

[109] A. Pullman and B. Pullman, *Q. Rev. Biophys.*, **1981**, *14*, 289-380.

[110] C. Zimmer and U. Wahnert, *Prog. Biophys. Mol. Biol.*, **1986**, *47*, 31-112.

[111] D. J. Patel, *Proc. Natl. Acad. Sci. U.S.A.*, **1982**, *79*, 6424 - 6428.

[112] M. L. Kopka, C. Yoon, D. Goodsell, P. Pjura, R. E. Dickerson, *Proc. Natl. Acad. Sci. U.S.A.*, **1985**, *82*, 1376 - 1380.

[113] M. Coll, C. A. Frederick, A. H. -J. Wang, A. Rich, *Proc. Natl. Acad. Sci. U.S.A*, **1987**, *84*, 8385 - 8389.

[114] J. G. Pelton and D. E. Wemmer, *Proc. Natl. Acad. Sci. U.S.A.*, **1989**, *86*, 5723-5727.

[115] J. G. Pelton and D. E. Wemmer, *J. Am. Chem. Soc.*, **1990**, *112*, 1393-1399.

[116] S. N. Mitra, M. C. Wahl and M. Sundaralingam, *Acta Crystallogr., Sect. D: Biol. Crystallogr.*, **1999**, *55*, 602-609.

[117] F. G. Lootiens, L.W. McLaughlin, S. Diekmann and R.M.Clegg, *Biochemistry*, **1991**, *30*, 182-189.

[118] A. Abu-Daya, P. M. Brown and K. R. Fox, *Nuceic Acids Res.*, **1995**, *23*, 3385-3392.

[119] M. K. Teng, N. Usman, C. A. Frederick, A. H. Wang, *Nucleic Acids Res.*, **1988**, *16*, 2671-90.

[120] L. S. Lerman, *J. Mol. Biol.*, **1961**, *3*, 18-30.

[121] L. S. Lerman, *Proc. Natl Acad Sci. U.S.A.*, **1963**, *49*, 94.

[122] S. Satyanarayana, J. C. Dabrowiak, J. B. Chaires, *Biochemistry*, **1993**, *32*, 2573.

[123] E. C. Long and J. K. Barton, *Acc. Chem. Res.*, **1990**, *23*, 271-273.

[124] S. Dongchul and J. B. Chaires, *Bioorg. & Med. Chem.*, **1995**, *3*, 723-728.

[125] M. J. Waring, *J. Mol. Biol.* **1965**, *13*, 269.

[126] I.-L. M. Sobell, C. Tsai, S. C. Jain and S. Gilbert, *J. Mol. Biol.*, **1977**, *114*, 333.

[127] C. Tsai, S. C. Jain, I.-L. M. Sobell, *Proc. Natl Acad Sci. U.S.A.*, **1975**, *72*, 628.

[128] J. B. Chaires, *Biochemistry*, **1983**, *22*, 4204-4211.

[129] J. B. Chaires, N. Dattagupta and D. M. Crothers, *Biochemistry*, **1982**, *21*, 3933-3940.

[130] A. H. J. Wang, G. Ughetto, G. J. Quigley and A. Rich, *Biochemistry*, **1987**, *26*, 1152-1163.

[131] S. Kamitori and F. Takusagawa, *J. Mol. Biol*, **1992**, *225*, 445-456.

[132] T. Phillips, I. Haq, A. J. H. M. Meijer, H. Adams, I. Soutar, L. Swanson, M. J. Sykes, and J. A. Thomas, *Biochemistry*, **2004**, 43, 13657-13665.

[133] T. Phillips, C. Rajput, L. Twyman, I. Haq and J. A. Thomas, *Chem. Commun.*, **2005**, 4327–4329.

[134] F. M. Chen, *Biochemistry*, **1988**, *27*, 1843.

[135] K. W. Jennette, S. J. Lippard, G. A. Vassiliades and W. R. Bauer, *Proc. Natl. Acad. Sci. U.S.A.*, **1974**, *71*, 3839-3843.

[136] J. K. Barton, A. Danishefsky and J. Goldberg, *J. Am. Chem. Soc.*, **1984**, *106*, 2172-2176.

[137] J. K. Barton, J. M. Goldberg, C. V. Kumar and N. J. Turro, *J. Am. Chem. Soc.*, **1986**, *108*, 2081-2088.

[138] J. K. Barton, *Science*, **1986**, *233*, 727.

[139] C. Hiort, B. Nordén and A. Rodger, *J. Am. Chem. Soc.*, **1990**, *112*, 1971-1982.

[140] S. Satyanarayana, J. C. Dabrowiak and J. B. Chaires, *Biochemistry*, **1992**, *31*, 9319-9324.

[141] D. Z. M. Coggan, I. S. Haworth, P. J. Bates, A. Robinson and A. Rodger, *Inorg. Chem.*, **1999**, *38*, 4486-4497.

[142] C. Hiort, P. Lincoln and B. Nordén, *J. Am. Chem. Soc.*, **1993**, *115*, 3448-3454.

[143] E. Tuite, P. Lincoln and B. Nordén, *J. Am. Chem. Soc*, **1997**, *119*, 239-240.

[144] R. E. Holmlin, E. D. A. Stemp and J. K. Barton, *Inorg. Chem.*, **1998**, *37*, 29-34.

[145] C. M. Dupureur and J. K. Barton, *Inorg. Chem.*, **1997**, *36*, 33-43.

[146] I. Greguric, J. R. Aldrich-Wright and J. G. Collins, *J. Am. Chem. Soc.*, **1997**, *119*, 3621-3622.

[147] T. Biver, C. Cavazza, F. Secco and M. Venturini, *J. Inorg. Biochem.*, **2007**, *101*, 461-469.

[148] N. B. Thornton and K. S. Schanze, *Inorg. Chem.*, **1993**, *32*, 4994.

[149] D. R. Striplin, G. A. Crosby, *Chem. Phys. Lett.*, **1994**, *221*, 426.

[150] H. D. Stoeffler, N. B. Thornton, S. L. Temkin and K. S. Schanze, *J. Am. Chem. Soc.*, **1995**, *117*, 7119.

[151] V. W. W. Yam, K. K. W. Lo, K. K. Cheung and R. Y. C. Kong, *J. Chem. Soc.-Chem. Commun.*, **1995**, 1191-1193.

[152] V. W. W. Yam, K. K. W. Lo, K. K. Cheung, R. Y. C. Kong, *J. Chem. Soc.-Dalton Trans.*, **1997**, 2067-2072.

[153] I. Sasaki, M. Imberdis, A. Guademer, B. Drahi, D. Azhari and E. Amouyal, *New J. Chem.*, **1994**, *18*, 759.

[154] F. M. O'Reilly, J. M. Kelly and A. K.-D. Mesmaeker, *Chem. Commun.*, **1996**, 1013-1014.

[155] F. M. O'Reilly and J. M. Kelly, *New J. Chem.*, **1998**, *22*, 215-217.

[156] P. Lincoln and B. Nordén, *J. Chem. Soc., Chem. Comm.*, **1996**, 2145-2146.

[157] L. M. Wilhelmsson, F. Westerlund, P. Lincoln and B. Nordén, *J. Am. Chem. Soc.*, **2002**, *124*, 12092-12093.

[158] B. Onfelt, P. Lincoln, B. Nordén, *J. Am. Chem. Soc.*, **1999**, *121*, 10846-10847.

[159] C. Metcalfe, M. Webb and J. A. Thomas, *Chem. Commun.*, **2002**, 2026–2027.

[160] C. Metcalfe, I. Haq and J. A. Thomas, *Inorg. Chem.*, **2004**, *43*, 317-323.

[161] S. P. Foxon, T. Phillips, M. R. Gill, M. Towrie, A. W. Parker, M. Webb and J. A. Thomas, *Angew. Chem., Int. Ed.*, **2007**, *46*, 3686-3688.

[162] M. J. Hannon, V. Moreno, M. J. Prieto, E. Moldrheim, E. Sletten, I. Meistermann, C. J. Isaac, K. J. Sanders and A. Rodger, *Angew. Chem. Int. Ed.*, **2001**, *40*, 880.

[163] B. Schoentjes and J.-M. Lehn, *Helv. Chim. Acta*, **1995**, *78*, 1.

[164] I. Meistermann, V. Moreno, M. J. Prieto, E. Moldrheim, E. Sletten, S. Khalid, P. M. Rodger, J. C. Peberdy, C. J. Isaac, A. Rodger and M. J. Hannon, *Proc. Nat. Acad. Sci. U.S.A.*, **2002**, *99*, 5069-5074.

[165] G. I. Pascu, A. C. G. Hotze, C. S.-Cano, B. M. Kariuki and M. J. Hannon, *Angew. Chem. Int. Ed.*, **2007**, *46*, 4374-4378.

[166] M. A. Galindo, D. Olea, M. A. Romero, J. Gómez, P. del Castillo, M. J. Hannon, A. Rodger, F. Zamora and J. A. R. Navarro, *Chem. Eur. J.*, **2007**, *13*, 5075 – 5081.

[167] R. Kieltyka, P. Englebienne, J. Fakhoury, C. Autexier, N. Moitessier and H. F. Sleiman, *J. Am. Chem. Soc.*, **2008**, *130*, 10040-10041.

[168] D. Ghosh, H. Ahmad and J. A. Thomas, *Chem. Commun.*, **2009**, 2947.

[169] J. K. Barton and S. J. Lippard, *Biochemistry*, **1979**, *18*, 2661-2668.

[170] P. Job, *Ann. Chim. (paris)*, **1928**, *9*, 113-203.

[171] C. Y. Huang, *Methods Enzymol.*, **1982**, *87*, 509-525.

[172] J. Fees, W. Kaim, M. Moscherosch, W. Matheis, J. Klima, M. Krejcik, S. Zalis, *Inorg. Chem.*, **1993**, *32*, 166-174.

[173] G. Scatchard, *Ann. N. Y. Acad. Sci.*, **1949**, *51*, 660-672.

[174] J. D. McGhee and P. H. von Hippel, *J. Mol. Biol.*, **1974**, *86*, 469-489.

[175] T. Wiseman, S. Williston, J. F. Brandts and L. N. Lin, *Anal. Biochem.*, **1989**, *179*, 131-137.

[176] I. Haq, B. Z. Chowdhry and T. C. Jenkins, *Methods Enzymol.*, **2001**, *340*, 109-149.

[177] I. Haq, *Arc. Biochem. Biophys.*, **2002**, *403*, 1-15.

[178] I. Haq, *Biocalorimetry: Applications of Calorimetry in the Biological Sciences* (Ladbury, J. E., and B.Z.Chowdry, Eds.), **1998**, John Wiley & Sons Ltd., London.

[179] J. G. Liu, B. H. Ye, H. Li, Q. X. Zhen, L. N. Ji and Y. H. Fu, *J. Inorg. Biochem.*, **1999**, *76*, 265.

[180] J. Sun, S. Wub, Y. Han, J. Liu, L.-N. Ji, Z.-W. Mao, *Inorg. Chem. Commun.*, **2008**, *11*, 1382–1384.

[181] G. Dougherty, and J. R. Pilbrow, *Int. J. Biochem.* **1984** *16*, 1179-1192.

[182] R. E. Holmlin, J. A.Yao, and J. K. Barton, *Inorg. Chem.*, **1999**, *38*, 174-189.

[183] V. G. Vaidyanathan and B. U. Nair, *J. Inorg. Biochem.*, **2003**, *95*, 334-342.

[184] C. Metcalfe, H. Adams, I. Haq, J. A. Thomas, *Chem. Commun.*, **2003**, 1152 - 1153.

[185] R. J. Morgan, S. Chatterjee, A. D. Baker and T. C. Strekas, *Inorg. Chem.* **1991**, *30*, 2687 – 2692.

[186] D. E. V. Schmechel and D. M. Crothers. *Biopolymers*, **1971**, *10*, 465 - 480.

[187] S. P. Foxon, C. Metcalfe, H. Adams, M. Webb and J. A. Thomas, *Inorg. Chem.* , **2007**, *46*, 409-416.

[188] J. B. Chaires, W. Priebe, D. E. Graves, and T. G. Burke, *J. Am. Chem. Soc.*, **1993**, *115*, 5360-5364.

[189] H. P. Hopkins, J. Fumero and W. D. Wilson, *Biopolymers*, **1990**, *29*, 449-459.

[190] G. S. Manning, *J. Chem.Phys.*, **1969**, *51*, 924-933.

[191] M. T. Record, C. F. Anderson, T. M. Lohman, *Q. Rev. Biophys.*, **1978**, *11*, 103-178.

[192] B. M. Goldstein, J. K. Barton and H. M. Berman, *Inorg. Chem.*, **1986**, *25*, 842.

[193] C. Metcalfe, C. Rajput, J. A. Thomas, *J. Inorg. Biochem.*, **2006**, *100*, 1314–1319.

[194] R. B. Nair, E. S. Teng, S. L. Kirkland, C. J. Murphy, *Inorg. Chem.*, **1998**, *37*, 139 - 141.

[195] I. Haq, P. Lincoln, D. Suh, B. Nordén, B. Z. Chowdrey and J. B. Chaires, *J. Am. Chem. Soc.*, **1995**, *117*, 4788–4796

[196] R. Lin, T. F. Guarr, *Inorg. Chim. Acta,* **1990**, *167*, 149.

[197] R. Lin, T. F. Guarr, R. Duesing, *Inorg. Chem.* **1990**, *29*, 4169.

[198] J. A. Baiano and W. R. Murphy, Jr., *Inorg. Chem.*, **1991**, *30*, 4594.

[199] a) S. Goswami, D. Van Engen, A. D. Hamilton, *J. Am. Chem. Soc.*, **1989**, *111*, 3425 - 3426; b) S. C. Zimmerman, W. Wu, Z. Zeng, *J. Am. Chem. Soc.*, **1991**, *113*, 196 - 201; c) H. Ogoshi, H. Hatakeyama, J. Kotani, A. Kawashima, Y. Kuroda, *J. Am. Chem. Soc.*, **1991**, *113*, 8181 – 8183; d) R. Güther, M. Nieger, F. Vögtle, *Angew. Chem.*, **1993**, *105*, 647 – 649; *Angew. Chem. Int. Ed. Engl.*, **1993**, *32*, 601 –603.

[200] S. Mizukami, T. Nagano, Y. Urano, A. Odani, and K. Kikuchi, *J. Am. Chem. Soc.*, **2002**, *124*, 3920-3925.

[201] (a) G. Cohen and H. Eisenberg, *Biopolymers*, **1969**, *8*, 45–55; (b) L. Kapicak and E. J. Gabbay, *J. Am. Chem. Soc.*, **1975**, *97*, 403–408; (c) N. Dattagupta, M. Hogan and D. M. Crothers, *Proc. Natl. Acad. Sci. U. S. A.*, **1978**, *75*, 4286–4290; (d) L. P. G. Wakelin, A. Adams, C. Hunter and M. J. Waring, *Biochemistry*, **1981**, *20*, 5779–5787.

[202] (a) C. Moucheron, A. Kirsch-De Mesmaeker and J. M. Kelly, *J. Photochem. Photobiol., B*, **1997**, *40*, 91–106; (b) I. Ortmans, B. Elias, J. M. Kelly, C. Moucheron and A. Kirsch-De Mesmaeker, *Dalton Trans.*, **2004**, 668.

[203] A. T. R. Williams, S. A. Winfield, J N. Miller, *Analyst*, **1983**, *108*, 1067.

[204] H. R. Revel, *Bacteriophage T4*, **1983**, (C. K. Mathews, E. M. Kutter, G. Mosig and P. B. Berget, Eds.) pp 156-165, American Society for Microbiology, Washington, DC.